

2016

A Search for baryon number violation by two units at the Super-Kamiokande detector

<https://hdl.handle.net/2144/17741>

Boston University

BOSTON UNIVERSITY
GRADUATE SCHOOL OF ARTS AND SCIENCES

Dissertation

**A SEARCH FOR BARYON NUMBER VIOLATION BY TWO UNITS
AT THE SUPER-KAMIOKANDE DETECTOR**

by

Jeffrey D. Gustafson

B.A., Macalester College, 2009

Submitted in partial fulfillment of the

requirements for the degree of

Doctor of Philosophy

2016

© Copyright by
JEFFREY GUSTAFSON
2016

Approved by

First Reader

Edward T. Kearns, Ph.D.
Professor of Physics

Second Reader

Robert Carey, Ph.D.
Professor of Physics

Acknowledgements

There are many, many people to whom I owe thanks for the successful completion of my Ph.D, and by extension, a completion of my life up to this point. I'll try to limit my scope to people who are in tangible danger of actually reading this.

My advisor, Professor Ed Kearns, cannot be thanked enough. Ed took me on knowing I had very little high energy physics experience, and was always extremely gracious and patient as I struggled to become a useful graduate student. His unparalleled mastery of neutrino physics, motivating attitude, generously-shared wisdom, and infectious sense of humor were instrumental in helping me graduate. Ed knew when to push, but he also taught me the valuable lesson of when to “declare victory”, for which this occasion is ideal.

It has been an enormous honor and privilege to work at the Super-Kamiokande experiment, which after 20 years (and a Nobel Prize!) remains one of the beacons of modern high-energy physics. The hard work and dedication of all collaborators past and present, those I have met and those I haven't, has been a continuous source of inspiration. In particular, the leadership of Spokesmen Yoichiro Suzuki and Masayuke Nakahata during my time on the experiment, and the leadership of the Atmospheric Neutrino and Proton Decay group by Professor Kearns and Masato Shiozawa, has ensured that Super-K continues to produce world-class physics at this late stage.

Within Super-K, I have been privileged to work closely with a number of great

physicists. With no pretense of exhaustion, I'd particularly like to thank Doctors Makoto Miura and Shunichi Mine for their proton decay expertise and suggestions, and setting outstanding examples with their highly methodical approaches; Dr. Jennifer Raaf, for patiently showing me the ropes on all things UPMU; Dr. Yoshinari Hayato, for promptly and kindly answering all of my dumb questions, particularly related to NEUT; and Dr. Roger Wendell, for a list of things that would probably reach the length of this thesis to properly do justice.

It has been a pleasure to work at the Boston University Department of Physics at all levels of the graduate school experience. I'd particularly like to thank each member of my committee — Professor Rob Carey for being my second reader and promptly providing helpful comments, Professor Shyam Erramilli for his friendly first-year lessons in electromagnetism (as well as the “conservation of pain”), Professor Tulika Bose for her valuable introduction to particle physics in PY551 that I somewhat belatedly took, and Professor Andy Cohen for kindly agreeing to be on my committee on short notice. I'd also like to thank my erstwhile committee member Professor Martin Schmaltz for his helpful comments on the theory of my analysis. At the administrative level, I'd like to thank Winna Somers for patiently dealing with my travel forms, which somehow confused me anew each time I went to Japan, and Mirtha Cabello for everything else. I've always felt good coming into work with office-mates and BU Neutrino group members like Chris Kachulis, Ryan Linehan, Flor de Maria Blaszczyk, and Dan Gastler.

The friends I've made at BU and elsewhere during my time in graduate school have been invaluable in making the experience great. In particular, the friendship of Alex Long helped keep me sane, especially in the first two years. I've had great times with Colin Howard over our shared love of music. Michael Chernicoff is, as far as I can tell, incapable of holding a dull conversation. While I did not see him nearly as

much as I would have liked, Euan Richard was always a good laugh.

My family has been a fundamental source of emotional, moral, and financial support since the day I was born. I am extremely fortunate to maintain a close relationship with my parents, Jim and Lori Gustafson, without whom I'd be nowhere. While I don't talk to her enough, my sister Katie has always been there for me. The broad wisdom and compassion of my aunt Aline has continually amazed me. Finally, I am proud to say I am the second physics Ph.D in the family, after my wonderful uncle Dr. Steve Gustafson, although now that we share the same title it will be somewhat less of an event when I beat him in chess.

**A SEARCH FOR BARYON NUMBER VIOLATION BY TWO UNITS
AT THE SUPER-KAMIOKANDE DETECTOR**

JEFFREY D. GUSTAFSON

Boston University Graduate School of Arts and Sciences, 2016

Major Professor: Edward T. Kearns, Professor of Physics

ABSTRACT

Baryon number B appears to be a conserved quantity in the Standard Model of particle physics, though there are compelling theoretical reasons to believe it isn't. This thesis describes searches for processes that violate B by two units with the Super-Kamiokande experiment. Two types of searches are performed. One is the simultaneous decay of two bound nucleons to pions (dinucleon decay), encompassing the modes $^{16}\text{O}(pp) \rightarrow ^{14}\text{C} \pi^+\pi^+$, $^{16}\text{O}(pn) \rightarrow ^{14}\text{N} \pi^+\pi^0$, and $^{16}\text{O}(nn) \rightarrow ^{14}\text{O} \pi^0\pi^0$. The second is a search for a neutron transforming into an antineutron, or neutron-antineutron oscillation $n \rightarrow \bar{n}$.

This thesis uses the full dataset across four Super-Kamiokande detector periods from April 1996 to March 2015, comprising 4972.4 livetime days (307 kiloton-years). Monte Carlo simulations of the signal processes and their background from atmospheric neutrino interactions are used to estimate signal efficiency, expected background, and their associated uncertainties. Both multivariate analyses and simple kinematical cuts are applied in these searches. This is the first search for dinucleon decay to pions in oxygen. The search for $n \rightarrow \bar{n}$ entails some important updates from a previous search at Super-Kamiokande, mainly increased exposure and an improved model of pion interactions.

In each mode investigated, no signal excess was observed, and all data are consistent with atmospheric neutrino background. In the absence of evidence for any

signal process, lower lifetimes are set at the 90% confidence level. For dinucleon decay, the limits are $\tau_{pp \rightarrow \pi^+ \pi^+} > 7.2 \times 10^{31}$ years, $\tau_{pn \rightarrow \pi^+ \pi^0} > 1.7 \times 10^{32}$ years, and $\tau_{nn \rightarrow \pi^0 \pi^0} > 4.0 \times 10^{32}$ years. These limits are about two orders of magnitude more stringent than those set by previous searches for dinucleon decay in iron. For $n \rightarrow \bar{n}$, the limit for bound neutrons is $\tau_{\text{bound}} > 2.4 \times 10^{32}$ years, corresponding to a free neutron lifetime $\tau_{\text{free}} > 3.8 \times 10^8$ s. This is comparable with previous results from Super-Kamiokande and other experiments.

Contents

Acknowledgements	iv
Abstract	vii
Table of Contents	ix
List of Tables	xiv
List of Figures	xxi
List of Abbreviations	xxxvii
1 Introduction	1
2 Motivation and Theory	4
2.1 Baryon Number	4
2.2 The Standard Model	5
2.3 Baryogenesis and Baryon Asymmetry	7
2.4 Models	10
2.5 Phenomenology and previous results	13
2.5.1 $n\bar{n}$ oscillations	14
2.5.2 Dinucleon Decay	19

3	The Super-Kamiokande Detector	22
3.1	Overview	22
3.2	Structure	24
3.2.1	Inner Detector (ID)	24
3.2.2	Outer Detector (OD)	25
3.3	Cherenkov Radiation	25
3.4	Photomultiplier tubes	27
3.4.1	Inner Detector	27
3.4.2	Outer Detector	28
3.5	Electronics and Data Acquisition (DAQ)	29
3.5.1	Inner Detector Electronics and DAQ (SK I-III)	30
3.5.2	Outer Detector Electronics and DAQ (SK-I-III)	31
3.5.3	Trigger (SK-I-III)	32
3.5.4	SK-IV Electronics and DAQ Upgrade	33
3.6	Water Purification System	35
3.7	Calibration	35
3.7.1	Water Calibration	36
3.7.2	Charge calibration	38
3.7.3	Timing Calibration	42
3.7.4	Energy Scale	43
4	Atmospheric Neutrino Simulation	48
4.1	Neutrino Flux	49
4.2	Neutrino interactions	51
4.2.1	(Quasi)-elastic scattering	52
4.2.2	Single meson production	52

4.2.3	Deep inelastic scattering	53
4.2.4	Nuclear effects	55
4.3	Detector Simulation	59
5	Signal Simulation	61
5.1	Dinucleon Decay	61
5.2	Neutron-antineutron oscillation	63
6	Reduction and Reconstruction	67
6.1	Fully Contained Reduction Steps	68
6.1.1	First Reduction	68
6.1.2	Second Reduction	68
6.1.3	Third Reduction	70
6.1.4	Fourth Reduction	75
6.1.5	Fifth reduction	76
6.1.6	Final FC sample	78
6.2	Event Reconstruction	79
6.2.1	Vertex fitting	80
6.2.2	Ring counting	82
6.2.3	Particle identification	84
6.2.4	Momentum reconstruction	88
6.2.5	Decay electrons	89
6.2.6	π^0 reconstruction	90
7	Dinucleon Decay Search	91
7.1	Boosted Decision Trees	92
7.2	$pp \rightarrow \pi^+\pi^+$	97

7.2.1	Pre-selection for $pp \rightarrow \pi^+\pi^+$	97
7.2.2	Multivariate analysis for $pp \rightarrow \pi^+\pi^+$	98
7.2.3	Final sample for $pp \rightarrow \pi^+\pi^+$	101
7.3	$pn \rightarrow \pi^+\pi^0$	108
7.3.1	Pre-selection for $pn \rightarrow \pi^+\pi^0$	108
7.3.2	Multivariate analysis for $pn \rightarrow \pi^+\pi^0$	111
7.3.3	Final sample for $pn \rightarrow \pi^+\pi^0$	112
7.4	$nn \rightarrow \pi^0\pi^0$	118
7.4.1	Selection criteria for $nn \rightarrow \pi^0\pi^0$	118
7.4.2	Final sample for $nn \rightarrow \pi^0\pi^0$	119
7.5	Systematic Uncertainties	122
7.5.1	Simulation Uncertainties	123
7.5.2	Reconstruction and BDT uncertainties	126
8	Neutron-Antineutron Oscillation Search	132
8.1	Pre-selection	132
8.2	Multivariate analysis	133
8.2.1	Standard variables	134
8.2.2	Non-standard variables	136
8.3	Final selection	138
8.3.1	Systematic uncertainties	143
8.3.2	Final cut	144
8.3.3	Data discrepancy	145
9	Results and discussion	153
9.1	Lifetime limits	153
9.1.1	Dinucleon decay	154

9.1.2	Neutron-antineutron oscillation	154
9.2	Discussion	155
9.2.1	Global BNV searches	155
9.2.2	Comparison with previous SK $n \rightarrow \bar{n}$ analysis	156
Appendices		161
A	$n \rightarrow \bar{n}$ Branching Fractions	162
B	Plots of Multivariate Input Variables for SK-I-III	166
C	Limit Calculations	182
Bibliography		186
Curriculum Vitae		193

List of Tables

2.1	Limits on bound neutron oscillation lifetimes from Irvine-Michigan-Brookhaven ([31]), Kamiokande([32]), Frejus ([33]), Soudan-II ([34]), Sudbury Neutrino Observatory([35]), and Super-Kamiokande ([23]). Limits are converted to a free oscillation time via Equation 2.16. See the text for a comparison to the free neutron experiment from [29]. The values of R for [31–35] are calculated in [36], while the value of R used for [23] incorporates a more recent calculation from [27]. The uncertainty in R is also incorporated in the conversion to the free lifetime in [23]. The study in [35] used a different search method than the other analyses listed, such that efficiency, background rate, and data candidates are not illuminating figures.	20
2.2	Summary of results for $NN \rightarrow \pi\pi$ from Frejus [39], and $pp \rightarrow K^+K^+$ [40] and $pp \rightarrow e^+e^+$ [41] from Super-Kamiokande. The Frejus searches were performed with 2.2×10^{31} iron-years of exposure, and the Super-Kamiokande searches with 3.06×10^{32} oxygen-years.	21
3.1	Specifications for the ID PMTs.	30
3.2	Specifications for the ATM.	31

4.1	Interactions modeled for each particle type. Cherenkov radiation is modeled for e^\pm , μ^\pm , and charged hadrons.	60
5.1	Number of pions for $pp \rightarrow \pi^+\pi^+$ (top), $pn \rightarrow \pi^+\pi^0$ (middle), and $nn \rightarrow \pi^0\pi^0$ (bottom) after nuclear effects. Percentages indicate the percentage of events with the specified number of π^+ 's (columns) and number of π^0 's (rows). Entries with a “—” indicate a small contribution ($<0.1\%$). π^+ 's are required to be above Cherenkov threshold. The number of pions prior to nuclear effects is boldened.	64
5.2	Percentage of pions undergoing different interactions for the analysis in [23], and this analysis. From left to right, the interactions are absorption, quasi-elastic scattering, charge exchange, π production, and no interaction. The * indicates that QE scattering and charge exchange are combined.	66
7.1	A set of common parameters used for the BDTs in the $pp \rightarrow \pi^+\pi^+$ and $pn \rightarrow \pi^+\pi^0$ searches.	96
7.2	Independent MC sample sizes used for each stage of the BDT for both the $pp \rightarrow \pi^+\pi^+$ and $pn \rightarrow \pi^+\pi^0$ searches, prior to any cuts. Dinucleon decay sample sizes show only the number of events, while the atmospheric neutrino sample sizes show the approximate number of events and the equivalent number of years. The same statistics are used for SKI-IV.	96

7.3	Efficiency, expected background, and data events after each precut for the $pp \rightarrow \pi^+\pi^+$ search. The FCFV cut is described in Section 6.1.6, and cuts (A1)-(A4) are described in the text. Expected background is weighted for oscillation effects, and scaled to the appropriate SK detector livetime (from the 200 year analysis sample).	99
7.4	Relative importance of each variable in the $pp \rightarrow \pi^+\pi^+$ search, averaged across SK periods.	101
7.5	Efficiency, expected background events, and candidate data events for SKI-IV $pp \rightarrow \pi^+\pi^+$ search. Background is quoted both for the appropriate SK livetime, and per megaton-year.	105
7.6	Atmospheric neutrino interaction modes in the remaining background for the $pp \rightarrow \pi^+\pi^+$ search by percentage, as estimated by atmospheric neutrino MC.	105
7.7	Candidate variable values, and mean variable values for signal and background distributions, for each of the variables used in the BDT for the $pp \rightarrow \pi^+\pi^+$ search. The description of each variable is in the text. Values are given for SK-II and SK-IV, for which single candidate events were found.	108
7.8	Efficiency, expected background, and data events after each precut for the $pn \rightarrow \pi^+\pi^0$ search. Cuts (B1)-(B5) are described in the text. Expected background is weighted for oscillation effects, and scaled to the appropriate SK detector livetime (from the 200 year analysis sample).	110
7.9	Relative importance of each variable in the $pn \rightarrow \pi^+\pi^0$ search, averaged across SK periods.	112

7.10	Final BDT cut value, efficiency, expected background, and candidate data events for the SKI-IV $pn \rightarrow \pi^+\pi^0$ search. Background rates are quoted for the appropriate SK livetime, and per megaton-year.	115
7.11	Neutrino interaction mode percentages for remaining background in the $pn \rightarrow \pi^+\pi^0$ search for SKI-IV.	117
7.12	Candidate variable values, and mean variable values for signal and background distributions, for each of the variables used in the BDT for the $pn \rightarrow \pi^+\pi^0$ search. Letters for each variable are assigned in the text. Values are given for SK-I, for which a single candidate event was found.	117
7.13	Efficiency, expected background, and data events for the SKI-IV $nn \rightarrow \pi^0\pi^0$ search, for each analysis cut. The cuts are described in the text.	120
7.14	Neutrino interaction mode percentages for the remaining background in the $nn \rightarrow \pi^0\pi^0$ search for SKI-IV.	122
7.15	Variations used to estimate systematic uncertainties from ion interactions for $NN \rightarrow \pi\pi$. The coefficients correspond to quasielastic scattering (QE), inelastic scattering including hadron production (INEL), absorption (ABS), and charge exchange (CX). Both QE and CX are considered in low- and high-energy contexts, with an “H” added for the latter. Because hadron production is only considered for high momenta ($p_\pi > 500$ MeV/c), variations that change hadron production are considered high-energy variations, which are of the most relevance for $NN \rightarrow \pi\pi$	124
7.16	Dominant interaction uncertainties that contribute to the overall atm.- ν uncertainty for the $NN \rightarrow \pi\pi$ searches.	125

7.17	Ring separation and PID errors, from the analysis in [61], for relevant samples in the $NN \rightarrow \pi\pi$ analyses. All samples are multi-ring.	126
7.18	Values for the absolute energy scale uncertainty in each SK period. . .	127
7.19	Systematic uncertainties in the $pp \rightarrow \pi^+\pi^+$ search.	129
7.20	Systematic uncertainties in the $pn \rightarrow \pi^+\pi^0$ search.	130
7.21	Systematic uncertainties in the $nn \rightarrow \pi^0\pi^0$ search. Note that the energy scale uncertainty is dominant for the background, unlike other searches in which the simulation uncertainties are dominant.	131
8.1	Efficiency, expected background, and data events after each precut for the $n \rightarrow \bar{n}$ search. The FCFV cut is described in Section 6.1.6, and cuts (D1)-(D3) are described in the text. Expected background is weighted by oscillation factors determined from the analysis in [86], and scaled to the appropriate SK detector livetime (from the 200 year analysis sample).	135
8.2	Relative importance of each variable in the $n \rightarrow \bar{n}$ search, averaged across SK periods.	142
8.3	Values for the DIS interaction uncertainty for $E_\nu < 10$ GeV.	144
8.4	Efficiency, expected background events, and candidate data events for the SKI-IV $n \rightarrow \bar{n}$ search. Background is quoted both for the appropriate SK livetime, and per megaton-year.	146
8.5	Atmospheric neutrino interaction modes in the remaining background for the $n \rightarrow \bar{n}$ search by percentage, as estimated by atmospheric neutrino MC.	147
8.6	Systematic uncertainties in the $n \rightarrow \bar{n}$ search.	148

8.7	Values of $ (\text{Mean}_{\text{data}} - \text{Mean}_{\text{atm.-}\nu}) / \text{Mean}_{\text{atm.-}\nu} $ for each variable in the $n \rightarrow \bar{n}$ analysis, following selections (D1)-(D3).	149
8.8	Values of the χ^2 test statistic between data and atm.- ν MC, whose value in $[0, 1]$ gives the probability that differences in distributions are due to statistical fluctuations, for each variable in the $n \rightarrow \bar{n}$ analysis, following selections (D1)-(D3).	150
8.9	Shift value in data and atm.- ν MC total momentum, and associated signal and background uncertainties in the $n \rightarrow \bar{n}$ search.	152
8.10	Summary of the adjustments made in SK-I/II/III to account for the discrepancy seen between data and atm.- ν MC, with original and adjusted efficiency and background rates at the final cut value, and corresponding signal and background uncertainties. The number of variables removed starts from variables with the largest values of the mean difference between data and atm.- ν MC (Table 8.7). Background rates show the nominal values $\pm 1\sigma$ systematic uncertainty, calculated with all the sources in Table 8.6.	152
9.1	Lower lifetimes on $NN \rightarrow \pi\pi$ modes from this analysis, compared to the results of [39].	154
9.2	Bound $n \rightarrow \bar{n}$ limit τ_{90} and $\tau_{90}(n_{\text{cand}} = n_{\text{exp. bkg.}})$ for the SK-I analysis in [23], and this analysis. Note that $\tau_{90}(n_{\text{cand}} = n_{\text{exp. bkg.}})$ for this analysis does not include the additional systematic uncertainties described in Table 8.10, while τ_{90} with the actual number of candidates does.	154
9.3	Free $n \rightarrow \bar{n}$ lifetime limits, as measured in [29], and as calculated in [23] and this thesis. The calculations incorporate theoretical uncertainty on the nuclear suppression R as calculated in [27].	156

9.4	Comparison of efficiencies, background rates, systematic uncertainties, and data candidates from the SK-I analysis in [23], the new analysis MC using the same cut method, and the new analysis as described in Chapter 8. The background rates are shown with $\pm 1\text{-}\sigma$ systematic uncertainties to better compare to the number of data events.	159
A.1	Branching fractions used in the SK-I $n \rightarrow \bar{n}$ analysis in [23]. The values are taken from bubble chamber experiments [75–77]	164
A.2	Purely pionic branching fractions used in this analysis. The data for $\bar{n}n$ is from data in [78]. Some of the data for $\bar{n}p$ has been updated from results in the OBELIX experiment, though most is replicated from [23].	164
A.3	Branching fractions with one or more intermediate resonances this analysis. Data for $\bar{n}n$ annihilation is taken from [78] and [79].	165
A.4	Branching fractions with one or more strange particles in this analysis for $\bar{n}n$ annihilation, from data in [78].	165
A.5	Efficiency after each of the $n \rightarrow \bar{n}$ selection pre-cuts, for three different MC sets: MC from the old SK simulation, MC with the new pion model but same branching fractions as the old SK simulation, and MC with both updated pion model and branching fractions (this analysis).	165

List of Figures

2.1	Feynman diagram for $n \rightarrow \bar{n}$ (top) and $NN \rightarrow \pi\pi$ (bottom) from one of the models discussed in [22]. Spectator quarks $q_1, q_2 \in (u, d)$ are required for $NN \rightarrow \pi\pi$. The X_1 and X_2 scalar particles belong to $(\bar{6}, 1, -\frac{1}{3})$ and $(\bar{6}, 1, \frac{2}{3})$ representations of the Standard Model $SU(3) \otimes SU(2) \otimes U(1)$ gauge group.	13
2.2	The reduced \bar{n} radial wavefunction (top) and the \bar{n} nuclear potential for a $p_{1/2}$ -state \bar{n} (bottom), from [27].	17
3.1	The SK detector [43].	23
3.2	Relative spectrum of Cherenkov light in pure water, with quantum efficiency of the ID PMT overlaid [43].	27
3.3	A schematic of the 20-inch PMT used in the ID [42].	28
3.4	Left: pulse height distribution for a single p.e. in a 20-inch PMT. The peak near zero is from dark current. Right: relative transit time for a 20-inch PMT illuminated with light of 410 nm wavelength, for single p.e. intensity. Both from [42].	29
3.5	A schematic of the ID DAQ for SK-I-III [42].	32
3.6	A schematic of the OD DAQ for SK-I-III [43].	33
3.7	A schematic of the SK-I-III trigger system [43].	34

3.8	The SK water purification system [42].	36
3.9	Attenuation measurements and fitted curves using the nitrogen laser [50]. Measured values for SK-IV are similar.	38
3.10	Plot of $\log\left(\frac{Q(\ell)-\ell}{f(\theta)}\right)$ vs. ℓ (in cm) for a typical run (top); variation of the attenuation length in the SK-I-III periods (bottom). Both from [50]. The time variation of the length is sensitive to water quality, and time- dependent attenuation lengths are used in data processing.	39
3.11	A plot of the time vs. charge for a typical readout channel [49]. The time of each hit is corrected for time of flight.	43
3.12	Left: double ratio R_{MC}/R_{data} , where R is the ratio of measured mo- mentum to momentum inferred from the Cherenkov angle, for low mo- mentum stopping muons. Right: ratio of momentum to range for high momentum stopping muons. Both from [42]	45
3.13	Momentum of decay electrons for data (crosses) and MC (solid his- togram) [42].	45
3.14	Invariant mass of the π^0 sample (two showering rings), between data (crosses) and MC (boxes) [42].	46
3.15	Energy scale uncertainty vs. momentum range used for calibration measurements in SK-I [42], in order of increasing energy: decay elec- trons (solid circles), single π^0 's (solid triangles), low-energy stopping muons (open squares), and high-energy stopping muons (solid squares). 47	47

4.1	The primary cosmic ray flux for protons (at solar minimum), as calculated in [54]. Overlaid data points (see [54] for references) come Webber (crosses), MASS (open circles), LEAP (closed upward triangles), IMAX (closed downward triangles), CAPRICE-94 (closed vertical diamonds), CAPRICE-98 (open vertical diamonds), BESS (closed circles), AMS (closed horizontal diamonds), BESS-TeV (open upward triangles), Ryan et al (closed horizontal diamonds), JACEE (large open downward triangles), RUNJOB (large open diamonds), Ivanenko et al. (large open upward triangles), and Kawamura et al. (large open squares). Dashed lines indicate calculations from a fitting procedure, and the solid line includes additional corrections explained in [54]. . .	50
4.2	The atmospheric neutrino flux (left) and neutrino flavor ratios (right) up to 50 GeV. The solid line indicates the calculation of [53], the dot-dashed line an earlier calculation from Honda et al. [55], the long dashed line the BARTOL calculation [57], and the short dashed line the FLUKA calculation [56].	51
4.3	Cross-sections for various $CC1\pi$ interactions, with solid lines showing the fit used in NEUT [58]. See [58] for details on the data points. . .	54
4.4	Total charged-current cross-section for neutrinos (upper lines) and antineutrinos (lower lines). The lines show a comparison of different parton distribution functions, with and without corrections from Bodek and Young [64]. See [58] for details on the data points.	56
4.5	Pion interaction cross sections as a function of lab momentum, for π^+ (left) and π^- (right) [68]. The “TunedFSI” plots are used in the most recent MC simulation. See [68] for details on the data points.	57

5.1	Fermi momentum predictions (solid line) and data (crosses) from [73]. The left shows a p-state nucleon, and the right an s-state in ^{12}C	62
5.2	Invariant mass for $pp \rightarrow \pi^+\pi^+$. The modes $pn \rightarrow \pi^+\pi^0$ and $nn \rightarrow \pi^0\pi^0$ are essentially identical. The dotted histogram shows events with a correlated decay.	63
5.3	The integrand in the numerator of Equation 2.14 for an s-state and p-state neutron in ^{16}O . The solid and dotted lines show calculations for two different approximations.	65
5.4	Charged, neutral, and total pion multiplicity (top left, top right, and bottom left), and average charged pion momentum (bottom right) for $n \rightarrow \bar{n}$ MC. The blue histogram shows the simulation of [23], the red histogram shows the simulation using the same branching fractions as [23] but the updated pion-nucleon model described in Section 4.2.4, and the green histogram shows the simulation using new branching fractions and the updated pion model.	66
6.1	The second reduction cut 2a) for data (top), MC (middle), and MC nor- malized to data events after the selection (bottom) in SK-IV. The small number of events for which $\text{NHITA}_{800} > 25$ have $\text{PE}_{\text{total}} > 100,000$. Taken from [61].	69
6.2	The goodness parameter (Equation 6.1) for thrugoing (top) and stop- ping muons (bottom) in SK-IV, normalized to data taken over two days (red crosses). The blue histogram shows data over the previous two months.	72
6.3	A schematic of one of the cable holes with a veto counter.	73

6.4	Typical distributions of N_{MIN100} for a flasher (top) and an atmospheric neutrino MC event (bottom). The arrows indicate the region that is removed with the third reduction flasher cut. Taken from [61].	74
6.5	A plot of the event rate across each reduction stage in SK-IV, with first (black), second (red), third (cyan), fourth (dark blue), fifth (yellow), and FCFV (magenta). There is a slight gain increase with time most apparent in the first two reductions. This is due to degrading PMT quality, and is accounted for in event reconstruction.	79
6.6	The Hough transform method. The grey area corresponds to hit PMTs, and the dashed circles are drawn around each hit PMT with a 42-degree opening angle. The ring center is determined by the point at which the most circles overlap.	82
6.7	Ring-counting likelihood in SK-IV, for the sub-GeV ($E_{vis} < 1.3$ GeV) sample. The MC is normalized to data events (crosses) and separated by neutrino interaction type.	83
6.8	A simulated μ^+ (top) and e^+ (bottom), both with momentum 800 MeV/c. The charge pattern is notably sharper for the μ^+ and more diffuse for the e^+ . The intensity scale indicates the amount of charge deposited on the PMTs. The main display shows the ID, while the small display on the top right shows the OD, in which there is negligible activity. Both displays show the detector “unrolled” from its cylindrical shape. The white +’s indicate the horizontal and vertical location of the reconstructed vertex, projected onto the detector wall.	85
6.9	Distributons of RTOT vs. momentum up to 2000 MeV/c for both e -like and μ -like rings.	89

7.1	An example tree for the $pn \rightarrow \pi^+\pi^0$ analysis. The tree has a depth of four. The variables used are the reconstructed π^0 momentum (“pi0ptot”), the visible energy (“evis”), the $\pi^0 - \pi^+$ opening angle (“opang”), and the ratio of charge carried in the highest-energy ring (“qratio”), all of which are described in the text. Nodes that split to the left are more signal-like, and nodes that split to the right more background-like. . .	93
7.2	Selection criteria (A1) (top left), (A3) (top right), and (A4) (bottom left) for $pp \rightarrow \pi^+\pi^+$ MC (blue histogram), atm.- ν background (red histogram), and data (crosses) for SK-IV. All plots are area-normalized to the data. The green line indicates the placement of the cuts described in the text.	98
7.3	The angle between μ -like rings, the strongest discriminatory for the $pp \rightarrow \pi^+\pi^+$ search, for signal MC (solid histogram), atm.- ν MC (dashed histogram), and data (crosses). Distributions are shown for SK-IV and normalized to the number of events in the data.	102
7.4	The ratio of charge carried by the leading ring (top left), the visible energy (top right), the maximum distance between the primary vertex and a decay electron vertex (middle left), the largest angle between a μ -like ring and decay electron vertex (middle right), the magnitude of the vector sum of RTOT (bottom left), and the number of Cherenkov rings (bottom right) for the $pp \rightarrow \pi^+\pi^+$ search, for signal MC (solid histogram), atm.- ν MC (dashed histogram), and data (crosses). Distributions are for SK-IV, and are normalized to the number of events in the data. Details of each variable are described in the text.	103

7.5	The number of decay electrons (left) and the number of μ -like rings (right) for the $pp \rightarrow \pi^+\pi^+$ search, for signal MC (solid histogram), atm.- ν MC (dashed histogram), and data (crosses). Distributions are shown for SK-IV, and are normalized to the number of events in the data. Details of each variable are described in the text.	104
7.6	BDT output for $pp \rightarrow \pi^+\pi^+$ signal (solid), atm.- ν background (dashed), and data (crosses). The vertical green line indicates the BDT cut value, and the arrow indicates that only events to the right of the cut are kept.	104
7.7	A $pp \rightarrow \pi^+\pi^+$ MC event. The two solid orange rings correspond to true π^+ 's, and have an angle of 164 degrees between them. The dashed cyan ring is fit as e -like, but is actually a hard scatter of one of the π^+ 's.	106
7.8	Surviving atmospheric neutrino MC event for the $pp \rightarrow \pi^+\pi^+$ search. The interaction type is ν_μ charged-current single π^+ production. The uppermost μ -like ring corresponds to a μ^- , while the smaller μ -like ring is a π^+ . The e -like ring is mis-fit, as it comes from a hard scatter of the π^+ . The angle between the two μ -like rings is 170 degrees, thereby mimicking the main event signature. The momentum of the muon μ -like ring is 402 MeV/c, and the momentum of the π^+ μ -like ring is 301.3 MeV/c	106
7.9	$pp \rightarrow \pi^+\pi^+$ candidate event in SK-II. The two μ -like rings are strikingly back-to-back, at almost exactly 180 degrees to each other. The e -like ring could be due to a hard scatter. There is one Michel electron, not shown. The μ -like rings have momenta of 399.0 MeV/c (solid) and 280.5 MeV/c (dashed), and the e -like ring has momentum 42.0 MeV/c. The visible energy is 387.0 MeV, the total momentum 124.2 MeV/c, and the invariant mass 710.9 MeV/c ²	107

7.10 $pp \rightarrow \pi^+\pi^+$ candidate event in SK-IV. The two μ -like rings are at an angle of 151 degrees to each other, with momenta of 541.4 and 389.5 MeV/c. The dashed e -like ring could be due to a hard scatter. There are 2 Michel electrons, not shown. The visible energy is 742.8 MeV, the total momentum is 445.8 MeV/c, and the invariant mass is 1022.3 MeV/c². 107

7.11 Selection criteria (B1) (top left), (B3) (top right), (B4) (bottom left) and (B5) (bottom right) for $pn \rightarrow \pi^+\pi^0$ MC (blue histogram), atm.- ν background (red histogram), and data (crosses) for SK-IV. All plots are area-normalized to the data. The green line indicates the placement of the cuts described in the text. 109

7.12 The total momentum of the π^0 candidate in SK-IV, the best discriminating variable for the $pn \rightarrow \pi^+\pi^0$ search, for signal MC (solid histogram), atm.- ν MC (dashed histogram), and data (crosses). Distributions are normalized to the number of events in the data. 113

7.13 The opening angle between the π^0 and π^+ candidate rings (top left), the momentum of the π^+ candidate (top right), the invariant mass of the π^0 candidate (middle left), the ratio of charge carried by the most energetic ring (middle right), the visible energy (bottom left), and the number of decay electrons (bottom right) for the $pn \rightarrow \pi^+\pi^0$ search in SK-IV, for signal MC (solid histogram), atm.- ν MC (dashed histogram), and data (crosses). Distributions are normalized to the number of events in the data. Details of each variable are described in the text. 114

7.14	BDT output for $pn \rightarrow \pi^+\pi^0$ signal (solid), atmospheric neutrino background (dashed), and data (crosses). The green vertical line indicates the BDT cut value, and the arrow indicates that only events to the right of the cut are kept. One candidate event can be seen in the SK-I data distribution, just to the right of the cut at 0.19.	115
7.15	A $pn \rightarrow \pi^+\pi^0$ MC event. The μ -like ring corresponds to a true π^+ . The e -like ring contains two overlapping γ 's from a π^0 . The angle between the μ - and e -like rings is 165 degrees. The e -like ring has a reconstructed momentum of 893 MeV/c, while the original π^0 had momentum 876 MeV/c.	116
7.16	A surviving atmospheric neutrino MC event for the $pn \rightarrow \pi^+\pi^0$ search. The interaction type is CC1 π^0 , $\nu_\mu n \rightarrow \mu^-\pi^0 p$. The two overlapping e -like rings are photons from a π^0 , with total momentum 939 MeV/c. The μ -like ring corresponds to the μ^- , with momentum 410 MeV/c. The angle between them is 151 degrees, thereby appearing back-to-back.	116
7.17	The $pn \rightarrow \pi^+\pi^0$ candidate in SK-I. The e -like and μ -like rings are at an angle of 140 degrees. The e -like ring has a high momentum of 987 MeV/c, but its fit π^0 mass is low, at 10 MeV/ c^2 . The μ -like ring has a momentum of 460.0 MeV/c. The total momentum and invariant mass are 700.1 MeV/c and 1266.4 MeV/ c^2 , respectively.	117
7.18	Total momentum (left) and invariant mass (right) for data (crosses), $nn \rightarrow \pi^0\pi^0$ MC (solid histogram), and atmospheric neutrino MC (dashed histogram). Cuts (C1)-(C3) are applied to both plots. The invariant mass cut (C5) has been applied to the total momentum, and the total momentum cut (C4) to the invariant mass. The thin green vertical lines indicate the locations of the final cuts for each variable.	119

7.19	The total momentum and invariant mass distributions for $nn \rightarrow \pi^0\pi^0$ MC (left), atmospheric neutrino MC (center), and data (right) combined for SK I-IV. Events have passed cuts (C1)-(C3). The solid box indicates the total momentum and invariant mass cuts ((C4) and (C5) in the text).	121
7.20	A $nn \rightarrow \pi^0\pi^0$ MC event. The two overlapping e -like rings on the top left correspond to two γ 's from a π^0 decay, and the other ring also corresponds to a π^0 . The true momentum of the π^0 corresponding to the two-ring fit is 872.7 MeV/c, and the true momentum of the π^0 corresponding to the one-ring fit is 936.7 MeV/c. The total reconstructed momentum of this event is 219 MeV/c, and the reconstructed invariant mass is 1793 MeV/c ²	121
7.21	Surviving atmospheric neutrino MC event for the $nn \rightarrow \pi^0\pi^0$ search. The interaction is ν_μ neutral current deep-inelastic scattering. In particular, the interaction produced a π^0 and an η meson, from which four γ 's are produced. All but the left-most ring correspond to true photons from the π^0 and η meson. Many additional charged pions are also produced, concentrated near the center of the display, thereby complicating reconstruction. The left-most ring corresponds to a charged pion. There is a ring near the center from multiple, closely overlapping charged pion tracks, which is not found by the reconstruction program. The total reconstructed momentum is 553 MeV/c, and the reconstructed invariant mass is 1763 MeV/c ²	122

7.22	The BDT output for $pn \rightarrow \pi^+\pi^0$ signal, for standard (solid histogram) and FSI-varied MC (dashed histogram). The varied MC output is from the decreased hadron production set of variations. This decrease in hadron production leads to a clearer signal.	125
7.23	The invariant mass distribution of the $nn \rightarrow \pi^0\pi^0$ atm.- ν background in SK-IV, after selections (C1)-(C4), with a function of the form $\exp(p_0 + p_1x)$ fit to the region $600 \text{ MeV}/c^2 < M_{\text{inv}} < 2000 \text{ MeV}/c^2$. The uncertainty was estimated by integrating the function between the invariant mass cut values, and finding the difference in the integral when the cut values were shifted. A similar procedure was done for the total momentum, and the larger value was taken for the uncertainty.	128
8.1	Selection criteria (D1)-(D3) for $n \rightarrow \bar{n}$ MC (blue histogram), atm.- ν background (red histogram), and data (crosses) in SK-IV. All plots are area-normalized to the data. The green line indicates the placement of the cuts described in the text.	134
8.2	A comparison of the atm.- ν weight using two-flavor oscillation and small corrections from the flux in [53] (blue curve), and the atm.- ν weight using the full oscillation analysis in [86] (red curve), for all atm.- ν events passing the selection pre-cuts (D1)-(D3).	136

8.3	The total momentum (top left), invariant mass (top right), $(E_{\text{tot}} - E_{\text{primary}})/E_{\text{tot}}$ (middle left), PID likelihood difference of the leading ring (middle right), number of decay electrons (bottom left), and maximum distance between the primary vertex and a decay electron vertex (bottom right) for the $n \rightarrow \bar{n}$ search in SK-IV, for signal MC (solid histogram), atm.- ν MC (dashed histogram), and data (crosses). Distributions are normalized to the number of events in the data. Details of each variable are described in the text.	139
8.4	The sphericity (top left), number of potential rings (top right), first Fox-Wolfram moment (bottom left), and second Fox-Wolfram moment (bottom right) for the $n \rightarrow \bar{n}$ search in SK-IV, for signal MC (solid histogram), atm.- ν MC (dashed histogram), and data (crosses). Distributions are normalized to the number of events in the data. Details of each variable are described in the text.	140
8.5	BDT output for $n \rightarrow \bar{n}$ signal and atm.- ν background (top), and the remaining signal efficiency and scaled background in SK-I as a function of BDT cut (bottom). The BDT outputs are area-normalized	141
8.6	atm.- ν BDT output for SK-I MC, categorized by neutrino interaction mode.	144
8.7	Lifetime limit vs. BDT cut assuming the number of candidates is equal to the number of background events. The value is maximized for a cut of 0.35.	145
8.8	BDT output for $n \rightarrow \bar{n}$ signal (blue), atm.- ν background (red), and data (crosses). All histograms are normalized to the number of data entries. The vertical green line indicates the BDT cut value, and the arrow indicates that only events to the right of the cut are kept. . . .	146

8.9	Remaining events as a function of the BDT cut, for data (crosses) and atm.- ν MC (red histogram). The atm.- ν MC is normalized by the appropriate livetime. The cyan curves show the one-sigma systematic uncertainties (Table 8.6).	149
8.10	Total momentum in SK-I, for data (crosses), atm.- ν MC (red), and atm.- ν MC shifted to match the data (green).	151
8.11	Remaining events as a function of the BDT cut, for data (crosses) and atm.- ν MC (red histogram). The atm.- ν MC is normalized by the appropriate livetime. The cyan curves show the one-sigma systematic uncertainties (Table 8.6).	151
9.1	Total momentum vs. invariant mass following selections A) and B) for $n \rightarrow \bar{n}$ signal (top), atm.- ν background (middle), and SK-I data (bottom) for the analysis in [23], with boxes indicating selections C) and D).	158
B.1	The angle between μ -like rings (left) and the ratio of charge carried by the most-energetic ring (right) for the $pp \rightarrow \pi^+\pi^+$ search, for signal MC (solid histogram), atm.- ν MC (dashed histogram), and data (crosses). Distributions are normalized to the number of events in the data. Details of each variable are described in the text, in Section 7.2.2.	167
B.2	The visible energy (left) and the maximum distance between the primary vertex and a decay electron vertex (right) for the $pp \rightarrow \pi^+\pi^+$ search, for signal MC (solid histogram), atm.- ν MC (dashed histogram), and data (crosses). Distributions are normalized to the number of events in the data. Details of each variable are described in the text, in Section 7.2.2.	168

B.3	The largest angle between a μ -like ring direction and a decay electron vertex (left) and the magnitude of the vector sum of RTOT (right) for the $pp \rightarrow \pi^+\pi^+$ search, for signal MC (solid histogram), atm.- ν MC (dashed histogram), and data (crosses). Distributions are normalized to the number of events in the data. Details of each variable are described in the text, in Section 7.2.2.	169
B.4	The number of Cherenkov rings (left) and the number of decay electrons (right) for the $pp \rightarrow \pi^+\pi^+$ search, for signal MC (solid histogram), atm.- ν MC (dashed histogram), and data (crosses). Distributions are normalized to the number of events in the data. Details of each variable are described in the text, in Section 7.2.2.	170
B.5	The number of μ -like rings for the $pp \rightarrow \pi^+\pi^+$ search, for signal MC (solid histogram), atm.- ν MC (dashed histogram), and data (crosses). Distributions are normalized to the number of events in the data. Details are described in the text, in Section 7.2.2.	171
B.6	The π^0 candidate momentum (left) and the angle between the π^0 and π^+ candidate rings (right) for the $pn \rightarrow \pi^+\pi^0$ search, for signal MC (solid histogram), atm.- ν MC (dashed histogram), and data (crosses). Distributions are normalized to the number of events in the data. Details of each variable are described in the text, in Section 7.3.2.	172
B.7	The π^+ candidate momentum (left) and the invariant mass of the π^0 candidate (right) for the $pn \rightarrow \pi^+\pi^0$ search, for signal MC (solid histogram), atm.- ν MC (dashed histogram), and data (crosses). Distributions are normalized to the number of events in the data. Details of each variable are described in the text, in Section 7.3.2.	173

B.8 The ratio of charge carried by the most energetic ring (left) and the visible energy (right) for the $pn \rightarrow \pi^+\pi^0$ search, for signal MC (solid histogram), atm.- ν MC (dashed histogram), and data (crosses). Distributions are normalized to the number of events in the data. Details of each variable are described in the text, in Section 7.3.2. 174

B.9 The number of decay electrons for the $pn \rightarrow \pi^+\pi^0$ search, for signal MC (solid histogram), atm.- ν MC (dashed histogram), and data (crosses). Distributions are normalized to the number of events in the data. Details of each variable are described in the text, in Section 7.3.2. 175

B.10 Total momentum (left) and invariant mass (right) for data (crosses), $nn \rightarrow \pi^0\pi^0$ MC (solid histogram), and atmospheric neutrino MC (dashed histogram). Cuts (C1)-(C3) are applied to both plots. The invariant mass cut (C5) has been applied to the total momentum, and the total momentum cut (C4) to the invariant mass. The thin green vertical lines indicate the locations of the final cuts for each variable. Details of the selection criteria can be found in Section 7.4.1. 176

B.11 The total momentum (left) and invariant mass (right) for the $n \rightarrow \bar{n}$ search, for signal MC (solid histogram), atm.- ν MC (dashed histogram), and data (crosses). Distributions are normalized to the number of events in the data. Details of each variable are described in the text, in Section 8.2. 177

B.12 $(E_{\text{total}}-E_{\text{primary}})/E_{\text{total}}$ (left) and the PID likelihood difference of the leading ring (right) for the $n \rightarrow \bar{n}$ search, for signal MC (solid histogram), atm.- ν MC (dashed histogram), and data (crosses). Distributions are normalized to the number of events in the data. Details of each variable are described in the text, in Section 8.2. 178

B.13 The number of decay electrons (left) and the maximum distance from the primary vertex to a decay electron vertex (right) for the $n \rightarrow \bar{n}$ search, for signal MC (solid histogram), atm.- ν MC (dashed histogram), and data (crosses). Distributions are normalized to the number of events in the data. Details of each variable are described in the text, in Section 8.2. The distance is only shown for events with one or more decay electron. 179

B.14 The sphericity (left) and the number of potential rings (right) for the $n \rightarrow \bar{n}$ search, for signal MC (solid histogram), atm.- ν MC (dashed histogram), and data (crosses). Distributions are normalized to the number of events in the data. Details of each variable are described in the text, in Section 8.2. 180

B.15 The first and second Fox-Wolfram moments (left and right, respectively) for the $n \rightarrow \bar{n}$ search, for signal MC (solid histogram), atm.- ν MC (dashed histogram), and data (crosses). Distributions are normalized to the number of events in the data. Details of each variable are described in the text, in Section 8.2. 181

List of Abbreviations

1π	Single Pion Production
ADC	Analog to Digital Converter
ATM	Analog Timing Module
B	Baryon Number
BDT	Boosted Decision Tree
BNV	Baryon Number Violation
CC	Charged Current
DAQ	Data Acquisition
DIS	Deep Inelastic Scattering
FC	Fully contained
FSI	Final State Interaction
FV	Fiducial volume
GUT	Grand Unified Theory
ID	Inner Detector
L	Lepton Number
MC	Monte Carlo
NC	Neutral Current
$n \rightarrow \bar{n}$	Neutron-antineutron oscillation
$NN \rightarrow \pi\pi$	Dinucleon decay to pions
OD	Outer Detector
p.e.	photoelectron
PID	particle identification
PMT	Photomultiplier Tube
QBEE	QTC Based Electronics with Ethernet

QE	Quasi-elastic
QTC	Charge to Time Converter
SK	Super-Kamiokande
SM	Standard Model
TDC	Time to Digital Converter
TKO	Tristan KEK Online

Chapter 1

Introduction

The basic stability of matter is an intuitive necessity. In the language of particle physics, everyday matter is composed of *baryons*, protons and neutrons that fill atomic nuclei. While certain unstable atoms are known to decay, the decay of individual baryons would make life as we know it impossible.

Thankfully, matter appears to be stable for all practical purposes. More specifically, baryon number appears to be conserved — that is, the total number of baryons before and after an interaction, such as a decay or a high-energy collision, is constant. Some physicists have suggested that baryon number is absolutely conserved, in the same manner as properties like energy, momentum, and electric charge. Even those who have predicted that baryons are ultimately unstable have predicted that baryons decay with lifetimes of 10^{29} years or higher — roughly 10^{19} times longer than the known universe.

The apparent stability of matter does not imply that it is absolutely stable, and thus baryon number is not necessarily an absolutely conserved quantity. There are compelling theoretical reasons to believe that baryon number is *not* exactly conserved, and the attempt to observe a baryon number non-conserving process has been a

continuous experimental goal for decades. The discovery of such a process would be a spectacular confirmation of new physics, while non-observation places important constraints on the theories that predict such processes. The goal of this thesis is to probe a subset of these processes (“B” indicates the baryon number):

- Dinucleon decay to pions, the simultaneous decay of two bound nucleons ($B = 2$) into pions ($B = 0$), encompassing the decay channels $^{16}\text{O}(pp) \rightarrow ^{14}\text{C}(\pi^+\pi^+)$, $^{16}\text{O}(pn) \rightarrow ^{14}\text{N}(\pi^+\pi^0)$, and $^{16}\text{O}(nn) \rightarrow ^{14}\text{O}(\pi^0\pi^0)$;
- Neutron-antineutron oscillation, the transformation of a neutron ($B = 1$) into its antiparticle ($B = -1$).

Each of these processes have been sought by experiments before. They have been constrained to occur on timescales on the order of 10^{30} years or longer, depending on the specific channel.

The search in this thesis follows the same basic logic as previous searches. Since an experiment cannot reasonably run for longer than a few decades, it must consist of as large a sample of matter as possible. The potential to discover these processes (or further constrain them) scales with the product of the number of nucleons and the running time of the experiment. In this thesis, data from the Super-Kamiokande water Cherenkov detector is used. With a tank volume containing 7.5×10^{32} water molecules and a running time of nearly two decades, Super-Kamiokande has by far the largest exposure of any comparable experiment. The full dataset is used for these searches.

This thesis is organized as follows. In Chapter 2, I discuss the underlying theory and motivation of these searches, as well as relevant results from previous experiments. In Chapter 3, I describe the Super-Kamiokande detector, including its basic structure, data acquisition system, and calibration sources. In Chapter 4, I

describe the simulation of atmospheric neutrino Monte Carlo, a simulation used by all analyses that use Super-Kamiokande data, and the main source of background to these searches. In Chapter 5, I describe the simulation of both dinucleon decay to pions and neutron-antineutron oscillation. Chapter 6 describes the data reduction and event reconstruction algorithms common for all data and Monte Carlo samples. Chapter 7 describes the dinucleon decay searches; the features of each search are distinct, and prominently include multivariate analysis techniques. Chapter 8 discusses the neutron-antineutron oscillation search. In Chapter 9, I present and discuss the results.

Chapter 2

Motivation and Theory

Observation of neutron-antineutron oscillation or the related process of dinucleon decay to pions can illuminate profound issues inexplicable within our current understanding of the Standard Model of particle physics. Here I describe the underlying motivation and theory of these searches, as well as relevant previous experimental results.

2.1 Baryon Number

Baryon number is defined in terms of the quark content of a system of particles:

$$B = \frac{1}{3} (n_q - n_{\bar{q}}), \quad (2.1)$$

where q and \bar{q} refer to quarks and antiquarks, respectively. Thus individual quarks (antiquarks) have $B = 1/3$ ($B = -1/3$); baryons, made of three quarks, have $B = 1$; antibaryons have $B = -1$; mesons, composed of a quark and antiquark, have $B = 0$; and leptons, which have no quarks or antiquarks, have $B = 0$. Though not fundamental to this thesis, lepton number is defined similarly:

$$L = n_\ell - n_{\bar{\ell}}, \quad (2.2)$$

where ℓ and $\bar{\ell}$ refer to leptons and antileptons, respectively.

The conservation of baryon number was first suggested by Weyl in 1929 [1]. It was framed as a conservation of both positive and negative charges; given the known particles of the time, this meant the conservation of proton number and electron number. The extension to baryons was made by Stueckelberg [2] and Wigner [3].

The necessarily long minimum lifetime of baryonic matter was known, in a rough quantitative sense, before any dedicated experiment. For instance, Goldhaber deduced as far back as the 1950s that the proton lifetime had to be at least 10^{16} years, because if it were any shorter than this, radiation due to energetic particles from decaying protons in the $\sim 10^{27}$ nucleons in the human body would exceed the maximum dosage for radiation workers [4]. The first experiment probing nucleon stability was indirect, and looked for the spontaneous fission of ^{232}Th resulting from excitation from the decay of one of its nucleons. As no such fission was observed, this method resulted in a lower nucleon lifetime of 2×10^{23} years [5]. A detailed history of nucleon decay experiments can be found in [6].

2.2 The Standard Model

The Standard Model of particle physics has been spectacularly successful in explaining the subatomic universe as we know it. Like any physical theory, the Standard Model has various conserved quantities. The conservation of some of these quantities is exact, such as energy, momentum, and angular momentum. Noether's theorem dictates that any conserved quantity is associated with an underlying symmetry —

more formally, if the action is invariant under a group of symmetry transformations, there is a corresponding conserved current. For the absolute quantities above, the corresponding symmetries are translation in time, translation in space, and rotation in space, respectively.

Aside from these absolutes, quantities conserved within the Standard Model are associated with its group structure:

$$G_{SM} \supset SU(3)_C \times SU(2)_L \times U(1)_Y. \quad (2.3)$$

Here $SU(3)_C$ encodes the color conservation of the strongly-interacting quarks and their messenger particles, gluons. The group $SU(2)_L$ characterizes the weak force, with the L indicating that only left-handed particles (or right-handed antiparticles) interact with this force. The conserved quantity here is weak isospin, associated with the three $SU(2)$ gauge bosons. Finally, $U(1)_Y$ conserves the weak hypercharge, which is defined in terms of both the weak isospin and the more familiar electromagnetic charge Q_{EM} . It has been well-known since the pioneering work of Glashow, Weinberg, and Salam [7–9] that the subgroup $SU(2)_L \times U(1)_Y$ spontaneously breaks to a single $U(1)_{EM}$ that conserves the electromagnetic charge, while the three weak $SU(2)$ bosons and single $U(1)$ hypercharge boson mix to create the massive charged W bosons, the massive neutral Z boson, and the massless neutral photon. The Higgs mechanism by which the bosons obtain mass was recently vindicated with the thrilling discovery by both the ATLAS [10] and CMS [11] detectors of a neutral particle consistent with the Standard Model Higgs boson.

The Standard Model gauge group reveals some interesting features about the nature of conserved quantities. For instance, even though parity was once thought to be conserved in fundamental interactions, the fact that the $SU(2)_L$ weak force only

interacts with left-handed particles means that it violates parity (or spatial inversion) maximally. It is natural to question whether other quantities may be non-conserved, even if they appear conserved in all observations thus far. One such quantity is baryon number.

Although no baryon number violating process has been observed, baryon number is not strictly conserved within the Standard Model¹. Whether such processes occur at an observable level is still an interesting question, and both neutron-antineutron oscillation and dinucleon decay to pions (hereafter “ $n \rightarrow \bar{n}$ ” and “ $NN \rightarrow \pi\pi$ ”) violate baryon number by two units.

2.3 Baryogenesis and Baryon Asymmetry

Despite its success, there are several unresolved issues within the Standard Model, as well as explanations that are incomplete or unsatisfactory. One such issue is the observed excess of matter to antimatter. Indeed, the level of antimatter in the universe is negligible. In the Standard Model, processes which produce particles and their associated antiparticles should occur at equal rates, thus leading to no net excess. Baryogenesis - a set of processes and conditions that produced the observed excess in baryons to antibaryons - is thus difficult to explain.

Sakharov [12] developed three necessary conditions for generating this imbalance, often called the Baryon Asymmetry of the Universe (BAU):

- I. There must be one or more baryon number violating (BNV) processes.
- II. There must be charge and charge-parity violation. If there weren't, any baryon number violating process would be matched by its charge and charge-parity

¹If it were, Equation 2.3 would have an additional U(1) symmetry for baryon number, analogous to weak hypercharge.

conjugate processes, thereby leading to no net (anti-)baryon excess.

- III. There must be interactions outside of thermal equilibrium. At thermal equilibrium, the energy difference between baryons and anti-baryons is zero, and thus the Boltzmann distribution indicates that there should be equal amounts of matter and anti-matter.

BNV processes have been studied extensively. In particular, single nucleon decay has been a topic of strong experimental interest for decades, with the most stringent results coming from Super-Kamiokande [13–17]. Modes such as $p \rightarrow e^+\pi^0$, in addition to having a clear experimental signature, are predicted to occur at an observable rate in Grand Unified Theories (GUTs). Such GUTs predict that the three subatomic forces of the Standard Model - strong, weak, and electromagnetic - should have equal strength at an unobservably high energy of $\sim 10^{14} - 10^{16}$ GeV. This scale is determined from an extrapolation of the observed change with energy of the strong, weak, and electromagnetic coupling constants, to the point where they become approximately equal. For many physicists, these theories provide satisfying closure to the seemingly arbitrary differences present in the three forces at observable energy scales. Though the current lower lifetime on $p \rightarrow e^+\pi^0$ of 1.2×10^{34} years [18] has ruled out the simplest GUTs, such as those based on the gauge group $SU(5)$ [19], an unstable proton (or bound neutron) is the only observable aspect of many GUTs, and thus its discovery would be a profound revelation.

In one sense, then, the search for processes like $n \rightarrow \bar{n}$ and $NN \rightarrow \pi\pi$ are complementary to searches for single nucleon decay. Given the non-observation of single nucleon decay despite many years of searches, any additional avenues are welcome. It should also be noted that most single proton decay modes of interest violate both

baryon number B and lepton number L by one unit, but conserve $B - L^2$. Both $n \rightarrow \bar{n}$ and $NN \rightarrow \pi\pi$ violate B by two units and do not involve L , so they also violate $B - L$ by two units. This is an important distinction. As mentioned, no BNV process has been observed, but such processes occur in the Standard Model. In the electroweak component of the Standard Model, B and L are violated by anomalous “sphaleron” processes that convert three baryons to three antileptons, and vice-versa. Such processes conserve $B - L$, however, and thus the difference $B - L$ is a conserved quantity of the Standard Model. In the current universe, these interactions are highly suppressed. In the early universe, however, when the temperature was at or above the electroweak scale $T \sim 100$ GeV and below the GUT scale $T \sim 10^{14} - 10^{16}$ GeV, such processes occurred rapidly, such that any previously generated baryon asymmetry that conserved $B - L$ would have been washed out [20]. Thus, while proton decay is extremely important as a signifier of GUT-scale physics, its conservation of the quantity $B - L$ makes it unlikely to contribute to the BAU. Neutron-antineutron oscillation and dinucleon decay to pions remain good candidate processes.

There are other options for generating the BAU, apart from the $\Delta B = 2$ processes analyzed in this thesis. One such option is baryogenesis via leptogenesis, first suggested in [20]. Leptogenesis is just the analogue to baryogenesis for leptons. This option makes use of L -violating processes above the scale in which sphalerons are active, which are then converted to the BAU via the sphaleron mechanism of converting antileptons to baryons. This scenario is attractive particularly in light of the strong theoretical suspicion that neutrinos are Majorana particles that acquire mass via a $\Delta L = 2$ operator, a possibility that is being probed in neutrinoless double beta decay experiments. The same logic to $\Delta B = 2$ processes is relevant, in that the Standard

²An exception to this is a trilepton decay mode like $p \rightarrow e^+\nu\nu$ [14], which violates $B - L$ by two units assuming two normal neutrinos. In general, a single nucleon decay must have an odd number of leptons in the final state, to conserve spin.

Model-conserved difference $B - L$ is violated by two units.

2.4 Models

For a $\Delta B = 2$ process, the Lagrangian requires an effective six-quark operator of the form:

$$O_{\Delta B=2} = \frac{1}{M^n} O_{6Q}, \quad (2.4)$$

where O_{6Q} is an operator with two up-type and four down-type quarks, and M is a mass scale that suppresses the operator. For all first-generation quarks, this operator leads to $n \rightarrow \bar{n}$ and $NN \rightarrow \pi\pi$. The power of the mass scale n depends on additional details of the operator. If all other parameters are dimensionless, it follows from dimensional analysis that $n = 5$, since quark operators have dimension $3/2$.

A crude estimation of the $n \rightarrow \bar{n}$ rate can be obtained from this operator, by absorbing additional details of the operator into the suppression scale M . The (free) $n \rightarrow \bar{n}$ transition rate δm is

$$\delta m = \frac{1}{M^5} \langle \bar{n} | UDDUDD | n \rangle. \quad (2.5)$$

The matrix element $\langle \bar{n} | UDDUDD | n \rangle$ is difficult to calculate. Though there is considerable uncertainty, theorists typically estimate it to be $\Lambda^6 \approx 1 \times 10^{-4} \text{ GeV}^6$, or $\Lambda \approx 200 \text{ MeV}$, based on a calculation in [21]. Thus the $n \rightarrow \bar{n}$ lifetime $\tau_{n\bar{n}} = 1/\delta m$ depends only on the suppression scale M and a calculable, if uncertain, hadronic matrix element:

$$\tau_{n\bar{n}} \approx \frac{M^5}{\Lambda^6}. \quad (2.6)$$

Again roughly, the current lower limit on the $n \rightarrow \bar{n}$ lifetime of about 10^8 s implies that $M > 10^6$ GeV. This is an interesting scale - it is above the ~ 10 TeV scale achievable at the Large Hadron Collider, yet is well below the GUT scale that motivates searches for many other BNV processes.

It should be noted that the operator in Equation 2.5 is not renormalizable. In fact, no operator that causes BNV is renormalizable, and since the Standard Model Lagrangian only has renormalizable operators, B is sometimes called an “accidental” symmetry of the Standard Model. However, because the suppression scale M is much higher than the ~ 100 MeV scale of nuclear interactions, the operator is valid in an effective field theory context.

There are several broad classes of models that feature $n \rightarrow \bar{n}$, some of which explicitly forbid single proton decay [22]. For example, one model described in [22] includes the Lagrangian terms

$$\begin{aligned} \mathcal{L} = & -g_1^{ab} X_1^{\alpha\beta} (Q_{L\alpha}^a \epsilon Q_{L\beta}^b) - g_2^{ab} X_2^{\alpha\beta} (d_{R\alpha}^a d_{R\beta}^b) - g_1'^{ab} X_1^{\alpha\beta} (u_{R\alpha}^a d_{R\beta}^b) \\ & + \lambda X_1^{\alpha\alpha'} X_1^{\beta\beta'} X_2^{\gamma\gamma'} \epsilon_{\alpha\beta\gamma} \epsilon_{\alpha'\beta'\gamma'}. \end{aligned} \quad (2.7)$$

Here Q is an $SU(2)_L$ quark doublet; u_R and d_R are right-handed $SU(2)$ up- and down-type quark singlets; g_1 , g_2 , and g_1' are dimensionless couplings; and λ is a coupling with dimension one. Roman indices indicate quark generation, and Greek indices indicate color. The X_1 and X_2 particles are heavy scalars introduced by the model that couple to pairs of quarks, with $X_1 \in (\bar{6}, 1, -\frac{1}{3})$ and $X_2 \in (\bar{6}, 1, \frac{2}{3})$ representations of the Standard Model $SU(3) \times SU(2) \times U(1)$ gauge group. These terms lead to an effective operator shown in Figure 2.1. Note that the diagrams for $n \rightarrow \bar{n}$ and $NN \rightarrow \pi\pi$ are the same under crossing symmetry; the latter simply requires spectator

quarks of appropriate charge.

Following [22], the mixing element $\delta m = 1/\tau_{n \rightarrow \bar{n}}$, where $\tau_{n \rightarrow \bar{n}}$ is the $n \rightarrow \bar{n}$ lifetime, is calculated with

$$\delta m = \langle \bar{n} | H_{eff} | n \rangle \quad (2.8)$$

where

$$H_{eff} = -\frac{(g_1^{11})^2 g_2^{11} \lambda}{4M_1^4 M_2^2} d_R d_R u_R d_R u_R d_R \times N_{contraction} \quad (2.9)$$

and $N_{contraction}$ is a factor accounting for all spin and color contractions. The mixing element is estimated to be

$$\delta m \approx 2\lambda \Lambda^6 \frac{|(g_1^{11})^2 g_2^{11}|}{3M_1^4 M_2^2}. \quad (2.10)$$

Here Λ is the same hadronic matrix element discussed above. To get a rough sense of the lower bounds on the mass scale, consider the simple scenario $g_1^{11} = g_2^{11} = 1$, and $M_1 = M_2 = \lambda = M$. The upper limit on δm , is $1/\tau_{lim} = 2.4 \times 10^{-33}$ GeV, where $\tau_{lim} = 2.7 \times 10^8$ s from [23]. Plugging this into 2.10, we get $M > 600$ TeV.

Some models that predict $\Delta B = 2$ processes are driven specifically by the BAU. One recent model is called ‘‘Post-Sphaleron Baryogenesis’’ [24–26]. As the name implies, the model provides a BNV mechanism that occurs after sphaleron processes have been suppressed, when the universal temperature has cooled below 100 GeV or so. The mechanism involves the direct decay of a scalar particle to six quarks, and a set of scalar particles like the X_i bosons from the generic model of [22] with masses that cannot be much higher than the TeV scale. This model has a number of testable features. It predicts an upper limit on the $n \rightarrow \bar{n}$ oscillation time $\tau_{n \rightarrow \bar{n}} \leq 5 \times 10^{10}$

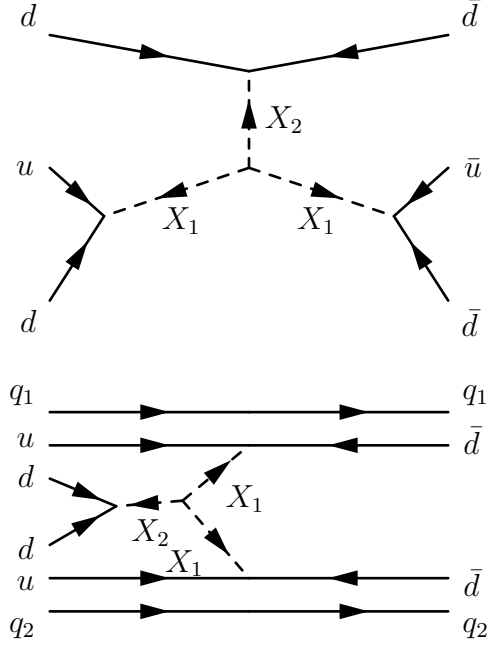


Figure 2.1: Feynman diagram for $n \rightarrow \bar{n}$ (top) and $NN \rightarrow \pi\pi$ (bottom) from one of the models discussed in [22]. Spectator quarks $q_1, q_2 \in (u, d)$ are required for $NN \rightarrow \pi\pi$. The X_1 and X_2 scalar particles belong to $(\bar{6}, 1, -\frac{1}{3})$ and $(\bar{6}, 1, \frac{2}{3})$ representations of the Standard Model $SU(3) \otimes SU(2) \otimes U(1)$ gauge group.

s [26], which is about two orders of magnitude beyond the current limit. It is also sensitive to the neutrino mass hierarchy, and is only valid if the so-called inverted hierarchy is discovered by neutrino experiments [25]. Finally, the TeV-scale scalar particles can be sought directly at the Large Hadron Collider.

2.5 Phenomenology and previous results

Here I discuss the phenomenology of $n \rightarrow \bar{n}$ and $NN \rightarrow \pi\pi$. Though the context for this study is bound neutrons in ^{16}O , the phenomenology of free neutron oscillations is instructive, and so I discuss it also.

2.5.1 $n\bar{n}$ oscillations

Free Neutrons

The probability of a free neutron oscillating to an antineutron can be parametrized with a simple 2×2 Hamiltonian, as in a textbook example of a two-state system:

$$i \frac{d}{dt} \begin{pmatrix} n \\ \bar{n} \end{pmatrix} = \begin{pmatrix} E_n & \delta m \\ \delta m & E_{\bar{n}} \end{pmatrix} \begin{pmatrix} n \\ \bar{n} \end{pmatrix} \quad (2.11)$$

where n and \bar{n} denote the neutron and antineutron wavefunctions, E_n and $E_{\bar{n}}$ their energies, $\delta m = 1/\tau_{n\bar{n}}$ a mixing element that provides the oscillation, and $\tau_{n\bar{n}}$ is the neutron oscillation time. From this, we obtain the probability for $n\bar{n}$ oscillations:

$$P_{n \rightarrow \bar{n}}(t) = \frac{\delta m^2}{\Delta E^2 + \delta m^2} \sin^2 \left(\sqrt{\Delta E^2 + \delta m^2} t \right) \quad (2.12)$$

where $\Delta E = E_n - E_{\bar{n}}$. If the energy levels are degenerate, as is the case in past and proposed experimental contexts, the probability simplifies to $P_{n \rightarrow \bar{n}}(t) \approx (\delta m t)^2 = (t/\tau_{n\bar{n}})^2$. Thus the probability scales simply with both the time of observation and the neutron oscillation time.

Bound neutrons

To study the possibility of $n \rightarrow \bar{n}$ in nuclei, we must account for the different nuclear potentials felt by neutrons and antineutrons. Here we follow the work of Friedman and Gal [27].

The radial wavefunctions of the neutron and antineutron satisfy a coupled set of differential equations:

$$\begin{aligned}
& -\frac{\hbar^2}{2\mu} \frac{d^2}{dr^2} u_{\nu\ell j}(r) + \frac{\hbar^2 \ell(\ell+1)}{2\mu r^2} u_{\nu\ell j}(r) - U_n(r) u_{\nu\ell j}(r) \\
& \qquad - E_{\nu\ell j} u_{\nu\ell j}(r) + \delta m w_{\nu\ell j}(r) = 0 \\
& -\frac{\hbar^2}{2\mu} \frac{d^2}{dr^2} w_{\nu\ell j}(r) + \frac{\hbar^2 \ell(\ell+1)}{2\mu r^2} w_{\nu\ell j}(r) \\
& - (U_{\bar{n}}(r) + iW_{\bar{n}}) w_{\nu\ell j}(r) - E_{\nu\ell j} w_{\nu\ell j}(r) + \delta m u_{\nu\ell j}(r) = 0.
\end{aligned}$$

Here u and w are the radial wavefunctions for the neutron and antineutron, respectively; ℓ , ν , and j are the principal, orbital, and magnetic quantum numbers; μ is the reduced nuclear mass; δm is the mixing element mentioned in the free neutron case; and $E_{\nu\ell j}$ are the energy eigenvalues. The nuclear potentials corresponding to the neutron and antineutron wavefunctions are real and complex, respectively, with the imaginary part of the antineutron potential $W_{\bar{n}}$ responsible for inducing oscillations. Though data on antineutron scattering is sparse, the identical interactions of (anti)-protons and (anti)-neutrons at the nuclear level enable $U_{\bar{n}}(r)$ to be fit with recent antiproton scattering data. The energy eigenvalues $E_{\nu\ell j}$ are also complex, with $E_{\nu\ell j} = -B_{\nu\ell j} - i\Gamma_{\nu\ell j}/2$, where Γ is the oscillation width. Equations 2.13 can be algebraically manipulated and integrated over r from zero to infinity to produce an expression for the width,

$$\Gamma_{\nu\ell j} = \frac{-2\delta m \int \text{Im} (w_{\nu\ell j}(r) u_{\nu\ell j}^*(r)) dr}{\int |u_{\nu\ell j}(r)|^2 dr} \quad (2.13)$$

Assuming the initial condition of a pure neutron state, the ratio $|w/u| \sim \delta m$, and therefore $\Gamma_{\nu\ell j} \sim \delta m^2$. Equation 2.13 can be re-arranged, dropping higher order terms, and to a good approximation Equation 2.13 is

$$\Gamma_{\nu\ell j} \approx \frac{2\delta m^2 \int W_{\bar{n}}(r) |v_{\nu\ell j}(r)|^2 dr}{\int u_{\nu\ell j}^2(r) dr} \quad (2.14)$$

where $v_{\nu\ell j} = w_{\nu\ell j}/\delta m$ is the reduced antineutron wavefunction, and $u_{\nu\ell j}$ is approximated as real. Thus the disappearance width is proportional to the overlap of the neutron and antineutron wavefunctions (Equation 2.13), and the imaginary part of the antineutron potential (Equation 2.14). Equation 2.14, or rather $\Gamma_{\nu\ell j}/\delta m^2$, can be calculated numerically for a given atomic state. Plots of the reduced wavefunction and \bar{n} nuclear potential can be seen in Figure 2.2.

The average disappearance width per neutron is then

$$\Gamma_d = \frac{1}{N} \sum_{\nu\ell j} n_{\nu\ell j} \Gamma_{\nu\ell j} \quad (2.15)$$

where N is the number of neutrons in the atom and $n_{\nu\ell j}$ is the occupancy of state $\nu\ell j$. For oxygen, $N = 8$, and there are four $p_{3/2}$, two $p_{1/2}$, and two $s_{1/2}$ states. Then the nuclear disappearance time T_d is

$$T_d = \frac{1}{\Gamma_d} = \left(\frac{1}{\Gamma_d \tau_{n\bar{n}}^2} \right) \tau_{n\bar{n}}^2 = R \tau_{n\bar{n}}^2. \quad (2.16)$$

R is typically called the nuclear suppression factor. The numerical value of R is calculated in [27] for oxygen as $0.517 \times 10^{23} \text{ s}^{-1}$.

One can arrive at the same approximate result as the careful analysis of [27] using a simpler argument. Neutrons bound in nuclei are quasi-free for a time $t_f \sim 1/E_b$, where $E_b \approx 30 \text{ MeV}$ is a typical nuclear binding energy. During this time, the probability of oscillation is given by Equation 2.12. This quasi-free condition occurs $1/t_f$ times per second, and the nuclear oscillation probability per second P_{nuc} is then

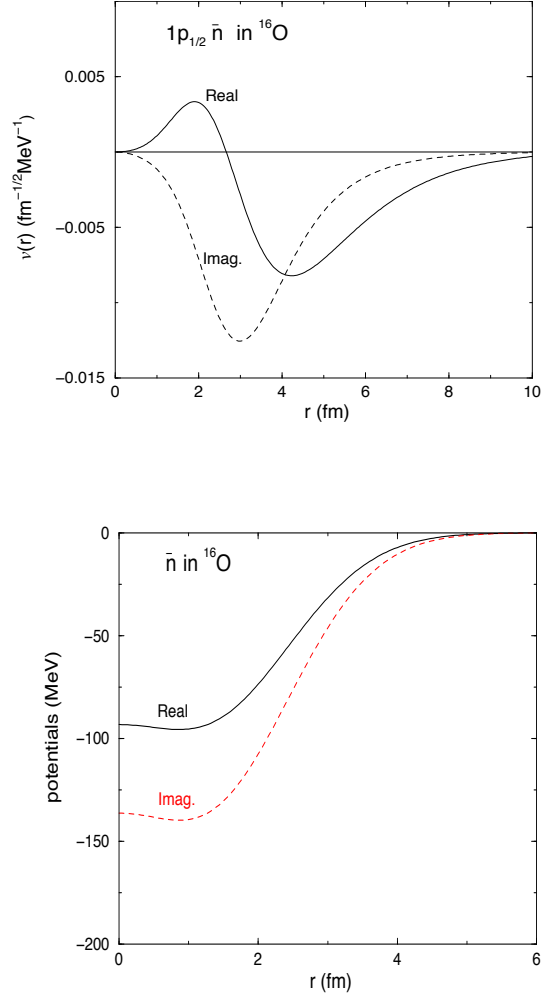


Figure 2.2: The reduced \bar{n} radial wavefunction (top) and the \bar{n} nuclear potential for a $p_{1/2}$ -state \bar{n} (bottom), from [27].

$$P_{nuc}(n \rightarrow \bar{n}) = \frac{1}{T_{nuc}} \approx \left(\frac{t_f}{\tau_{n\bar{n}}} \right)^2 \times \left(\frac{1}{t_f} \right). \quad (2.17)$$

. Thus, the nuclear $n\bar{n}$ transition time T_{nuc} can be estimated as $T_{nuc} = R\tau_{n\bar{n}}^2$, with $R = 1/t_f = E_b/\hbar \approx 0.45 \times 10^{23} \text{ s}^{-1}$.

Experimental issues - free vs. bound

Both free and bound $n \rightarrow \bar{n}$ searches have been conducted in the past. There are relative advantages and drawbacks to each, which I describe briefly here.

Free and bound $n \rightarrow \bar{n}$ searches rely on the same basic experimental signature. A neutron that has oscillated will quickly annihilate with a nearby nucleon, resulting in multiple pions. For bound neutrons this is just a nucleon in the surrounding atom, and for free neutrons this is a nucleon contained in a target material.

A typical free neutron experimental setup consists of a beam of non-relativistic neutrons traveling through a de-magnetized vacuum chamber³, with an annihilation target material at the end. The sensitivity of such a setup depends on the flight time t and the number of neutrons observed N , with a figure of merit Nt^2 , where the square dependence on t follows from Equation 2.12. The most sensitive free neutron experiment to date was performed at Grenoble [29], for which the flight time was $t \sim 0.1$ s and the flux of neutrons was $\Phi \sim 10^{11}$ neutrons/second. The experiment ran for about a year, thus producing a total of $N \sim 3 \times 10^{18}$ neutrons. With no candidates seen, the lower lifetime for $n \rightarrow \bar{n}$ was set at $\tau_{n \rightarrow \bar{n}} > 0.86 \times 10^8$ s.

Free neutron experiments have the extremely attractive feature that they are essentially background-free, but they are limited by the flux of free neutrons that can be feasibly produced. By contrast, bound neutron experiments such as Super-Kamiokande have abundant neutrons at any given time. Super-Kamiokande's fiducial volume, for instance, contains $\approx 6 \times 10^{33}$ neutrons bound in oxygen — more than sufficient to account for the suppression factor that bound neutrons suffer. Bound

³This is because the Earth's magnetic field will cause an energy splitting in the neutron and antineutron of $\mu_n B \approx 3 \times 10^{-21}$ GeV, where μ_n is the neutron magnetic moment. This splitting would suppress the $n \rightarrow \bar{n}$ probability (Equation 2.12), although it has been recently argued in [28] that a proper tuning of the magnetic field would *not* suppress the $n \rightarrow \bar{n}$ transition rate, if spin is taken into account.

neutron experiments are limited by constant atmospheric neutrino background, however. In particular, it is difficult to separate the multi-pion signal of $n \rightarrow \bar{n}$ from the final state particles in a deep inelastic scattering neutrino interaction, which produces multiple hadrons. Also, the density of the material in bound neutron experiments can significantly distort the $n \rightarrow \bar{n}$ signal, due to pion-nucleon interactions.

Despite being very different experiments, the null results from free and bound neutron searches have resulted in lower limits on the $n \rightarrow \bar{n}$ oscillation time within the same order of magnitude. Table 2.1 shows the limits set by bound neutron experiments. The background limitation of such neutron experiments is evident; notice, for instance, that even though Super-Kamiokande has a larger neutron exposure than Soudan-II by more than a factor of ten, the Super-Kamiokande limit is less than a factor of three more stringent than that of Soudan-II. Future free neutron experiments, in particular the proposed NNbarX experiment [30], intend to incorporate novel technologies to greatly increase the flux of free neutrons relative to [29], with projected sensitivities reaching $\tau_{n \rightarrow \bar{n}} \geq 10^{10}$ s.

2.5.2 Dinucleon Decay

The same operator 2.4 contributes to dinucleon decay: $NN \rightarrow \pi\pi$. The $NN \rightarrow \pi\pi$ decay rate is calculated with Fermi's Golden Rule:

$$\Gamma(NN \rightarrow \pi\pi) = \frac{1}{(2\pi)^3 \rho_N} \int d^3k_1 d^3k_2 \rho(k_1) \rho(k_2) v_{rel} (1 - \vec{v}_1 \cdot \vec{v}_2) \sigma_{tot}(NN \rightarrow \pi\pi) \quad (2.18)$$

where $\rho_N \approx 0.25 \text{ fm}^{-3}$ is the average nuclear density, $\rho(k_1)$ and $\rho(k_2)$ are the densities of nucleon 1 and 2 in momentum space, v_1 and v_2 are the (small) velocities of each nucleon and v_{rel} their small relative velocity, and $\sigma(NN \rightarrow \pi\pi)$ is the cross-section

Experiment	IMB	KAM	Frejus	SD2	SNO	SK-I
Material	oxygen	oxygen	iron	iron	deuterium	oxygen
Exposure (10^{32} n-yr)	3.2	3.0	5.0	21.9	0.55	245
Efficiency	50.0%	33.0%	30.0%	18.0%	—	12.1%
Scaled background	—	0.9	2.5	4.5	—	24.1
Data candidates	3	0	0	5	—	24
$T_{n \rightarrow \bar{n}}$ (10^{32} yr)	0.24	0.43	0.65	0.72	0.11	1.9
R (10^{23} s $^{-1}$)	1.0	1.0	1.4	1.4	0.25	0.52
$\tau_{n \rightarrow \bar{n}}$ (10^8 s)	0.88	1.2	1.2	1.3	1.2	2.7

Table 2.1: Limits on bound neutron oscillation lifetimes from Irvine-Michigan-Brookhaven ([31]), Kamiokande([32]), Frejus ([33]), Soudan-II ([34]), Sudbury Neutrino Observatory([35]), and Super-Kamiokande ([23]). Limits are converted to a free oscillation time via Equation 2.16. See the text for a comparison to the free neutron experiment from [29]. The values of R for [31–35] are calculated in [36], while the value of R used for [23] incorporates a more recent calculation from [27]. The uncertainty in R is also incorporated in the conversion to the free lifetime in [23]. The study in [35] used a different search method than the other analyses listed, such that efficiency, background rate, and data candidates are not illuminating figures.

for the process. A specific calculation within the context of a supersymmetric model is done in [37], while [38] does the same calculation for a more general $\Delta B = 2$ operator. The result for the lifetime $\tau_{NN \rightarrow \pi\pi} = 1/\Gamma(NN \rightarrow \pi\pi)$ is

$$\tau_{NN \rightarrow \pi\pi} \approx \frac{\pi M_N^2 M^{10}}{8\rho_N \Lambda^{10}} \quad (2.19)$$

where M_N is the nucleon mass, Λ the same hadronic matrix element from $n \rightarrow \bar{n}$, and M the suppression scale in Equation 2.4. Recalling Equation 2.6, we can rewrite this as

$$\tau_{NN \rightarrow \pi\pi} \approx \frac{\pi M_N^2}{8\rho_N} \Lambda^2 \tau_{n\bar{n}}^2. \quad (2.20)$$

We see, then, that the $NN \rightarrow \pi\pi$ lifetime scales with the square of the free $n \rightarrow \bar{n}$ lifetime, as does the bound $n \rightarrow \bar{n}$ lifetime. We can think of the prefactor as a nuclear

mode	Material	Efficiency	Background	Candidates	T_{lim}
$pp \rightarrow \pi^+\pi^+$	Iron	19.0%	2.34	4	7.0×10^{29} yrs
$pn \rightarrow \pi^+\pi^0$	Iron	23.4%	0.31	0	2.0×10^{30} yrs
$nn \rightarrow \pi^0\pi^0$	Iron	36.7%	0.78	0	3.4×10^{30} yrs
$pp \rightarrow K^+K^+$	Oxygen	12.6%	0.28	0	1.77×10^{32} yrs
$pp \rightarrow e^+e^+$	Oxygen	79.2%	≈ 0	0	1.0×10^{33} yrs

Table 2.2: Summary of results for $NN \rightarrow \pi\pi$ from Frejus [39], and $pp \rightarrow K^+K^+$ [40] and $pp \rightarrow e^+e^+$ [41] from Super-Kamiokande. The Frejus searches were performed with 2.2×10^{31} iron-years of exposure, and the Super-Kamiokande searches with 3.06×10^{32} oxygen-years.

suppression factor, although the source of the suppression is different. In $n \rightarrow \bar{n}$, the suppression arises from the difference in nuclear potentials felt by neutrons and antineutrons, while for $NN \rightarrow \pi\pi$ it arises from the requirement of overlapping wavefunctions in two bound nucleons.

Searches for dinucleon decay via any mode are less common than searches for single nucleon decay and $n \rightarrow \bar{n}$ (Table 2.2). A search for the modes discussed in this thesis, among many other $B - L$ violating modes, was conducted by Frejus [39]. Searches for $pp \rightarrow K^+K^+$ and $pp \rightarrow e^+e^+$ have been performed at Super-Kamiokande [40, 41]. The searches are distinct, both in their experimental signatures and theoretical framework. For instance, although $NN \rightarrow \pi\pi$ and $pp \rightarrow K^+K^+$ are superficially similar, as they both involve decay to two light mesons, the search in [40] is motivated by supersymmetric models discussed in [37] in which the BNV operator has two down-type quarks of different generations. For $NN \rightarrow \pi\pi$, all quarks are first generation, and thus such supersymmetric models are insensitive to $NN \rightarrow \pi\pi$ (at least at tree level). At the experimental level, pions interact heavily with both the residual nucleus and the surrounding medium, while kaons suffer fewer hadronic interactions, and have distinctive subsequent decays.

Chapter 3

The Super-Kamiokande Detector

In this chapter, I describe the Super-Kamiokande detector, the experimental apparatus used to perform the searches for $\Delta B = 2$ processes. Full details of the detector can be found in [42].

3.1 Overview

Super-Kamiokande (hereafter “SK”) is a large cylindrical water Cherenkov detector. It is located underneath Mount Ikenoyama, inside the Kamioka Observatory in Gifu Prefecture, Japan. Figure 3.1 shows a basic detector schematic. The detector is operated by the University of Tokyo’s Institute for Cosmic Ray Research. It contains 50 kilotons of ultra-pure water, surrounded by photomultiplier tubes (PMTs) to detect Cherenkov radiation from charged particles. It has been taking data since April 1996.

The main purpose of the SK detector is to search for nucleon decay¹, as well as study neutrinos from various extraterrestrial sources. Since 2010, it has also been

¹The extra “nde” after “Kamioka” is for “nucleon decay experiment.”

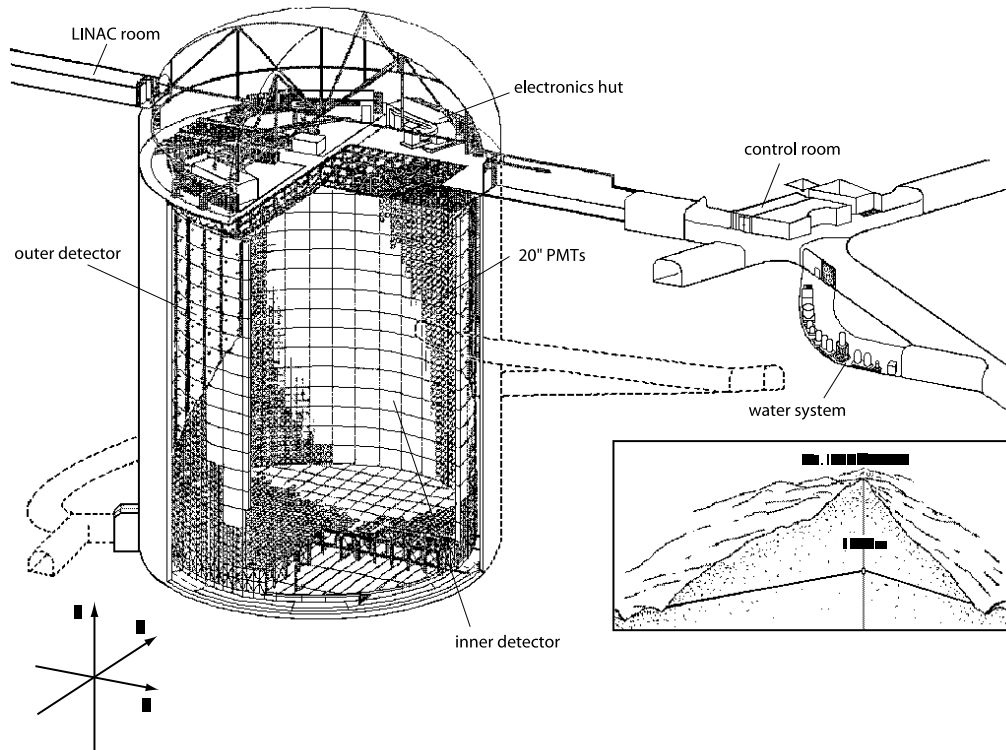


Figure 3.1: The SK detector [43].

used as a far-detector for the Tokai-to-Kamioka long-baseline neutrino experiment.

Datasets have been collected in four different detector configurations. The first period, called “SK-I”, consisted of 1489.2 livetime days from April 1996 to July 2001. Following this, there was a planned maintenance for several months. An accident occurred during water refilling in November 2001, causing over half of the inward-facing PMTs to implode. The remaining PMTs were quickly re-distributed uniformly throughout the detector surface, and the detector resumed taking data in October 2002. This second period, called “SK-II”, comprised 798.6 livetime days, ending in October 2005. The original SK-I PMT coverage was restored, and data-taking resumed in June 2006. This third period, called “SK-III”, comprised 518.1 livetime days until the summer of 2008. Significant upgrades to the detector electronics were

made prior to the resumption of data-taking in September 2008. This fourth period, called “SK-IV”, is the current configuration of the detector. As of March 2015, its dataset comprises 2166.5 livetime days.

This thesis uses the SK-I-IV dataset from April 1996 to March 2015, comprising 4972.4 livetime days, or 307 kiloton-years.

3.2 Structure

The 50 kilotons of water are held in a stainless steel, cylindrical tank. The detector has a full diameter of 39.3 m and a height of 41.4 m. The tank has two optically separated regions — a smaller concentric cylinder called the inner detector (ID) containing inward-facing PMTs, and an outer detector (OD) containing outward-facing PMTs. The two regions are separated by a 55 cm thick stainless steel support structure on which the PMTs are mounted.

3.2.1 Inner Detector (ID)

The ID is 33.8 meters wide by 36.2 meters tall, and contains 32 kilotons of ultra-pure water. A large number of 20-inch, inward-facing PMTs are arranged uniformly on its boundaries. For the SK-I data-taking period, there were 11,146 PMTs, such that about 40% of the ID surface was covered by photocathode. For SK-II, there were 5,182 PMTs remaining after the accident, corresponding to about 19% photocathode coverage. For SK-III and IV, the coverage is nearly the same as SK-I, with 11,129 PMTs.

3.2.2 Outer Detector (OD)

The OD surrounds the ID on all sides. It has 1,885 outward-facing 8-inch PMTs. Each PMT is embedded in the center of a 60 cm \times 60 cm wavelength-shifting plate to increase the effective photosensitive area. White Tyvek sheets are placed beneath the OD PMTs to maximize reflectivity. The main purpose of the OD is to veto cosmic ray muons, as well as to shield the detector from low-energy radioactivity in the surrounding rock. Though the 1 km rock overburden (2.7 km water equivalent) of Mount Ikenoyama reduces the flux of cosmic ray muons by five orders of magnitude, it is still the most persistent source of background at SK, and the OD is indispensable in rejecting it.

3.3 Cherenkov Radiation

The fundamental phenomenon by which SK reconstructs physics events is Cherenkov radiation. Cherenkov radiation is light emitted when a relativistic charged particle passes through a medium at a speed greater than the speed of light within that medium. The condition for such radiation is seen in the simple inequality

$$\beta > \frac{1}{n} \tag{3.1}$$

where $\beta = v/c$, v being the speed of the particle, and n is the index of refraction of the material. For the ultra-pure water of SK, $n = 1.33$, so that $1/n \approx 0.75$.

Cherenkov light is emitted at an acute angle with respect to the direction the particle is traveling. This produces a cone, whose half-angle θ_C (typically called the

Cherenkov angle) is simply determined by

$$\cos(\theta_C) = \frac{1}{n\beta}. \quad (3.2)$$

Often we are interested in the ultra-relativistic limit $\beta \approx 1$, in which case θ_C reaches a maximum of about 42 degrees. The Cherenkov angle is an important quantity for determining what kind of particle is traveling through the detector. For instance, lighter particles such as electrons almost always produce a cone at the ultra-relativistic angle, while heavier particles like muons, pions, and protons are often somewhat collapsed, due to the higher momentum threshold they must reach.

The Cherenkov radiation spectrum is described by the formula:

$$\frac{d^2N}{dx d\lambda} = \frac{2\pi\alpha}{\lambda^2} \left(1 - \frac{1}{n^2\beta^2}\right). \quad (3.3)$$

Here N is the number of photons emitted, λ is the wavelength of light, x is the distance the particle has traveled, and $\alpha = 1/137$ is the fine structure constant. In the sensitive wavelength region of the SK PMTs (300-600 nm), about 340 photons are emitted per centimeter traveled (Figure 3.2).

The Cherenkov light emitted by a relativistic charged particle is collected by the ID PMTs and converted to an electronic signal of photoelectrons (p.e.'s), or "hit." The projection on the ID wall is a ring of hits. The charge and time information of each hit is used to determine crucial information such as the event vertex, particle identification, and momentum. Information from the OD is crucial for determining whether the event came from outside the tank, and if it had enough energy to escape the ID. Event reconstruction will be described in detail in Chapter 6.

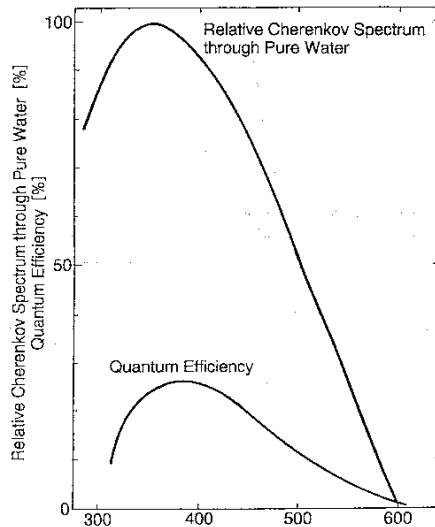


Figure 3.2: Relative spectrum of Cherenkov light in pure water, with quantum efficiency of the ID PMT overlaid [43].

3.4 Photomultiplier tubes

3.4.1 Inner Detector

The ID uses 20-inch diameter Hamamatsu R3600 PMTs (Figure 3.3), developed by Hamamatsu Photonics K.K. in cooperation with Kamiokande collaborators [44]. The dynode structure and bleeder circuit were modified to improve timing response and collection efficiency for SK [45]. The photocathode of the ID PMT is coated with bi-alkali that has high sensitivity to Cherenkov light and low thermionic emission. A peak quantum efficiency of 22% is found in the 360-400 nm region, as seen in Figure 3.2. The single p.e. and transit time distributions can be seen in Figure 3.4. Table 3.1 lists additional specifications for the ID PMTs.

The geomagnetic field of ≈ 450 mG at the detector site affects the flow of photoelectrons in the ID PMTs, which degrades the timing resolution. To compensate, 26 sets of Helmholtz coils are arranged around the tank, reducing the magnetic field to ≈ 50 mG.

Following the accident in November 2001, ID PMTs have been instrumented with acrylic covers. A clear 12 mm UV-transparent acrylic dome is put over the photocathode area of each PMT, and the side of each PMT is protected with fiber-reinforced plastic, with holes allowing water to flow freely in and out of the case. The transparency of the acrylic cover for photons at normal incidence is $>96\%$ above 350 nm wavelength.

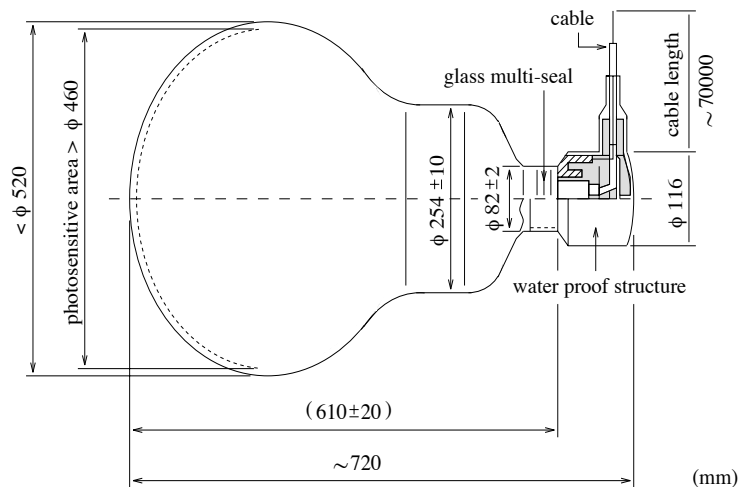


Figure 3.3: A schematic of the 20-inch PMT used in the ID [42].

3.4.2 Outer Detector

The 8-inch OD PMTs are Hamamatsu R1408 PMTs obtained from the decommissioned IMB experiment. The photocathodes of the PMTs are fitted with a 60 cm \times 60 cm wavelength shifter plate [46], which increases the total OD light collection efficiency by about 50%. The plates degrade the timing resolution of the OD PMTs

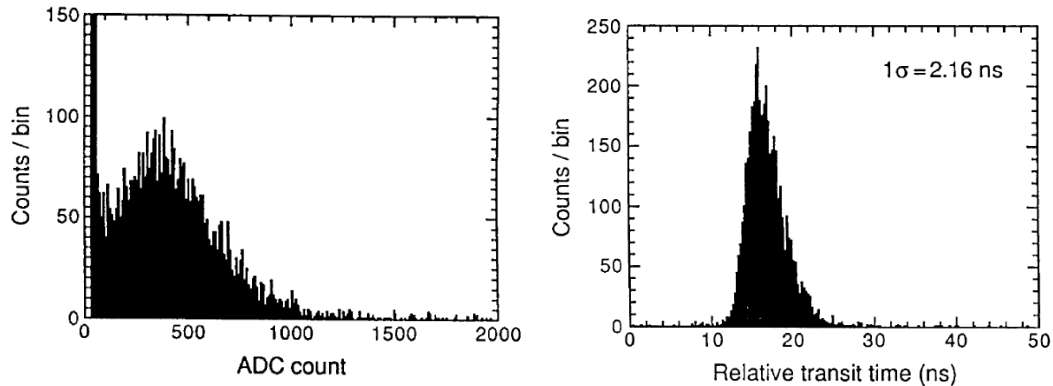


Figure 3.4: Left: pulse height distribution for a single p.e. in a 20-inch PMT. The peak near zero is from dark current. Right: relative transit time for a 20-inch PMT illuminated with light of 410 nm wavelength, for single p.e. intensity. Both from [42].

from 11 ns to 15 ns. However, as the primary function of the OD is to veto cosmic ray muons, light collection efficiency far outranks sharp timing resolution as an experimental necessity.

3.5 Electronics and Data Acquisition (DAQ)

The Super-Kamiokande electronics and data acquisition systems (DAQ) were optimized to handle signals from a large number of channels quickly and efficiently. In the ID in particular, rapid processing of events occurring closely in time is necessary, such as a stopping muon followed by its decay electron, or a quick burst of neutrinos from a supernova. Here I describe basic features of the SK electronics and DAQ system.

Shape	Hemispherical
Photocathode area	50 inch diameter
Window material	Bi-alkali (Sb-K-Cs)
Quantum efficiency	22% at 390 nm
Dynodes	11-stage Venetian blind
Gain	10^7 at 1500-2000 V
Dark current	200 nA at 10^7 gain
Dark pulse rate	3 kHz at 10^7 gain
Cathode non-uniformity	<10%
Anode non-uniformity	<40%
Transit time	90 ns at 10^7 gain
Transit time spread	2.2 ns (1σ) for 1 p.e. equivalent signal
Weight	13 kg
Pressure tolerance	6 kg/cm ² water proof

Table 3.1: Specifications for the ID PMTs.

3.5.1 Inner Detector Electronics and DAQ (SK I-III)

For the first three running periods, the ID PMT signals were processed by custom analog timing modules (or ATMs) of the Tristan KEK Online standard (or TKO). The ATMs recorded integrated charge and arrival time information of all ID PMTs. Each ATM received signals from 12 PMTs. Each ATM was housed in a crate containing 20 ATMs, with a total of 48 crates distributed evenly among four electronics huts situated above the detector tank.

Each channel of the ATMs has two pairs of Charge to Analog and Time to Analog Converters (QAC and TAC, respectively). The inclusion of two channels minimizes dead time, in particular for physics processes in which there may be two stages occurring in rapid succession. Detailed specifications of the ATM are shown in Table 3.2.

Along with the ATMs, each TKO crate contains additional elements of the ID DAQ system. There is a go/no-go (GONG) trigger control module through which the global trigger signal is distributed, and a super control header (SCH). The SCH sends

Number of channels	12/board
One hit processing time	$\sim 5.5 \mu\text{s}$
Charge dynamic range	$\sim 400\text{-}600 \text{ pC}$ (12-bit)
Timing dynamic range	$\sim 1300 \text{ ns}$ (12-bit)
Charge resolution (LSB)	0.2 pC
Charge resolution (RMS)	0.2 pC
Timing resolution (LSB)	$\sim 0.3\text{-}0.4 \text{ ns}$
Timing resolution (RMS)	0.4 ns
Temperature dependence (QAC)	3 Count/deg. \leftrightarrow 0.6 pC/deg.
Temperature dependence (TAC)	2 Count/deg. \leftrightarrow 0.8 ns/deg.
Event number	8-bit
Data size of one hit	6 bytes
FIFO	2 kBytes (~ 340 hits)

Table 3.2: Specifications for the ATM.

the ATM information to the super memory partner (SMP) when a trigger is received (see Section 3.5.3). It acts as a data buffer to be read out by an online computer workstation. Each electronics hut contains two such workstations, each handling six SMP modules. All eight workstations feed into a central online workstation, which assembles all of the PMT information collected by the ATMs, and sends it away to an offline computer where it can be stored and analyzed. Figure 3.5 shows a schematic of the SK-I-III ID DAQ system.

3.5.2 Outer Detector Electronics and DAQ (SK-I-III)

Signals from OD PMTs are passed through the same coaxial cable that provides them with high voltage. The high voltage for OD PMTs is distributed through “paddle cards”, and PMT signals are picked off by a capacitor on the same paddle cards. From the paddle cards, the signal is fed into custom charge-to-time converters (QTCs) containing LeCroy MQT200 chips and comparators. Each QTC contains four paddle cards, each of which feed out to 12 PMTs. The QTCs measure the charge and

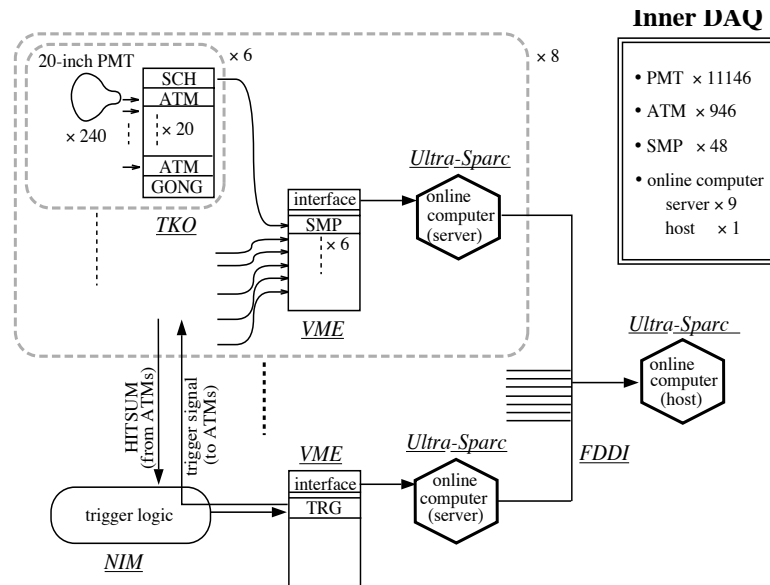


Figure 3.5: A schematic of the ID DAQ for SK-I-III [42].

timing information from the OD PMTs, and then send them to a LeCroy 1877 time-to-digital converter (TDC). The TDC modules can record up to eight QTC output pulses with a resolution of 0.5 ns. The dynamic range of the module is set to $16 \mu\text{s}$ ($10 \mu\text{s}$ before and $6 \mu\text{s}$ after the trigger time). The data are then stored in a large VME dual-port memory buffer (DPM), and sent to an event builder process that runs on an online host CPU that merges OD and ID data to form a full event. Figure 3.6 shows a schematic of the SK-I-III OD DAQ system.

3.5.3 Trigger (SK-I-III)

The ID trigger system is determined by the number of hit PMTs in the ID within a 200 ns time window (HITSUM in Figure 3.5). A “hit” corresponds to about 0.25 p.e. Three types of triggers are generated, based on the HITSUM signal. The high energy (HE) trigger is signaled if HITSUM exceeds 31 hits (SK-I). For the low energy (LE)

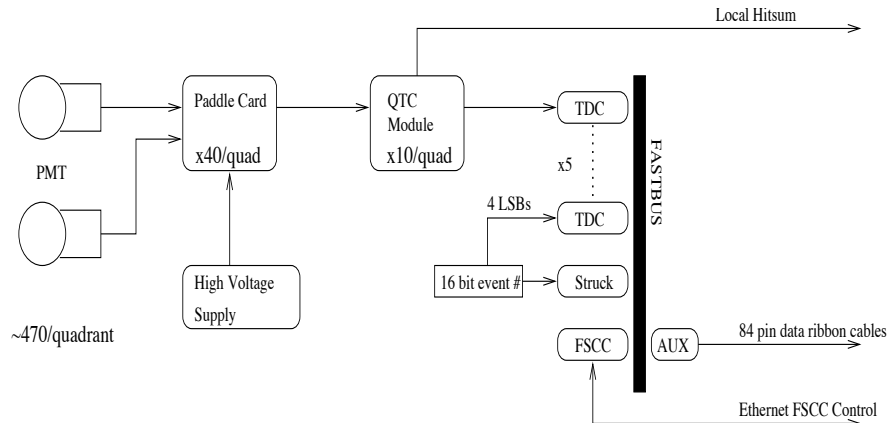


Figure 3.6: A schematic of the OD DAQ for SK-I-III [43].

trigger, the threshold is 29 hits (SK-I)². Finally, a super low energy (SLE) trigger was implemented about a year into the SK-I period to lower the solar neutrino analysis threshold. SK-II and SK-III implement similar schemes, with detector-dependent variations on the threshold values. For this thesis, the HE trigger is the starting point for relevant data.

The OD trigger system works similarly, with a trigger threshold of 19 hits within a 200 ns time window. All four trigger signals (HE, LE, SLE, OD) are fed into a hardware trigger module (TRG) that generates a global trigger signal when any of them are activated. Figure 3.7 shows the different levels of the global trigger system.

3.5.4 SK-IV Electronics and DAQ Upgrade

For the SK-IV data-taking period, the SK front-end electronics and DAQ system were upgraded [47, 48]. The main motivations for this upgrade were to increase the number of events that could be detected in relevant time windows for neutrinos from

²The LE threshold corresponds to the number of hits generated by a 5.7 MeV electron, assuming 50% trigger efficiency. As there are roughly 5 hits per MeV, the corresponding energy for the HE trigger is similar. The HE trigger value is very conservative, given that the HE analyses typically require 30 MeV of visible energy.

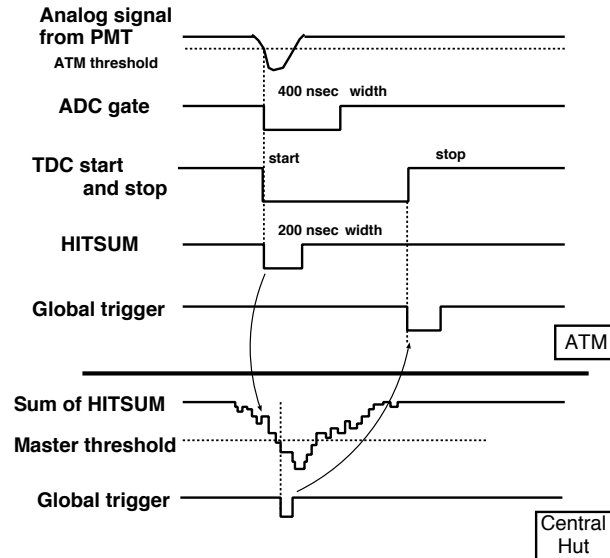


Figure 3.7: A schematic of the SK-I-III trigger system [43].

supernova bursts, obtain more precise measurements of solar neutrino parameters, and improve searches for supernova relic neutrinos. Here I describe the main aspects of the upgrade.

The new front-end electronics modules are QTC-based electronics with Ethernet (or QBEE). Each QBEE contains a custom application-specific integrated circuit (ASIC) with a QTC. The QTC has three measurement ranges (small, medium, large) that covers a wider dynamic range than the ATMs. The ATMs were charge-saturated at 600 pC, while the new QTC can reach over 2000 pC. The timing and charge resolution are similar to that of the ATMs. The QTC outputs a pulse whose leading edge contains timing information and width is proportional to the total charge. The ethernet cables improve data flow and reduce congestion relative to the old TKO readout.

The hardware trigger system has been replaced by a software trigger that contains all PMT hit information. The software trigger makes selections based on the same

hit threshold mechanism described above for the SK-I-III trigger system.

3.6 Water Purification System

The 50 kilotons of water in the SK tank must be as transparent as possible to maximize the light seen by interesting physics events. The transparency should also be stable, thereby allowing accurate modeling of light attenuation effects. To achieve this, the water is continuously circulated to remove various sources of impurity at a rate of about 30 tons/hour, which encompasses the entire tank volume in about 70 days.

The water is first passed through 1 μm mesh filters to reduce dust and other particles. It is then passed through a heat exchanger that cools the water from 14.2°C to 12.9°C, and suppresses the growth of bacteria. Following this, a cartridge polisher removes heavy ions, and a UV sterilizer kills remaining bacteria. It then goes through a reverse osmosis and vacuum degassifier system, which removes radon and other dissolved gases (keeping radon levels low is especially important, as radon constitutes one of the main backgrounds to the low-energy neutrinos from supernovas). A second filtering stage removes particles larger than ~ 10 nm, and a membrane degassifier further lowers radon levels. The water is then returned to the tank. Figure 3.8 shows each stage of the water purification system.

3.7 Calibration

The detector is calibrated via a number of sources, all of which are essential for its stable operation. Here I describe the main sources. Calibration procedures for SK-I are described in [42]. A recent, detailed description of detector calibration for SK-IV

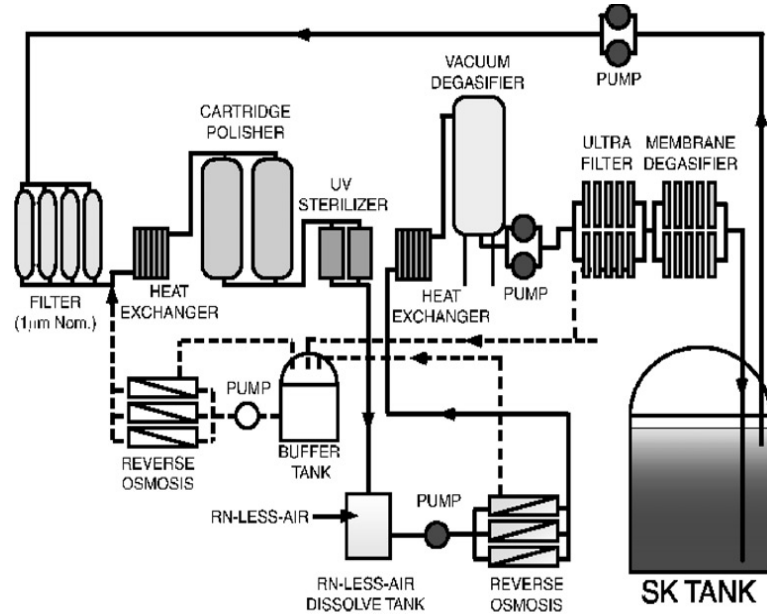


Figure 3.8: The SK water purification system [42].

can be found in [49].

3.7.1 Water Calibration

Laser absorption and scattering

The intensity of light as it travels through the ultra-pure water of SK changes with distance. It is described simply by the function

$$I(L) = I_0 e^{-L/L_{atten}} \quad (3.4)$$

where I is the intensity, I_0 the intensity at the point the light is emitted, L the distance traveled, and L_{atten} the attenuation length of the water. L_{atten} is wavelength-

dependent, and must account for both scattering and absorption. In SK, the relevant scattering processes are Rayleigh and Mie scattering. Rayleigh scattering is relevant in the case where the scattering object is much smaller than the wavelength of light, while Mie scattering is relevant when the length scales are comparable (such as with a large, ~ 100 nm impurity in the water). Thus the attenuation length can be described by three parameters:

$$L_{atten}(\lambda) = \frac{1}{\alpha_{Ray}(\lambda) + \alpha_{Mie}(\lambda) + \alpha_{abs}(\lambda)}. \quad (3.5)$$

To determine these parameters, laser light was injected from an optical fiber from eight different positions. In SK-I-III, a 337 nm nitrogen laser was used in conjunction with wavelength-shifting laser dyes, such that data was taken for wavelengths 337, 365, 400, and 420 nm. For SK-IV, a laser diode system was used, with slightly different wavelengths. The hit and timing information from the laser light was used to tune the water parameters in Monte Carlo simulations (MC) until good agreement with the data was found. Figure 3.9 shows measured values of these parameters.

Cosmic ray muons

Downward-going cosmic ray muons occur at a rate of a few Hz at SK, making up a majority of triggered high energy events. Below energies of ~ 100 GeV, they predictably lose energy via ionization at a rate of about 2 MeV/cm. Thus, they are a valuable natural calibration source, and cover a much broader spectrum than the laser sources described above.

The number of photoelectrons detected by a cosmic ray muon is given by

$$Q(\ell) = Q_0 \frac{f(\theta)}{\ell} e^{-\ell/L_{atten}} \quad (3.6)$$

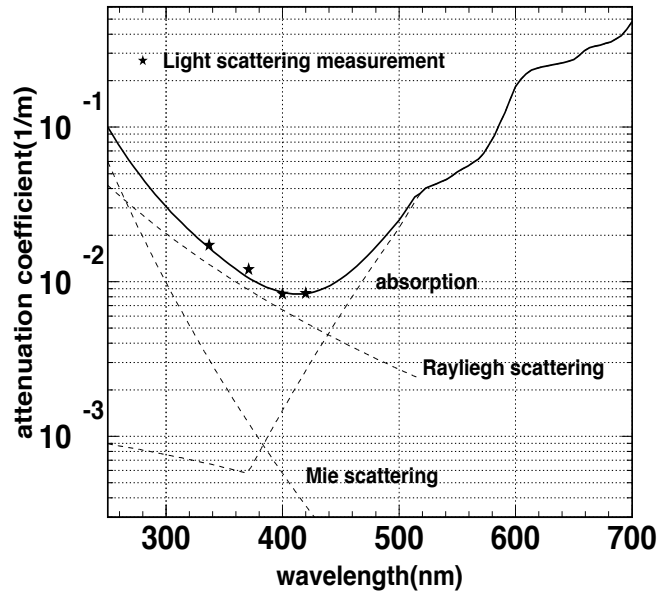


Figure 3.9: Attenuation measurements and fitted curves using the nitrogen laser [50]. Measured values for SK-IV are similar.

where Q_0 is a constant, $f(\theta)$ is the PMT angular acceptance with θ being the angle with respect to the normal, ℓ is the photon path length, and L_{atten} is the attenuation length. From cosmic ray data, the attenuation length is measured to be about 95 m. Figure 3.10 shows measurements of Equation 3.6, as well as time variation of the attenuation length.

3.7.2 Charge calibration

Various measures must be undertaken to ensure that the PMT response to Cherenkov radiation is well-understood, for both measurement and simulation. I briefly describe these measures here. More details on charge calibration can be found in [51].

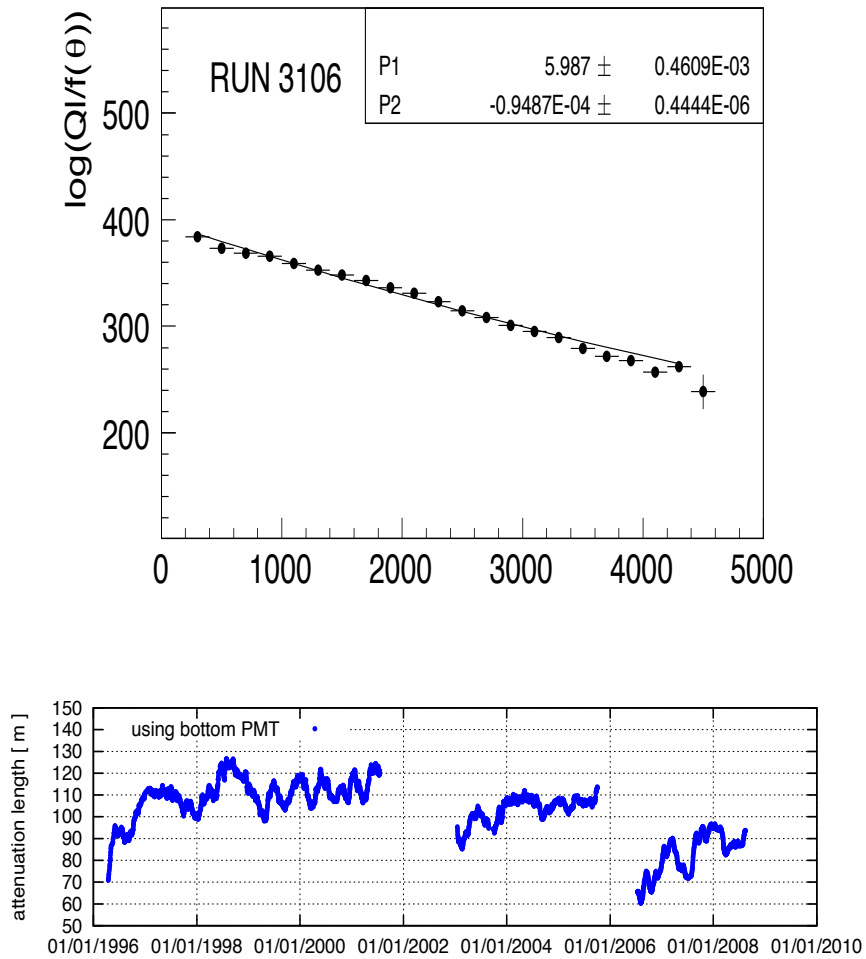


Figure 3.10: Plot of $\log\left(\frac{Q(\ell)\cdot\ell}{f(\theta)}\right)$ vs. ℓ (in cm) for a typical run (top); variation of the attenuation length in the SK-I-III periods (bottom). Both from [50]. The time variation of the length is sensitive to water quality, and time-dependent attenuation lengths are used in data processing.

High voltage determination

The charge response for a given PMT can be quantified in terms of its gain and quantum efficiency. The gain of a given PMT is controlled by the high voltage (HV) that is supplied to its dynodes, as seen in the simple relationship

$$\text{Gain} \propto \alpha V^\beta. \quad (3.7)$$

Here V is the voltage, and α and β are parameters specific to each PMT. The observed charge, in turn, is proportional to the gain, as well as the number of incident photons and the quantum efficiency (QE):

$$Q_{obs} \propto N_{photon} \times QE \times Gain. \quad (3.8)$$

The charge response was most recently calibrated as follows. In 2005, before the start of the SK-III data-taking, a group of so-called “standard PMTs” was calibrated prior to installation in the ID. They were placed in a dark box with a xenon lamp source passed through a UV filter requiring $\lambda < 400$ nm, and a scintillator ball. A total of 420 PMTs underwent this process. Their HV was adjusted so that the charge output matched that of a reference avalanche photodiode (APD).

Upon installation, the ID PMTs were placed into 25 different groups, so that each group had 9-12 of these standard PMTs. The same xenon lamp and scintillator ball was placed in the center of the tank and used for calibration. The PMTs were adjusted such that their charge response matched the average charge response of the standard PMTs in a given group.

Gain calibration

Two kinds of gain calibration are performed at SK: absolute and relative. I describe each briefly here.

For the absolute calibration, the single p.e. distribution must be measured, and so a low-energy source is used. Specifically, the calibration used a Californium ^{252}Cf source, surrounded by a spherical mixture of nickel oxide and polyethylene. The signal

from this source is produced as follows: spontaneous fission of the ^{252}Cf produces neutrons that are brought to thermal equilibrium by the polyethylene, and then captured by the nickel. Upon capture, the nickel then emits a gamma ray of about 9 MeV. The emission yield is about 100 p.e., low enough that most hit PMTs will have only a single p.e. With this measurement, the gain, or the ratio of the final PMT charge output to the p.e. input, can be determined.

The relative gain calibration describes the response of each PMT relative to the average. Measurements are made with a dye/nitrogen laser, for both high and low intensity light. The relative gain can be determined for the i^{th} PMT via

$$\text{Gain}(i) \propto \frac{Q_{obs}(i)}{N_{hit}(i)}, \quad (3.9)$$

where Q_{obs} is the observed charge and N_{hit} is the number of photons reaching the PMT cathode. To get the relative gain, this value is normalized by the mean for all PMTs.

QBEE Charge linearity

For the QBEE modules in SK-IV, it was necessary to measure the charge linearity, defined as the ratio of observed to expected charge. The response in the full ~ 1 -1000 pe range of the QBEEs was measured. The nitrogen laser mentioned previously was used.

Monitor PMTs with well-known responses were used for reference. Their linearity was measured by placing the light source at various distances, and also scanning over gain. This monitor PMT charge was used to predict the expected charge for other ID PMTs via

$$Q_{exp}^{(i,m)} = Q_{mon}^m \times \frac{Q_{mean}^{(i,n)}}{Q_{mon}^n}, \quad (3.10)$$

where i indexes the PMT, m and n index the monitor and normalizing runs (runs in which the monitor and remaining PMT responses were measured, respectively), Q_{mon} is the monitor PMT charge, and Q_{mean} is the mean output charge per event for the i^{th} PMT.

Non-linearity is most noticeable at high charges, and comes from two sources. One is the fact that the input signal is read out by more than one of the three available QBEE channels. The second source is the PMTs themselves, whose response falls off by 2% at larger currents. The QBEE multi-hit effect can be corrected for, such that the overall charge non-linearity is $\sim 1\%$ up to about 100 p.e. It becomes worse as the charge increases up to the QBEE saturation point around 1200 p.e. Non-linearity effects are included in Monte-Carlo simulations.

3.7.3 Timing Calibration

The hit times of PMTs are crucial for accurate vertex reconstruction. Several time scales must be taken into account for timing calibration measurements:

- The photon time-of-flight from its emission point along the particle track to the PMT surface;
- The time for the photoelectron cascade to pass through the PMT;
- The time to travel through the cable from the PMT to the ATM or QBEE;
- The readout time.

The latter three intervals are unique to each PMT. In addition, they exhibit charge dependence, since events with higher charge will pass the discriminator threshold

sooner than events with less charge. The purpose of the timing calibration is to measure these time intervals for each PMT as a function of charge, model the dependence, and use this to apply a correction factor such that the hit timing is independent of charge. The same nitrogen/dye laser described previously is used for a calibration light source. A typical plot of the timing charge dependence is shown in Figure 3.11.

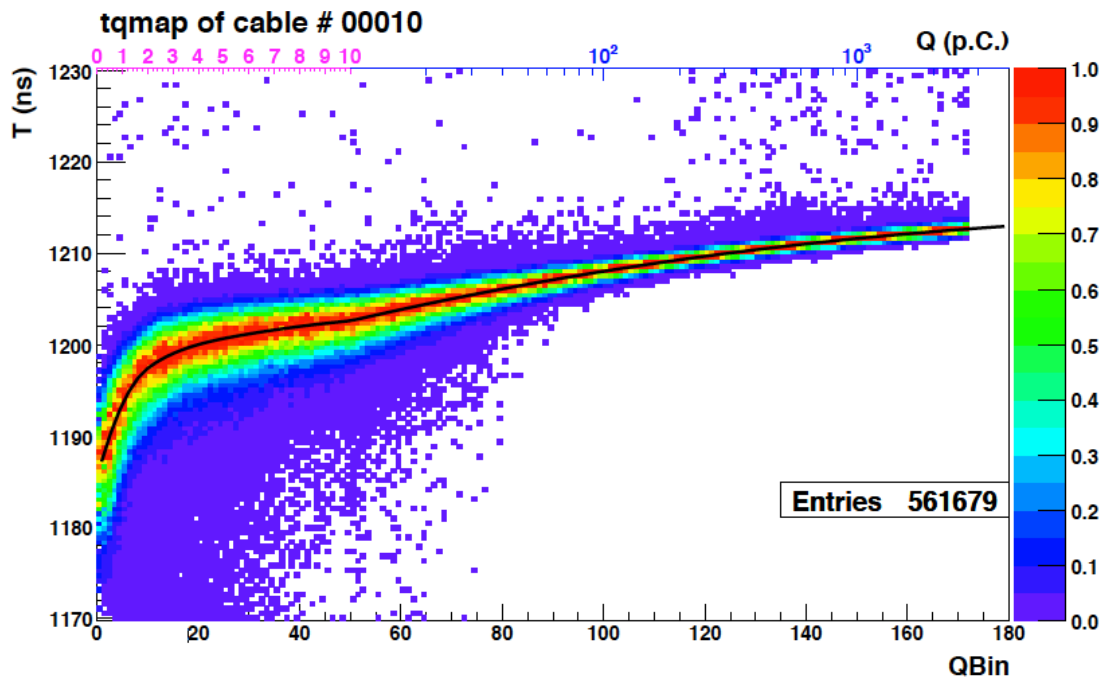


Figure 3.11: A plot of the time vs. charge for a typical readout channel [49]. The time of each hit is corrected for time of flight.

3.7.4 Energy Scale

Precise knowledge of the detector energy scale is extremely important, as virtually all SK physics analyses depend on energy reconstruction. Here I describe sources of energy scale calibration for the high energy dataset; for low energy, see [52].

Stopping Muons

Stopping muons are useful energy calibration sources by way of two quantities: their Cherenkov angle, and their range. The momentum of any charged particle of mass m above Cherenkov threshold can be written as a function of the Cherenkov angle θ_C (in natural units):

$$p = \frac{m}{\sqrt{(n \cos \theta_C)^2 - 1}}. \quad (3.11)$$

The Cherenkov angle reaches a limiting value for higher muon momenta, so only muons with momenta ~ 400 MeV/c or less are useful when considering this relationship. It is a good check on momentum reconstruction, as it depends only on θ_C and not any more complicated charge pattern.

At higher energy, the momentum loss of stopping muons can be reliably determined by measuring their range, as muons below ~ 100 GeV/c are minimum ionizing particles that lose energy at a rate of about 2 MeV/cm in water. The range is measured from the entrance point in the detector, to the vertex of the decay electron. Figure 3.12 shows comparisons of data and MC for both low- and high-momentum muons.

Decay electrons

As with stopping muons, their resultant decay electrons are also an abundant calibration source at SK. The decay electron spectrum is useful for calibrating the tens of MeV energy region (Figure 3.13). Not all stopping muons produce decay electrons, as μ^- are susceptible to muon capture by protons. Specific selection criteria for decay electrons will be described in detail in Chapter 6.

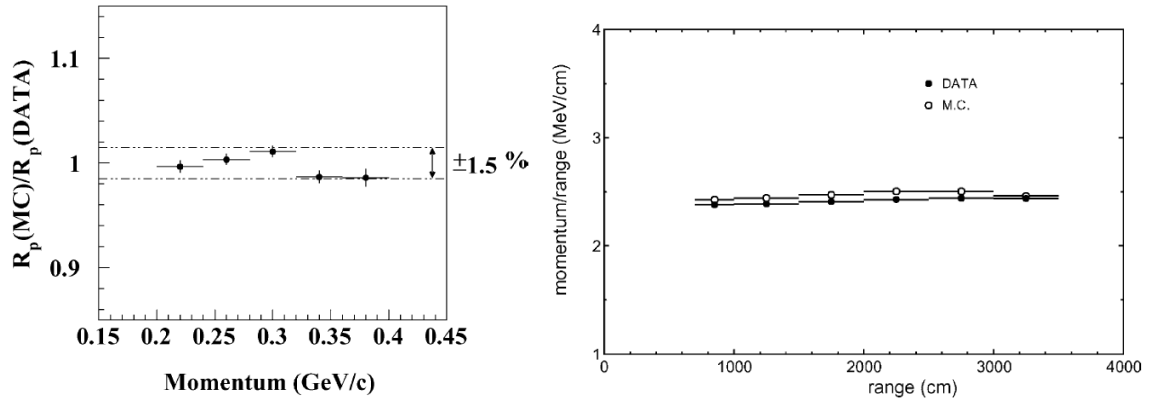


Figure 3.12: Left: double ratio R_{MC}/R_{data} , where R is the ratio of measured momentum to momentum inferred from the Cherenkov angle, for low momentum stopping muons. Right: ratio of momentum to range for high momentum stopping muons. Both from [42]

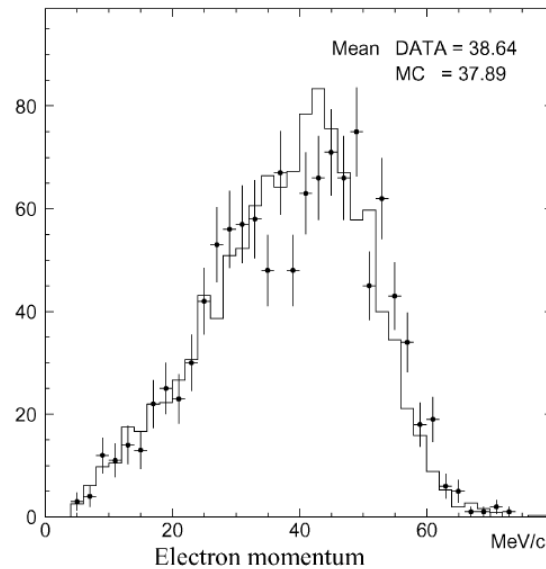


Figure 3.13: Momentum of decay electrons for data (crosses) and MC (solid histogram) [42].

Neutral pions

Neutral current interactions in the detector often produce single π^0 's, which then decay into two photons. The photons typically create two showering rings (rings that exhibit the effects of electromagnetic showers, which will be described in further detail in Chapter 6). The combination of two showering rings with some other requirements, such as no detected decay electron, creates a mostly pure single π^0 sample. The invariant mass of the two showering rings can be reconstructed and compared between data and MC (Figure 3.14).

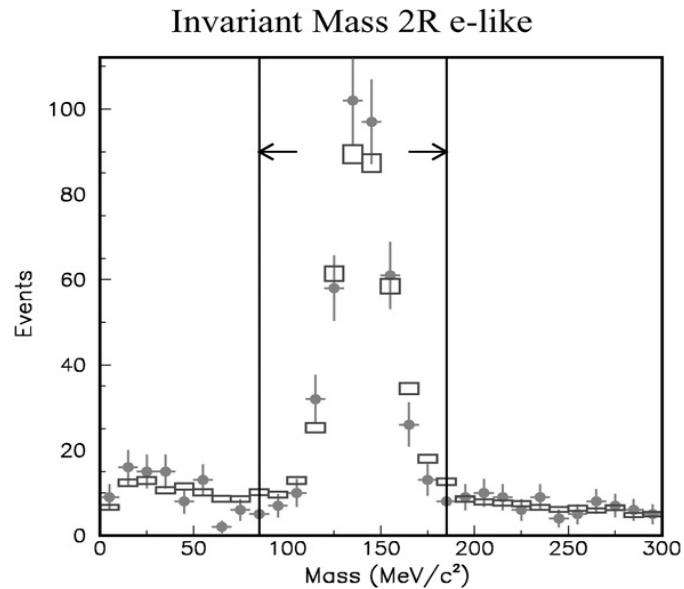


Figure 3.14: Invariant mass of the π^0 sample (two showering rings), between data (crosses) and MC (boxes) [42].

Summary

Figure 3.15 shows the energy scale uncertainty as a function of momentum for the calibration samples described above. The agreement between data and MC is generally quite good, such that the uncertainty is less than 3% for all samples considered.

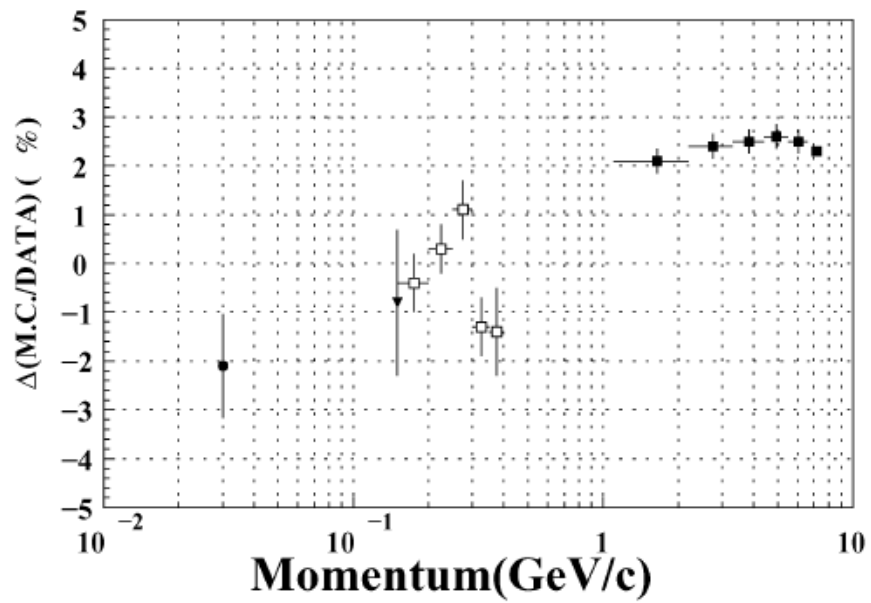


Figure 3.15: Energy scale uncertainty vs. momentum range used for calibration measurements in SK-I [42], in order of increasing energy: decay electrons (solid circles), single π^0 's (solid triangles), low-energy stopping muons (open squares), and high-energy stopping muons (solid squares).

Chapter 4

Atmospheric Neutrino Simulation

The only background to the $\Delta B = 2$ searches in this thesis comes from neutrino interactions in the water. The features of Super-Kamiokande that make it an ideal detector for BNV searches — large exposure, natural shielding from most noise sources, 4π coverage — also make it ideal for the study of neutrinos. Neutrino Monte Carlo simulations for each SK-I-IV detector phase are necessary to estimate the background rate and its associated systematic uncertainties for these searches.

The particular type of neutrinos that concern this thesis come from the earth's atmosphere. Most of these neutrinos pass through the earth without interacting, but a small fraction do. At Super-Kamiokande, the rate of neutrino events after data reduction is about 8/day. When summed over nearly two decades of data, this amounts to a large background, particularly given that $\Delta B = 2$ processes are already constrained to be quite rare if they occur at all. Thus, it is extremely important to understand atmospheric neutrinos as accurately as possible, both their interactions in the detector and their origins outside of it.

4.1 Neutrino Flux

The atmospheric neutrino flux starts from the flux of cosmic rays. Primary cosmic rays — mainly energetic H nuclei — bombard the earth’s atmosphere from all directions. They interact hadronically with air molecules, producing additional hadrons, mainly pions and kaons. The hadrons decay in stages to produce a large flux of neutrinos before reaching sea level.

The primary cosmic ray flux and resulting neutrino flux is fairly well-known below momenta of about 100 GeV/c, which encompasses the relevant scale of this thesis of $2M_{\text{nucleon}} \approx 2 \text{ GeV}$. For SK analyses, the most recent flux calculated by M. Honda and collaborators is used [53], which compared to previous works [54, 55] contains improvements at low energy. The effects of the earth’s geomagnetic field, as well as the magnetic field from the solar wind, which are especially prominent at low cosmic ray momenta ($\sim 1 \text{ GeV}/c$), are taken into account in these calculations. Other flux calculations, namely FLUKA [56] and BARTOL [57], are used to estimate systematic uncertainties. Figure 4.1 shows the primary cosmic ray flux, and Figure 4.2 shows the neutrino flux and flavor ratios up to 50 GeV.

Unless otherwise noted, the atmospheric neutrino rates in this thesis are weighted to include effects of two-flavor neutrino oscillation, namely the $\mu - \tau$ oscillation probability:

$$P(\nu_\mu \rightarrow \nu_\tau) = \sin^2(2\theta_{23}) \sin^2\left(\frac{1.27 \times \Delta m^2 \times L}{E}\right). \quad (4.1)$$

Here θ_{23} is the mixing angle between the second and third neutrino mass eigenstates, assumed to be maximal ($\theta_{23} = 45^\circ$), $\Delta m^2 = 2.5 \times 10^{-3} \text{ eV}^2$ is the fitted value of the mass splitting between these eigenstates, L is the length (in km) between the neutrino’s creation and interaction points, and E (in GeV) is the true neutrino en-

ergy at the interaction point. Smaller weight factors from the flux in [53] are also applied, related to effects of the solar wind. In principle a full three-flavor oscillation probability should be used, although the $\mu - e$ oscillation probability is quite small in the atmospheric neutrino energy regime.

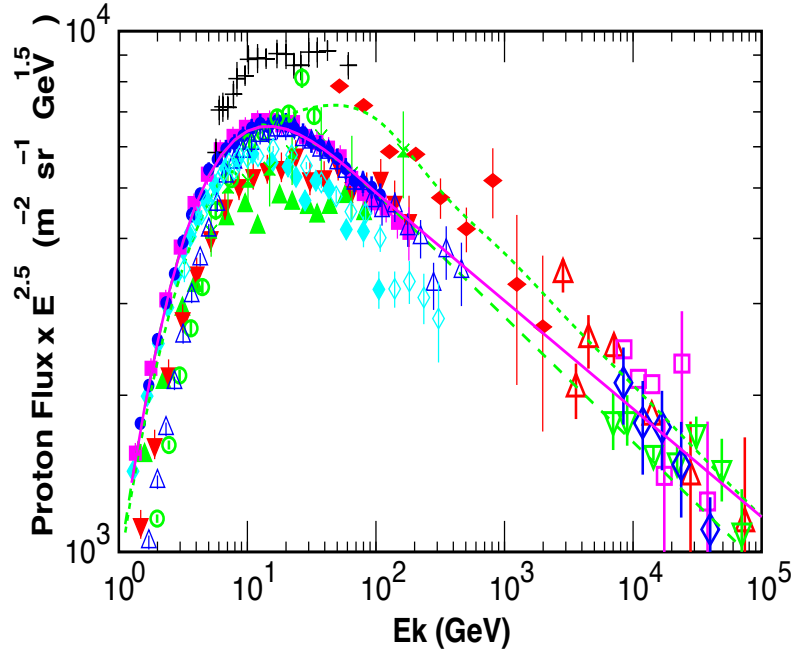


Figure 4.1: The primary cosmic ray flux for protons (at solar minimum), as calculated in [54]. Overlaid data points (see [54] for references) come Webber (crosses), MASS (open circles), LEAP (closed upward triangles), IMAX (closed downward triangles), CAPRICE-94 (closed vertical diamonds), CAPRICE-98 (open vertical diamonds), BESS (closed circles), AMS (closed horizontal diamonds), BESS-TeV (open upward triangles), Ryan et al (closed horizontal diamonds), JACEE (large open downward triangles), RUNJOB (large open diamonds), Ivanenko et al. (large open upward triangles), and Kawamura et al. (large open squares). Dashed lines indicate calculations from a fitting procedure, and the solid line includes additional corrections explained in [54].

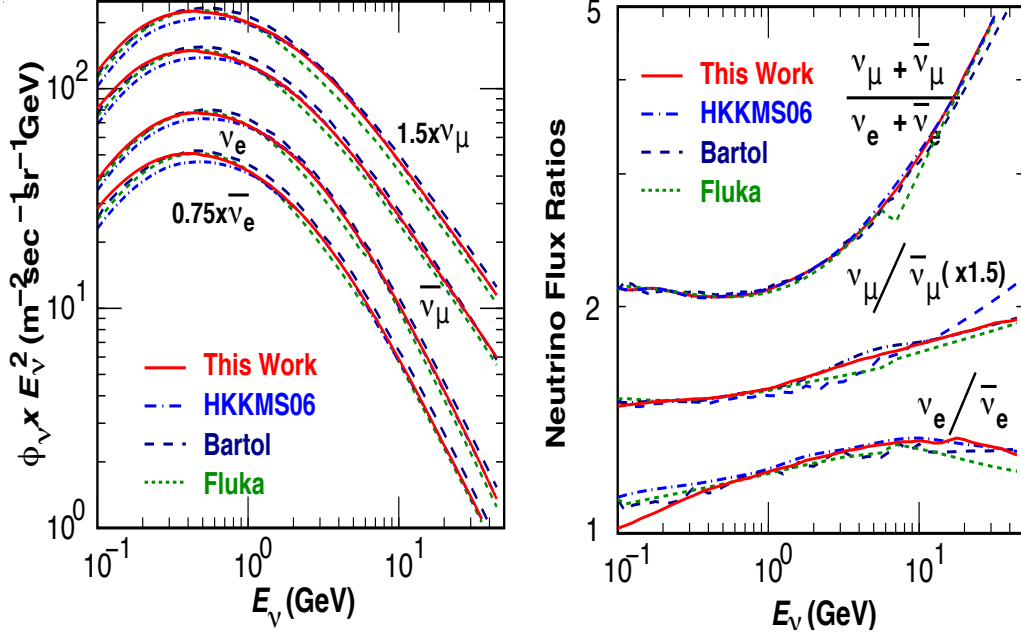


Figure 4.2: The atmospheric neutrino flux (left) and neutrino flavor ratios (right) up to 50 GeV. The solid line indicates the calculation of [53], the dot-dashed line an earlier calculation from Honda et al. [55], the long dashed line the BARTOL calculation [57], and the short dashed line the FLUKA calculation [56].

4.2 Neutrino interactions

Four main types of interactions are simulated:

- (quasi-) elastic scattering: $\nu + N \rightarrow \ell + N'$
- single meson production: $\nu + N \rightarrow \ell + N' + m$
- deep inelastic scattering: $\nu + N \rightarrow \ell + N' + \text{hadrons}$
- coherent pion production: $\nu + {}^{16}\text{O} \rightarrow \ell + {}^{16}\text{O} + \pi$

Here ν is a neutrino or anti-neutrino of any flavor, N and N' are the incoming and outgoing nucleons, respectively, and ℓ is the outgoing lepton. All four of these

interactions can occur in charged current (CC) and neutral current (NC) modes. The outgoing lepton may be either charged or neutral.

Neutrino interactions are simulated with the NEUT [58] neutrino interaction and nuclear effects simulator. The interactions are described below.

4.2.1 (Quasi)-elastic scattering

Charged current quasi-elastic scattering (CCQE) is simulated for both free protons and bound nucleons, following the models of Llewellyn Smith [59] and Smith and Moniz [60], respectively. The bound nucleon calculation uses a relativistic Fermi gas model. In both cases, the cross section uses vector and axial vector form factors. The axial vector mass is set to $1.2 \text{ GeV}/c^2$ to align it with neutrino experiments. Neutral current elastic cross sections are determined by constant coefficient scaling with their charged current quasi-elastic counterparts.

Charged-current quasielastic scattering is the single most common interaction seen in SK, and is of fundamental importance for both atmospheric and accelerator neutrino analyses. There is typically only one visible Cherenkov ring formed from the charged lepton. Since the $\Delta B = 2$ processes in this thesis involve two or more energetic final state pions forming more than one ring, CCQE is not a major source of background ¹. More details on this mode can be found in [61].

4.2.2 Single meson production

Single meson production is the dominant hadron production mechanism in the region $W < 2.0 \text{ GeV}/c^2$, where W is the hadronic invariant mass. We follow the model of Rein and Sehgal [62]. Pions, kaons, and η mesons are produced via

¹It can still constitute background if, for instance, the outgoing nucleon has enough energy to interact with another nucleon and produce a secondary hadron.

$$\nu + N \rightarrow \ell + N^* \implies N^* \rightarrow N' + meson \quad (4.2)$$

where, as before, ν is the incoming neutrino, ℓ the outgoing lepton, and N and N' are the incoming and outgoing nucleon. Here N^* is a short-lived baryon resonance. In total, 18 resonances under $2.0 \text{ GeV}/c^2$ are considered. The pion angular distribution was calculated from the Rein and Sehgal model for the $\Delta(1232)$ resonance, and was assumed to be isotropic for other resonances. Charged current single pion interactions ($CC1\pi$) are a common source of background for $NN \rightarrow \pi\pi$, as a pion that is produced with a sufficiently large angle with respect to the outgoing lepton can simulate the “back-to-back” signal of two pions decaying from a low momentum initial dinucleon state. The Pauli blocking effect is considered in the resonance decay, by requiring that the outgoing nucleon has momentum greater than the Fermi surface momentum. Finally, absorption of pions is also considered, and about 20% of single pion production interactions have only an outgoing lepton and nucleon.

Coherent pion production constitutes a small subset of single meson production. In this interaction, the nucleus is unchanged, but a final state lepton and pion are still present.

4.2.3 Deep inelastic scattering

Deep inelastic scattering interactions are relevant in the region $W > 1.3 \text{ GeV}/c^2$, and they are the dominant interaction for $W > 2.0 \text{ GeV}/c^2$. The charged current cross section is given by

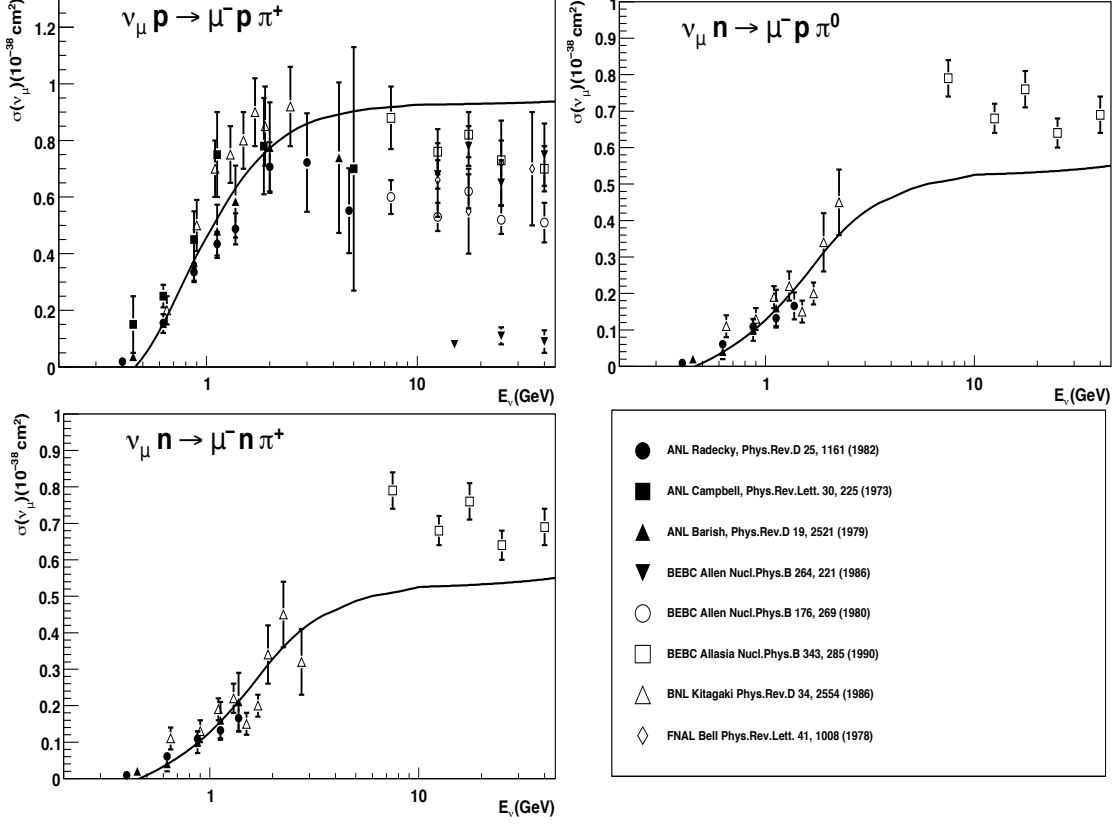


Figure 4.3: Cross-sections for various CC1 π interactions, with solid lines showing the fit used in NEUT [58]. See [58] for details on the data points.

$$\begin{aligned}
 \frac{d^2\sigma}{dx dy} &= \frac{G_F^2 M_N E_\nu}{\pi} \left((1 - y + y^2 + C_1) F_2(x, q^2) \pm y \left(1 - \frac{y}{2} + C_2 \right) x F_3(x, q^2) \right), \\
 C_1 &= \frac{y M_\ell^2}{4 M_N E_\nu x} - \frac{xy M_N}{2 E_\nu} - \frac{M_\ell^2}{4 E_\nu^2} - \frac{M_\ell^2}{2 M_N E_\nu x}, \\
 C_2 &= -\frac{M_\ell^2}{4 M_N E_\nu x},
 \end{aligned} \tag{4.3}$$

where M_N and M_ℓ are the nucleon and outgoing lepton masses, E_ν is the neutrino energy, q^2 is the squared momentum transfer, and $x = -q^2 / (2M_N (E_\nu - E_\ell))$ and $y =$

$(E_\nu - E_\ell) / E_\nu$ are the Bjorken scaling parameters. The $F_i(x, q^2)$ are nucleon structure functions, taken from the GRV98 parton distribution functions [63], with corrections from Bodek and Yang [64]. For the charged current cross-section, NEUT integrates Equation 4.3 directly. The neutral current cross section is obtained by multiplying the CC cross section by linear functions of the neutrino energy, for different energy ranges. See [58] for details.

In the region $1.3 \text{ GeV}/c^2 < W < 2.0 \text{ GeV}/c^2$, only pions are considered as outgoing mesons, with $n_\pi \geq 2$. Average pion multiplicities are estimated from the Fermilab 15-foot hydrogen bubble chamber experiment [65]:

$$\langle n_\pi \rangle = 0.09 + 1.83 \ln(W^2). \quad (4.4)$$

In addition, the ratio of forward/backward pion production in the hadronic center of mass is taken from the BEBC experiment [66], using

$$\frac{n_\pi^F}{n_\pi^B} = \frac{0.35 + 0.41 \ln(W^2)}{0.05 + 0.09 \ln(W^2)}. \quad (4.5)$$

The low W region is particularly important for $n \rightarrow \bar{n}$, since an ideal $n \rightarrow \bar{n}$ event has an isotropic spread of pions, e.g. a similar number of pions in the forward and backward direction. For $W > 2.0 \text{ GeV}/c^2$, hadron kinematics are determined by PYTHIA/JETSET [67], and additional hadrons such as kaons and η mesons are considered.

4.2.4 Nuclear effects

The interactions of hadrons in the nucleus are an extremely important component of MC simulation, both for $n \rightarrow \bar{n}$ and $NN \rightarrow \pi\pi$ signals and atmospheric neutrino

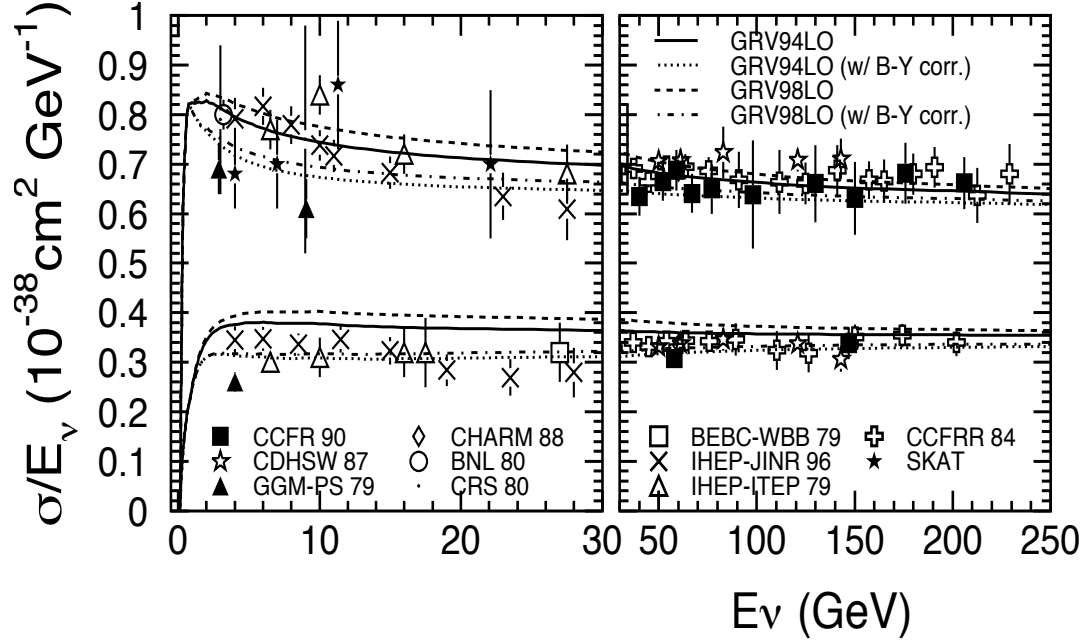


Figure 4.4: Total charged-current cross-section for neutrinos (upper lines) and antineutrinos (lower lines). The lines show a comparison of different parton distribution functions, with and without corrections from Bodek and Young [64]. See [58] for details on the data points.

backgrounds. Thus, a careful consideration of hadron Final State Interactions (FSI) is necessary following the calculation of outgoing particle kinematics.

For pions in particular, the interaction probabilities inside ^{16}O are large. The following pion interactions are considered:

- Quasi-elastic (QE) scattering, in which pion of the same charge is in the initial and final state, with some energy loss;
- absorption, e.g. $\pi^+ + n \rightarrow p$;
- charge exchange, e.g. $\pi^+ + n \rightarrow p + \pi^0$;
- pion production, e.g. $\pi^+ + n \rightarrow \pi^+ + \pi^0 + n$.

Figure 4.5 shows these interactions as a function of pion momentum.

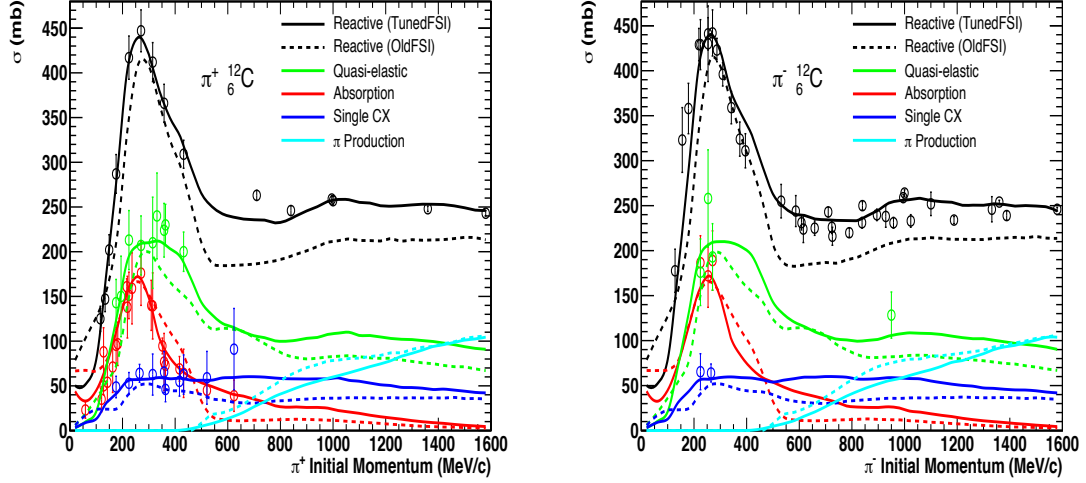


Figure 4.5: Pion interaction cross sections as a function of lab momentum, for π^+ (left) and π^- (right) [68]. The “TunedFSI” plots are used in the most recent MC simulation. See [68] for details on the data points.

To simulate pion interactions in the nucleus, each pion is propagated in a stepwise fashion from its starting point, with interactions determined by the individual interaction probabilities at each step. This is done until the pion escapes the nucleus, or is absorbed. The starting point of pions in the nucleus is determined using a Woods-Saxon type distribution:

$$\rho(r) = \frac{Z}{A} \frac{\rho_0}{1 + \exp\left(\frac{r-c}{a}\right)}, \quad (4.6)$$

where r is the distance from the nuclear center, Z and A are the proton and mass numbers, ρ_0 is the average nuclear density, and a and c are additional density parameters. For ^{16}O , $Z = 8$, $A = 16$, $\rho_0 = 0.48m_\pi^3$, $a = 0.41$ fm, and $c = 2.69$ fm. For DIS interactions, this starting position is shifted slightly by the formation length, accounting for the fact that hadronization is not instantaneous. The formation length

L for a given hadron is defined as $L = p/\mu^2$, where p is the momentum of the outgoing hadron and $\mu^2 = 0.08 \text{ GeV}^2$ is an experimentally determined parameter.

In considering pion interactions, two momentum regions are used — low momentum ($p_\pi < 500 \text{ MeV}/c$) and high momentum ($p_\pi > 500 \text{ MeV}/c$). For low momenta, the interaction probabilities per step are calculated according to the model of Salcedo and Oset [69]. The Fermi surface momenta of the nucleons is determined with Equation 4.6 via $p_F(r) = \left(\frac{3}{2}\pi^2\rho(r)\right)^{-1/3}$. Pauli blocking is taken into account by requiring that, following an interaction, the nucleon momentum exceeds the Fermi surface momentum. Thus, the interaction probabilities are density dependent. The scattering kinematics are drawn from a phase-shift analysis of pion interactions on free nucleons. Recently, the low momentum interaction probabilities in NEUT were tuned to achieve better agreement with π^+ scattering on ^{12}C [68].

For pions above $500 \text{ MeV}/c$, nucleons are treated as quasi-free particles. QE scattering, which is dominant up to very high pion momenta (Figure 4.5) is defined as [68]

$$\sigma_{QE} = \frac{1}{2}\sigma_{\pi d} \left(\frac{\sigma_{QE}^{free}}{\sigma_{tot}^{free}} \right), \quad (4.7)$$

where $\sigma_{\pi d}$ is the total cross section for pion scattering on deuterons, and σ_{QE}^{free} and σ_{tot}^{free} are cross sections for scattering on free protons. The hadron production cross section, which is only considered in the high momentum region, is defined similarly:

$$\sigma_{had} = \frac{1}{2}\sigma_{\pi d} \left(1 - \frac{\sigma_{QE}^{free}}{\sigma_{tot}^{free}} \right). \quad (4.8)$$

The same phase-shift kinematics as the low momentum pions is used.

4.3 Detector Simulation

After the neutrino interactions and nuclear effects of outgoing particles are modeled by NEUT, final-state particles are put through a custom detector simulation program. The simulation tracks particles (both from the primary interaction and secondary particles from interactions in the water), models Cherenkov radiation and PMT response, and accounts for other detector-specific phenomena, such as reflection from Tyvek in the detector scaffolding. The simulation is based on CERN's GEANT3 package [70].

Cherenkov radiation is modeled using inputs from the water calibration procedures described in the previous chapter. Reflection and absorption off of different detector surfaces is also modeled from calibration measurements. PMT response is modeled by using the measured quantum efficiency of each PMT. The charge of each PMT is taken to be the sum of all p.e.'s weighted by the single p.e. distribution, and the hit timing is smeared by the PMT timing resolution.

As with the treatment of hadronic interactions in the nucleus, hadronic interactions in the water are treated differently in the high and low momentum regions. For $p_\pi < 500 \text{ MeV}/c$, custom code [71] is used. The low momentum simulations were recently updated and tuned to recent ^{16}O data, and use the same NEUT interaction model described for intranuclear effects. For high momenta, the GCALOR package [72] is used.

γ	e^\pm pair production Compton scattering photoelectric effect
e^\pm	multiple scattering ionization and δ -ray production Bremsstrahlung positron annihilation
μ^\pm	decay in flight multiple scattering ionization and δ -ray production Bremsstrahlung direct e^\pm pair production nuclear interactions
Hadrons	decay in flight multiple scattering ionization and δ -ray production hadronic interactions

Table 4.1: Interactions modeled for each particle type. Cherenkov radiation is modeled for e^\pm , μ^\pm , and charged hadrons.

Chapter 5

Signal Simulation

Four signal processes are studied in this thesis. Three fall under the category of dinucleon decay, or $NN \rightarrow \pi\pi$, encompassing the modes $^{16}\text{O}(pp) \rightarrow ^{14}\text{C}(\pi^+\pi^+)$, $^{16}\text{O}(pn) \rightarrow ^{14}\text{N}(\pi^+\pi^0)$, and $^{16}\text{O}(nn) \rightarrow ^{14}\text{O}(\pi^0\pi^0)$ (truncated throughout to $pp \rightarrow \pi^+\pi^+$, $nn \rightarrow \pi^0\pi^0$, and $pn \rightarrow \pi^+\pi^0$). The fourth process is neutron-antineutron oscillation, or $n \rightarrow \bar{n}$. These processes are united by similar underlying physics ($\Delta B = 2$, all first-generation quarks), but entail different simulation and signal extraction methods.

The intranuclear simulation for each process follows a similar pattern. Two bound nucleons release ≈ 2 GeV of energy in the form of pions, which then propagate through the residual nucleus as described in Section 4.2.4. Outgoing particles are then passed through the detector simulation described in Section 4.3.

5.1 Dinucleon Decay

The starting point for the $NN \rightarrow \pi\pi$ simulation is two bound nucleons. The nucleons are chosen randomly from the 16 available nucleons in ^{16}O (for nucleons of

appropriate charge for the outgoing pions), which consists of two $s_{1/2}$, two $p_{1/2}$, and four $p_{3/2}$ protons and neutrons. The nucleon momenta are determined from electron- ^{12}C scattering data [73] (Figure 5.1). Nuclear binding energy is also taken into account by subtracting it from the nucleon masses — 39.0 MeV and 15.5 MeV for s-state and p-state nucleons, respectively. The two nucleons are approximated as starting in the same nuclear position with the Woods-Saxon distribution (Equation 4.6).

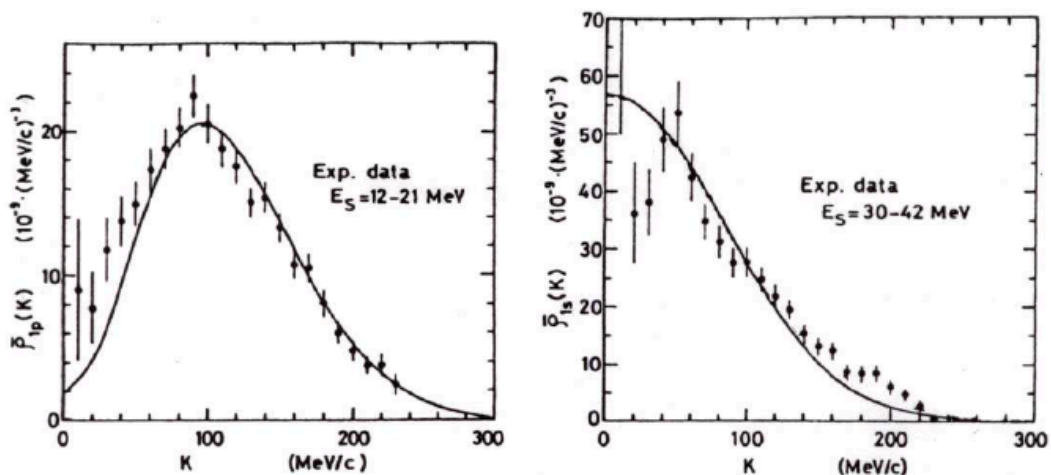


Figure 5.1: Fermi momentum predictions (solid line) and data (crosses) from [73]. The left shows a p-state nucleon, and the right an s-state in ^{12}C .

The momenta of the outgoing pions are mostly determined with normal two-body decay kinematics. There is an additional effect called “correlated decay”, in which the wavefunction of an additional nucleon overlaps with that of a dinucleon decay pair. Reference [74] estimates that 10% of single-nucleon decays will have a correlated nucleon, and we assume the same percentage of correlation in dinucleon decays. Events with a correlated decay are essentially three-body decays, with the momenta of the outgoing pions affected by the momentum absorbed by the third nucleon (which escapes notice, as it is below Cherenkov threshold). Figure 5.2 shows the effect of correlated decay on the invariant mass of the $NN \rightarrow \pi\pi$ system.

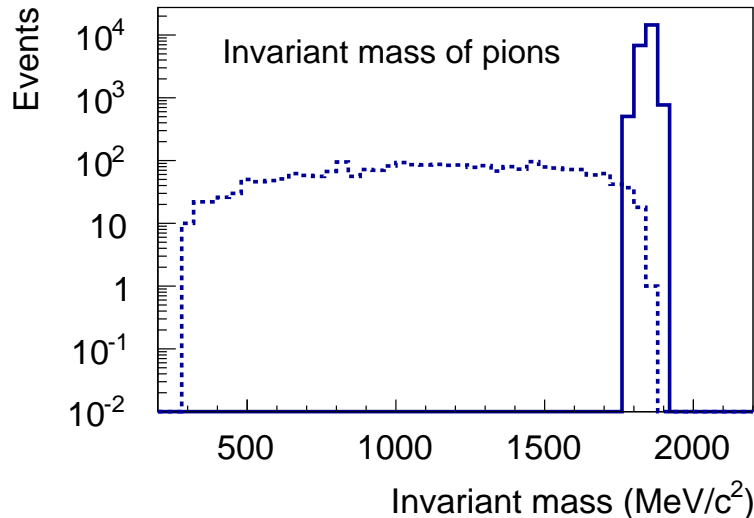


Figure 5.2: Invariant mass for $pp \rightarrow \pi^+\pi^+$. The modes $pn \rightarrow \pi^+\pi^0$ and $nn \rightarrow \pi^0\pi^0$ are essentially identical. The dotted histogram shows events with a correlated decay.

The nuclear effects described in Section 4.2.4 affect the final state pions significantly. About 40% of events in each mode remain in their initial pion configurations upon leaving the nucleus. Table 5.1 shows the number of pions after intranuclear simulation.

5.2 Neutron-antineutron oscillation

For $n \rightarrow \bar{n}$, the signal process is not the oscillation itself, but the subsequent annihilation. A neutron in ^{16}O that has oscillated to an antineutron will quickly annihilate with one of the other nucleons, which results in multiple pions.

The oscillation position in the nucleus is estimated from Equation 2.14 (Figure 5.3), which gives approximately the same result as the Woods-Saxon distribution. The same Fermi momentum simulation and binding energy modifications described

$pp \rightarrow \pi^+ \pi^+$				
N_π	0	1	2	3
0	—	11.8%	45.1%	2.4%
1	2.7%	21.8%	5.2%	—
2	2.8%	3.0%	—	—

$pn \rightarrow \pi^+ \pi^0$				
N_π	0	1	2	3
0	—	6.8%	12.3%	1.4%
1	7.1%	46.8%	3.7%	—
2	10.5%	4.1%	—	—

$nn \rightarrow \pi^0 \pi^0$			
N_π	0	1	2
0	—	2.6%	3.5%
1	11.5%	25.1%	2.8%
2	43.0%	4.2%	—

Table 5.1: Number of pions for $pp \rightarrow \pi^+ \pi^+$ (top), $pn \rightarrow \pi^+ \pi^0$ (middle), and $nn \rightarrow \pi^0 \pi^0$ (bottom) after nuclear effects. Percentages indicate the percentage of events with the specified number of π^+ 's (columns) and number of π^0 's (rows). Entries with a “—” indicate a small contribution ($<0.1\%$). π^+ 's are required to be above Cherenkov threshold. The number of pions prior to nuclear effects is boldened.

for $NN \rightarrow \pi\pi$ are used for $n \rightarrow \bar{n}$.

Following the oscillation, the antineutron is assumed to have an equal probability of annihilating with any of the remaining nucleons. Unlike the $NN \rightarrow \pi\pi$ modes, the final state of $n \rightarrow \bar{n}$ has many non-negligible contributions for both $\bar{n}n$ and $\bar{n}p$ annihilation.

The final states are determined from antinucleon scattering data. Antineutron data is sparse, and so the annihilation branching fractions for $\bar{n}n$ and $\bar{n}p$ are mainly drawn from $\bar{p}p$ and $\bar{p}n$ data, which should be equivalent from isospin considerations (and appropriate adjustments to outgoing charged particles in the case of $\bar{p}n$). The analysis in [23] used cross sections from old bubble chamber data [75–77]. More recent

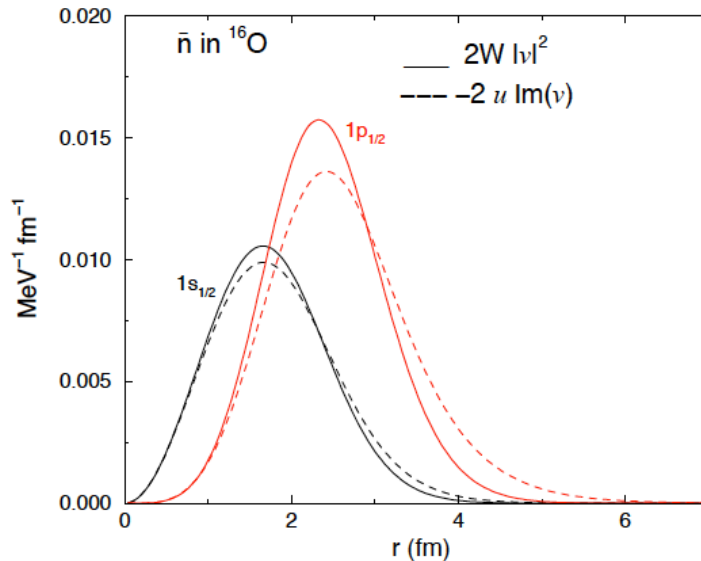


Figure 5.3: The integrand in the numerator of Equation 2.14 for an s-state and p-state neutron in ^{16}O . The solid and dotted lines show calculations for two different approximations.

$\bar{p}p$ data from the Crystal Barrel experiment [78, 79] is available, and is especially abundant for branching fractions with more than one neutral particle in the final state. The OBELIX experiment [80] has also collected data for low-energy antineutrons in $\bar{n}p$ annihilation. Details on the branching fractions can be found in Appendix A.

Regardless of the specific branching fractions used, the annihilation products follow a similar pattern — there are typically ≥ 3 pions that must then be propagated through the residual nucleus. In addition to the branching fractions, the pion-nucleon model described in Section 4.2.4 is a different model than that used in [23]. The outgoing pion characteristics are similar. Figure 5.4 shows the pion multiplicities and average charged pion momentum for pions emerging from the nucleus, and Table 5.2 shows the percentage of pions that undergo intranuclear interactions. Overall, the updated pion model is more interactive.

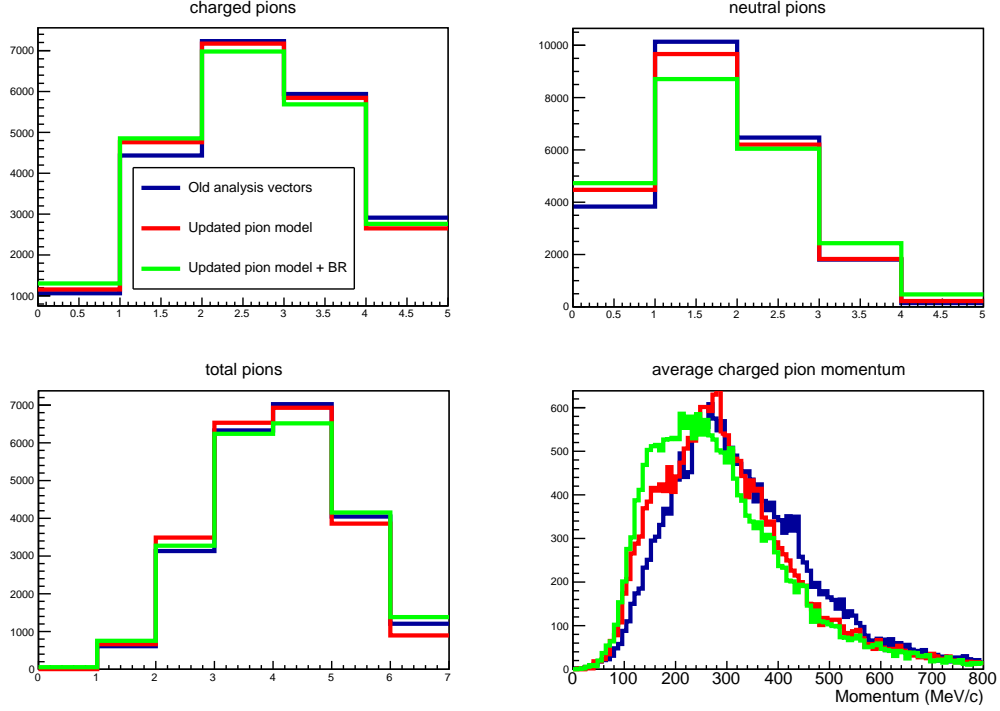


Figure 5.4: Charged, neutral, and total pion multiplicity (top left, top right, and bottom left), and average charged pion momentum (bottom right) for $n \rightarrow \bar{n}$ MC. The blue histogram shows the simulation of [23], the red histogram shows the simulation using the same branching fractions as [23] but the updated pion-nucleon model described in Section 4.2.4, and the green histogram shows the simulation using new branching fractions and the updated pion model.

	Abs.	QE	QX	π prod.	No int.
Ref. [23] (SK-I)	24%	24%*		3%	49%
This analysis	21%	20%	23%	3%	30%

Table 5.2: Percentage of pions undergoing different interactions for the analysis in [23], and this analysis. From left to right, the interactions are absorption, quasi-elastic scattering, charge exchange, π production, and no interaction. The * indicates that QE scattering and charge exchange are combined.

Chapter 6

Reduction and Reconstruction

Dedicated reduction and reconstruction algorithms are required to retain and analyze interesting physics events at Super-Kamiokande. Prior to any reduction, $\sim 10^6$ events are recorded. Most of these are from low-energy radioactivity surrounding the detector, at a rate of about 11 Hz. The high-energy region is dominated by cosmic ray muons, at a rate of about 3 Hz.

The Super-Kamiokande dataset is split into three categories:

- Fully contained events, in which all of the energy is deposited in the ID;
- Partially contained events, which originate in the ID but have enough energy to escape the detector, depositing significant energy in the OD;
- Upward-going muons, high-energy muons produced by subterrestrial neutrino interactions that enter the detector from below the horizon.

While each of these event categories are crucial for a variety of Super-Kamiokande physics analyses, the $\Delta B = 2$ processes in this thesis must originate inside the water tank, and are not sufficiently energetic to escape. Thus, I restrict attention to the

fully contained (FC) reduction and reconstruction algorithms. A recent description of the reduction and reconstruction of all event categories can be found in [81].

6.1 Fully Contained Reduction Steps

There are five FC reduction stages, each aimed at retaining true atmospheric neutrinos and rejecting both high-energy cosmic rays and low-energy radioactivity. Each selection is briefly described below.

6.1.1 First Reduction

The majority of background events are removed by the first reduction, which makes the following requirements:

- 1a) $PE_{300} > 200$ (100 for SK-II¹), where PE_{300} is the total number of ID photoelectrons seen in a 300 ns time window;
- 1b) $NHITA_{800} \leq 50$ (55 for SK-IV), where $NHITA_{800}$ is the total number of OD tubes hit within a time window (-500 ns, +300 ns) relative to the trigger time.

The first criterion corresponds to a 22 MeV/c electron, and removes most of the background from low-energy radioactivity. The second criterion removes most cosmic ray muons. Following the first reduction, about 3000 events/day remain from the initial $\sim 10^6$ /day.

6.1.2 Second Reduction

The second reduction also contains a set of simple cuts, and removes most of the background remaining after the first reduction:

¹SK-II has modified criteria relative to other SK periods, due to the decreased photocoverage.

2a) $\text{NHITA}_{800} \leq 25$ for events with $\text{PE}_{\text{total}} < 100,000$ (50,000 for SK-II);

2b) $\text{PE}_{\text{max}}/\text{PE}_{\text{total}} < 0.5$, where PE_{max} is the largest number of p.e.'s observed in a single PMT.

Criterion 2a) further removes cosmic ray muons, while still allowing very high-energy events originating in the ID. Criterion 2b) removes events caused by electronic noise, which tend to have a single PMT discharge containing much more charge than an average PMT. After the second reduction, a few hundred events per day remain.

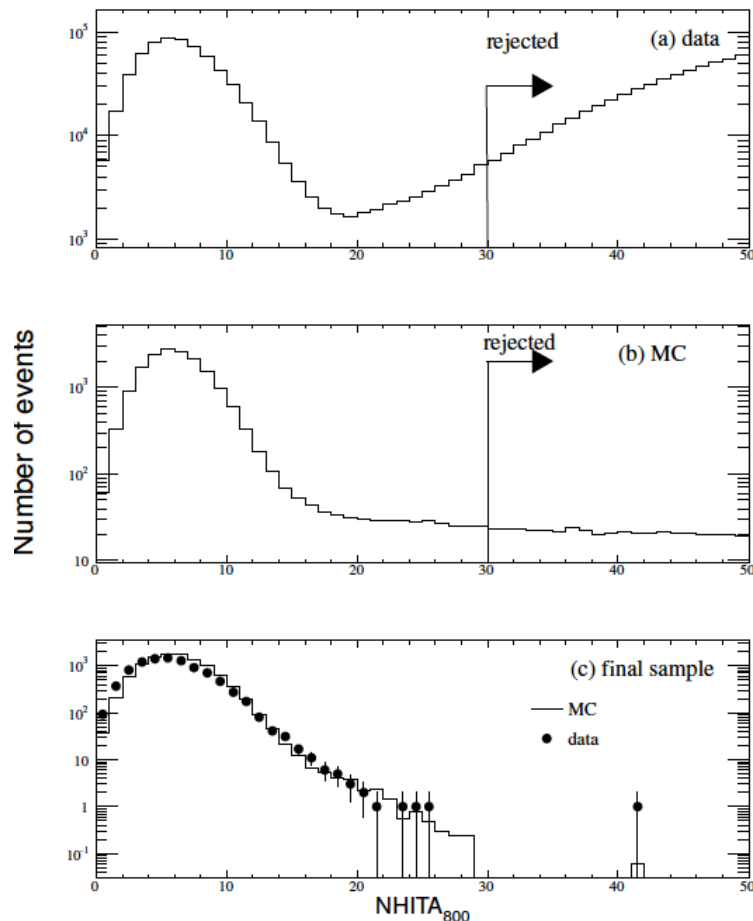


Figure 6.1: The second reduction cut 2a) for data (top), MC (middle), and MC normalized to data events after the selection (bottom) in SK-IV. The small number of events for which $\text{NHITA}_{800} > 25$ have $\text{PE}_{\text{total}} > 100,000$. Taken from [61].

6.1.3 Third Reduction

The third FC reduction more specifically targets remaining cosmic ray muon events, as well as low-energy radioactivity. In particular, cosmic ray muons without much OD activity are targeted. After these more specific selections, about 45 events/day remain.

Through-going muons

Muons that enter and exit the tank may not leave much of a trace in the OD, depositing most of their energy in the ID. To be considered for this category, the ID must have over 1000 hit PMTs, with PE_{\max} more than 230 p.e.'s for at least one PMT. If these criteria are met, a through-going muon fitter is applied that assumes an entry point, taken to be the first hit PMT in the ID entrance cluster, and an exit point, taken to be the centroid of the ID exit cluster². A set of expected hit timing values T_i is determined using MC simulations, and a goodness-of-fit parameter is calculated:

$$\text{goodness} = \frac{1}{\sum_i \frac{1}{\sigma_i^2}} \times \sum_i \frac{1}{\sigma_i^2} \exp\left(-\frac{(t_i - T_i)^2}{3\sigma_i^2}\right), \quad (6.1)$$

where t_i and σ_i are the hit timing and timing resolution of the i^{th} PMT. The through-going muon cut removes events that satisfy the following criteria:

3a) goodness > 0.75;

3b) $NHITA_{\text{in}} > 10$ and $NHITA_{\text{out}} > 10$, where $NHITA_{\text{in,out}}$ is the number of hit OD PMTs within 8 meters of the fitted entry and exit point.

²Clusters are just sets of contiguous hit ID PMTs, with the largest two corresponding to entrance and exit.

An additional cut is made for high-energy throughgoing muons. Muons have a critical energy of about 1 TeV, above which their predictable ionization energy loss of 2 MeV/cm becomes secondary to more random processes, such as bremsstrahlung and pair production. These processes can produce a large number of hits in a short time interval. Events satisfying the following cut are removed:

$$3c) \text{ NHITA}_{500} > 40,$$

where NHITA_{500} is the number of OD hits within a 500 ns sliding time window.

Stopping muons

The stopping muon cut follows the same logic as the through-going muon cut, except there is no exit point. The direction of the muon can still be reconstructed by maximizing the charge seen by the PMTs within a 42-degree opening angle from the entry point. A goodness parameter similar to Equation 6.1 is calculated, and events are rejected as stopping muons if the following criteria are met:

$$4a) \text{ The goodness} \geq 0 \text{ and } \text{NHITA}_{\text{in}} \geq 10;$$

$$4b) \text{ (SK-I only) the goodness} > 0.5 \text{ and } \text{NHITA}_{\text{in}} \geq 5;$$

Figure 6.2 shows the goodness parameter for both throughgoing and stopping muons.

Cable hole muons

One source of missing OD activity comes from slight asymmetries in the OD PMT distributions. In particular, there are 12 holes in SK, starting in the ID and going to the electronics huts, through which cables are threaded. These holes interrupt the distribution of OD PMTs (Figure 6.3), so that muons passing through these holes may escape notice by the OD.

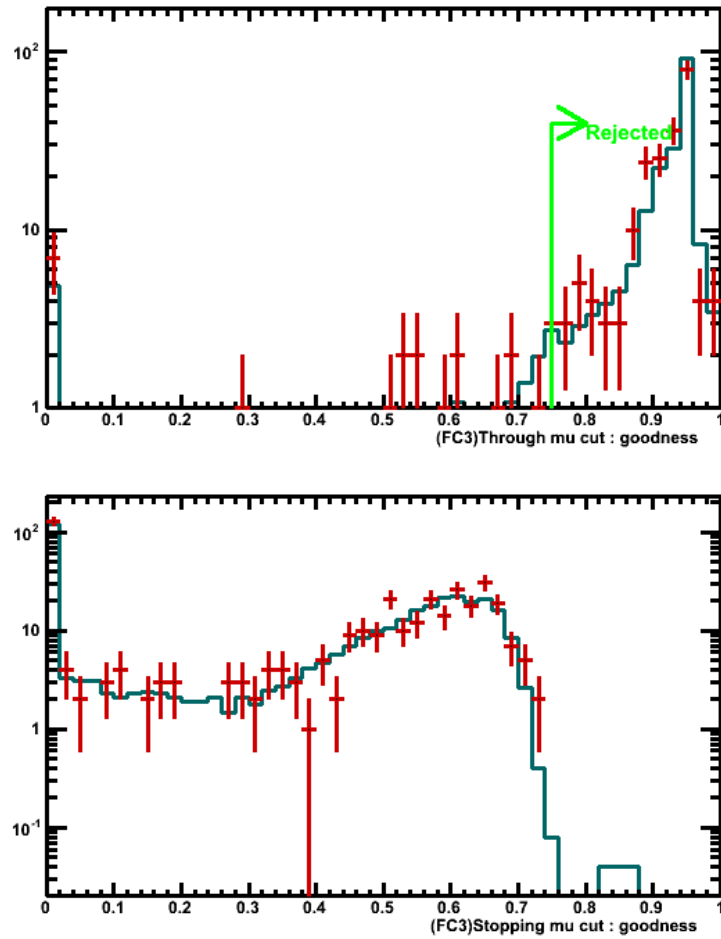


Figure 6.2: The goodnes parameter (Equation 6.1) for throughgoing (top) and stopping muons (bottom) in SK-IV, normalized to data taken over two days (red crosses). The blue histogram shows data over the previous two months.

To partially account for muons that pass through these holes, four of the twelve have plastic scintillator veto counters installed. An event is removed if:

- 5a) the cable hole veto counter is hit;
- 5b) the entry or exit point is within 4 m of the veto counter.

In SK-IV only, a tighter selection is made to reject stopping cable hole muons. Events that satisfy the following criteria are rejected:

- 6a) The stopping muon goodness is greater than 0.4;
- 6b) $PE_{\text{total}} > 4000$;
- 6c) The muon's zenith angle is more vertical than horizontal: $\cos \theta < -0.6$;
- 6d) The entry point is within 2.5 meters of the nearest cable hole.

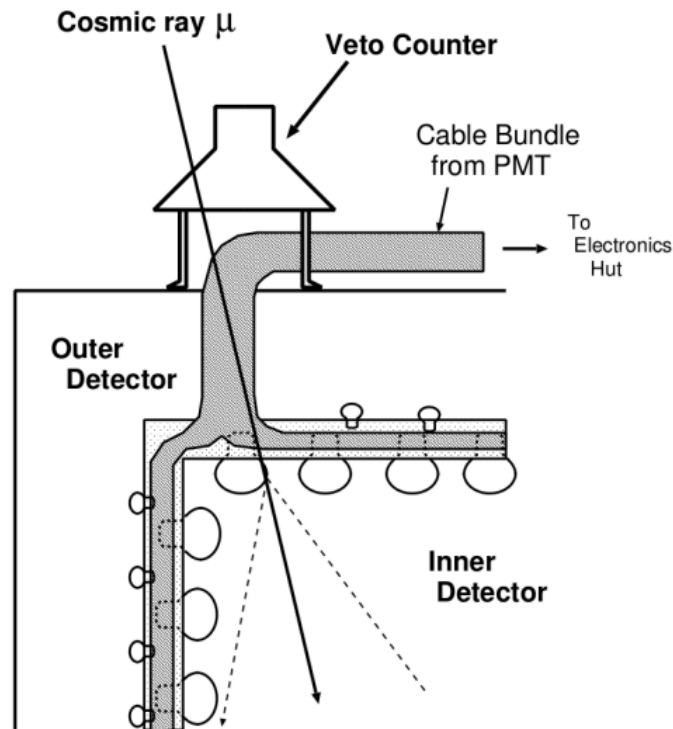


Figure 6.3: A schematic of one of the cable holes with a veto counter.

Flasher PMTs

A “flasher” refers to when there is a repetitive discharge in the dynode of a PMT, which may also affect nearby PMTs. Such events are characterized by abnormally broad hit timing distributions. They can be rejected if they exhibit too much ID activity well after the trigger time. Events that satisfy the following detector-specific cuts are removed:

7a) (SK-I) $N_{\text{MIN}_{100}} \geq 15$ if $N_{\text{hit}} > 800$, and $N_{\text{MIN}_{100}} \geq 10$ otherwise. Here $N_{\text{MIN}_{100}}$ is the number of hits in the ID in a 100 ns time window from 200 ns to 700 ns after the trigger time, and N_{hit} is just the total number of ID hits.

7b) (SK-II to IV) $N_{\text{MIN}_{100}} \geq 20$.

Figure 6.4 shows the hit time distributions for a flasher, compared to an atmospheric neutrino.

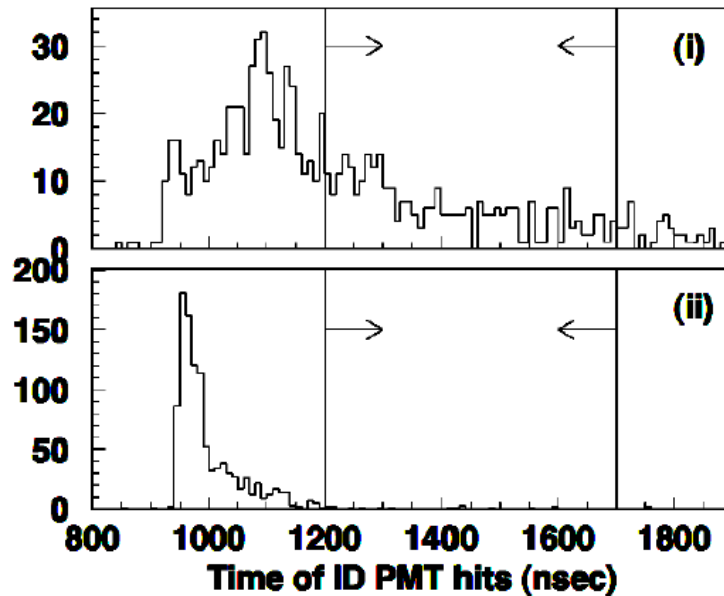


Figure 6.4: Typical distributions of $N_{\text{MIN}_{100}}$ for a flasher (top) and an atmospheric neutrino MC event (bottom). The arrows indicate the region that is removed with the third reduction flasher cut. Taken from [61].

Coincidence muons

Sometimes there is a coincidence between a high-energy cosmic ray muon and a low-energy event. If the low energy event occurs slightly earlier and starts the trigger, it can avoid the previous cuts designed to remove low-energy events, due to the energy deposited by the muon, and conversely avoid the high-energy cuts, since

the OD activity of the muon is recorded too late. Events passing the following criteria are rejected:

- 8a) $\text{NHITA}_{\text{off}} \geq 20$, where $\text{NHITA}_{\text{off}}$ is the number of OD hits between 300 ns and 800 ns after the trigger time;
- 8b) $\text{PE}_{\text{off}} > 5000$ (2500 for SK-II), where PE_{off} is the total number of p.e.'s in the ID for the same time window.

Low energy events

Finally, a more specific cut aimed at low energy events is applied. Events are rejected if $\text{NHIT}_{50} < 50$ (25 for SK-II), where NHIT_{50} is the number of hit ID PMTs within a sliding 50 ns time window. The time window uses the residual time. This takes into account the time-of-flight of the photons, assumed to come from a single vertex.

6.1.4 Fourth Reduction

The fourth FC reduction more specifically seeks to eliminate flasher events. Flashers typically have a highly-correlated charge pattern that extends across several event timing windows, and thus a pattern-matching algorithm is applied to reject them:

- 1) The ID tank wall is divided into 1450 roughly equal partitions.
- 2) For each patch, a correlation is calculated:

$$r = \frac{1}{N} \sum_i \frac{(Q_i^A - \langle Q^A \rangle) \times (Q_i^B - \langle Q^B \rangle)}{\sigma_A \times \sigma_B}, \quad (6.2)$$

where N is the total number of patches, A and B are the two events being compared in different timing windows, Q_i and $\langle Q \rangle$ are the charge in patch i and the average charge in the event, and σ is the charge resolution.

- 3) The distance d_{\max} between the PMTs with the maximum charge in each event is calculated. For $d_{\max} < 0.75$ m, the correlation in Equation 6.2 is incremented: $r = r + 0.15$.
- 4) Two events are defined as a match if their correlation exceeds a threshold r_{thresh} :

$$r_{\text{thresh}} = 0.168 \times \log_{10} \left(\frac{PE_{\text{tot}}^A + PE_{\text{tot}}^B}{2} \right) + 0.130, \quad (6.3)$$

where PE_{tot} is the total number of p.e.'s observed in the respective events.

- 5) Repeat the correlation calculation for 10,000 events near the target event, and reject events with a large number of matches.

Following the fourth reduction, about 18 events/day remain.

6.1.5 Fifth reduction

The fifth reduction is aimed at removing three specific categories of remaining background: invisible muons, coincidence muons, and long-tail flashers. After the fifth reduction, about 16 events/day remain.

Invisible muons

Muons below Cherenkov threshold will escape notice from any of the criteria described above, but they can still activate the trigger via their decay electron. They

can be rejected as cosmic-ray muons if some OD activity is found. Events satisfying the following criteria are rejected:

- 9a) $PE_{\text{total}} < 1000$ (500 in SK-II), where as before PE_{total} is just the total charge in the ID;
- 9b) $NHITAC_{\text{early}} + NHITAC_{500} \geq 10$ if $Dist_{\text{clust}} < 500$ cm; $NHITAC_{\text{early}} > 9$ otherwise.

Here $NHITAC$ is the number of hit OD PMTs in the largest cluster. $NHITAC_{\text{early}}$ is defined in a 200 ns time window from -9000 to -200 ns prior to the primary trigger time, $NHITAC_{500}$ is the hits corresponding to -200 to 300 ns, and $Dist_{\text{clust}}$ is the distance between the centroids of these clusters. Selection 9a) corresponds to about the maximum p.e. yield for a Michel electron, while 9b) indicates significant early OD activity.

Coincidence muons

Coincidence muons remaining after the cuts in the third reduction are subjected to another set of cuts, scanning for low-energy events in the main time window and scanning for off-trigger OD activity in a longer time window than in the third reduction. Events meeting the following criteria are rejected:

- 10a) $PE_{\text{total}} < 300$ (150 for SK-II);
- 10b) $NHITA_{\text{late}} \geq 20$, where $NHITA_{\text{late}}$ is the number of hit OD PMTs in the OD in a 200 ns sliding time window from 300 to 2100 ns.

Long tail flashers

Flasher events remaining after the cuts in the third reduction are removed by requiring the Cherenkov ring to be reasonably well-fit, which is typically not the case for the charge pattern created by flashers. These cuts use a goodness-of-fit parameter that will be described in detail later in this chapter:

11a) $N_{MIN_{100}} \geq 6$ if the goodness-of-fit is less than 0.4, where $N_{MIN_{100}}$ is as defined in the third reduction flasher reduction;

11b) (SK-II to SK-IV only) $N_{MIN_{100}} \leq 5$ if the goodness-of-fit is less than 0.3.

6.1.6 Final FC sample

Of the remaining events after the five reduction stages, a final selection is made using more specific reconstruction information. The final sample is defined by the following selections:

- $d_{wall} > 200$ cm, where d_{wall} is the distance from the reconstructed vertex to the nearest ID wall. This further removes background coming from outside the detector, and also ensures that the event has a reasonably well-reconstructed vertex;
- $N_{HITAC} < 16$ (10 for SK-I), where N_{HITAC} is the number of hit OD PMTs in the largest cluster. This further removes high-energy events coming from outside the detector;
- $E_{vis} > 30$ MeV, where E_{vis} is the visible energy, defined as the energy of a single electron that would produce the equivalent amount of charge seen in the ID. This further removes low-energy background.

These cuts are defined as the Fully-Contained Fiducial Volume cuts (FCFV), which is the starting point for all analyses in this thesis. After these cuts, about 8 events/day remain. The efficiency of each cut is estimated from MC samples, and defined as the ratio of true FC events that survive each cut. Following the FCFV selection, the efficiency is estimated to be $>99\%$, with a systematic uncertainty of $<1\%$ for each reduction step, and background contamination $<1\%$.

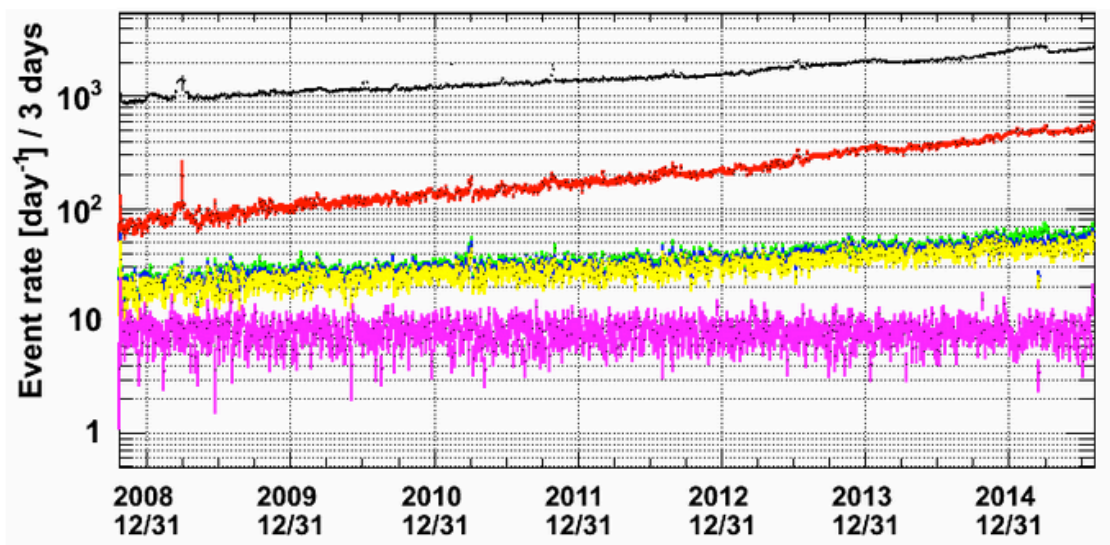


Figure 6.5: A plot of the event rate across each reduction stage in SK-IV, with first (black), second (red), third (cyan), fourth (dark blue), fifth (yellow), and FCFV (magenta). There is a slight gain increase with time most apparent in the first two reductions. This is due to degrading PMT quality, and is accounted for in event reconstruction.

6.2 Event Reconstruction

Following the FC reduction, remaining events are put through a set of reconstruction algorithms that convert the charge and timing information into kinematical variables suitable for physics analyses. The same reconstruction algorithms are applied to data and MC. First, an overall event vertex is determined using PMT timing

information³. Following this, Cherenkov rings are sought using an iterative Hough transform method. More detailed information on each ring, such as direction, particle identification, and momentum, is then calculated. I describe this process here, along with some other essential reconstruction algorithms independent of the main ring-counting program.

6.2.1 Vertex fitting

The event vertex is calculated in three steps. The first is simple, and uses ID PMT hit residual times (with time-of-flight subtracted) to maximize a goodness of fit parameter:

$$G_P = \frac{1}{N} \sum_i \exp \left(-\frac{(t_i - t_0)^2}{2(1.5 \times \sigma)^2} \right), \quad (6.4)$$

where N is the total number of hit PMTs, t_i is the residual time of the i^{th} PMT, t_0 is a free parameter chosen to maximize the goodness G_P , and σ is the timing resolution, chosen to be constant at 2.5 ns. Upon taking the vertex that maximizes G_P , the overall direction is estimated by taking a charge-weighted sum of each ID PMT.

From these initial vertex and direction calculations, the brightest Cherenkov ring is sought. The edge of the ring is determined by

$$Q(\theta_{edge}) = \frac{\int_0^{\theta_{edge}} PE(\theta)}{\sin \theta_{edge}} \times \left(\frac{dPE(\theta)}{d\theta} \right)^2 \times \exp \left(-\frac{(\theta_{edge} - \theta_{exp})^2}{2\sigma_\theta^2} \right). \quad (6.5)$$

Here $PE(\theta)$ is the angular distribution of the observed charge with respect to opening

³For most SK analyses, including this one, a single event vertex is assumed, though this is sometimes not the case. For instance, a search for $pp \rightarrow K^+K^+$ used an algorithm that sought multiple vertices, corresponding to the decay positions of the charged kaons. See [82] for more details.

angle θ , taken to be the angle between the charge-weighted direction and the ring edge being tested θ_{edge} ; θ_{exp} is the expected angle based on the charge in the cone; and σ_θ is the angular resolution. The charge in $PE(\theta)$ is corrected for attenuation and PMT angular acceptance. The overall ring direction, initially calculated only from PMT charge and opening angle θ_{edge} , are varied to maximize $Q(\theta_{edge})$.

A final, more precise vertex fit is performed that takes into account scattering of Cherenkov light and the track length of the charged particle. Instead of calculating the residuals from their location relative to an assumed vertex as in the initial fit of Equation 6.4, the residuals are calculated as follows:

$$t_i = t_i^0 - \frac{1}{c}|\vec{X}_i - \vec{O}_i| - \frac{n}{c}|\vec{P}_i - \vec{X}_i| \text{ for PMTs within the Cherenkov ring edge;}$$

$$t_i = t_i^0 - \frac{n}{c}|\vec{P}_i - \vec{X}_i| \text{ for PMTs outside the Cherenkov ring edge.}$$

Here \vec{O} is the vertex position, \vec{X}_i is the emission point along the particle track that hits PMT i , \vec{P}_i is the position of the i^{th} PMT, and n is the index of refraction. Thus PMTs within the ring edge take into account both light emitted along the particle track, and scattered light (the $1/c$ and n/c terms, respectively), and PMTs outside the ring consider only scattered light.

From these residuals, an improved goodness of fit parameter is calculated. For PMTs within the ring edge, the calculation is similar to Equation 6.4. For those outside, scattering effects are also included. More details can be found in [83].

The quality of vertex reconstruction is assessed using MC. The resolution of the true MC vertex with the reconstructed vertex is measured for different samples. The resolution for multi-ring samples, of interest for this thesis, range from about 50 to 100 cm, although the analyses do not depend very much on precise vertex reconstruction, so that it is not a significant source of systematic uncertainty.

6.2.2 Ring counting

The vertex reconstruction algorithms locate the main Cherenkov ring. Other ring candidates are sought using a Hough transform method. Figure 6.6 shows the basic logic of the algorithm. Each hit PMT has a ring with a 42-degree angle drawn around it, with the center of the ring taken to be the point at which many of these drawn rings intersect. The diagram in Figure 6.6 is a simplification, in that the actual expected charge pattern is more complicated than a circle, and depends on the angle with respect to the normal line for each PMT.

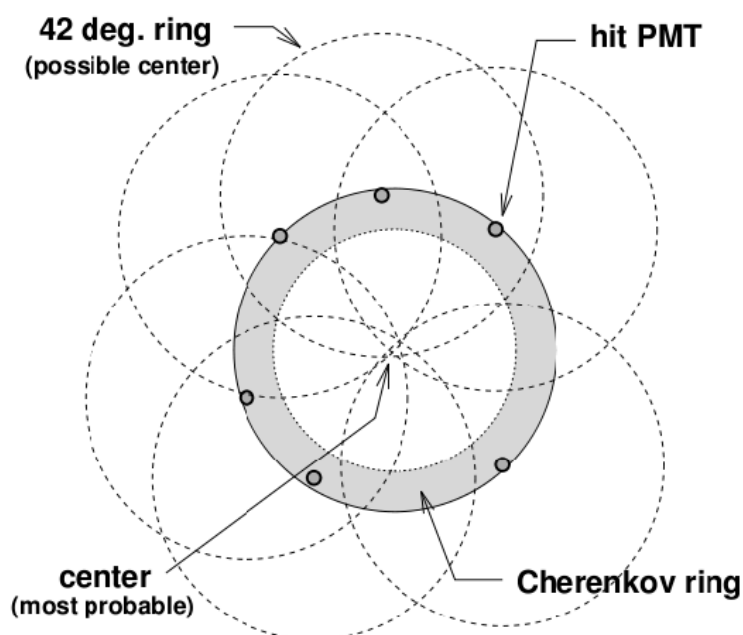


Figure 6.6: The Hough transform method. The grey area corresponds to hit PMTs, and the dashed circles are drawn around each hit PMT with a 42-degree opening angle. The ring center is determined by the point at which the most circles overlap.

Rings are counted iteratively via a likelihood method. The hypothesis of $(N+1)$ rings is tested against N rings, up to a maximum of five rings. The likelihood is defined as:

$$L_N = \sum_i \log \left(P \left(q_i^{obs}, \sum_{n=1}^N \alpha_n q_{i,n}^{exp} \right) \right), \quad (6.6)$$

where α_n is a weight for ring n , allowed to vary to maximize the likelihood, and P is a Gaussian probability:

$$P(q_i^{obs}, q_i^{exp}) = \frac{1}{\sqrt{2\pi\sigma^2}} \exp \left(-\frac{(q_i^{obs} - q_i^{exp})^2}{2\sigma^2} \right). \quad (6.7)$$

Figure 6.7 shows the ring-counting likelihood for data and MC. The starting point for analyses in this thesis is the multi-ring sample, for which $L_2 > L_1$.

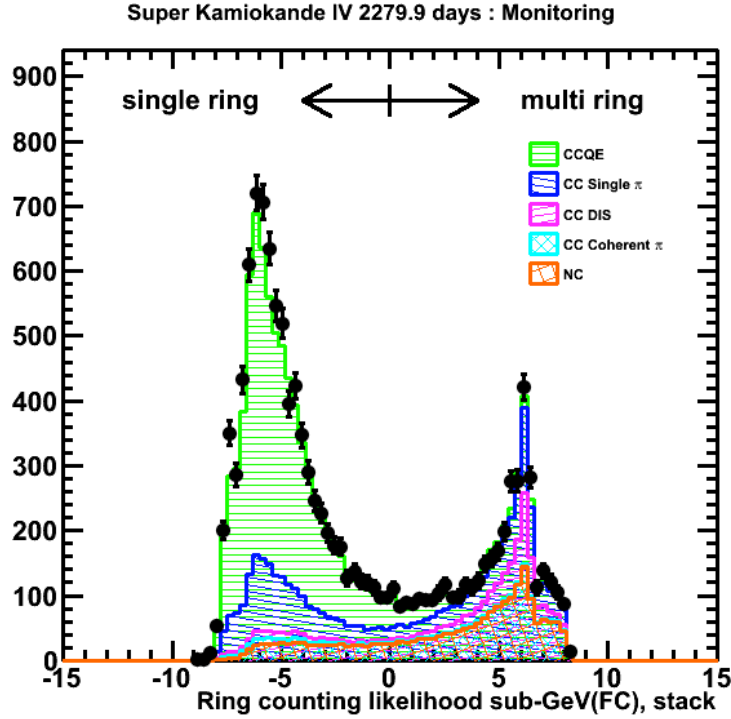


Figure 6.7: Ring-counting likelihood in SK-IV, for the sub-GeV ($E_{vis} < 1.3$ GeV) sample. The MC is normalized to data events (crosses) and separated by neutrino interaction type.

6.2.3 Particle identification

Classifying the relativistic charged particles passing through the detector is important for most physics analyses. In SK, Cherenkov rings are classified in two broad categories, corresponding to muons and electrons, the two leptons produced in CC neutrino interactions⁴ The terms *e*-like and *μ*-like will be used hereafter.

High-energy electrons produce electromagnetic showers that create diffuse ring patterns. Specifically, they interact via the chain of bremsstrahlung ($e^\pm \rightarrow e^\pm\gamma$) and photon pair production ($\gamma \rightarrow e^+e^-$). Though neutral, photons also produce electromagnetic showers via pair production. The more massive muons (and charged mesons and protons) interact negligibly via Bremsstrahlung, as the cross section is proportional to $1/m^2$. Muons interact primarily via ionization, and thus produce rings with sharp, thick edges. Charged mesons, particularly pions, are subject to hadronic interactions that can suddenly alter their path. As a result, the rings they form are usually thinner than those of muons, though the absence of electromagnetic showers still gives them sharp edges. Figure 6.8 shows examples of *μ*-like and *e*-like rings.

The particle identification algorithm (or PID) mainly works by comparing the observed charge with an expected charge, for the *e*-like or *μ*-like hypothesis. The expected charge distributions for the i^{th} PMT are calculated as follows:

⁴ τ leptons are also produced in CC ν_τ interactions, although they decay rapidly and require a specialized analysis to properly identify. See [84] for details.

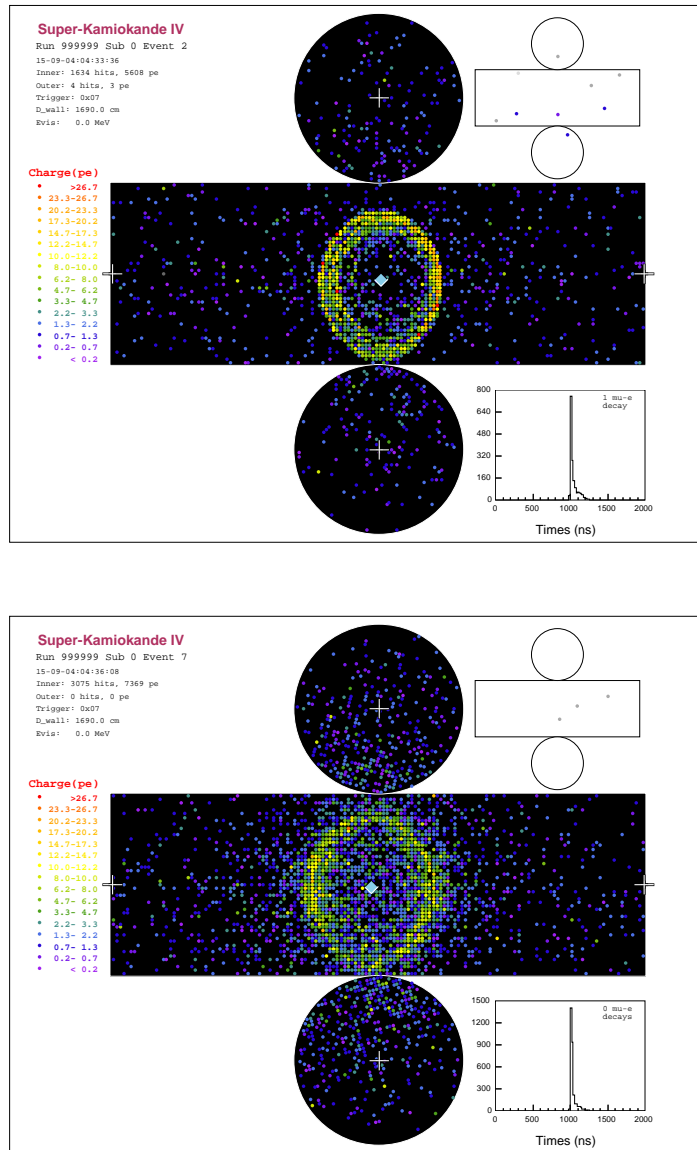


Figure 6.8: A simulated μ^+ (top) and e^+ (bottom), both with momentum 800 MeV/c. The charge pattern is notably sharper for the μ^+ and more diffuse for the e^+ . The intensity scale indicates the amount of charge deposited on the PMTs. The main display shows the ID, while the small display on the top right shows the OD, in which there is negligible activity. Both displays show the detector “unrolled” from its cylindrical shape. The white +’s indicate the horizontal and vertical location of the reconstructed vertex, projected onto the detector wall.

$$\begin{aligned}
q_i^{exp}(e) &= \alpha_e \times Q^{exp}(p_e, \theta_i) \times \left(\frac{R}{r_i}\right)^{1.5} \times \frac{1}{e^{r_i/L}} \times f(\Theta) + q_i^{scat}, \\
q_i^{exp}(\mu) &= \left(\alpha_\mu \times \frac{\sin^2 \theta_{x_i}}{r_i \left(\sin \theta_{x_i} + r_i \frac{d\theta}{dx} \Big|_{x=x_i} \right)} + q_i^{knock} \right) \\
&\quad \times \frac{1}{e^{r_i/L}} \times f(\Theta) + q_i^{scat}. \tag{6.8}
\end{aligned}$$

In these equations, $\alpha_{e,\mu}$ are normalization factors, θ_i the angle between the i^{th} PMT and the ring direction, $f(\Theta)$ the PMT acceptance as a function of incident angle Θ_i , r_i the distance from the vertex to the i^{th} PMT, L the attenuation length, and q_i^{scat} the expected charge for the i^{th} PMT due to scattering.

For the e -like hypothesis, MC simulations are used to estimate $Q^{exp}(p_e, \theta_i)$, the expected charge as a function of momentum p_e and θ_i . The simulations use a test vertex located $R=16.9$ m from the ID wall. The factor of $(R/r_i)^{1.5}$ accounts for the difference in diffusion between the test radius track length and the actual track length. The expected charge accounts for scattering, light attenuation, and geometric factors. For the μ -like hypothesis, the muon track length x is taken into account, with x_i referring to the estimated point along the muon track from which photons at the i^{th} PMT were received. The μ -like hypothesis also includes contributions from q^{knock} , so-called ‘‘knock-on’’ electrons that are ionized by the passing muons. This effect is estimated with MC simulations.

The PID likelihood function is calculated from the observed and expected charge for the n^{th} ring as

$$L_n(e, \mu) = \prod_{\theta_i < 1.5 \times \theta_C} P \left(q_i^{obs}, q_{i,n}^{exp}(e, \mu) + \sum_{n' \neq n} q_{i,n'}^{exp} \right), \quad (6.9)$$

where the product is over all PMTs within the Cherenkov cone $\theta_C \times 1.5$, P is the Gaussian probability defined in Equation 6.7 and the sum over n' accounts for light from overlapping rings. The expected e -like and μ -like charges are optimized by altering the direction and opening angle of each ring to maximize the likelihood.

The charge pattern likelihood 6.9 is converted to a χ^2 parameter,

$$\chi_n^2(e, \mu) = -2 \log L_n(e, \mu) + \text{const}, \quad (6.10)$$

which is then used to construct a probability based on the charge pattern:

$$P_n^{pattern}(e, \mu) = \exp \left(- \frac{(\chi_n^2(e, \mu) - \min(\chi_n^2(e), \chi_n^2(\mu)))^2}{2\sigma_{\chi_n^2}^2} \right), \quad (6.11)$$

where $\sigma_{\chi_n^2} = \sqrt{2N}$ for N PMTs in the likelihood calculation.

For single-ring events, a second probability is used in the PID determination, based on the Cherenkov angle:

$$P^{angle}(e, \mu) = \exp \left(- \frac{(\theta^{obs} - \theta^{exp}(e, \mu))^2}{2\delta\theta^2} \right), \quad (6.12)$$

where θ^{obs} is the reconstructed Cherenkov angle, $\delta\theta$ the angle fitting error, and $\theta^{exp}(e, \mu)$ the expected angle based on the reconstructed e/μ -like momentum.

The final PID probability is the product of these two estimators:

$$P(e, \mu) = P^{pattern}(e, \mu) \times P^{angle}(e, \mu). \quad (6.13)$$

Note that for multi-ring events, only the light pattern is used, so that $P^{angle} = 1$.

The final PID likelihood is defined as

$$L_{PID} = \sqrt{-\log P(\mu)} - \sqrt{-\log P(e)}. \quad (6.14)$$

For positive values, the ring is fit as μ -like, and negative as e -like.

6.2.4 Momentum reconstruction

The momentum of a ring is determined by the charge observed around the ring, and the energy scale calibration described in Chapter 3. Specifically, the corrected charge in a 70-degree half-angle cone of a ring's direction, called "RTOT", is used to determine its momentum. The charge is restricted to a (-50, 250) ns time window relative to the time-of-flight subtracted timing peak, to avoid charge due to decay electrons. It is corrected for angular acceptance, water attenuation, contributions from scattered light, and PMT gain as follows:

$$\text{RTOT} = \frac{G_{MC}}{G_{DATA}} \left(\alpha \times \sum_i \left(q_i^{obs} \times e^{r_i/L} \times \frac{\cos \Theta_i}{f(\Theta_i)} \right) - \sum_i S_i \right). \quad (6.15)$$

Here $G_{MC/DATA}$ is the relative PMT gain for MC and data, α is a normalization factor, r_i is the distance from the i^{th} PMT to the event vertex, L is the water attenuation length, $f(\Theta)$ is the acceptance of the PMT for incident angle Θ , S_i is the expected charge for the i^{th} PMT from scattered photons, and the sums are over all PMTs meeting the timing and angular requirements described above. Figure 6.9 shows the linear relationship of RTOT and momentum. The conversion between RTOT and momentum is determined by MC simulation, by simply calculating the RTOT values for particles of known momenta.

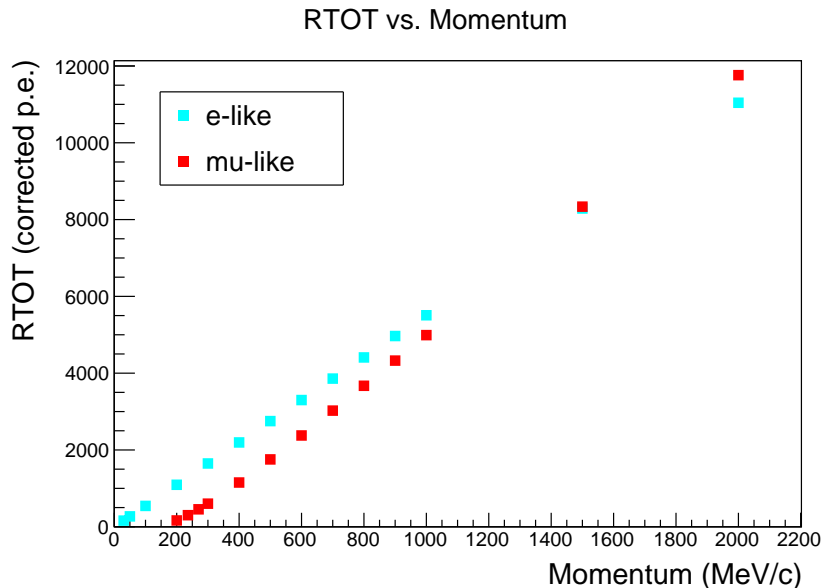


Figure 6.9: Distributions of RTOT vs. momentum up to 2000 MeV/c for both e -like and μ -like rings.

6.2.5 Decay electrons

Decay electrons are a valuable indicator of the presence of a muon — and, in the context of this thesis, a charged pion. They provide a relatively independent source of event information from the Cherenkov rings produced by primary particles.

The decay electron search window extends to 20 μs after the event trigger. Decay electron candidates are classified as primary or “in-gate” events, or sub-events, depending on their timing. In SK-I-III, the primary event requirements are as follows:

- $0.1 \mu s < t < 0.8 \mu s$;
- $NHIT_{30} \geq 60$ (30 in SK-II).

Here t is the time after the event trigger, and $NHIT_{30}$ is the number of hits in a 30 ns time window. Requirements for sub-events are defined similarly:

- $1.2 \mu s < t < 20 \mu s$;

- $\text{NHIT}_{30} \geq 40$ (20 in SK-II).

In addition, both primary and sub-event types are required to have at least 50 hit ID PMTs (25 for SK-II), and the vertex goodness (Equation 6.4) is required to be greater than 0.5. The ID PMT cut is designed to remove low-energy photons radiated from μ^- capture in oxygen.

The decay electron detection efficiency varied significantly between SK-I-III and SK-IV. In SK-I-III, an impedance mismatch in the DAQ electronics required that the time interval ($800 \text{ ns} < \Delta t < 1200 \text{ ns}$) be excluded from the search, where Δt is the time difference from the primary event peak. The upgraded electronics of SK-IV removed this mismatch, so that this interval is now included. Also, the overall hit ID PMT cut is removed. Both of these changes increase the decay electron tagging efficiency. In SK-I-III, the efficiency is 80% for μ^+ and 63% for μ^- ; in SK-IV, it is 96% for μ^+ and 80% for μ^- . In all cases, the efficiency is estimated with MC.

6.2.6 π^0 reconstruction

Ideally, a π^0 produces two showering rings, one from each photon from the decay $\pi^0 \rightarrow \gamma\gamma$. Sometimes, only one ring will be detected, if one of the two photons receives very little of the decay energy, or there is a close overlap between the two photons, such that they do not create distinct rings. In such cases, a π^0 reconstruction algorithm described in detail in [85] is useful. It does not seek individual Cherenkov rings, but rather assumes two photons, and constructs a likelihood based purely on the observed light pattern. This algorithm has been used in atmospheric [86] and long-baseline [87] neutrino experiments to identify and reject neutral-current single π^0 events. In the $pn \rightarrow \pi^+\pi^0$ search, it is used to reconstruct the π^0 candidate mass, which is used as a variable in the analysis.

Chapter 7

Dinucleon Decay Search

The experimental signature of a dinucleon decay to pions event, for all three modes considered, is two back-to-back pions, each forming at least one Cherenkov ring of the correct type. Cleanly identifying such events is complicated largely due to the interactions of charged pions in both the residual ^{16}O nucleus and the water. Interactions in the water can suddenly interrupt the pion's path, which typically lead to poor momentum reconstruction. Thus, for modes involving at least one π^+ ($pp \rightarrow \pi^+\pi^+$ and $pn \rightarrow \pi^+\pi^0$), simple cuts on kinematic variables such as the total momentum and invariant mass that are used in other nucleon decay analyses do not give optimal sensitivity. For these modes, a multivariate method is applied to better exploit event variables. Specifically, a boosted decision tree (BDT) method is used. The method is implemented in the ROOT-based TMVA [88] analysis library. This was also used in the dinucleon decay search for $pp \rightarrow K^+K^+$ in [40].

For $nn \rightarrow \pi^0\pi^0$, the situation is more straightforward, as the π^0 's that escape the nucleus decay to energetic photons before interaction in the water, and their momentum is well-reconstructed. For this mode, simple kinematic cuts are sufficient for the analysis.

7.1 Boosted Decision Trees

Here I describe some relevant details of the BDT, applicable for both $pp \rightarrow \pi^+\pi^+$ and $pn \rightarrow \pi^+\pi^0$ searches (and the $n \rightarrow \bar{n}$ search in the next chapter). The BDT method was chosen among other multivariate analysis options, such as the artificial neural network and likelihood methods. It was found that, for the same set of input variables, BDTs generally performed better in basic signal and background separation. BDTs have found diverse applications in particle physics. In addition to the $pp \rightarrow K^+K^+$ analysis in [40], they have been used for identifying electron neutrinos in MiniBooNE [89] and single top quark production at D0 [90], among others.

Similar to other multivariate methods, a BDT takes a set of input variables – in this case, reconstructed information for both dinucleon decay signal and atmospheric neutrino background – with the goal of producing a single discriminating output variable that separates signal and background. To get to this single variable, three stages are required. They are referred to as training, testing, and analysis, and each uses separate sets of signal and background MC. I describe the process briefly.

Boosted decision trees are sets of individual decision trees, simple binary trees formed by cuts on single variables. Trees are built using the training sample as follows. Starting with the full training sample, a cut on a single variable is made that best separates signal and background. For the analyses in this paper, this optimal separation is determined by the Gini index $g = p(1 - p)$, where p is the purity of the sample after the cut. Other separation types exist, though they don't lead to significantly different performance [88]. The sample then splits off into two samples, or nodes, based on this cut. Each of the daughter nodes does the same thing, separately finding the variable that best separates signal and background, and so forth until some stopping criterion is reached (such as a minimum number of events remaining

on a node). Terminal nodes are declared signal-like or background-like based on the purity of signal events in the node. Figure 7.1 shows an example tree used in the training process for the $pn \rightarrow \pi^+\pi^0$ search.

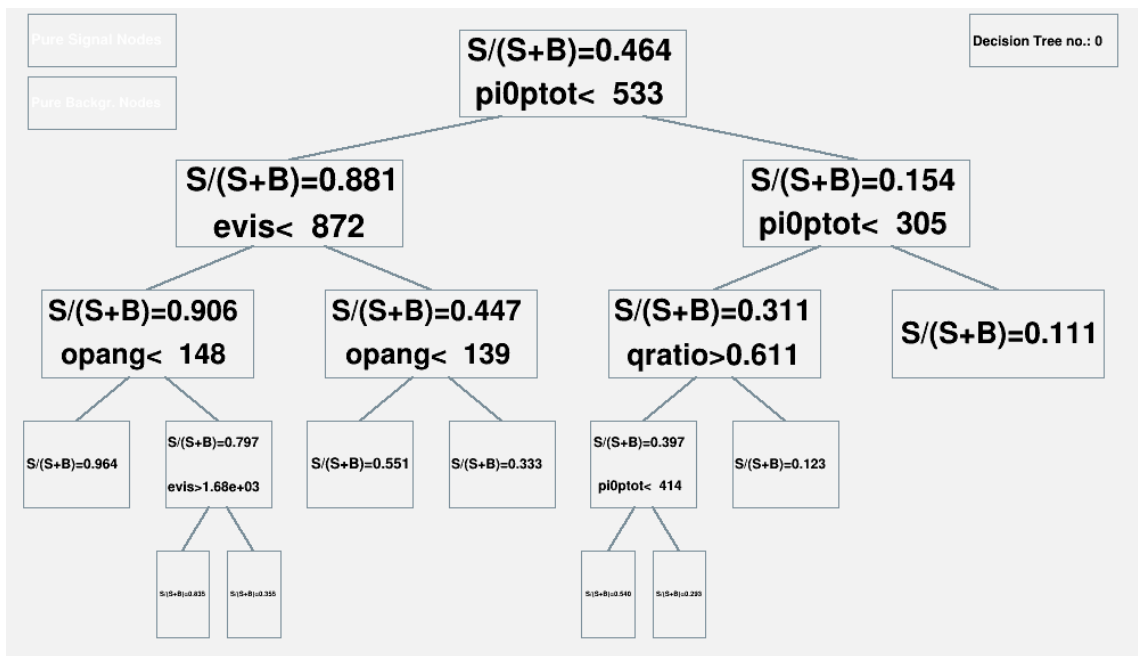


Figure 7.1: An example tree for the $pn \rightarrow \pi^+\pi^0$ analysis. The tree has a depth of four. The variables used are the reconstructed π^0 momentum (“pi0ptot”), the visible energy (“evis”), the $\pi^0 - \pi^+$ opening angle (“opang”), and the ratio of charge carried in the highest-energy ring (“qratio”), all of which are described in the text. Nodes that split to the left are more signal-like, and nodes that split to the right more background-like.

On their own, decision trees are weak classifiers, providing no more discriminatory power than a simple set of cuts. They are also unstable, prone to potentially large changes from statistical fluctuations. The idea behind a BDT is that many such trees can combine to form a single, strong classifier. The training process continues over many such trees (typically 1000 or so) using the same training sample, with the prescription that events in subsequent trees are re-weighted, or “boosted.” Upon re-weighting, the best set of discriminating variables may change. Variables can also

be used in more than one cut on a given tree.

Once all the trees are done, additional datasets may pass through the trained set of trees. On an event-by-event basis, the final BDT output is given by

$$Y_{BDT} = \frac{1}{N_{tree}} \sum_{i=1}^{N_{tree}} w_i h_i(x). \quad (7.1)$$

Here N_{tree} is the size of the ensemble of trees, w_i is the weight of each tree in the ensemble, determined by the boosting method, h_i is the “performance” of each event for the i^{th} tree (whether it ended on a signal or background-like node) and x is the set of input variables. Variables are given a ranking, or “importance,” a numerical value that roughly corresponds to the number of times the variable is used in the training process relative to the other variables in the set.

Once the BDT is trained, two additional, statistically independent sets of signal and background MC are necessary. The test samples are used to determine optimal parameters for the BDT. These parameters include:

- The boost method — this determines how events are re-weighted, or “boosted”, in the training process. Several boosting algorithms exist, and are described in detail in [88].¹ Two types of boosts are considered in this thesis — the adaptive boost, and the gradient boost.

The adaptive boost uses a simple formula for determining the weight w_i in Equation 7.1. It takes the misclassification error of the previous tree (the ratio of signal events that ended up in background nodes, and vice-versa) and defines

$$w_i(\text{adaptive}) = \ln \left(\frac{1 - \text{err}}{\text{err}} \right). \quad (7.2)$$

¹See especially Section 7, “Boosting and Bagging.”

The gradient boost method is more complicated, and doesn't have a set formula for its re-weighting procedure. It attempts to minimize a loss function that measures the difference between the value from a given tree, and the true value known from the training process².

In general, the adaptive boost method works well in situations with a small misclassification error, thereby maximizing the boosted weight in Equation 7.2. In noisier settings prone to a higher error, the gradient boost method is often superior.

- The number of trees — how many trees are used in the training process (N_{tree} in Equation 7.1). More trees generally lead to a more stable performance.
- The maximum depth — how many decisions are allowed to be made from the first node in each tree. Figure 7.1 shows a tree with depth 4. Setting the maximum depth too high can lead to overtraining (described below).
- The size of the cut grid — how many cuts are considered for each variable in optimizing the separation at each node.
- The minimum number of events in a node — the minimum number of events such that no further decisions will be made.

The boost method is the most consequential parameter for the BDT. Adjusting the other parameters was not found to change signal and background separation very much.

²Actually, both adaptive and gradient boosts operate on the principle of minimizing a loss function. However, the adaptive boost loss function leads to the simple formula for re-weighting in Equation 7.2, while the gradient boost formula must be approximated via steepest-descent approach — hence its name.

The analysis samples are used to obtain the final sensitivity. Unlike in the training and testing process, the BDT does not know the composition of the analysis samples. Both the test and analysis samples are also important in detecting training bias in the BDT. This bias is a situation in which the BDT has been trained to model statistical fluctuations in the training sample, as opposed to modeling from general trends in the input variables. Such overtraining can lead to different performance between MC samples, even if they are statistically similar.

Table 7.1 shows a set of common parameters used in the $NN \rightarrow \pi\pi$ analyses, and Table 7.2 breaks down the signal and background MC samples used for each stage. Separate trees are trained, tested, and analyzed for each SK period. Real data are processed through the trained BDTs as a final step.

Parameter	Value
Number of trees	1000
Maximum depth	4
Size of cut grid	20
Minimum events on a node	100

Table 7.1: A set of common parameters used for the BDTs in the $pp \rightarrow \pi^+\pi^+$ and $pn \rightarrow \pi^+\pi^0$ searches.

	training	testing	analysis
$NN \rightarrow \pi\pi$	25000 ev.	25000 ev.	25000 ev.
atm- ν	$\sim 750,000$ ev. (150 yr.)	$\sim 750,000$ ev. (150 yr.)	$\sim 1,000,000$ ev. (200 yr.)

Table 7.2: Independent MC sample sizes used for each stage of the BDT for both the $pp \rightarrow \pi^+\pi^+$ and $pn \rightarrow \pi^+\pi^0$ searches, prior to any cuts. Dinucleon decay sample sizes show only the number of events, while the atmospheric neutrino sample sizes show the approximate number of events and the equivalent number of years. The same statistics are used for SKI-IV.

7.2 $pp \rightarrow \pi^+ \pi^+$

7.2.1 Pre-selection for $pp \rightarrow \pi^+ \pi^+$

The interactions of π^+ 's in the nucleus and the water complicate the event signature for $pp \rightarrow \pi^+ \pi^+$. A set of precuts is applied to keep $pp \rightarrow \pi^+ \pi^+$ events, and reduce the atmospheric neutrino background. The key characteristics are that the event has two “back-to-back” rings, as the ring-finding algorithm is still good at reconstructing the ring direction even with the poor momentum resolution, and that the rings are identified as μ -like. Hadronic interactions in the water can sometimes appear like electromagnetic showers, thereby causing π^+ 's to be mis-identified as e -like. However, the converse – in which rings produced by electrons or photons are misidentified as μ -like – is rare. The following precuts are applied:

- (A1) There is more than one Cherenkov ring.
- (A2) The two most energetic rings are μ -like. These are assumed to correspond to the π^+ candidates.
- (A3) The angle between the two most energetic rings is greater than 120 degrees, a minimal requirement for “back-to-back” pions.
- (A4) The total visible energy is less than 1600 MeV, approximately the maximum visible energy expected from a dinucleon decay event ($2M_p - 2M_{\pi^+}$), where M_p is the proton and M_{π^+} the pion mass.

Table 7.3 shows the remaining efficiencies, background rates, and data events after each precut. Figure 7.2 shows the selections graphically.

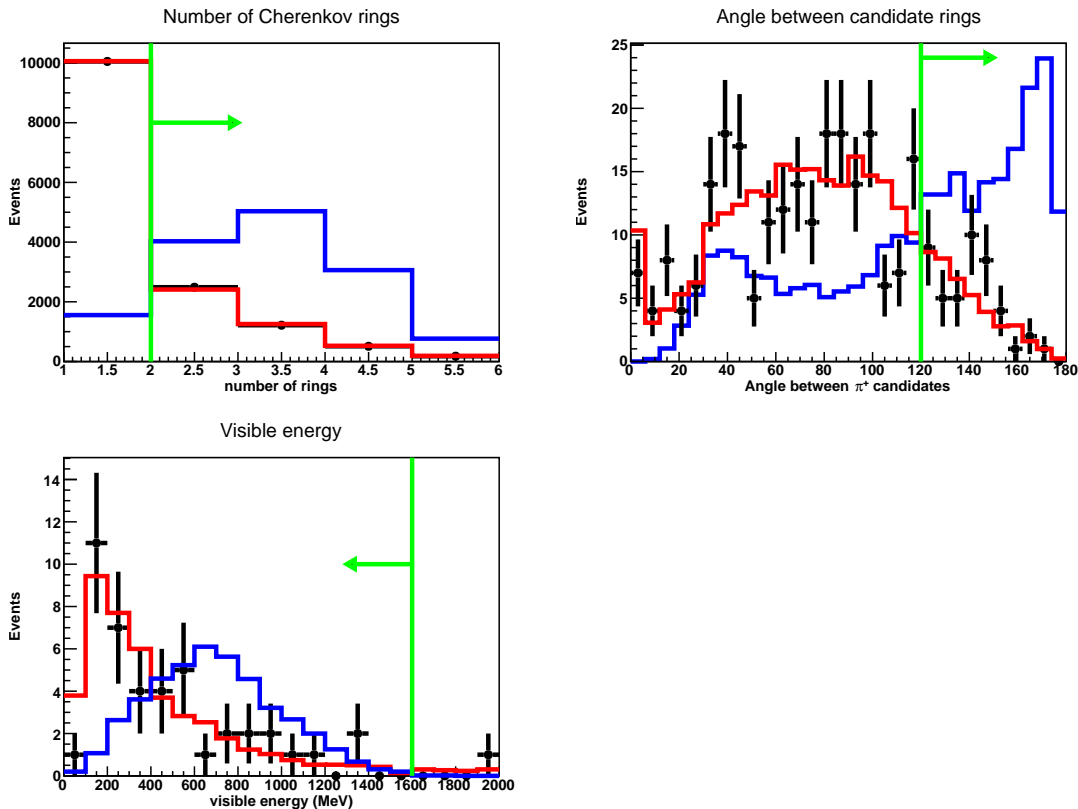


Figure 7.2: Selection criteria (A1) (top left), (A3) (top right), and (A4) (bottom left) for $pp \rightarrow \pi^+\pi^+$ MC (blue histogram), atm.- ν background (red histogram), and data (crosses) for SK-IV. All plots are area-normalized to the data. The green line indicates the placement of the cuts described in the text.

7.2.2 Multivariate analysis for $pp \rightarrow \pi^+\pi^+$

After applying these precuts, remaining events are processed by the BDT. The following set of input variables is used, ordered by their relative importance, as described above in Section 7.1:

- (a1) The angle between the two most energetic μ -like rings. It is expected to peak around a perfect “back-to-back” angle of 180 degrees for the signal, and have a falling spectrum for increasing angle in the background.

	SK-I	SK-II	SK-III	SK-IV
FCFV				
Eff. (%)	95.1	97.1	95.7	95.7
Bkg.	11889	6415	4206	14266
Data	12299	6610	4355	14444
(A1)				
Eff. (%)	84.2	85.1	85.3	85.4
Bkg.	3595	1944	1266	4330
Data	3691	2056	1292	4392
(A2)				
Eff. (%)	19.7	18.8	21.4	21.2
Bkg.	245	117	96	327
Data	222	106	78	273
(A3)				
Eff. (%)	11.3	10.5	12.0	12.1
Bkg.	36	18	14	49
Data	28	14	8	45
(A4)				
Eff. (%)	11.2	10.5	12.0	12.1
Bkg.	33	17	13	45
Data	27	14	8	43

Table 7.3: Efficiency, expected background, and data events after each precut for the $pp \rightarrow \pi^+\pi^+$ search. The FCFV cut is described in Section 6.1.6, and cuts (A1)-(A4) are described in the text. Expected background is weighted for oscillation effects, and scaled to the appropriate SK detector livetime (from the 200 year analysis sample).

- (a2) The ratio of charge carried by the highest-energy ring to the total charge of all rings. This is expected to be smaller for signal, since the pions are expected to have roughly equal energy. By contrast, we expect most of the energy from a charged-current (CC) atmospheric neutrino event to be in the charged lepton ring.

- (a3) The total visible energy. This has a broad distribution up to 1600 MeV for the signal, but peaks at a lower value for the background around 200 MeV.
- (a4) The maximum distance between a decay electron vertex and the primary event vertex. We expect this to be larger for energetic muons than for pions, since the muons penetrate water without sudden hadronic interactions. Muons above Cherenkov threshold sometimes appear in the signal (about 9% of the time), but are much more common in the background, due to charged-current ν_μ interactions such as single pion production.
- (a5) The maximum angle between any μ -like ring direction vector, and any Michel electron vertex vector (as pointed to from the primary vertex). Similar to (a1), this is designed to look for “back-to-back” events, and is an additional check on the topology of the μ -like rings.
- (a6) The magnitude of the vector sum of corrected charge associated with all rings (or each ring’s RTOT, as described in Section 6.2.4). This is similar to the total momentum, since the corrected charge associated with each ring is used to determine its momentum. Due to typically poor momentum resolution from hadronic energy losses, it is preferable to use this variable instead of the total momentum.
- (a7) The number of Cherenkov rings. Though we are trying to isolate two pions, they typically interact in the water, often producing visible secondary tracks, so that the number of rings distribution peaks at three. By contrast, the Cherenkov ring spectrum for the background falls with increasing ring number.
- (a8) The number of decay electrons. Naively we would expect two Michel electrons from two charged pions. However, the pions could undergo charge exchange or absorption, leading to zero or one Michel electrons. Though the signal and background distributions both peak at one decay electron, this variable is rela-

tively independent of most of the other variables, which depend on Cherenkov ring-counting.

- (a9) The number of μ -like rings. Similar to the total number of rings, this variable specifically seeks scatters that produce a secondary charged pion.

Figures 7.3-7.5 show distributions of each input variable for SK-IV. The corresponding plots for SK-I-III are similar, and can be found in Appendix B. The number of events remaining in the data after the pre-cuts is small, but the distributions generally agree with the atm.- ν MC. The relative importance of all input variables is shown in Table 7.4.

Variable	Importance
Angle between μ -like rings	0.16
Ratio of charge carried by most energetic ring	0.15
Visible energy	0.15
Max. distance to decay electron vertex	0.13
Max. angle between μ -like ring and Michel vertex	0.13
Magnitude of vector sum of corrected charge	0.12
Number of rings	0.071
Number of Michel electrons	0.055
Number of μ -like rings	0.045

Table 7.4: Relative importance of each variable in the $pp \rightarrow \pi^+\pi^+$ search, averaged across SK periods.

The final distributions of the BDT output for all SK periods are shown in Figure 7.6. For $pp \rightarrow \pi^+\pi^+$, the gradient boost [88] method is used. The final efficiencies, backgrounds, and candidate data events are shown in Table 7.5.

7.2.3 Final sample for $pp \rightarrow \pi^+\pi^+$

The final cut on the BDT output was determined using only signal and background MC, not the real data. The cut takes two basic considerations into account: (1) the

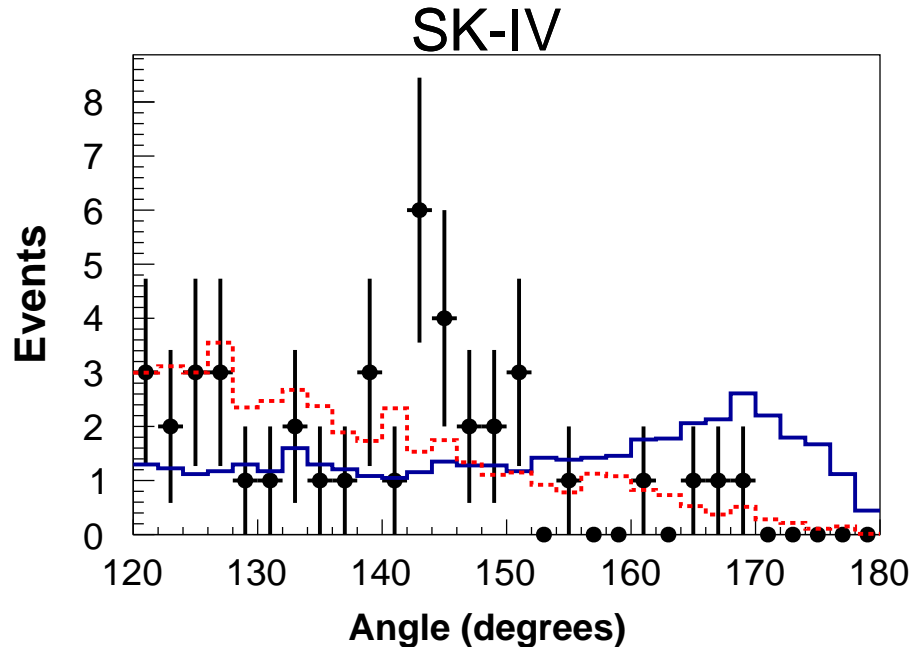


Figure 7.3: The angle between μ -like rings, the strongest discriminatory for the $pp \rightarrow \pi^+\pi^+$ search, for signal MC (solid histogram), atm.- ν MC (dashed histogram), and data (crosses). Distributions are shown for SK-IV and normalized to the number of events in the data.

cut maximizes ϵ/\sqrt{b} , where ϵ is signal efficiency and b is the background rate; and (2) the cut is not too close to the signal peak, since variations are propagated through the BDT to estimate systematics, and the part of the distribution near the peak changes the most under these variations. For (2), 0.7 was the closest value to the peak that we considered. As the efficiency (background) distribution increases (decreases) nearly monotonically for all SK periods, it was found that a cut at 0.7 satisfied (1) while obeying the constraint of (2).

The largest component ($\sim 40\%$) of the remaining atm.- ν background is from charged current single pion production (CC1 π). In this mode, typically a ν_μ will produce a muon and a charged pion at a large angle, thus passing the π^+ candidate angle requirement. Other contributing background interaction modes include charged- and

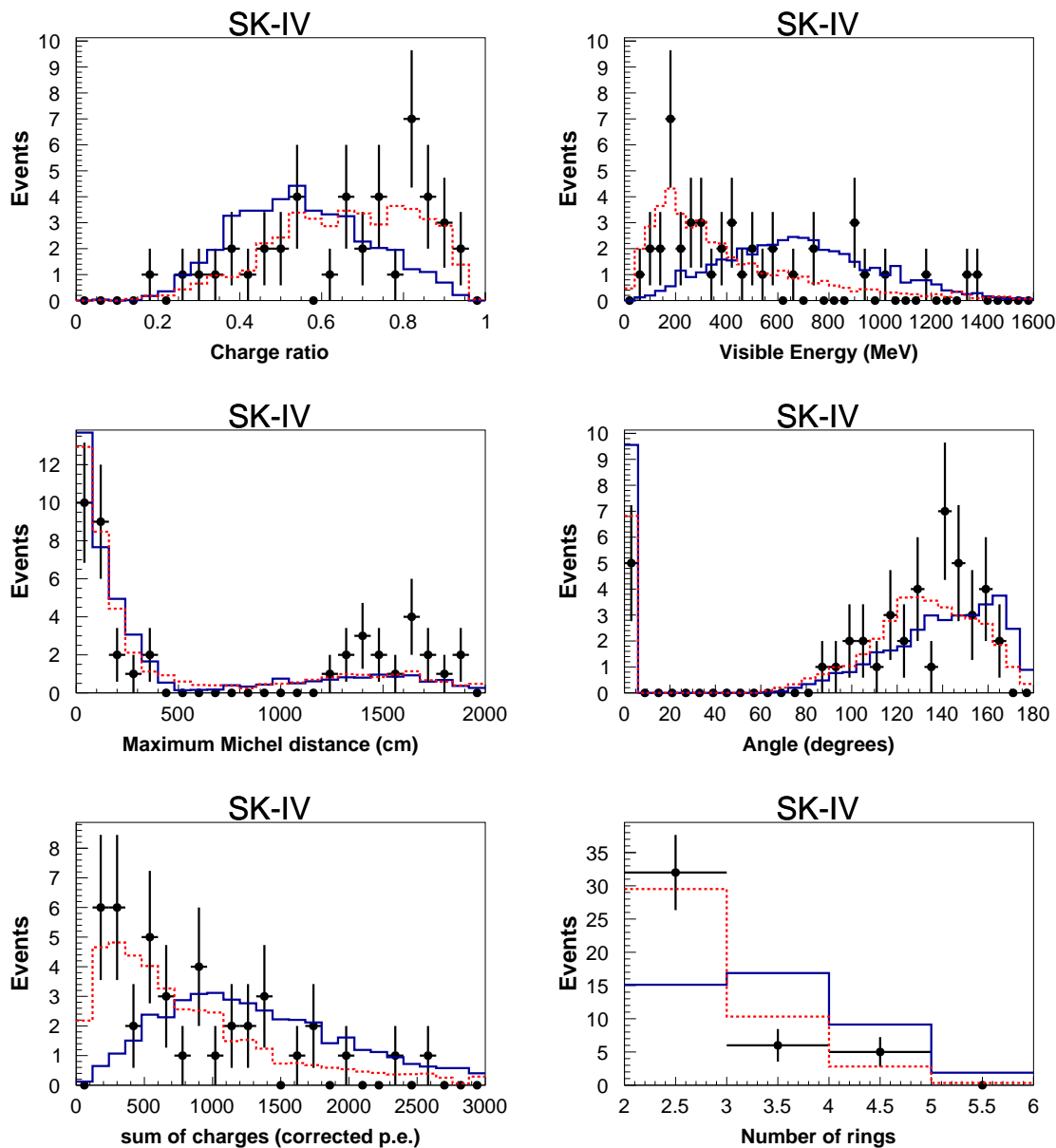


Figure 7.4: The ratio of charge carried by the leading ring (top left), the visible energy (top right), the maximum distance between the primary vertex and a decay electron vertex (middle left), the largest angle between a μ -like ring and decay electron vertex (middle right), the magnitude of the vector sum of RTOT (bottom left), and the number of Cherenkov rings (bottom right) for the $pp \rightarrow \pi^+\pi^+$ search, for signal MC (solid histogram), atm.- ν MC (dashed histogram), and data (crosses). Distributions are for SK-IV, and are normalized to the number of events in the data. Details of each variable are described in the text.

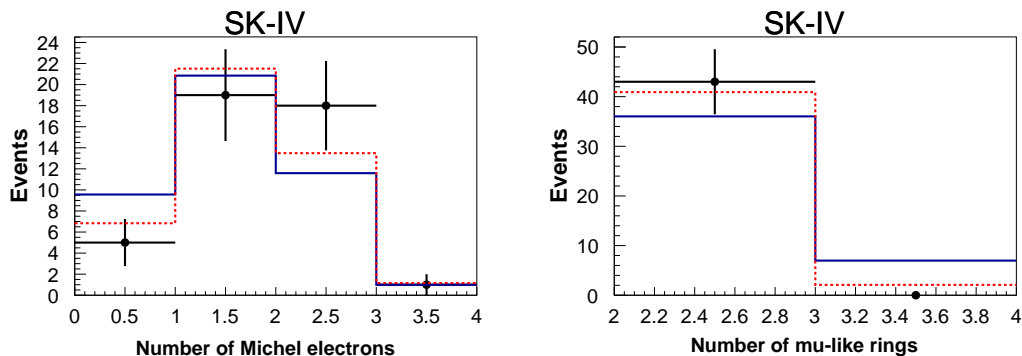


Figure 7.5: The number of decay electrons (left) and the number of μ -like rings (right) for the $pp \rightarrow \pi^+\pi^+$ search, for signal MC (solid histogram), atm.- ν MC (dashed histogram), and data (crosses). Distributions are shown for SK-IV, and are normalized to the number of events in the data. Details of each variable are described in the text.

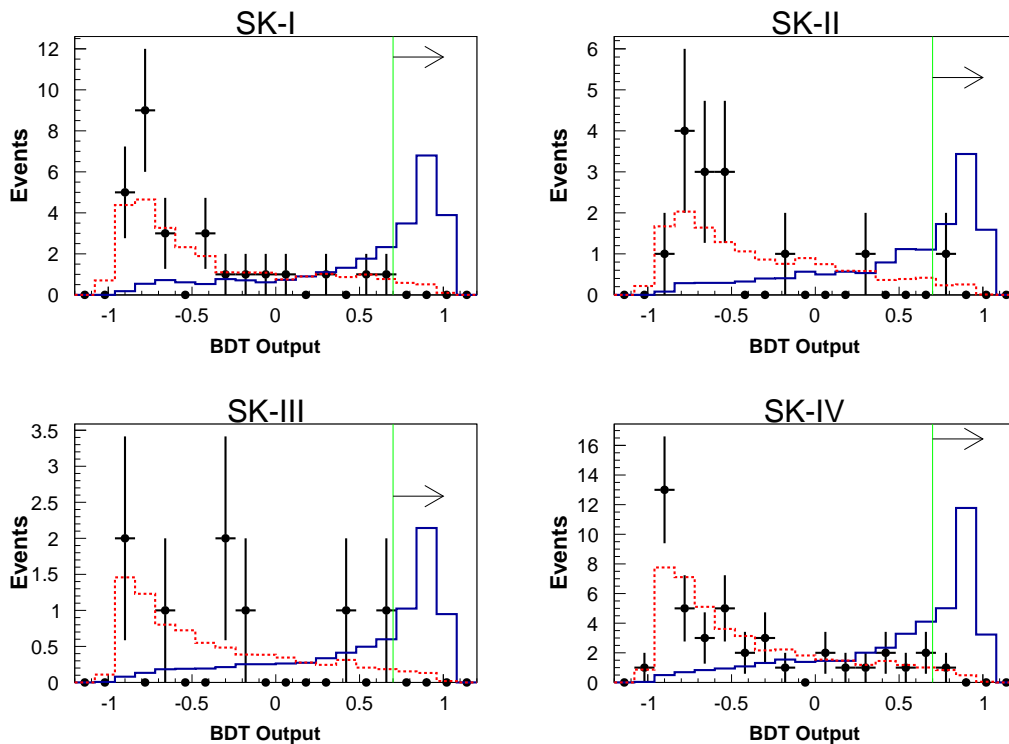


Figure 7.6: BDT output for $pp \rightarrow \pi^+\pi^+$ signal (solid), atm.- ν background (dashed), and data (crosses). The vertical green line indicates the BDT cut value, and the arrow indicates that only events to the right of the cut are kept.

	SK-I	SK-II	SK-III	SK-IV
Eff. (%)	6.1	5.3	6.4	5.8
Bkg. (MT-yr)	17.8	14.3	17.4	14.2
Bkg. (SK live.)	1.6	0.70	0.56	1.6
Candidates	0	1	0	1

Table 7.5: Efficiency, expected background events, and candidate data events for SKI-IV $pp \rightarrow \pi^+\pi^+$ search. Background is quoted both for the appropriate SK livetime, and per megaton-year.

mode	SK-I	SK-II	SK-III	SK-IV
CC1 π	45%	42%	51%	42%
CCDIS	30%	31%	24%	34%
NCDIS	10%	9%	6%	13%
CCQE	9%	9%	10%	10%
NC1 π	5%	8%	8%	0%

Table 7.6: Atmospheric neutrino interaction modes in the remaining background for the $pp \rightarrow \pi^+\pi^+$ search by percentage, as estimated by atmospheric neutrino MC.

neutral-current deep inelastic scattering (CCDIS and NCDIS), charged-current quasi-elastic (CCQE) and neutral-current single pion production (NC1 π). See Table 7.6 for a breakdown of the neutrino interaction modes for remaining background.

A $pp \rightarrow \pi^+\pi^+$ MC event is shown in Figure 7.7. An atmospheric neutrino event surviving all cuts is shown in Figure 7.8. Two candidate events were found, one in SK-II (Figure 7.9) and another in SK-IV (Figure 7.10). No events are observed in SK-I or SK-III. Table 7.7 shows values of the BDT input variables for each candidate, compared to the means of the signal and background distributions. While both candidate events appear signal-like in some variables, particularly the angle between μ -like rings (both candidates) and energy variables (SK-IV candidate), the candidates are consistent with the expected background rate for each SK period (Table 7.5). Thus, we conclude that there is no evidence for $pp \rightarrow \pi^+\pi^+$ in the data.

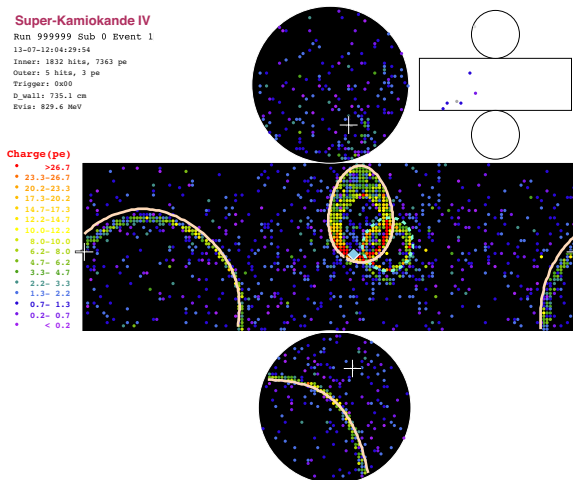


Figure 7.7: A $pp \rightarrow \pi^+\pi^+$ MC event. The two solid orange rings correspond to true π^+ 's, and have an angle of 164 degrees between them. The dashed cyan ring is fit as e -like, but is actually a hard scatter of one of the π^+ 's.

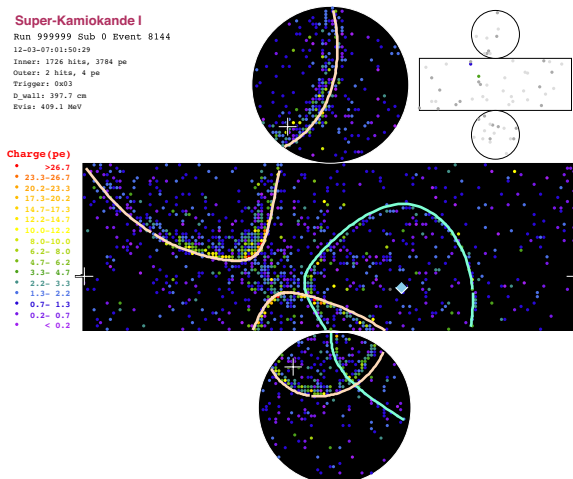


Figure 7.8: Surviving atmospheric neutrino MC event for the $pp \rightarrow \pi^+\pi^+$ search. The interaction type is ν_μ charged-current single π^+ production. The uppermost μ -like ring corresponds to a μ^- , while the smaller μ -like ring is a π^+ . The e -like ring is mis-fit, as it comes from a hard scatter of the π^+ . The angle between the two μ -like rings is 170 degrees, thereby mimicking the main event signature. The momentum of the muon μ -like ring is 402 MeV/c, and the momentum of the π^+ μ -like ring is 301.3 MeV/c

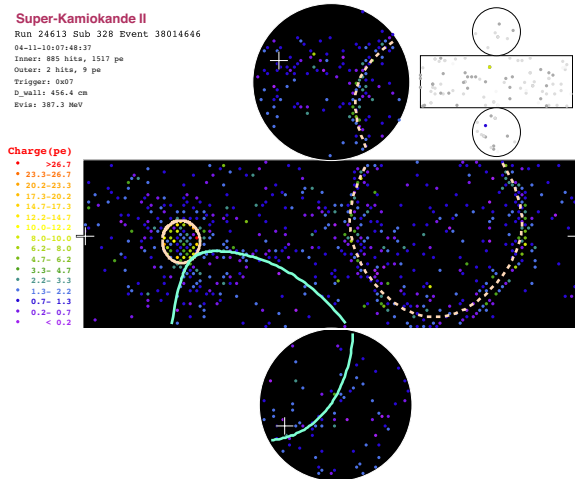


Figure 7.9: $pp \rightarrow \pi^+\pi^+$ candidate event in SK-II. The two μ -like rings are strikingly back-to-back, at almost exactly 180 degrees to each other. The e -like ring could be due to a hard scatter. There is one Michel electron, not shown. The μ -like rings have momenta of 399.0 MeV/c (solid) and 280.5 MeV/c (dashed), and the e -like ring has momentum 42.0 MeV/c. The visible energy is 387.0 MeV, the total momentum 124.2 MeV/c, and the invariant mass 710.9 MeV/ c^2 .

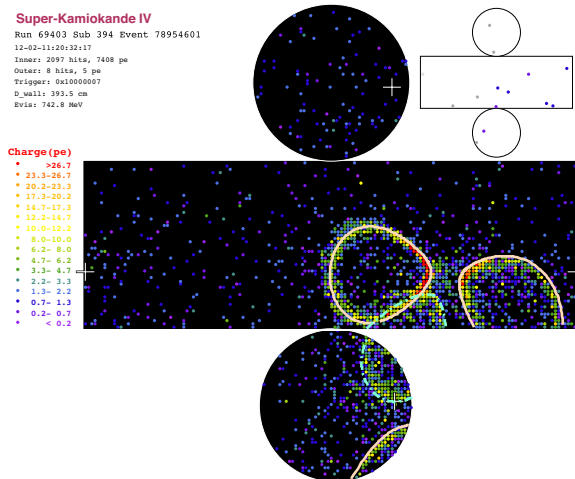


Figure 7.10: $pp \rightarrow \pi^+\pi^+$ candidate event in SK-IV. The two μ -like rings are at an angle of 151 degrees to each other, with momenta of 541.4 and 389.5 MeV/c. The dashed e -like ring could be due to a hard scatter. There are 2 Michel electrons, not shown. The visible energy is 742.8 MeV, the total momentum is 445.8 MeV/c, and the invariant mass is 1022.3 MeV/ c^2 .

Variable	Candidate		Signal		Background	
	SK-II	SK-IV	SK-II	SK-IV	SK-II	SK-IV
a1 (degrees)	177.7	151.8	152.3	152.1	138.3	138.1
a2 (dimensionless)	0.60	0.46	0.55	0.55	0.66	0.66
a3 (MeV)	400.0	745.6	680.5	693.7	440.2	407.3
a4 (cm)	1245.6	1420.1	440.7	424.8	523.0	459.2
a5 (degrees)	166.3	111.9	94.2	109.0	93.2	110.9
a6 (corrected p.e.)	306.9	1799.5	601.3	1310.0	448.7	797.5
a7 (dimensionless)	3	3	2.89	2.95	2.39	2.40
a8 (dimensionless)	1	2	0.91	1.09	1.00	1.21
a9 (dimensionless)	2	2	2.14	2.16	2.05	2.05

Table 7.7: Candidate variable values, and mean variable values for signal and background distributions, for each of the variables used in the BDT for the $pp \rightarrow \pi^+\pi^+$ search. The description of each variable is in the text. Values are given for SK-II and SK-IV, for which single candidate events were found.

7.3 $pn \rightarrow \pi^+\pi^0$

There are many similarities between the $pn \rightarrow \pi^+\pi^0$ search and the $pp \rightarrow \pi^+\pi^+$ search. The main difference is that the π^0 provides a new set of discriminatory variables, and some of the variables only apply to the reconstructed π^0 .

7.3.1 Pre-selection for $pn \rightarrow \pi^+\pi^0$

Following largely the same logic of the $pp \rightarrow \pi^+\pi^+$ search, a set of pre-cuts is applied:

- (B1) There is more than one Cherenkov ring.
- (B2) There is at least one e -like and one μ -like ring. The π^+ is assumed to correspond to the most energetic μ -like ring, while the π^0 is assumed to correspond to the e -like ring (if one e -like ring is found) or the two most energetic e -like rings (if more than one is found).

(B3) The number of Michel electrons is no more than one.

(B4) The “reduced” visible energy, defined as the total visible energy minus the energy of the π^0 as defined in the previous cut, is less than 800 MeV. This is similar to cut (A4) used in the $pp \rightarrow \pi^+\pi^+$ search - the maximum visible energy from the π^+ is $M_{proton} - M_{\pi^+} \approx 800$ MeV.

(B5) The angle between the reconstructed π^+ and π^0 is greater than 120 degrees.

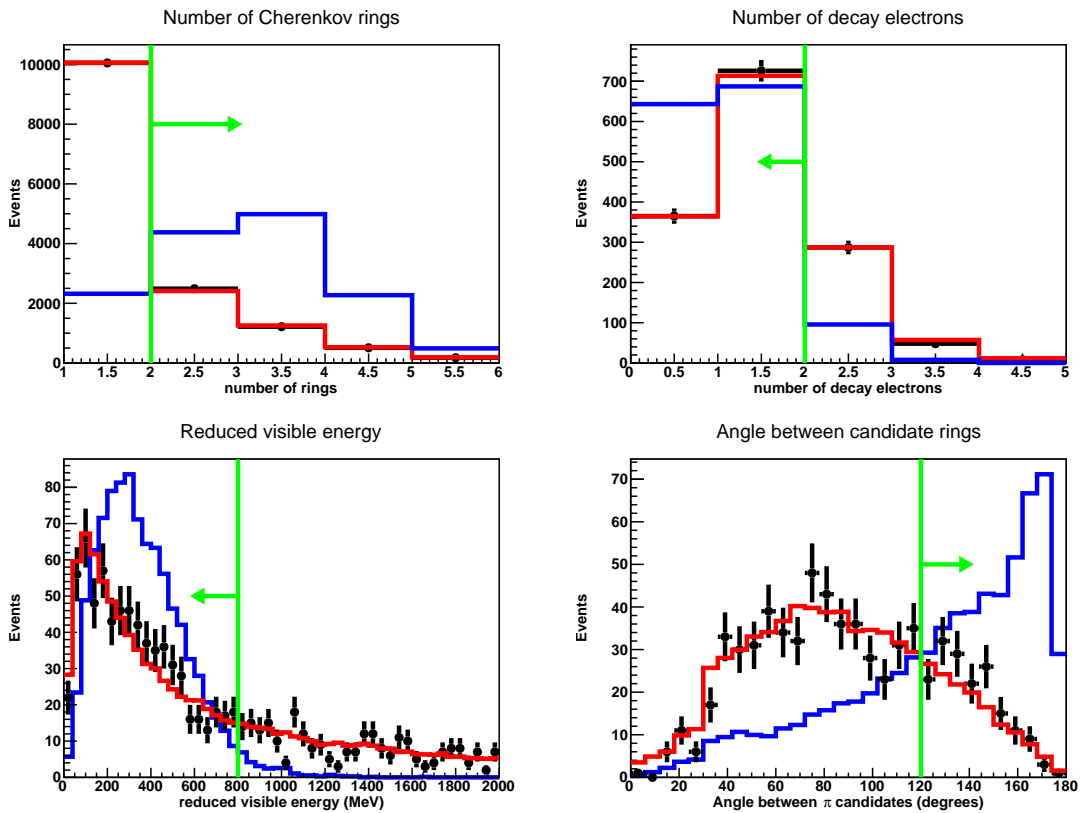


Figure 7.11: Selection criteria (B1) (top left), (B3) (top right), (B4) (bottom left) and (B5) (bottom right) for $pn \rightarrow \pi^+\pi^0$ MC (blue histogram), atm.- ν background (red histogram), and data (crosses) for SK-IV. All plots are area-normalized to the data. The green line indicates the placement of the cuts described in the text.

Table 7.8 shows the remaining efficiencies, background rates, and data events after each precut.

	SK-I	SK-II	SK-III	SK-IV
FCFV				
Eff. (%)	94.0	96.8	96.1	94.9
Bkg.	11889	6415	4206	14266
Data	12299	6610	4355	14444
(B1)				
Eff. (%)	78.6	79.7	79.8	79.6
Bkg.	3595	1944	1266	4330
Data	3691	2056	1292	4392
(B2)				
Eff. (%)	34.9	36.0	36.1	36.3
Bkg.	1178	615	428	1469
Data	1176	645	414	1437
(B3)				
Eff. (%)	32.9	34.1	34.1	33.6
Bkg.	995	521	361	1101
Data	1009	554	360	1091
(B4)				
Eff. (%)	32.3	33.4	33.2	33.7
Bkg.	622	330	224	693
Data	665	349	237	691
(B5)				
Eff. (%)	21.0	21.9	21.6	21.1
Bkg.	132	69	48	147
Data	136	66	45	171

Table 7.8: Efficiency, expected background, and data events after each precut for the $pn \rightarrow \pi^+\pi^0$ search. Cuts (B1)-(B5) are described in the text. Expected background is weighted for oscillation effects, and scaled to the appropriate SK detector livetime (from the 200 year analysis sample).

7.3.2 Multivariate analysis for $pn \rightarrow \pi^+\pi^0$

As with $pp \rightarrow \pi^+\pi^+$, events surviving the precuts are passed into a BDT. The following set of input variables is used, ordered according to variable importance:

- (b1) The momentum of the π^0 candidate. The π^0 momentum peaks near 1 GeV for the signal, which is typically well-reconstructed. The background peaks at a much lower value of ~ 200 MeV.
- (b2) The angle between the reconstructed π^+ and π^0 . This peaks near 180 degrees for the signal.
- (b3) The momentum of the π^+ candidate. The momentum resolution for charged pions from dinucleon decay is typically poor. Despite this, it still peaks at a higher value in the signal than the background (470 MeV/c vs. 390 MeV/c), and is relatively independent of the better-reconstructed π^0 momentum.
- (b4) The invariant mass of the π^0 . This can be estimated for both one and two-ring π^0 hypotheses, by means of the specialized algorithm referred to in Section 6.2.6.
- (b5) The ratio of charge carried by the highest-energy ring to the total charge of all rings.
- (b6) The total visible energy.
- (b7) The number of decay electrons.

Variables (b5), (b6), and (b7) were described for the $pp \rightarrow \pi^+\pi^+$ search. Figures 7.12-7.13 show distributions of each input variable for SK-IV; analogous distributions for SK-I-III can be found in Appendix B. The data distributions generally agree with the atm.- ν MC. The relative importance of all input variables is shown in Table 7.9.

Variable	Importance
π^0 candidate momentum	0.19
Angle between π^0 and π^+ candidates	0.17
π^+ candidate momentum	0.16
π^0 candidate invariant mass	0.15
Ratio of charge carried by most energetic ring	0.14
Visible energy	0.14
Number of decay electrons	0.058

Table 7.9: Relative importance of each variable in the $pn \rightarrow \pi^+\pi^0$ search, averaged across SK periods.

7.3.3 Final sample for $pn \rightarrow \pi^+\pi^0$

The final BDT outputs are shown in Figure 7.14. For the $pn \rightarrow \pi^+\pi^0$ search, an adaptive boost method [88] was chosen. The discriminatory power of the π^0 momentum (Figure 7.12) in particular helped keep the misclassification rate low, thus increasing the boosted weights for the adaptive boost (Equation 7.2). The final cut was designed so that less than one background event was expected across all SK periods, with contributions from each SK period ordered by their livetime. It is determined with MC only. The total expected background is 0.75 events, consistent with the one candidate event found in SK-I. Unlike the $pp \rightarrow \pi^+\pi^+$ search, the signal distributions are not sharply peaked, so that the efficiency does not change drastically as the cut value is shifted.

The cut on the final BDT output, efficiencies, background rates, and candidates are shown in Table 7.10. CCDIS and CC1 π are the main components of the remaining background, detailed in Table 7.11.

An example $pn \rightarrow \pi^+\pi^0$ MC event display is shown in Figure 7.15, and an example background MC event is shown in Figure 7.16. One candidate is found in SK-I, shown in Figure 7.17. Table 7.12 shows the values of the BDT input variables

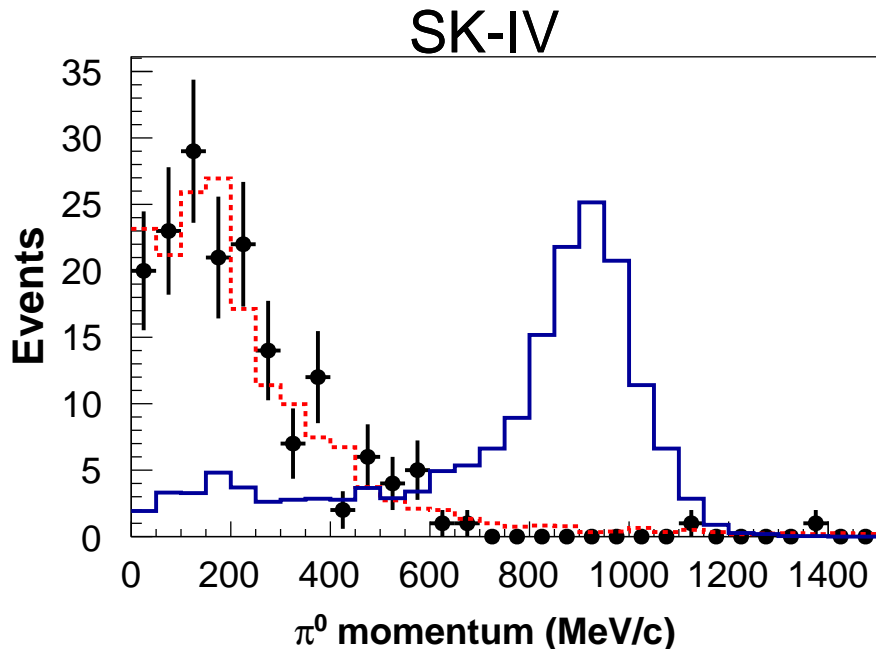


Figure 7.12: The total momentum of the π^0 candidate in SK-IV, the best discriminating variable for the $pn \rightarrow \pi^+\pi^0$ search, for signal MC (solid histogram), atm.- ν MC (dashed histogram), and data (crosses). Distributions are normalized to the number of events in the data.

for the candidate event, compared with the means of the signal and background distributions. While the candidate event appears closer to the signal mean values for energy-related variables, it appears more background-like for the $\pi^0 - \pi^+$ angle and the reconstructed π^0 mass. There are no candidate events in SKII-IV data. The probability of observing one or more background event in SK-I, without incorporating systematic uncertainties, is 22%. This is consistent with a background event. Further, the low π^0 mass of the candidate event, as reconstructed by the specialized algorithm discussed in Section 6.2.6, suggests that it is not a $pn \rightarrow \pi^+\pi^0$ signal. The showering ring is more likely to be an electron from, for instance, a $CC\nu_e 1\pi$ event. Thus, I conclude that there is no evidence for $pn \rightarrow \pi^+\pi^0$ in the SK-I-IV dataset.

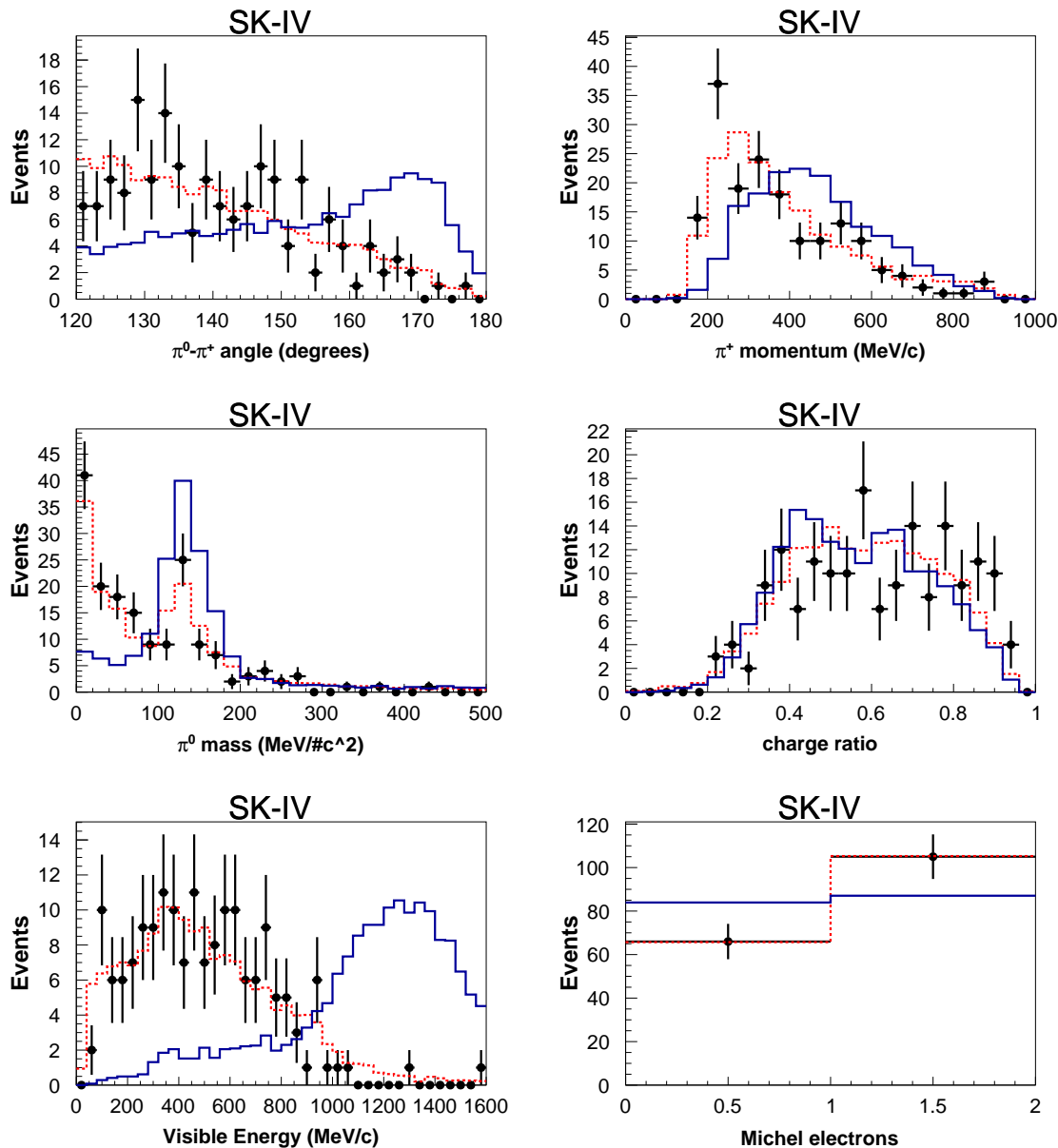


Figure 7.13: The opening angle between the π^0 and π^+ candidate rings (top left), the momentum of the π^+ candidate (top right), the invariant mass of the π^0 candidate (middle left), the ratio of charge carried by the most energetic ring (middle right), the visible energy (bottom left), and the number of decay electrons (bottom right) for the $pn \rightarrow \pi^+\pi^0$ search in SK-IV, for signal MC (solid histogram), atm.- ν MC (dashed histogram), and data (crosses). Distributions are normalized to the number of events in the data. Details of each variable are described in the text.

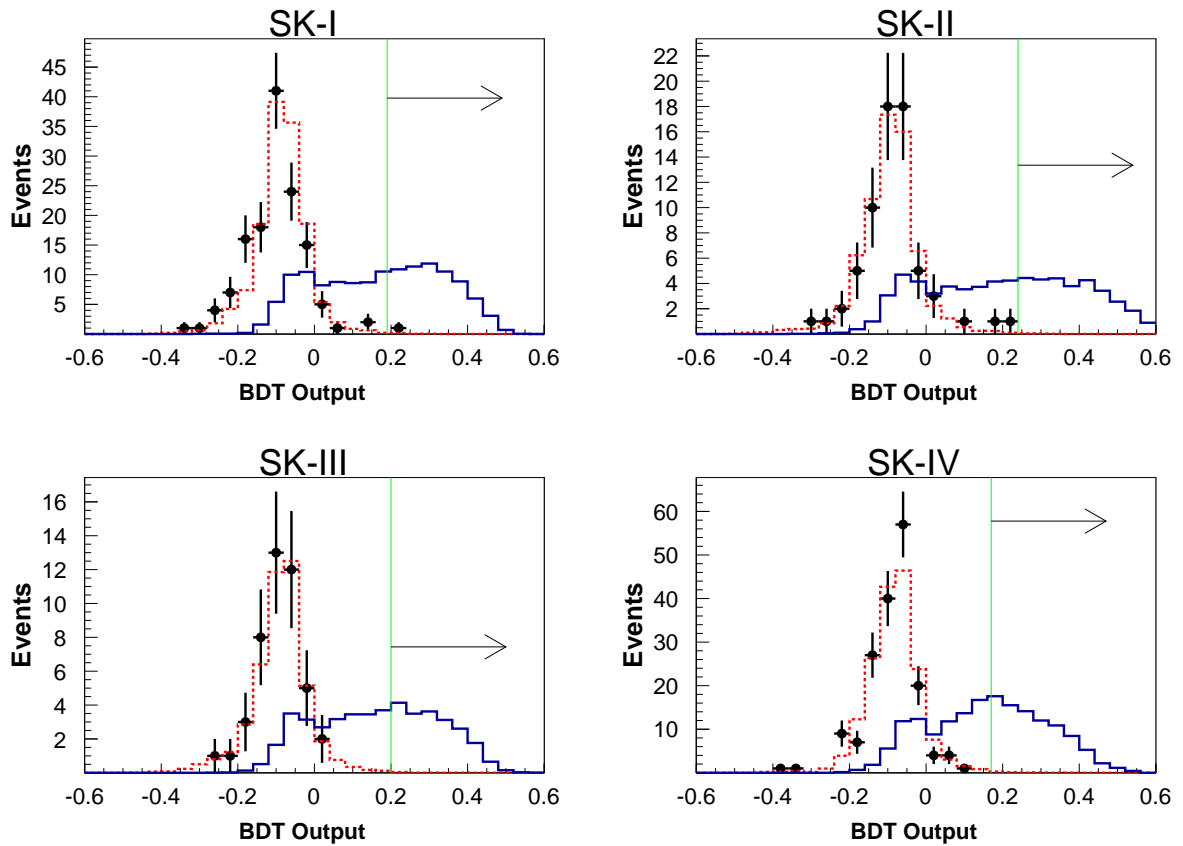


Figure 7.14: BDT output for $pn \rightarrow \pi^+\pi^0$ signal (solid), atmospheric neutrino background (dashed), and data (crosses). The green vertical line indicates the BDT cut value, and the arrow indicates that only events to the right of the cut are kept. One candidate event can be seen in the SK-I data distribution, just to the right of the cut at 0.19.

	SK-I	SK-II	SK-III	SK-IV
Cut	0.19	0.24	0.20	0.17
Eff. (%)	10.2	10.0	9.4	10.4
Bkg. (MT-yr)	2.7	2.3	2.2	2.9
Bkg. (SK live.)	0.25	0.11	0.07	0.32
Candidates	1	0	0	0

Table 7.10: Final BDT cut value, efficiency, expected background, and candidate data events for the SKI-IV $pn \rightarrow \pi^+\pi^0$ search. Background rates are quoted for the appropriate SK livetime, and per megaton-year.

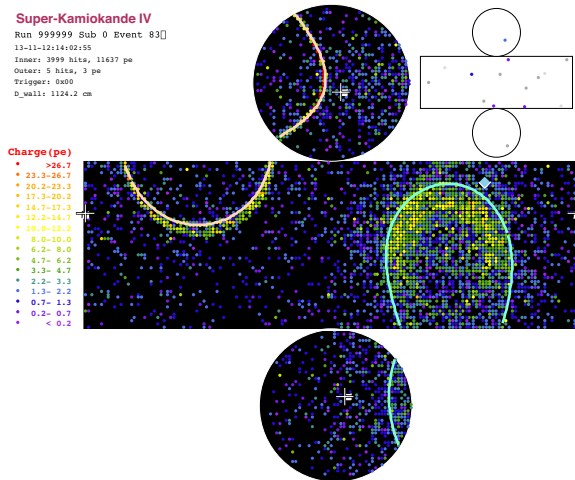


Figure 7.15: A $pn \rightarrow \pi^+\pi^0$ MC event. The μ -like ring corresponds to a true π^+ . The e -like ring contains two overlapping γ 's from a π^0 . The angle between the μ - and e -like rings is 165 degrees. The e -like ring has a reconstructed momentum of 893 MeV/c, while the original π^0 had momentum 876 MeV/c.

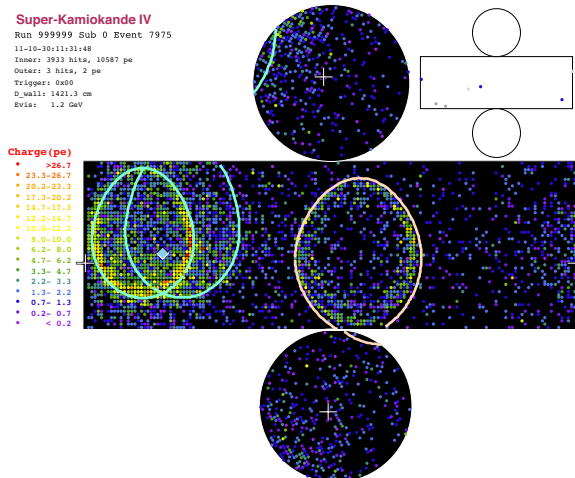


Figure 7.16: A surviving atmospheric neutrino MC event for the $pn \rightarrow \pi^+\pi^0$ search. The interaction type is $CC1\pi^0$, $\nu_\mu n \rightarrow \mu^-\pi^0 p$. The two overlapping e -like rings are photons from a π^0 , with total momentum 939 MeV/c. The μ -like ring corresponds to the μ^- , with momentum 410 MeV/c. The angle between them is 151 degrees, thereby appearing back-to-back.

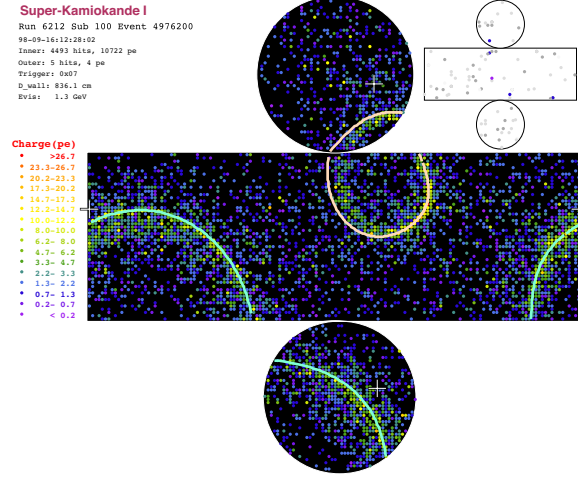


Figure 7.17: The $pn \rightarrow \pi^+\pi^0$ candidate in SK-I. The e -like and μ -like rings are at an angle of 140 degrees. The e -like ring has a high momentum of 987 MeV/c, but its fit π^0 mass is low, at 10 MeV/ c^2 . The μ -like ring has a momentum of 460.0 MeV/c. The total momentum and invariant mass are 700.1 MeV/c and 1266.4 MeV/ c^2 , respectively.

mode	SK-I	SK-II	SK-III	SK-IV
CC1 π	33%	29%	43%	45%
CCDIS	38%	46%	31%	40%
NCDIS	8%	20%	21%	8%
CCQE	8%	5%	5%	8%

Table 7.11: Neutrino interaction mode percentages for remaining background in the $pn \rightarrow \pi^+\pi^0$ search for SKI-IV.

Variable	Candidate	Signal	Background
b1 (MeV/c)	986.5	756.0	233.7
b2 (degrees)	142.8	152.9	140.4
b3 (MeV/c)	459.5	470.3	394.5
b4 (MeV/ c^2)	10.0	143.0	102.2
b5 (dimensionless)	0.77	0.56	0.58
b6 (MeV)	1171.6	1098.6	495.0
b7 (dimensionless)	0	0.40	0.51

Table 7.12: Candidate variable values, and mean variable values for signal and background distributions, for each of the variables used in the BDT for the $pn \rightarrow \pi^+\pi^0$ search. Letters for each variable are assigned in the text. Values are given for SK-I, for which a single candidate event was found.

7.4 $nn \rightarrow \pi^0\pi^0$

7.4.1 Selection criteria for $nn \rightarrow \pi^0\pi^0$

The $nn \rightarrow \pi^0\pi^0$ search is distinct from the other two searches, in that no multivariate method is used. Similar to other nucleon decay searches at SK, the total momentum and invariant mass are highly discriminatory variables, so that the search proceeds with a simple set of cuts. The cuts are similar to those used for the $p \rightarrow e^+\pi^0$ analysis [16].

$$(C1) \quad 2 \leq N_{\text{ring}} \leq 4;$$

$$(C2) \quad \text{all rings are } e\text{-like};$$

$$(C3) \quad \text{no decay electrons};$$

$$(C4) \quad P_{\text{tot}} \leq 600 \text{ MeV}/c;$$

$$(C5) \quad 1600 \text{ MeV}/c^2 \leq M_{\text{inv}} \leq 2000 \text{ MeV}/c^2.$$

Here N_{ring} is the number of Cherenkov rings, $P_{\text{tot}} = |\sum_{i=1}^{N_{\text{ring}}} \vec{p}_i|$ is the total momentum over all rings, and $M_{\text{inv}} = \sqrt{E_{\text{tot}}^2 - P_{\text{tot}}^2}$, where $E_{\text{tot}} = \sum_{i=1}^{N_{\text{ring}}} |\vec{p}_i|$ (the rings are assumed to be massless, coming from photons).

Criterion (C1) allows for both one- and two-ring π^0 fits. Criteria (C2) and (C3) ensure that all rings come from true electromagnetic showers, with (C3) removing charged pions that may have been misidentified as e -like. Criterion (C4) ensures a low total momentum, and (C5) covers the invariant mass region $\sim 2M_N$ as tightly as possible without getting too close to the signal peak. (C5) eliminates nearly all background, which peaks sharply near M_{π^0} . Figure 7.18 shows one-dimensional distributions for (C4) and (C5), and Figure 7.19 shows two-dimensional plots of P_{tot} vs.

M_{inv} for all SK periods combined. Figures 7.20 and 7.21 show typical $nn \rightarrow \pi^0\pi^0$ and background MC events surviving all cuts.

7.4.2 Final sample for $nn \rightarrow \pi^0\pi^0$

The signal efficiency, expected background, and data events after each cut are shown in Table 7.13. The remaining background after all cuts is mostly NCDIS (Table 7.14). The expected background rate in SK-IV is lower than the other SK periods despite its longer livetime, due to the increased efficiency of decay electron tagging in (C3). No candidates are found in the data, consistent with the near-zero expected background. Thus, I conclude that there is no evidence for $nn \rightarrow \pi^0\pi^0$.

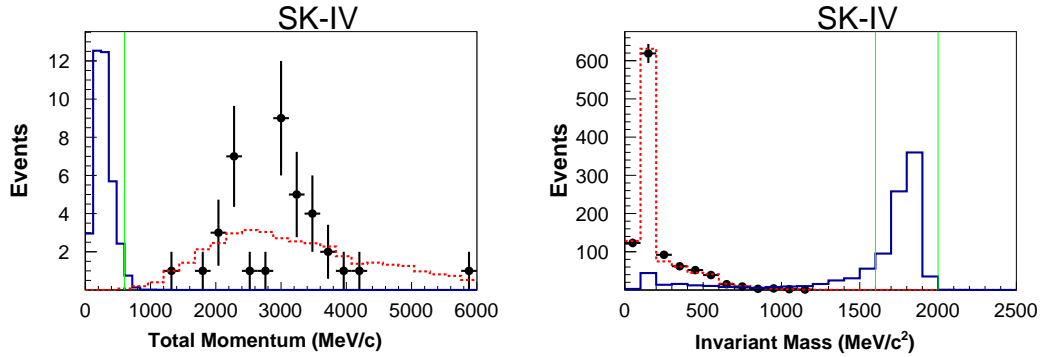


Figure 7.18: Total momentum (left) and invariant mass (right) for data (crosses), $nn \rightarrow \pi^0\pi^0$ MC (solid histogram), and atmospheric neutrino MC (dashed histogram). Cuts (C1)-(C3) are applied to both plots. The invariant mass cut (C5) has been applied to the total momentum, and the total momentum cut (C4) to the invariant mass. The thin green vertical lines indicate the locations of the final cuts for each variable.

	SK-I	SK-II	SK-III	SK-IV
FCFV				
Eff. (%)	94.1	96.6	94.4	94.1
Bkg.	11846	6389	4187	14214
Data	12299	6610	4355	14444
(C1)				
Eff. (%)	76.7	76.4	76.6	76.8
Bkg.	3434	1846	1204	4135
Data	3558	1969	1239	4215
(C2)				
Eff. (%)	61.0	59.1	59.6	60.1
Bkg.	2131	1175	728	2502
Data	2249	1268	782	2623
(C3)				
Eff. (%)	54.4	52.6	52.8	52.1
Bkg.	1441	799	497	1543
Data	1492	837	529	1627
(C4)				
Eff. (%)	30.1	27.0	29.1	29.3
Bkg.	837	470	290	940
Data	853	503	310	1021
(C5)				
Eff. (%)	22.1	18.8	20.9	21.4
Bkg.	0.05	0.04	0.03	0.02
Data	0	0	0	0

Table 7.13: Efficiency, expected background, and data events for the SKI-IV $nn \rightarrow \pi^0\pi^0$ search, for each analysis cut. The cuts are described in the text.

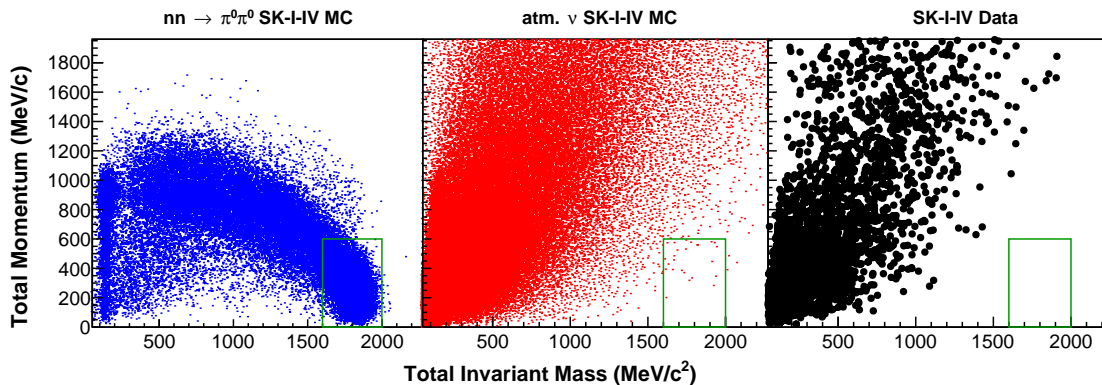


Figure 7.19: The total momentum and invariant mass distributions for $nn \rightarrow \pi^0\pi^0$ MC (left), atmospheric neutrino MC (center), and data (right) combined for SK I-IV. Events have passed cuts (C1)-(C3). The solid box indicates the total momentum and invariant mass cuts ((C4) and (C5) in the text).

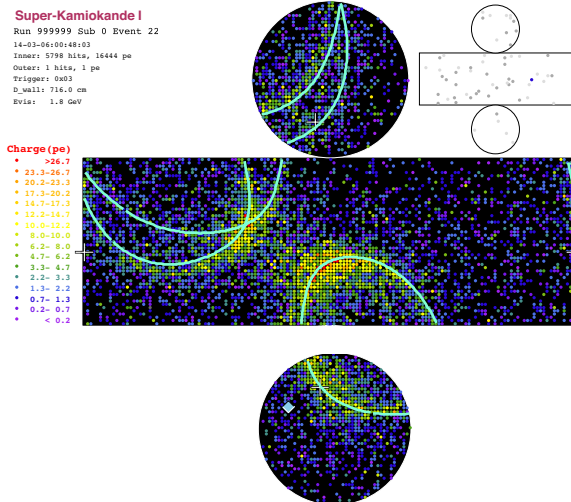


Figure 7.20: A $nn \rightarrow \pi^0\pi^0$ MC event. The two overlapping e -like rings on the top left correspond to two γ 's from a π^0 decay, and the other ring also corresponds to a π^0 . The true momentum of the π^0 corresponding to the two-ring fit is 872.7 MeV/c, and the true momentum of the π^0 corresponding to the one-ring fit is 936.7 MeV/c. The total reconstructed momentum of this event is 219 MeV/c, and the reconstructed invariant mass is 1793 MeV/c².

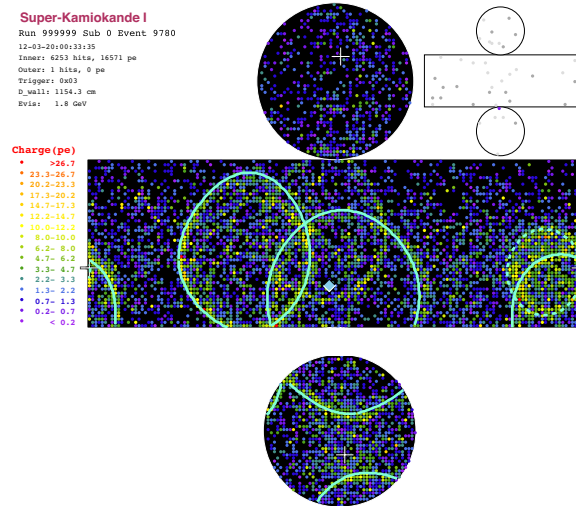


Figure 7.21: Surviving atmospheric neutrino MC event for the $nn \rightarrow \pi^0\pi^0$ search. The interaction is ν_μ neutral current deep-inelastic scattering. In particular, the interaction produced a π^0 and an η meson, from which four γ 's are produced. All but the left-most ring correspond to true photons from the π^0 and η meson. Many additional charged pions are also produced, concentrated near the center of the display, thereby complicating reconstruction. The left-most ring corresponds to a charged pion. There is a ring near the center from multiple, closely overlapping charged pion tracks, which is not found by the reconstruction program. The total reconstructed momentum is 553 MeV/c, and the reconstructed invariant mass is 1763 MeV/ c^2 .

mode	SK-I	SK-II	SK-III	SK-IV
NCDIS	63%	30%	67%	49%
CCDIS	16%	50%	24%	0.0%
CC1 π	21%	20%	9%	51%

Table 7.14: Neutrino interaction mode percentages for the remaining background in the $nn \rightarrow \pi^0\pi^0$ search for SKI-IV.

7.5 Systematic Uncertainties

Systematic uncertainties in each of the $NN \rightarrow \pi\pi$ searches are large, and considerably affect interpretation of the results. Sources of uncertainty can be split into three categories — MC simulation, reconstruction/detection, and BDT-related (for $pp \rightarrow \pi^+\pi^+$ and $pn \rightarrow \pi^+\pi^0$).

7.5.1 Simulation Uncertainties

Signal

The dominant uncertainty for each $NN \rightarrow \pi\pi$ mode comes from the NEUT pion-nucleon interaction model, described in 4.2.4. To estimate the uncertainty, 1σ variations in the form of constant multiplicative coefficients are applied to each interaction cross-section based on fits to pion-nucleon scattering data. There are 24 variations in total, shown in Table 7.15. The same set of variations were used in the T2K ν_e appearance analysis [87]. Separate MC sets were generated for each set of variations, and were processed through each stage of the analysis (nuclear and detector simulation, reduction, reconstruction, and the appropriate $NN \rightarrow \pi\pi$ selection criteria). For $pp \rightarrow \pi^+\pi^+$ and $pn \rightarrow \pi^+\pi^0$, the MC sets were processed with the original trained BDT. The systematic uncertainty was conservatively taken to be the largest percent change in signal efficiency from all variations. Due to the high initial momentum of the pions in $NN \rightarrow \pi\pi$, the high-energy variations produced the largest change in efficiency. Figure 7.22 shows a comparison of a standard analysis distribution with its FSI-varied counterpart.

Other intranuclear uncertainties are also significant. The uncertainty in Fermi momentum is considered from a difference in Fermi momentum models, in particular the spectral functions used in the $NN \rightarrow \pi\pi$ and $n \rightarrow \bar{n}$ simulation (Figure 5.1), and the Fermi gas model used for the atm.- ν simulation. Another major source of uncertainty comes from correlated decay, described in Section 5.1. Due to the poor understanding of correlated decay, it is assigned a 100% uncertainty. However, it only affects 10% of all simulated events. For both Fermi motion and correlated decay, a re-weighting method is used to estimate the total uncertainty, as opposed to propagating the uncertainties through each stage of the analysis as for the pion-

nucleon uncertainties.

Variation type	QE	QEH	INEL	ABS	CX	CXH
Default	1.0	1.8	1.0	1.1	1.0	1.8
Low Energy	0.6	1.8	1.0	0.7	0.5	1.8
	0.6	1.8	1.0	0.7	1.6	1.8
	0.7	1.8	1.0	1.6	0.4	1.8
	0.7	1.8	1.0	1.6	1.6	1.8
	1.4	1.8	1.0	0.6	0.6	1.8
	1.3	1.8	1.0	0.7	1.6	1.8
	1.5	1.8	1.0	1.5	0.4	1.8
	1.6	1.8	1.0	1.6	1.6	1.8
Increased Hadron Production	0.6	1.1	1.5	0.7	0.5	2.3
	0.6	1.1	1.5	0.7	1.6	2.3
	0.7	1.1	1.5	1.6	0.4	2.3
	0.7	1.1	1.5	1.6	1.6	2.3
	1.4	1.1	1.5	0.6	0.6	2.3
	1.3	1.1	1.5	0.7	1.6	2.3
	1.5	1.1	1.5	1.5	0.4	2.3
	1.6	1.1	1.5	1.6	1.6	2.3
Decreased Hadron Production	0.6	2.3	0.5	0.7	0.5	1.3
	0.6	2.3	0.5	0.7	1.6	1.3
	0.7	2.3	0.5	1.6	0.4	1.3
	0.7	2.3	0.5	1.6	1.6	1.3
	1.4	2.3	0.5	0.6	0.6	1.3
	1.3	2.3	0.5	0.7	1.6	1.3
	1.5	2.3	0.5	1.5	0.4	1.3
	1.6	2.3	0.5	1.6	1.6	1.3

Table 7.15: Variations used to estimate systematic uncertainties from ion interactions for $NN \rightarrow \pi\pi$. The coefficients correspond to quasielastic scattering (QE), inelastic scattering including hadron production (INEL), absorption (ABS), and charge exchange (CX). Both QE and CX are considered in low- and high-energy contexts, with an “H” added for the latter. Because hadron production is only considered for high momenta ($p_\pi > 500$ MeV/c), variations that change hadron production are considered high-energy variations, which are of the most relevance for $NN \rightarrow \pi\pi$.

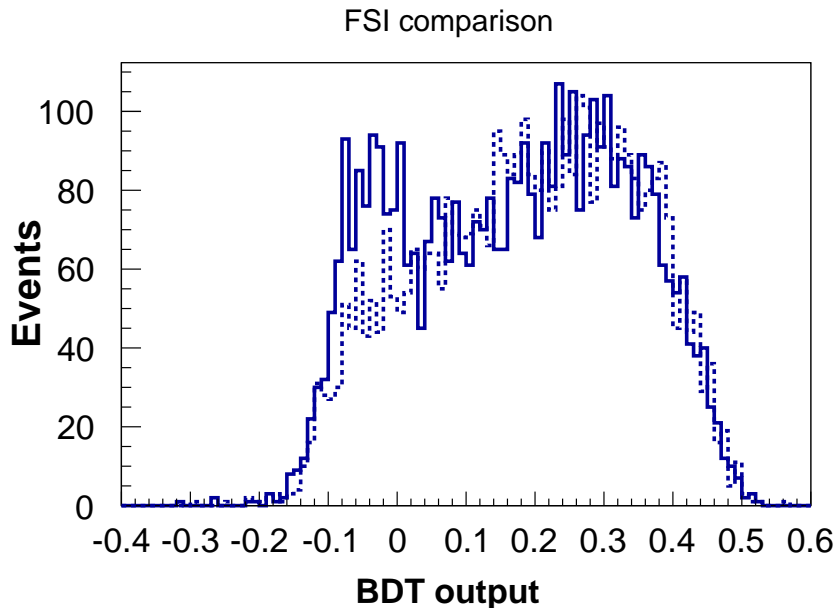


Figure 7.22: The BDT output for $pn \rightarrow \pi^+\pi^0$ signal, for standard (solid histogram) and FSI-varied MC (dashed histogram). The varied MC output is from the decreased hadron production set of variations. This decrease in hadron production leads to a clearer signal.

Background

Neutrino interaction uncertainties are significant for the interaction modes that survive the $NN \rightarrow \pi\pi$ analysis selection. In particular, single pion production uncertainties are large. A list of the main interaction uncertainties in this analysis are shown in Table 7.16.

Source	Uncertainty
Single pion π^0/π^\pm ratio	40%
Single meson total cross-section	20%
Axial mass in single pion production, CCQE	10%

Table 7.16: Dominant interaction uncertainties that contribute to the overall atm.- ν uncertainty for the $NN \rightarrow \pi\pi$ searches.

Other simulation uncertainties come from the overall neutrino flux, and the same

pion interaction uncertainties considered for the $NN \rightarrow \pi\pi$ signal. For the flux, the largest uncertainty comes from the absolute flux normalization in the energy range $1 \text{ GeV} < E_\nu < 10 \text{ GeV}$, which is 7%.

7.5.2 Reconstruction and BDT uncertainties

Reconstruction uncertainties are common to both signal and background. The main sources in these searches come from ring separation and PID, energy scale, and ring angular resolution.

For ring separation and PID systematics, results from a recent SK atmospheric neutrino oscillation analysis in [61] are used, in which the uncertainties are classified by event topology (single or multi-ring), leading ring PID, and visible energy. The final event samples in each $NN \rightarrow \pi\pi$ search are then re-weighted by the associated uncertainties. For $pp \rightarrow \pi^+\pi^+$, the sample is μ -like by definition, mostly in the sub-GeV ($E_{\text{vis}} < 1330 \text{ MeV}$) energy range. For $nn \rightarrow \pi^0\pi^0$, it is e -like by definition, in the multi-GeV ($E_{\text{vis}} > 1330 \text{ MeV}$) range. For $pn \rightarrow \pi^+\pi^0$, the sample is mostly e -like multi-GeV. The corresponding uncertainties for these samples are shown in Table 7.17.

Uncertainty	SK-I	SK-II	SK-III	SK-IV
Ring Separation, sub-GeV μ -like	4.5%	8.2%	2.6%	2.3%
Ring PID, sub-GeV μ -like	3.9%	2.2%	3.1%	2.2%
Ring Separation, multi-GeV e -like	3.1%	1.9%	1.1%	0.9%
Ring PID, multi-GeV e -like	1.7%	1.8%	2.5%	3.4%

Table 7.17: Ring separation and PID errors, from the analysis in [61], for relevant samples in the $NN \rightarrow \pi\pi$ analyses. All samples are multi-ring.

The energy-scale uncertainty is common to all energy-dependent variables. It is estimated from the calibration procedures described in Section 3.7.4. Table 7.18

shows the absolute energy scale uncertainty for each SK period. To estimate the uncertainty, each energy-dependent variable was varied by the appropriate energy scale error (both increased and decreased), and propagated through the analysis. For $pp \rightarrow \pi^+\pi^+$ and $pn \rightarrow \pi^+\pi^0$, this meant being processed by the original, unvaried BDT, while for $nn \rightarrow \pi^0\pi^0$ it simply meant putting events with varied total momentum and invariant mass through the same set of selection cuts.

SK-I	SK-II	SK-III	SK-IV
1.1%	1.7%	2.7%	2.3%

Table 7.18: Values for the absolute energy scale uncertainty in each SK period.

The energy scale uncertainty was estimated differently for signal and background. For signal, the uncertainty was just taken to be the percentage change in efficiency between the varied and unvaried MC. For background, and particularly the $nn \rightarrow \pi^0\pi^0$ search, this same method led to large fluctuations, due to low statistics after all selection cuts. To ensure that the uncertainty was not overestimated, a function was fit in the cut region. The uncertainty was then estimated by finding the difference in the integral of the function by shifting the cut value(s), or integration limit(s), by the energy scale uncertainty. An example of this procedure is shown in Figure 7.23.

The ring angular resolution was taken into account for the $pp \rightarrow \pi^+\pi^+$ and $pn \rightarrow \pi^+\pi^0$ searches, as the angle between pion candidates was crucial both in the pre-selection stage and the BDT stage. However, the angular resolution for rings from $pp \rightarrow \pi^+\pi^+$ and $pn \rightarrow \pi^+\pi^0$ simulation is quite good, and so varying the angle between pion candidates produced only a very small uncertainty.

Finally, a systematic uncertainty for the BDT was estimated for the $pp \rightarrow \pi^+\pi^+$ and $pn \rightarrow \pi^+\pi^0$ searches. This was done by assessing the difference in the BDT output distributions for the test sample and the final analysis sample (Table 7.2).

This uncertainty is essentially a measure of the amount of overtraining in the BDTs.

Tables 7.19, 7.20, and 7.21 show the systematic uncertainty contributions from each source described above, as well as the total uncertainty.

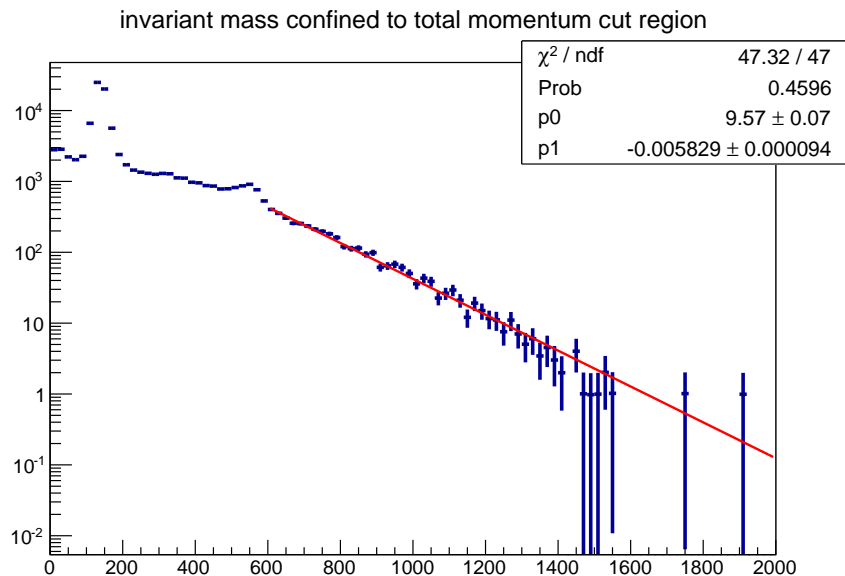


Figure 7.23: The invariant mass distribution of the $nn \rightarrow \pi^0\pi^0$ atm.- ν background in SK-IV, after selections (C1)-(C4), with a function of the form $\exp(p_0 + p_1x)$ fit to the region $600 \text{ MeV}/c^2 < M_{\text{inv}} < 2000 \text{ MeV}/c^2$. The uncertainty was estimated by integrating the function between the invariant mass cut values, and finding the difference in the integral when the cut values were shifted. A similar procedure was done for the total momentum, and the larger value was taken for the uncertainty.

	SK-I	SK-II	SK-III	SK-IV
Signal				
<u>Simulation</u>				
Pion FSI	26.9%	27.9%	25.1%	30.5%
Fermi motion	20.4%	18.8%	20.2%	21.5%
Correlated decay	9.9%	10.0%	9.4%	9.4%
<u>Reconstruction</u>				
Ring separation	4.5%	8.1%	2.6%	2.1%
Ring PID	3.9%	2.1%	3.1%	2.4%
Energy scale	<1%	1.0%	1.3%	<1%
Ring angle	<1%	2.0%	<1%	<1%
<u>BDT</u>	3.6%	2.2%	4.4%	2.0%
Total	35.9%	36.2%	34.1%	38.7%
Background				
<u>Simulation</u>				
Neutrino interaction	22.9%	22.9%	27.1%	19.7%
Pion FSI	16.4%	16.5%	22.2%	16.2%
Neutrino flux	7.3%	7.3%	7.3%	7.2%
<u>Reconstruction</u>				
Ring separation	4.5%	7.9%	2.6%	2.2%
Ring PID	3.9%	1.9%	3.2%	2.3%
Energy scale	1.2%	1.3%	2.4%	2.4%
Ring angle	<1%	<1%	<1%	<1%
<u>BDT</u>	6.8%	1.0%	4.3%	1.4%
Total	30.5%	30.3%	36.4%	26.8%

Table 7.19: Systematic uncertainties in the $pp \rightarrow \pi^+\pi^+$ search.

	SK-I	SK-II	SK-III	SK-IV
Signal				
<u>Simulation</u>				
Pion FSI	26.8%	24.6%	24.5%	28.7%
Fermi motion	17.2%	18.4%	10.9%	17.2%
Correlated decay	9.6%	9.6%	9.5%	10.1%
<u>Reconstruction</u>				
Ring separation	1.7%	<1%	<1%	<1%
Ring PID	<1%	<1%	1.6%	2.3%
Energy scale	2.5%	1.7%	4.9%	4.7%
Ring angle	1.3%	<1%	2.1%	1.9%
<u>BDT</u>	<1%	1.6%	<1%	<1%
Total	33.4%	32.3%	28.9%	35.3%
Background				
<u>Simulation</u>				
Neutrino interaction	18.2%	14.0%	20.1%	20.9%
Pion FSI	10.2%	12.2%	11.0%	13.7%
Neutrino flux	7.3%	7.2%	7.2%	7.2%
<u>Reconstruction</u>				
Ring separation	1.8%	<1%	<1%	<1%
Ring PID	<1%	<1%	<1%	2.0%
Energy scale	<1%	1.8%	3.3%	3.2%
Ring angle	<1%	<1%	<1%	<1%
<u>BDT</u>	6.3%	7.4%	10.3%	11.3%
Total	23.1%	21.3%	26.3%	28.6%

Table 7.20: Systematic uncertainties in the $pn \rightarrow \pi^+\pi^0$ search.

	SK-I	SK-II	SK-III	SK-IV
Signal				
<u>Simulation</u>				
Pion FSI	22.2%	26.8%	30.1%	24.9%
Fermi motion	19.6%	19.3%	19.8%	19.6%
Correlated decay	9.6%	9.5%	9.8%	9.6%
<u>Reconstruction</u>				
Ring separation	<1%	<1%	<1%	<1%
Ring PID	<1%	<1%	<1%	<1%
Energy scale	1.5%	1.7%	4.0%	3.6%
Total	31.2%	34.4%	37.6%	33.3%
Background				
<u>Simulation</u>				
Neutrino interaction	7.3%	10.9%	6.0%	9.1%
Pion FSI	8.9%	8.2%	11.0%	7.7%
Neutrino flux	7.3%	7.3%	7.3%	7.2%
<u>Reconstruction</u>				
Ring separation	<1%	<1%	<1%	<1%
Ring PID	<1%	<1%	<1%	<1%
Energy scale	10.9%	18.1%	28.9%	24.3%
Total	17.5%	24.0%	32.3%	28.0%

Table 7.21: Systematic uncertainties in the $nn \rightarrow \pi^0\pi^0$ search. Note that the energy scale uncertainty is dominant for the background, unlike other searches in which the simulation uncertainties are dominant.

Chapter 8

Neutron-Antineutron Oscillation Search

The search for $n \rightarrow \bar{n}$ follows much of the same pattern as the $NN \rightarrow \pi\pi$ searches. In particular, similar to $pp \rightarrow \pi^+\pi^+$ and $pn \rightarrow \pi^+\pi^0$, a multivariate analysis is used, with a boosted decision tree (BDT). Like $NN \rightarrow \pi\pi$, the final-state particles of $n \rightarrow \bar{n}$ are mostly pions, and the interactions of charged pions in particular can distort the event signature. Unlike $NN \rightarrow \pi\pi$, in which two relatively back-to-back pions were sought, there is no particular desired event topology in $n \rightarrow \bar{n}$, due to the many non-negligible final states.

8.1 Pre-selection

A set of selection criteria is first applied. The requirements are more lax than the $NN \rightarrow \pi\pi$ searches, and have no PID or topology requirements.

(D1) There is more than one Cherenkov ring;

(D2) The visible energy is between 400 and 1600 MeV;

(D3) The total momentum is less than 500 MeV/c.

Figure 8.1 shows plots of each event sample across selections (D1)-(D3), and Table 8.1 shows the remaining events in each sample following the selections.

For the $n \rightarrow \bar{n}$ search, the atm.- ν background is weighted differently than in the $NN \rightarrow \pi\pi$ search. The $NN \rightarrow \pi\pi$ search used the two-flavor oscillation probability, plus small correction factors from the Honda flux, as described by Equation 4.1 and Section 4.1. For $n \rightarrow \bar{n}$, a more accurate background weight estimation is used that takes into account the full three-flavor oscillation analysis in [86] — namely, it uses the fitted “pulls” from all the systematic error sources in the oscillation analysis. This new weighting procedure tends to increase the normalization (Figure 8.2).

8.2 Multivariate analysis

Ten variables are used for the $n \rightarrow \bar{n}$ multivariate analysis. Some have been described in the $NN \rightarrow \pi\pi$ analyses, while others are new to this analysis. Table 8.2 shows their relative importance in the BDT training. A larger set of variables was considered initially. Variables were removed on the basis of high correlation with other variables, and their relative importance. For instance, the total visible energy is highly correlated with the invariant mass. Because the invariant mass was a higher-ranked variable, the visible energy was removed.

Figures 8.3-8.4 show plots of each of the variables in SK-IV; analogous plots for SK-I/II/III can be found in Appendix B. For the BDT, the same set of parameters shown in Tables 7.1 and 7.2 are used. The gradient boost method [88] was chosen, as the $n \rightarrow \bar{n}$ signal is much more difficult to separate from the atm.- ν background than in any of the $NN \rightarrow \pi\pi$ analyses (detailed further below).

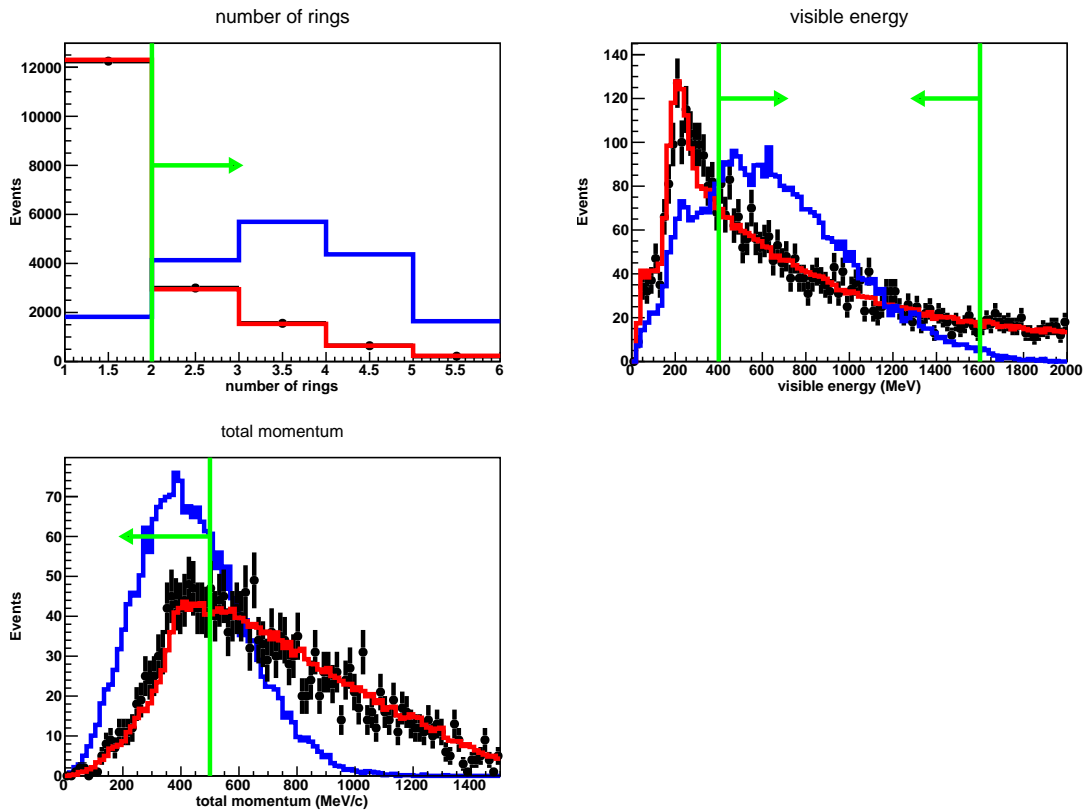


Figure 8.1: Selection criteria (D1)-(D3) for $n \rightarrow \bar{n}$ MC (blue histogram), atm.- ν background (red histogram), and data (crosses) in SK-IV. All plots are area-normalized to the data. The green line indicates the placement of the cuts described in the text.

8.2.1 Standard variables

The following variables are derived from the standard reconstruction algorithms described in Section 6.2:

- The total momentum, already required to be less than 500 MeV/c by selection (D3). This peaks at a higher value for the background than the signal;
- The invariant mass, which has a sharp peak at the π^0 mass for background and is more spread out for signal;

	SK-I	SK-II	SK-III	SK-IV
FCFV				
Eff. (%)	92.0	95.3	91.7	92.2
Bkg.	11889	6415	4206	17411
Data	12299	6610	4355	17664
(D1)				
Eff. (%)	82.6	84.2	82.2	82.7
Bkg.	3595	1944	1266	5283
Data	3691	2056	1292	5415
(D2)				
Eff. (%)	61.6	62.1	60.6	61.7
Bkg.	1456	784	516	2117
Data	1444	813	513	2145
(D3)				
Eff. (%)	39.6	39.7	39.1	40.5
Bkg.	446	238	159	660
Data	343	252	139	706

Table 8.1: Efficiency, expected background, and data events after each precut for the $n \rightarrow \bar{n}$ search. The FCFV cut is described in Section 6.1.6, and cuts (D1)-(D3) are described in the text. Expected background is weighted by oscillation factors determined from the analysis in [86], and scaled to the appropriate SK detector livetime (from the 200 year analysis sample).

- $(E_{\text{tot}} - E_{\text{primary}})/E_{\text{tot}}$, where E_{tot} is the total energy and E_{primary} the energy of the primary ring in the event. This peaks in a higher value for the signal than the background, since the energy is more evenly distributed among rings, while the background (especially for a CC interaction) will typically have more energy contained in a single ring;
- The PID likelihood difference of the first ring. The leading ring likelihood is slightly higher in the background (meaning the background is slightly more likely to be μ -like);

Background weight

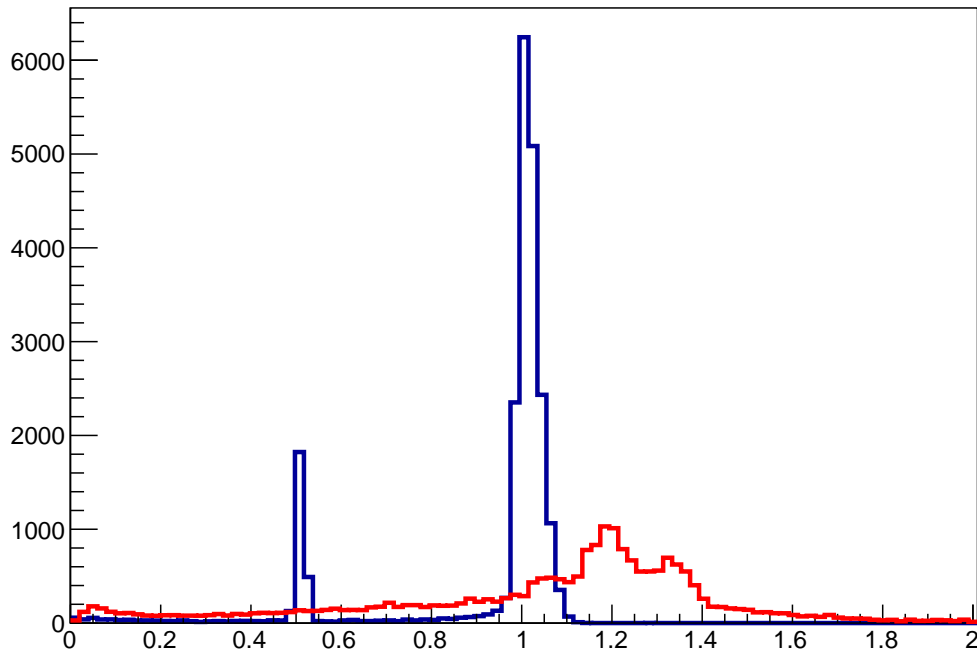


Figure 8.2: A comparison of the atm.- ν weight using two-flavor oscillation and small corrections from the flux in [53] (blue curve), and the atm.- ν weight using the full oscillation analysis in [86] (red curve), for all atm.- ν events passing the selection pre-cuts (D1)-(D3).

- The number of decay electrons. Typically non-zero in the signal due to the presence of charged pions, with a falling spectrum for the background;
- The maximum distance between a decay electron vertex and the primary event vertex, expected to be longer in the background particularly if it's a CC interaction with an energetic muon.

8.2.2 Non-standard variables

The standard ring-counting algorithm is limited with respect to the $n \rightarrow \bar{n}$ search. In particular, it has a maximum of five rings. It is often the case that there are more

than five visible particles in the final state of a $n \rightarrow \bar{n}$ interaction. Instead of trying to pick out individual particles, it is useful to extract variables from the detector-wide charge pattern, which are relatively independent of variables that rely on the standard ring-counting algorithm.

Sphericity

As its name implies, the sphericity S is a measure of how spherical an event is. It is commonly used to characterize hadronic jets in accelerator experiments. A perfectly isotropic event will have $S = 1$, while a perfectly one-directional event will have $S = 0$. An ideal $n \rightarrow \bar{n}$ event is isotropic, and while this is often not the case due to nuclear effects, it is still more isotropic than a typical atm.- ν event. The sphericity is defined in terms of the sphericity tensor, defined as:

$$S^{ab} = \frac{\sum_i p_i^a p_i^b}{\sum_i p_i^2}. \quad (8.1)$$

Here the sum is over bins in Hough space (the same space in which Cherenkov rings are found), p_i is the momentum in bin i , and $a, b = 1, 2, 3$ are the three cartesian directions. For our purposes, the “momentum” is actually just the charge, corrected for light attenuation and PMT angular acceptance. The sphericity is then defined in terms of the three eigenvalues of this tensor, $\lambda_1 \geq \lambda_2 \geq \lambda_3$:

$$S = \frac{3}{2}(\lambda_2 + \lambda_3). \quad (8.2)$$

The corresponding eigenvector for λ_1 spans the *event axis*, while those of λ_1 and λ_2 span the *event plane*. Another variable, aplanarity, defined as $A = \frac{3}{2}\lambda_3$, can also be defined from the sphericity tensor, although this is highly correlated with sphericity and is not used in the analysis.

Potential rings

While the ring-counting algorithm saturates at five rings, bins in Hough space that exceed a certain charge threshold are considered as *potential* rings, or “seeds.” This variable has no upper limit, and thus is sensitive to charge deposited by particles not found via normal ring-counting. An $n \rightarrow \bar{n}$ event typically has more seeds than atm.- ν background.

Fox-Wolfram moments

Fox-Wolfram moments are another set of variables used in accelerator physics that measure correlations between particle momenta. The ℓ^{th} Fox-Wolfram moment is defined as:

$$H_\ell = \sum_i \sum_j \frac{|\vec{p}_i||\vec{p}_j|}{E_{\text{vis}}^2} P_\ell(\cos\theta_{ij}). \quad (8.3)$$

Here \vec{p} are the momenta, E_{vis} is the visible energy, P_ℓ is the ℓ^{th} Legendre polynomial, and θ_{ij} is the angle between particle i and j . The sum is taken over potential rings, described above¹. As with sphericity, the momentum is the corrected charge in a given bin. The visible energy is the sum of all corrected charges. For $n \rightarrow \bar{n}$, H_1 and H_2 are used.

8.3 Final selection

The final selection on the BDT output for the $n \rightarrow \bar{n}$ search differs from the criteria used for the $NN \rightarrow \pi\pi$ searches. For the latter, background was minimized without regard for systematic uncertainties. For $n \rightarrow \bar{n}$, the background rate is high

¹In principle this calculation could be taken over all bins in Hough space, but it is computationally laborious and provides no additional discriminatory power between signal and background.

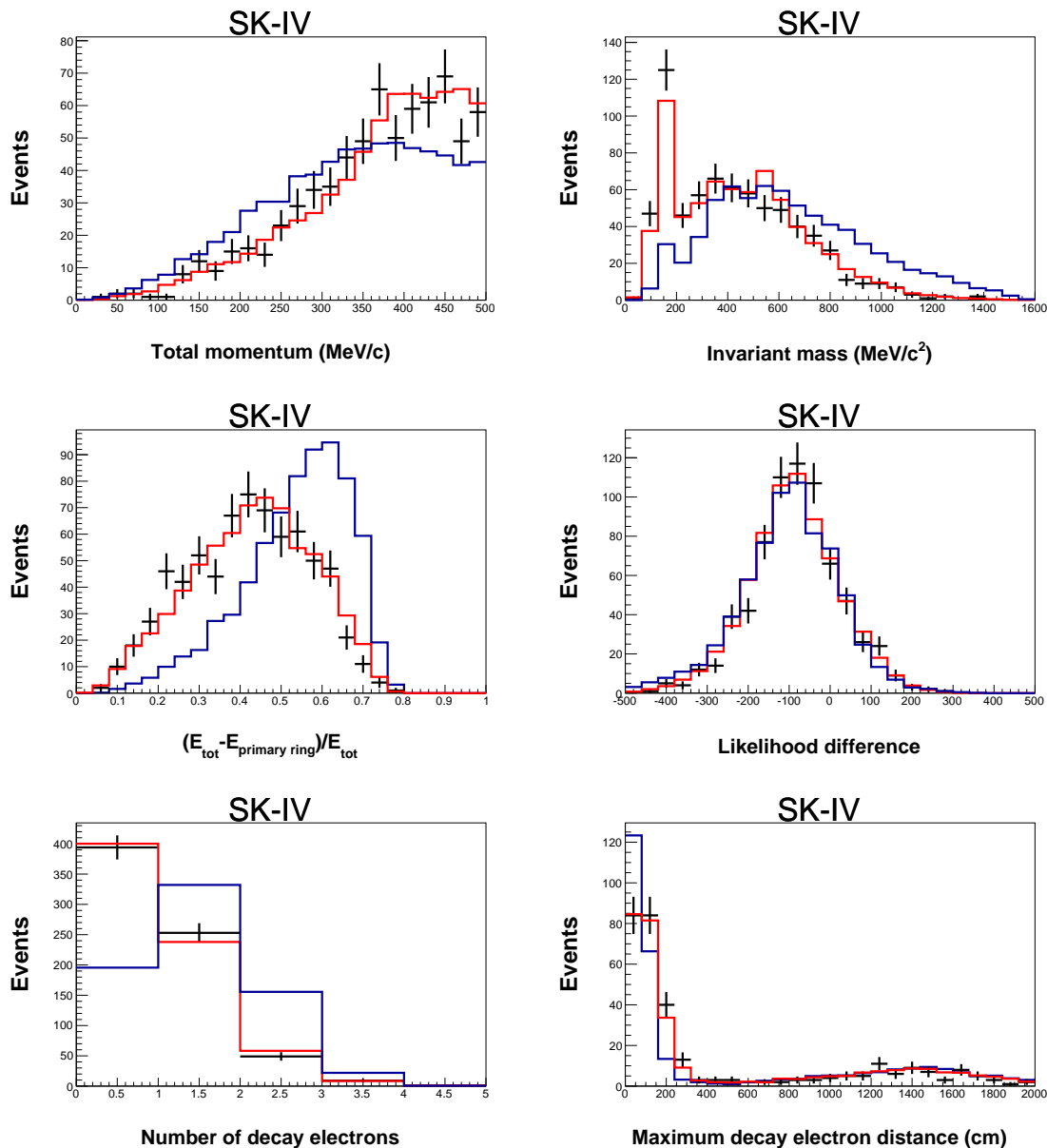


Figure 8.3: The total momentum (top left), invariant mass (top right), $(E_{\text{tot}} - E_{\text{primary}})/E_{\text{tot}}$ (middle left), PID likelihood difference of the leading ring (middle right), number of decay electrons (bottom left), and maximum distance between the primary vertex and a decay electron vertex (bottom right) for the $n \rightarrow \bar{n}$ search in SK-IV, for signal MC (solid histogram), atm.- ν MC (dashed histogram), and data (crosses). Distributions are normalized to the number of events in the data. Details of each variable are described in the text.

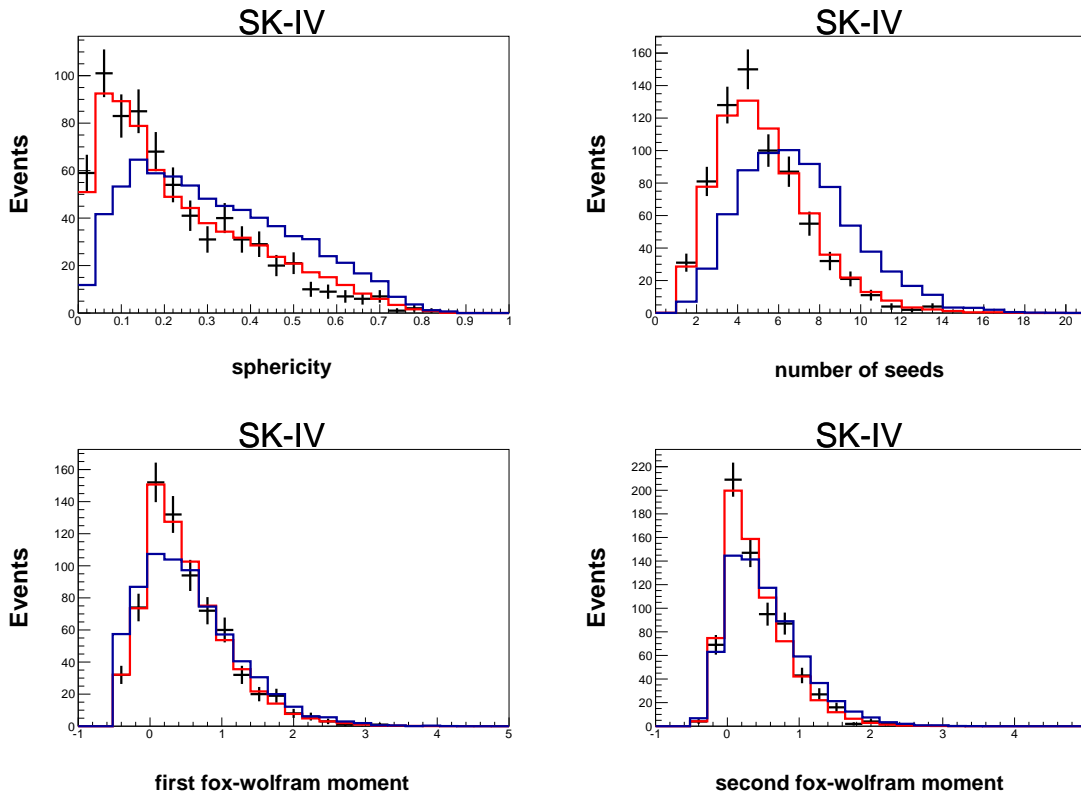


Figure 8.4: The sphericity (top left), number of potential rings (top right), first Fox-Wolfram moment (bottom left), and second Fox-Wolfram moment (bottom right) for the $n \rightarrow \bar{n}$ search in SK-IV, for signal MC (solid histogram), atm.- ν MC (dashed histogram), and data (crosses). Distributions are normalized to the number of events in the data. Details of each variable are described in the text.

for virtually all cut values. Figure 8.5 shows the BDT output and the remaining efficiency and scaled background as a function of BDT cut. Ideally, of course, the background rate is as close to zero as possible, such that the observation of even a single signal candidate event would be interesting. In the case of the $n \rightarrow \bar{n}$ search, reducing the background rate to <1 expected event would require a cut on the BDT output such that the signal efficiency is $<1\%$. This is undesirable, given that there are high uncertainties associated with both signal and background processes.

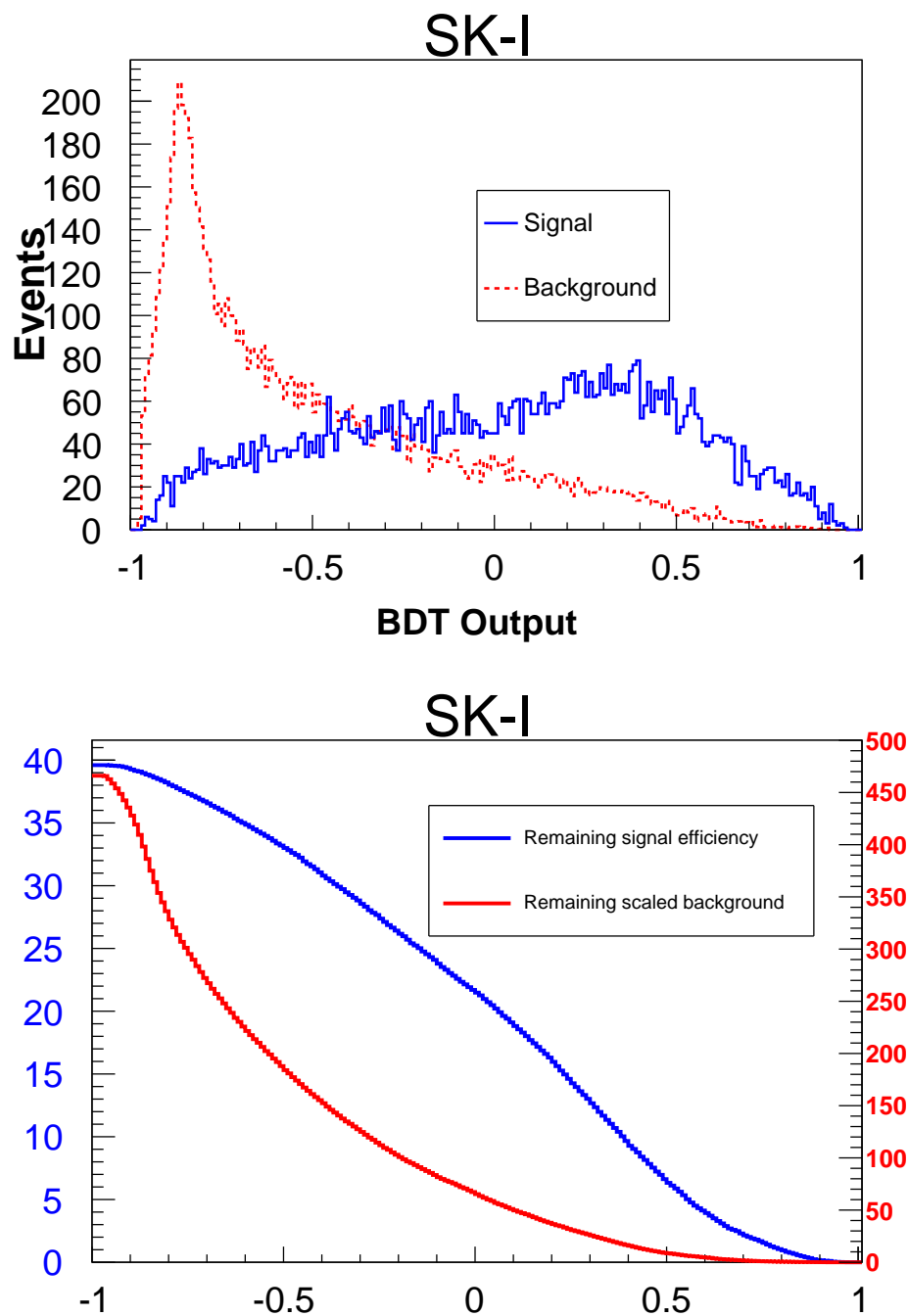


Figure 8.5: BDT output for $n \rightarrow \bar{n}$ signal and atm.- ν background (top), and the remaining signal efficiency and scaled background in SK-I as a function of BDT cut (bottom). The BDT outputs are area-normalized

Variable	Importance
Invariant mass	0.110
First Fox-Wolfram moment	0.109
Total momentum	0.105
Sphericity	0.104
Maximum distance from primary vertex to decay electron vertex	0.103
$(E_{\text{total}} - E_{\text{primary}}) / E_{\text{total}}$	0.102
PID likelihood difference of leading ring	0.099
Second Fox-Wolfram moment	0.090
Number of decay electrons	0.089
Number of potential rings	0.089

Table 8.2: Relative importance of each variable in the $n \rightarrow \bar{n}$ search, averaged across SK periods.

The high expected background for reasonable values of the signal efficiency, and large systematic uncertainties associated with each, suggests that an optimal cut should take more into account more than just the raw signal and background acceptance. One such value is the sensitivity, defined as

$$S = \sum_{n_{\text{cand}}=0}^{\infty} \tau(\epsilon, b, \lambda, n_{\text{cand}}) P(b, n_{\text{cand}}). \quad (8.4)$$

Here τ is the lower lifetime limit in the absence of signal, calculated with a Bayesian method described in Appendix C. It is a function of efficiency ϵ , background b , and exposure λ and their uncertainties, as well as the number of data candidates n_{cand} . The sum is weighted by the Poisson probability $P(b, n_{\text{cand}})$ of observing n_{cand} candidates assuming the background-only hypothesis. Due to the high remaining background of the $n \rightarrow \bar{n}$ search, S is very similar to a less cumbersome calculation, which is simply τ evaluated under the assumption that $n_{\text{cand}} = n_{\text{bkg}}$. This is the variable that we maximize with the final cut value.

8.3.1 Systematic uncertainties

Like $NN \rightarrow \pi\pi$, the dominant systematic uncertainties come from MC simulation in both signal and background, with smaller uncertainties associated with reconstruction.

Signal

The signal uncertainty is overwhelmingly due to the pion FSI variations described in Section 7.5.1. Specifically, the second variation from the top in Table 7.15 leads to the largest change in signal efficiency — decreased absorption and decreased QE scattering both contribute to a clearer multi-pion signal. The other main simulation uncertainty, from Fermi motion, is relatively small. Unlike in $NN \rightarrow \pi\pi$, the Fermi motion uncertainty was estimated by generating a separate set of MC using the Fermi gas model, as opposed to the spectral functions (Figure 5.1) used in the standard simulation. The same reconstruction and BDT-related uncertainties described in Section 7.5 are considered.

Background

The background uncertainty is also simulation-dominated. Given that the remaining background is much higher in $n \rightarrow \bar{n}$ than $NN \rightarrow \pi\pi$, it is important to treat background uncertainty carefully.

Neutrino interaction uncertainties depend on the value of the final cut. The tail region is dominated by both CC and NC DIS uncertainties (Figure 8.6). For the initial neutrino energy region relevant for this analysis ($E_\nu < 10$ GeV), there are large energy-dependent uncertainties associated with the DIS cross-section (Table 8.3).

Remaining sources of systematic uncertainty from pion interaction, oscillation,

reconstruction, and BDT performance are estimated in the same way as the $NN \rightarrow \pi\pi$ search.

Atm-nu MC BDT output

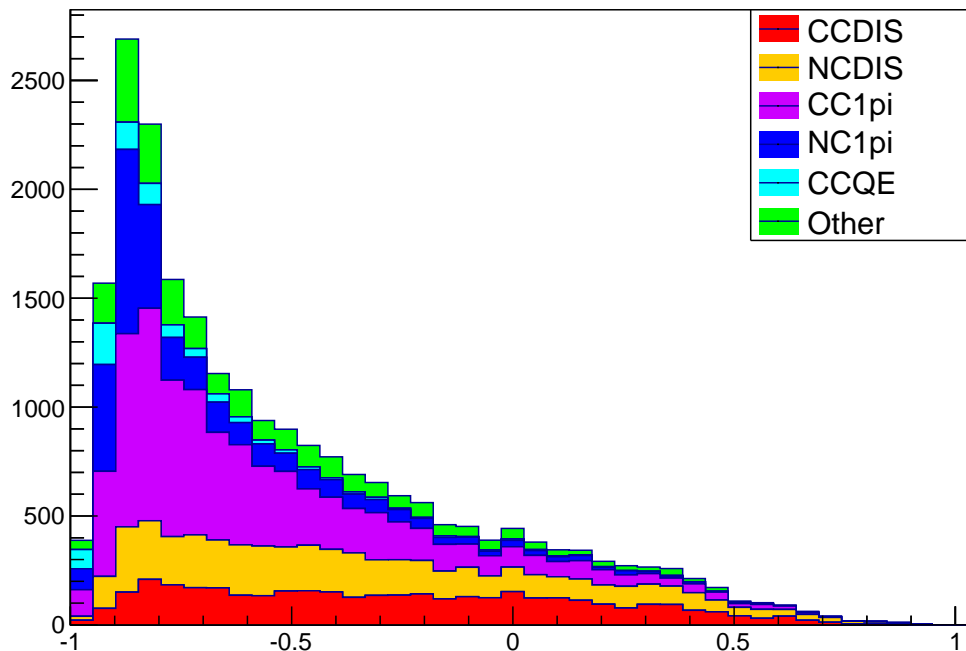


Figure 8.6: atm.- ν BDT output for SK-I MC, categorized by neutrino interaction mode.

Energy	0-2 GeV	2-3 GeV	3-5 GeV	5-10 GeV
ν	30%	50%	10%	40%
anti- ν	5%	20%	5%	10%

Table 8.3: Values for the DIS interaction uncertainty for $E_\nu < 10$ GeV.

8.3.2 Final cut

Figure 8.7 shows the value of $\tau(n_{cand} = n_{bkg})$ as a function of BDT cut. Since there is only a single value of $\tau(n_{cand} = n_{bkg})$ calculated across all SK periods (see

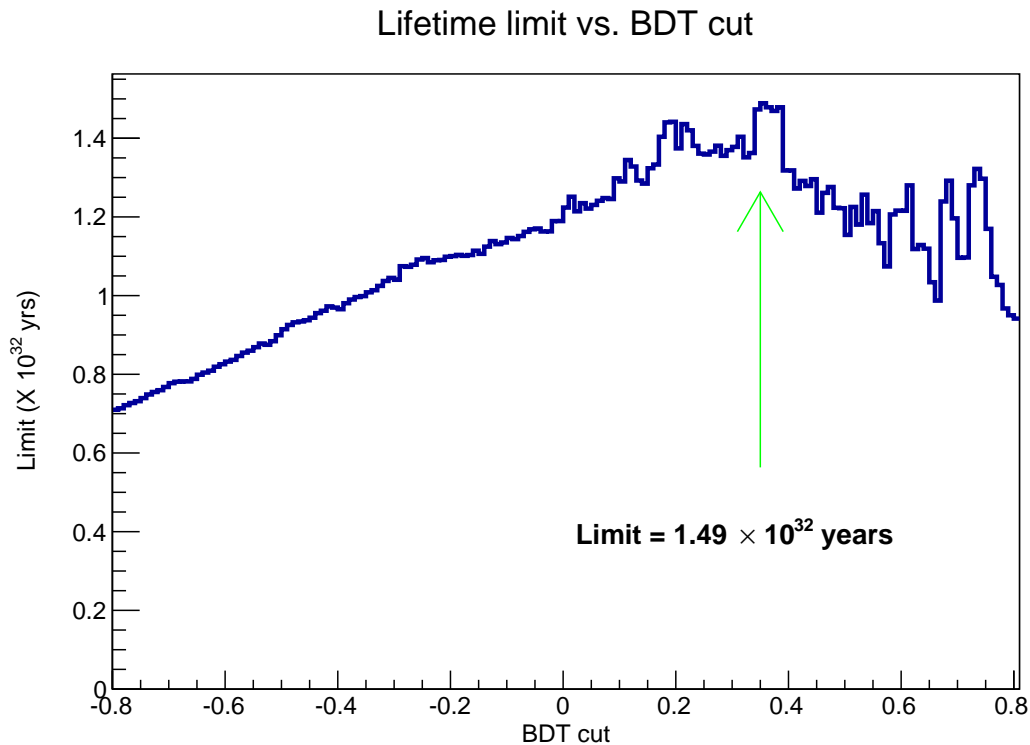


Figure 8.7: Lifetime limit vs. BDT cut assuming the number of candidates is equal to the number of background events. The value is maximized for a cut of 0.35.

Appendix C), the same cut value is used for each. Figure 8.8 shows the BDT output for all SK periods. Table 8.4 shows the final efficiencies, background rates, and data candidates. Table 8.5 shows the interaction modes of the remaining background, and Table 8.6 shows the systematic uncertainties for both $n \rightarrow \bar{n}$ signal and atm.- ν background. There is no excess of events in the data relative to the expected background, and thus there is no evidence for $n \rightarrow \bar{n}$ oscillation.

8.3.3 Data discrepancy

While the data is consistent with the atm.- ν background in terms of shape, there is a significant deficit in the number of data events relative to expected background at

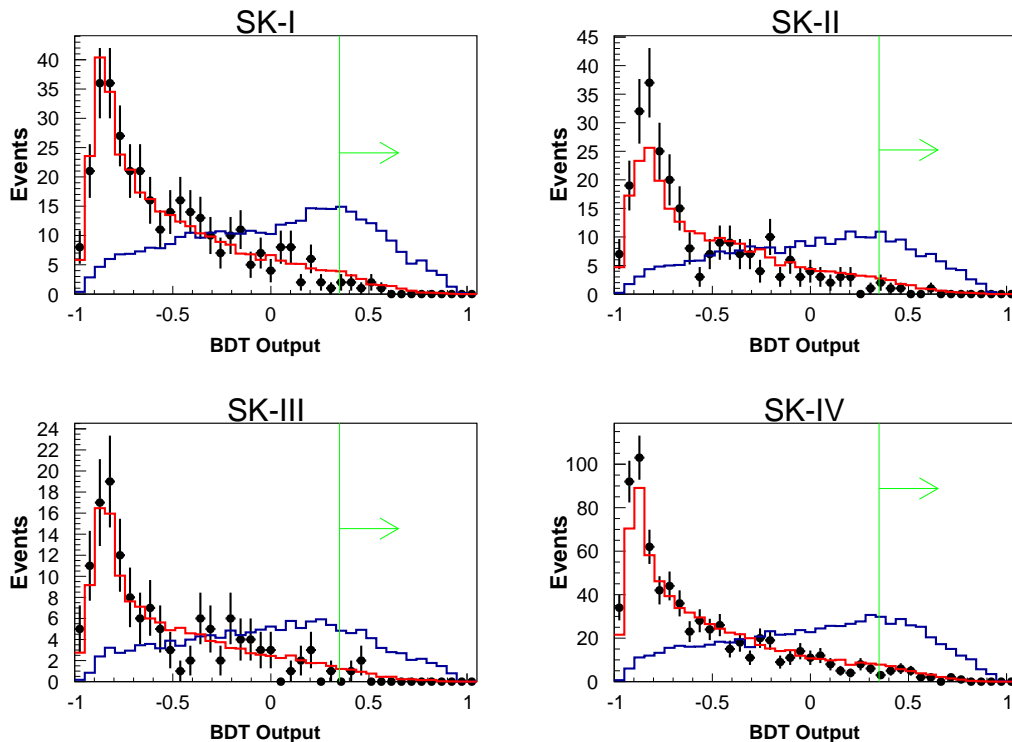


Figure 8.8: BDT output for $n \rightarrow \bar{n}$ signal (blue), atm.- ν background (red), and data (crosses). All histograms are normalized to the number of data entries. The vertical green line indicates the BDT cut value, and the arrow indicates that only events to the right of the cut are kept.

	SK-I	SK-II	SK-III	SK-IV
Eff. (%)	11.0	10.5	9.5	12.0
Bkg. (MT-yr)	223	217	204	254
Bkg. (SK live.)	20.5	10.7	6.5	33.9
Candidates	6	5	3	26

Table 8.4: Efficiency, expected background events, and candidate data events for the SK-IV $n \rightarrow \bar{n}$ search. Background is quoted both for the appropriate SK livetime, and per megaton-year.

the cut value for the first three SK periods, most seriously in SK-I. This can be seen in Table 8.4 and Figure 8.9. The sources of these discrepancy are detector-dependent. The better overall performance of SK-IV can be explained by a better data-MC

mode	SK-I	SK-II	SK-III	SK-IV
NCDIS	37%	39%	35%	38%
CCDIS	35%	38%	40%	38%
CC1 π	17%	15%	17%	14%
NC1 π	3%	3%	3%	3%
CCQE	<1%	<1%	1%	<1%

Table 8.5: Atmospheric neutrino interaction modes in the remaining background for the $n \rightarrow \bar{n}$ search by percentage, as estimated by atmospheric neutrino MC.

agreement in the multivariate input variables, evident from basic comparisons such as the mean difference between data and MC distributions (Table 8.7) and a χ^2 test statistic (Table 8.8).

One source of discrepancy comes from the pre-cut on total momentum. Particularly for SK-I, this cut leads to a large discrepancy between data and atm.- ν MC. This can be seen in Table 8.1, as well as Figure 8.9, in which the data is outside the one-sigma systematic uncertainty for all cut values. In SK-I, shifting the momentum of the background distribution by the difference of the mean with the data prior to applying selection (D3) is sufficient to explain the discrepancy. Figure 8.10 shows the SK-I total momentum distribution after selections (D1) and (D2), with and without this shift applied. Figure 8.11 shows the remaining events in SK-I as a function of BDT cut, analogous to Figure 8.9, but with the shift applied. The number of events is consistent between data and atm.- ν MC at the cut value.

An additional uncertainty is added to account for the total momentum shift. Similar to the energy scale uncertainty described in Section 7.5, both signal and background MC have the data—atm.- ν MC shift applied to the total momentum distributions, and this variation is propagated through the BDT. Table 8.9 shows the shift values, and the resulting uncertainties for signal and background. Predictably, SK-I has the largest associated uncertainty. Ideally, this uncertainty would have been

	SK-I	SK-II	SK-III	SK-IV
Signal				
<u>Simulation</u>				
Pion FSI	33.1%	41.3%	43.9%	45.1%
Fermi motion	4.9%	5.1%	5.0%	5.0%
<u>Reconstruction</u>				
Ring separation	1.0%	1.3%	<1%	<1%
Ring PID	<1%	<1%	<1%	<1%
Energy scale	1.0%	2.1%	1.6%	2.5%
<u>BDT</u>	3.3%	<1%	3.7%	8.7%
Total	33.6%	41.7%	44.4%	46.2%
Background				
<u>Simulation</u>				
Neutrino interaction	23.7%	24.5%	24.9%	25.2%
Pion FSI	18.0%	14.5%	19.4%	17.9%
Neutrino flux	7.2%	7.2%	7.1%	7.2%
<u>Reconstruction</u>				
Ring separation	<1%	1.3%	<1%	<1%
Ring PID	<1%	<1%	<1%	<1%
Energy scale	1.6%	2.9%	3.6%	5.6%
<u>BDT</u>	3.1%	2.4%	3.2%	3.8%
Total	30.8%	29.7%	32.8%	32.5%

Table 8.6: Systematic uncertainties in the $n \rightarrow \bar{n}$ search.

considered in the calculation of the expected lifetime limit (Figure 8.7), but because this uncertainty is associated with a pre-cut, it is relatively independent of the final BDT cut.

The discrepancy in SK-I is clear from the pre-selection stage. As there is no significant difference between data and expected background for SK-II and SK-III after selections (D1)-(D3), the sources of the discrepancies are not immediately clear.

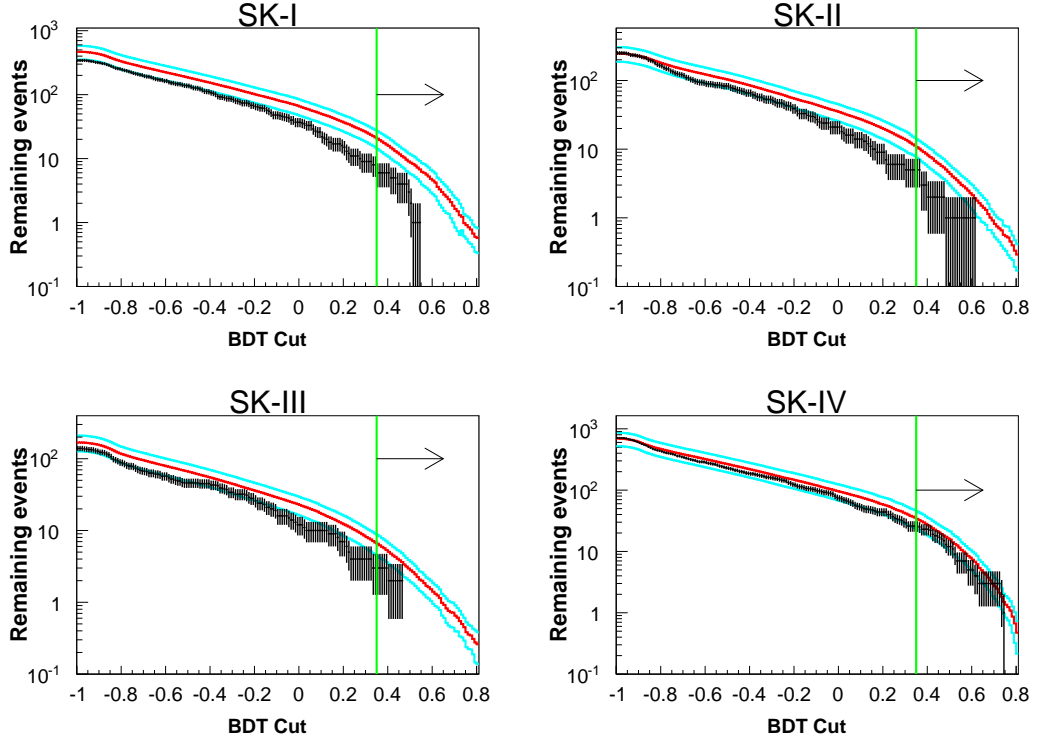


Figure 8.9: Remaining events as a function of the BDT cut, for data (crosses) and atm.- ν MC (red histogram). The atm.- ν MC is normalized by the appropriate livetime. The cyan curves show the one-sigma systematic uncertainties (Table 8.6).

Variable	SK-I	SK-II	SK-III	SK-IV
Total momentum	0.039	0.026	0.005	0.012
Invariant mass	0.054	0.097	0.001	0.062
$(E_{\text{total}} - E_{\text{primary}}) / E_{\text{total}}$	0.006	0.041	0.038	0.044
PID likelihood diff. of leading ring	0.068	0.046	0.11	0.11
Number of decay electrons	0.048	0.10	0.17	0.002
Max. distance from primary vertex to Michel vertex	0.085	0.095	0.20	0.078
Sphericity	0.007	0.075	0.016	0.082
Number of potential rings	0.018	0.11	0.086	0.047
First Fox-Wolfram moment	0.054	0.14	0.13	0.009
Second Fox-Wolfram moment	0.019	0.098	0.078	0.028

Table 8.7: Values of $|(\text{Mean}_{\text{data}} - \text{Mean}_{\text{atm.-}\nu}) / \text{Mean}_{\text{atm.-}\nu}|$ for each variable in the $n \rightarrow \bar{n}$ analysis, following selections (D1)-(D3).

Variable	SK-I	SK-II	SK-III	SK-IV
Total momentum	0.95	0.92	0.97	0.99
Invariant mass	0.95	0.75	1.0	0.96
$(E_{\text{total}} - E_{\text{primary}})/E_{\text{total}}$	0.94	0.98	0.99	0.68
PID likelihood diff. of leading ring	0.92	0.93	0.93	0.92
Number of decay electrons	0.16	0.78	0.59	0.95
Max. distance from primary vertex to Michel vertex	0.86	0.66	1.0	0.99
Sphericity	0.99	0.96	0.99	0.77
Number of potential rings	0.79	0.76	0.70	0.93
First Fox-Wolfram moment	0.96	0.92	0.95	0.99
Second Fox-Wolfram moment	0.86	0.38	0.81	0.92

Table 8.8: Values of the χ^2 test statistic between data and atm.- ν MC, whose value in $[0, 1]$ gives the probability that differences in distributions are due to statistical fluctuations, for each variable in the $n \rightarrow \bar{n}$ analysis, following selections (D1)-(D3).

The sources could come from individual BDT input variables, or parameters that dictate the training and testing of the BDT itself (as listed in Section 7.1). To address the discrepancies, individual SK-II and SK-III variables were removed from the training process, starting with variables that have the largest values in Table 8.7. In addition, the number of trees used in the training process was varied (N_{trees} in Equation 7.1). Increasing the number of trees generally improved data and atm.- ν MC agreement. The resulting data and expected background was then assessed until a sufficient set of adjustments was found, meaning that the data and expected background were consistent at the cut value. Then, as with the total momentum and energy scale errors, additional uncertainties were estimated in both the signal and background due to these adjustments. Table 8.10 summarizes the sources of discrepancy and associated uncertainties in SK-I/II/III.

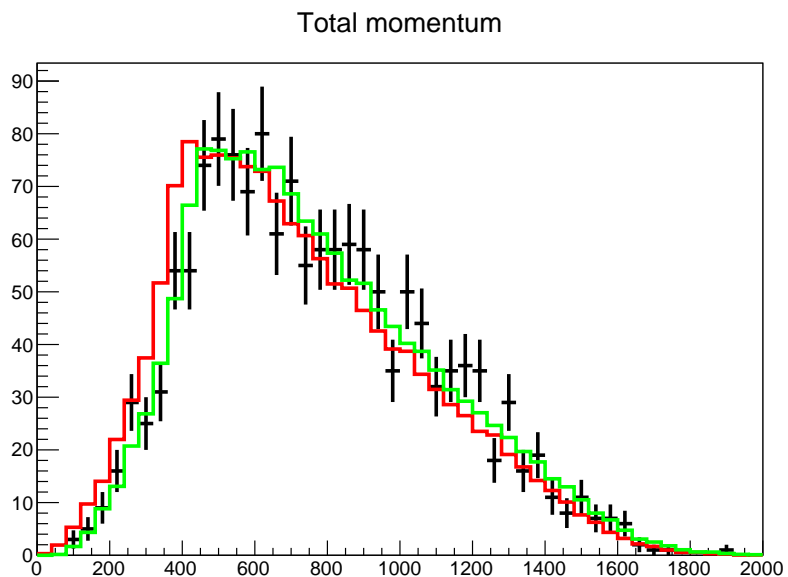


Figure 8.10: Total momentum in SK-I, for data (crosses), atm.- ν MC (red), and atm.- ν MC shifted to match the data (green).

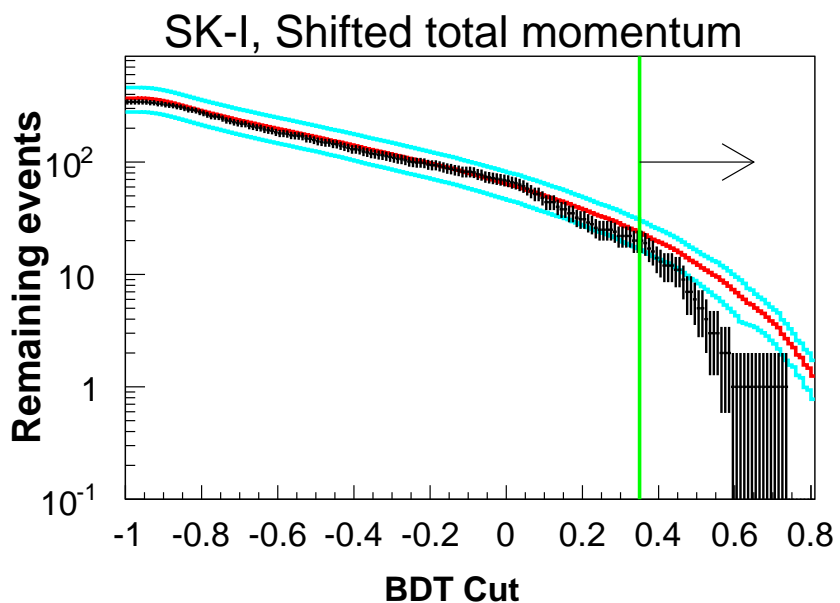


Figure 8.11: Remaining events as a function of the BDT cut, for data (crosses) and atm.- ν MC (red histogram). The atm.- ν MC is normalized by the appropriate livetime. The cyan curves show the one-sigma systematic uncertainties (Table 8.6).

	SK-I	SK-II	SK-III	SK-IV
Shift	48.1 MeV/c	-12.3 MeV/c	28.9 MeV/c	-22.8 MeV/c
σ_{sig}	17.4%	3.8%	9.1%	6.8%
σ_{bkg}	20.2%	7.0%	15.6%	9.5%

Table 8.9: Shift value in data and atm.- ν MC total momentum, and associated signal and background uncertainties in the $n \rightarrow \bar{n}$ search.

	SK-I	SK-II	SK-III
Exp. bkg. (orig.)	20.5 ± 6.3	10.7 ± 3.2	6.5 ± 2.2
Data (orig.)	6	5	3
Adjustment(s)	Shift total momentum	Remove 4 variables, increase N_{trees}	Remove 2 variables, increase N_{trees}
Exp. bkg. (adj.)	23.2 ± 6.7	12.2 ± 3.5	7.1 ± 2.0
Data (adj.)	20	9	7
σ_{sig}	17.4%	22.6%	18.3%
σ_{bkg}	20.2%	13.8%	8.5%

Table 8.10: Summary of the adjustments made in SK-I/II/III to account for the discrepancy seen between data and atm.- ν MC, with original and adjusted efficiency and background rates at the final cut value, and corresponding signal and background uncertainties. The number of variables removed starts from variables with the largest values of the mean difference between data and atm.- ν MC (Table 8.7). Background rates show the nominal values $\pm 1\sigma$ systematic uncertainty, calculated with all the sources in Table 8.6.

Chapter 9

Results and discussion

Searches for dinucleon decay to pions ($NN \rightarrow \pi\pi$) via $pp \rightarrow \pi^+\pi^+$, $pn \rightarrow \pi^+\pi^0$, and $nn \rightarrow \pi^0\pi^0$, and a search for neutron-antineutron oscillation ($n \rightarrow \bar{n}$), have been performed by the Super-Kamiokande detector. A total of 282 (307) kiloton-years of fully-contained data for the $NN \rightarrow \pi\pi$ ($n \rightarrow \bar{n}$) searches was used. No evidence for any of the sought-after processes was found, and the data are consistent with expectations from atmospheric neutrino background. Here I present the main results, and discuss some of the implications of these searches, both for global BNV searches and issues more specific to the analyses.

9.1 Lifetime limits

In the absence of evidence for either $NN \rightarrow \pi\pi$ or $n \rightarrow \bar{n}$, lower limits are set on the time scales for each process. The limits are calculated using a Bayesian method [91], described in detail in Appendix C.

9.1.1 Dinucleon decay

Table 9.1 shows the lower lifetime limits at 90% confidence level for $NN \rightarrow \pi\pi$ from this analysis, compared to the previous results obtained in [39]. The results in this analysis are about two orders of magnitude more stringent than those of [39], reflecting the large exposure of SK. Note also that the results of [39] do not incorporate systematic uncertainties, so that the results of this analysis are more conservative.

Mode	Frejus limit (^{56}Fe)	This analysis (^{16}O)
$pp \rightarrow \pi^+\pi^+$	7.0×10^{29} yrs	7.2×10^{31} yrs
$pn \rightarrow \pi^+\pi^0$	2.0×10^{30} yrs	1.7×10^{32} yrs
$nn \rightarrow \pi^0\pi^0$	3.4×10^{30} yrs	4.0×10^{32} yrs

Table 9.1: Lower lifetimes on $NN \rightarrow \pi\pi$ modes from this analysis, compared to the results of [39].

9.1.2 Neutron-antineutron oscillation

Table 9.2 shows the 90% C.L. lower (bound) neutron oscillation lifetime τ_{90} for this analysis, as well as the previous SK analysis in [23]. In addition, the value of the limit assuming $n_{\text{cand}} = n_{\text{exp. bkg.}}$ is shown. This is similar to the sensitivity for a high-background search like $n \rightarrow \bar{n}$.

SK-I analysis [23]		This analysis	
τ_{90}	$\tau_{90}(n_{\text{cand}} = n_{\text{exp. bkg.}})$	τ_{90}	$\tau_{90}(n_{\text{cand}} = n_{\text{exp. bkg.}})$
1.9×10^{32} yrs	1.9×10^{32} yrs	2.4×10^{32} yrs	1.5×10^{32} yrs

Table 9.2: Bound $n \rightarrow \bar{n}$ limit τ_{90} and $\tau_{90}(n_{\text{cand}} = n_{\text{exp. bkg.}})$ for the SK-I analysis in [23], and this analysis. Note that $\tau_{90}(n_{\text{cand}} = n_{\text{exp. bkg.}})$ for this analysis does not include the additional systematic uncertainties described in Table 8.10, while τ_{90} with the actual number of candidates does.

9.2 Discussion

9.2.1 Global BNV searches

The searches described in this thesis comprise a subset of searches for baryon number violating processes. As with all BNV searches, the results of this thesis are null, but they still represent important advances and updates relative to previous searches.

This thesis described the first search for the processes $pp \rightarrow \pi^+\pi^+$, $pn \rightarrow \pi^+\pi^0$, and $nn \rightarrow \pi^0\pi^0$ in a water Cherenkov detector, and only the second search for these processes ever made. Due mainly to Super-Kamiokande's large nucleon exposure, the null results of this thesis are about two orders of magnitude more stringent than those of [39]. As the world's current largest water Cherenkov detector, Super-Kamiokande is uniquely well-situated to study these decay modes. The mode corresponding to the simplest analysis, $nn \rightarrow \pi^0\pi^0$, also has the most stringent limit, and its potential for discovery or further constraint is the most promising of the three $NN \rightarrow \pi\pi$ modes studied. Further exposure both at SK and the similar but much larger proposed Hyper-Kamiokande detector [92] could provide valuable continuations of these searches.

This thesis described the most recent of several searches for $n \rightarrow \bar{n}$ with bound neutrons (Table 2.1). While this search contains important updates relative to previous searches, such as more data, an improved pion interaction model, and a novel search method, it still illustrates the severe limitations of bound $n \rightarrow \bar{n}$ searches. Even though this thesis contains a larger exposure by more than a factor of three than the next largest search, it does not place a more stringent limit on $n \rightarrow \bar{n}$. Indeed, its limit under the assumption $n_{\text{cand}} = n_{\text{bkg}}$ is slightly lower than the previous SK-I result. The reasons for this will be discussed in detail shortly.

Unlike $NN \rightarrow \pi\pi$, $n \rightarrow \bar{n}$ can be searched for with free neutrons. To compare with free neutron results from [29], the nuclear suppression factor R (Equation 2.16) is used to simply relate bound and free lifetimes. Table 9.3 shows the free $n \rightarrow \bar{n}$ limit from [29], as well as the calculated limits from [23] and this thesis. The calculations use the value $R = 0.517 \times 10^{23} s^{-1}$ from [27], and also take into account theoretical uncertainty, which [27] estimates to be 15%. The tradeoff between exposure and background as described in Section 2.5.1 for essentially zero background free neutron experiments, and large but background-limited bound neutron experiments, has so far led to more stringent limits from bound neutrons, by a factor of 3-4. However, the very low background of free neutron experiments means that they will likely be more competitive in the future, provided they can increase their exposure by more than this factor, which planned experiments like NNbarX [30] are poised to do.

Free neutron [29]	SK-I analysis [23]	This analysis
0.86×10^8 s	2.7×10^8 s	3.8×10^8 s

Table 9.3: Free $n \rightarrow \bar{n}$ lifetime limits, as measured in [29], and as calculated in [23] and this thesis. The calculations incorporate theoretical uncertainty on the nuclear suppression R as calculated in [27].

9.2.2 Comparison with previous SK $n \rightarrow \bar{n}$ analysis

Given that they were performed with the same detector and a subset of the same data, it is instructive to compare the $n \rightarrow \bar{n}$ search of this thesis to the previous search done in SK-I [23], not only in terms of the final result, but also the analysis method.

There are several differences in the simulation stage, described in Section 5.2 and Appendix A. Most significantly, the \bar{n} -nucleon annihilation branching fractions and the pion-nucleon interaction model have both been updated. While the outgoing pion

multiplicities are similar, the increased interactivity of the updated pion model leads to a smaller averaged charged pion momentum (Figure 5.4). This generally leads to less visible energy and fewer Cherenkov rings.

The search method following reconstruction is quite different. The original SK-I analysis used a set of simple cuts, following the FCFV cuts (Section 6.1.6):

- A) $N_{\text{ring}} > 1$;
- B) $700 \text{ MeV} < E_{\text{vis}} < 1300 \text{ MeV}$;
- C) $P_{\text{tot}} < 450 \text{ MeV}/c$;
- D) $750 \text{ MeV}/c^2 < M_{\text{inv}} < 1800 \text{ MeV}/c^2$.

Here P_{tot} and M_{inv} are defined as in Section 7.4.1. Selections C) and D) can be seen in Figure 9.1.

It is straightforward to apply the cut-based method of the SK-I analysis to the new MC, both for $n \rightarrow \bar{n}$ signal and atm.- ν background, to compare the cut-based method and the multivariate method described in Section 8.2. Table 9.4 shows the efficiencies, background rates, systematic uncertainties, and data candidates for the SK-I analysis, the cut-based method applied to the new analysis MC, and the full multivariate analysis described in Chapter 8.

The first two rows of Table 9.4 are useful for comparing changes in the MC simulation between the SK-I analysis in [23] and this analysis, as they both correspond to the SK-I period and use the same analysis method. The lower signal efficiency and higher signal systematic uncertainty in the new MC simulation can both be understood as consequences of the more interactive pion model. The increased interactions lead to fewer particles above Cherenkov threshold and lower visible energy (selections A) and B)), and also further distorts the isotropic spread of outgoing pions (selection

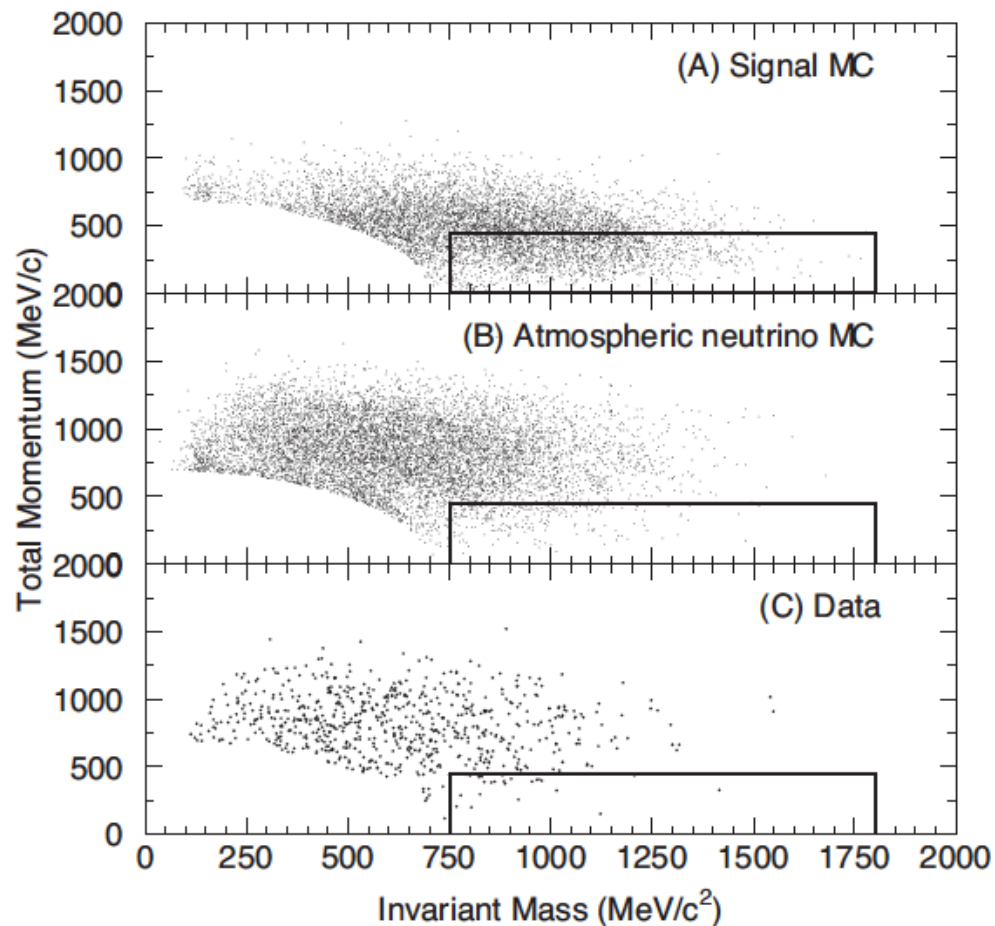


Figure 9.1: Total momentum vs. invariant mass following selections A) and B) for $n \rightarrow \bar{n}$ signal (top), atm.- ν background (middle), and SK-I data (bottom) for the analysis in [23], with boxes indicating selections C) and D).

C)). The slightly higher background rate can be understood from the new weighting procedure, which takes the full three-flavor oscillation analysis into account as opposed to the standard oscillation weight (Equation 4.1), and tends to increase the normalization (Figure 8.2). The updated pion model also leads to fewer particles above Cherenkov threshold and lower visible energy in the background interactions involving pions. However, it also leads to more background events passing selection C), as pions produced in neutrino interactions are generally not isotropic.

	Eff.	σ_{eff}	Bkg. (SK live)	Bkg. (MT-yr)	σ_{bkg}	n_{cand}
SK-I analysis	12.1%	22.9%	24.1 ± 5.7	263 ± 62	23.7%	24
New MC, cut method						
SK-I	8.35%	38.1%	27.9 ± 7.6	304 ± 83	27.2%	20
SK-II	8.49%	43.3%	14.9 ± 4.2	303 ± 85	28.0%	14
SK-III	8.04%	43.5%	10.7 ± 2.8	335 ± 88	26.2%	4
SK-IV	8.05%	45.4%	43.5 ± 11.7	327 ± 88	26.9%	44
New MC, new method						
SK-I	11.0%	37.9%	20.5 ± 7.5	223 ± 82	36.8%	6
SK-II	10.5%	47.6%	10.7 ± 3.6	217 ± 73	33.5%	5
SK-III	9.5%	48.9%	6.5 ± 2.4	204 ± 76	37.3%	3
SK-IV	12.0%	46.9%	33.9 ± 11.0	254 ± 83	32.5%	26

Table 9.4: Comparison of efficiencies, background rates, systematic uncertainties, and data candidates from the SK-I analysis in [23], the new analysis MC using the same cut method, and the new analysis as described in Chapter 8. The background rates are shown with $\pm 1\sigma$ systematic uncertainties to better compare to the number of data events.

It is clear from Table 9.4 that there are several advantages in the multivariate approach used in this analysis relative to the cut-based method of the SK-I analysis. Comparing the results using the new MC, the efficiencies are higher by 15-50% for the multivariate method relative to the cut method, with about the same systematic uncertainties. The expected backgrounds are also lower by 20-40% for the multivariate method relative to the cut method, although the systematic uncertainties are higher.

A crucial aspect in which the multivariate approach performs worse than the cut-based approach is only apparent upon looking at the real data. Data and expected background are consistent within about 1σ for the cut-based method, but they are not for the multivariate method in SK-I-III, reasons for which were discussed in

Section 8.3.3. While there is no ambiguity in interpreting the boosted decision tree output of the data as being consistent with the atm.- ν background in terms of shape (Figure 8.8), the number of events in the data is well below the expected background.

Overall, the increased systematic uncertainties especially in the signal relative to the SK-I search lead to a lower sensitivity than that analysis. Given the overwhelming role of pions in both $n \rightarrow \bar{n}$ and $NN \rightarrow \pi\pi$ — and to a lesser extent, the atm.- ν background that usually contains at least one produced pion — it would of course be good to reduce pion-nucleon interaction uncertainties for future analyses. As a more general prescription, multivariate analyses should be used with caution, particularly for searches with a high expected background. They are useful for increasing efficiency and reducing background relative to cut-based methods for analyses in which the signal process is difficult to extract. However, some more quantitative studies between input variables for MC and real data should be done to ensure the background is well-predicted, while also keeping the analyses sufficiently blind and not choosing any final selection based on the performance of the data.

Appendices

Appendix A

$n \rightarrow \bar{n}$ Branching Fractions

The final state of an antineutron annihilating with a proton or a neutron at low momentum in the residual ^{16}O nucleus is important for a good $n \rightarrow \bar{n}$ simulation. There are many non-negligible branching fractions in the final state, mostly involving multiple pions.

Previous $n \rightarrow \bar{n}$ searches have taken branching fractions from experimental data, and this thesis does the same. Data for antineutron annihilation is scarce, but there is plentiful data for low-energy antiproton annihilation. From isospin symmetry, the annihilations $\bar{p}n \rightarrow (\text{anything})$ and $\bar{p}p \rightarrow (\text{anything})$ are assumed to correspond to $\bar{n}p \rightarrow (\text{anything})$ and $\bar{n}n \rightarrow (\text{anything})$, respectively. In the former case, the sign of charged pions is reversed.

The $n \rightarrow \bar{n}$ search in [23] used $\bar{p}p$ and $\bar{p}d$ data from bubble chamber experiments (where d is deuterium). Branching fractions used in [23] are listed in Table A.1. This analysis used more recent data from the Crystal Barrel experiment [78, 79], which collected data on a large number of exclusive final states. The OBELIX experiment [80] has also collected data for low-energy antineutrons in $\bar{n}p$ annihilation, though for fewer branching fractions.

For $\bar{n}n$ annihilation, over half of the branching fractions are purely pionic (Table A.2). About 25% of branching fractions involve an intermediate resonance including ω , ρ , and η mesons (Table A.3), which mostly decay to pions as well. A smaller percentage of branching fractions involve strange particles (Table A.4). Nuclear effects are simulated for ω and η mesons, while ρ mesons decay rapidly before any interactions. More details on the treatment of resonances can be found in [16].

For $\bar{n}p$ annihilation, the branching fractions are largely the same as the old SK analysis. Some updates are made for particular branching fractions measured in the OBELIX experiment, particularly for the final state $2\pi^+\pi^-m\pi^0$, for $0 \leq m \leq 2$ [80]. Tables A.2 and A.3 show the branching fractions used for $\bar{n}p$ annihilation.

The updated branching fractions have less of an effect on the analysis than the updated pion model. Table A.5 shows the efficiency after each of the $nn \rightarrow \pi^0\pi^0$ selection pre-cuts for MC using the old SK analysis simulation, MC using the updated pion model but the same branching fractions as the old SK analysis, and the MC used in this analysis (both pion model and branching fractions updated). Though a full analysis was not performed with the two former MC sets, the efficiency following each selection pre-cut is more different between the old SK analysis simulation and simulations that use the updated pion model than it is between the latter two simulations.

$\bar{n}p$		$\bar{n}n$	
$\pi^+\pi^0$	1%	$\pi^+\pi^-$	2%
$\pi^+2\pi^0$	8%	$2\pi^0$	1.5%
$\pi^+3\pi^0$	10%	$\pi^+\pi^-\pi^0$	6.5%
$2\pi^+\pi^-\pi^0$	22%	$\pi^+\pi^-2\pi^0$	11%
$2\pi^+\pi^-2\pi^0$	36%	$\pi^+\pi^-3\pi^0$	28%
$2\pi^+\pi^-\omega$	16%	$2\pi^+2\pi^-$	7%
$3\pi^+2\pi^-\pi^0$	7%	$2\pi^+2\pi^-\pi^0$	24%
		$\pi^+\pi^-\omega$	10%
		$2\pi^+2\pi^-2\pi^0$	10%

Table A.1: Branching fractions used in the SK-I $n \rightarrow \bar{n}$ analysis in [23]. The values are taken from bubble chamber experiments [75–77]

$\bar{n}p$		$\bar{n}n$	
$2\pi^0$	0.07%		
$3\pi^0$	0.8%		
$4\pi^0$	0.3%		
$5\pi^0$	1.0%		
$6\pi^0$	0.01%		
$7\pi^0$	0.1%		
$\pi^+\pi^-$	0.3%		
$\pi^+\pi^-\pi^0$	1.6%	$\pi^+\pi^0$	0.1%
$\pi^+\pi^-2\pi^0$	13.0%	$\pi^+2\pi^0$	0.7%
$\pi^+\pi^-3\pi^0$	11.2%	$\pi^+3\pi^0$	14.8%
$\pi^+\pi^-4\pi^0$	3.3%	$\pi^+4\pi^0$	1.4%
$\pi^+\pi^-5\pi^0$	1.4%		
$2\pi^+2\pi^-$	6.0%	$2\pi^+\pi^-$	2.0%
$2\pi^+2\pi^-\pi^0$	13.5%	$2\pi^+\pi^-\pi^0$	17.0%
$2\pi^+2\pi^-2\pi^0$	16.6%	$2\pi^+\pi^-2\pi^0$	10.8%
$2\pi^+2\pi^-3\pi^0$	0.6%	$2\pi^+\pi^-3\pi^0$	30.1%
$3\pi^+3\pi^-$	2.2%	$3\pi^+2\pi^-$	5.5%
$3\pi^+3\pi^-\pi^0$	2.0%	$3\pi^+2\pi^-\pi^0$	3.2%

Table A.2: Purely pionic branching fractions used in this analysis. The data for $\bar{n}n$ is from data in [78]. Some of the data for $\bar{n}p$ has been updated from results in the OBELIX experiment, though most is replicated from [23].

$\bar{n}p$		$\bar{n}n$	
$\rho^0\pi^0$	1.8%		
$\rho^{+/-}\pi^{-/+}$	3.7%		
$\omega\omega$	3.5%		
$\rho^0\omega$	2.4%		
$\pi^0\pi^0\omega$	2.8%	$\pi^+\pi^0\omega$	2.0%
$\pi^+\pi^-\omega$	7.1%	$2\pi^+\pi^-\omega$	12.4%
$\eta\omega$	1.6%		
$\pi^+\pi^-\eta$	1.7%		

Table A.3: Branching fractions with one or more intermediate resonances this analysis. Data for $\bar{n}n$ annihilation is taken from [78] and [79].

K^+K^-	0.1%
ωK^+K^-	0.2%
$K_S K_S$	0.1%
$\pi^{+/-}K^{-/+}K_L$	0.3%
$\pi^{+/-}K^{-/+}K_S$	0.3%
$K^0 K^{+/-}\pi^{-/+}\pi^0$	1.0%
$K_S K_L \pi^+\pi^-$	0.3%

Table A.4: Branching fractions with one or more strange particles in this analysis for $\bar{n}n$ annihilation, from data in [78].

Pre-cut	Old SK	Updated pion model	This analysis
$N_{\text{ring}} > 1$	87.7%	83.1%	82.7%
$400 \text{ MeV} < E_{\text{vis}} < 1600 \text{ MeV}$	70.5%	62.6%	61.8%
$P_{\text{tot}} < 500 \text{ MeV}/c$	45.1%	39.0%	40.5%

Table A.5: Efficiency after each of the $n \rightarrow \bar{n}$ selection pre-cuts, for three different MC sets: MC from the old SK simulation, MC with the new pion model but same branching fractions as the old SK simulation, and MC with both updated pion model and branching fractions (this analysis).

Appendix B

Plots of Multivariate Input Variables for SK-I-III

The main text contains plots of each multivariate input variable for both $n \rightarrow \bar{n}$ and $NN \rightarrow \pi\pi$ for the current data-taking period, SK-IV. This appendix contains plots of the same variables for the SK-I-III data-taking period for reference. Though the plots are similar across detectors, they contain different data sets and Monte Carlo simulations.

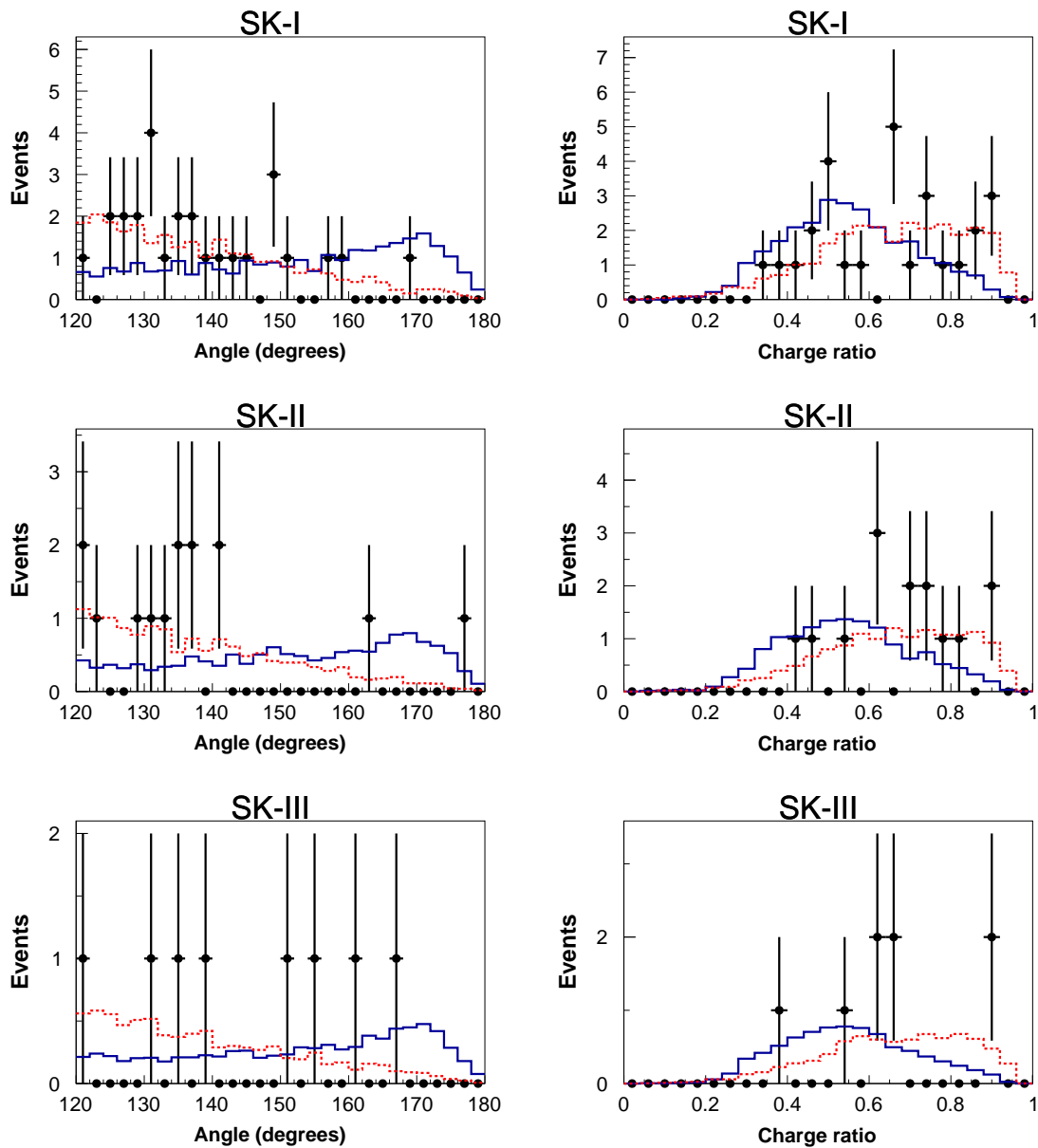


Figure B.1: The angle between μ -like rings (left) and the ratio of charge carried by the most-energetic ring (right) for the $pp \rightarrow \pi^+\pi^+$ search, for signal MC (solid histogram), atm.- ν MC (dashed histogram), and data (crosses). Distributions are normalized to the number of events in the data. Details of each variable are described in the text, in Section 7.2.2.

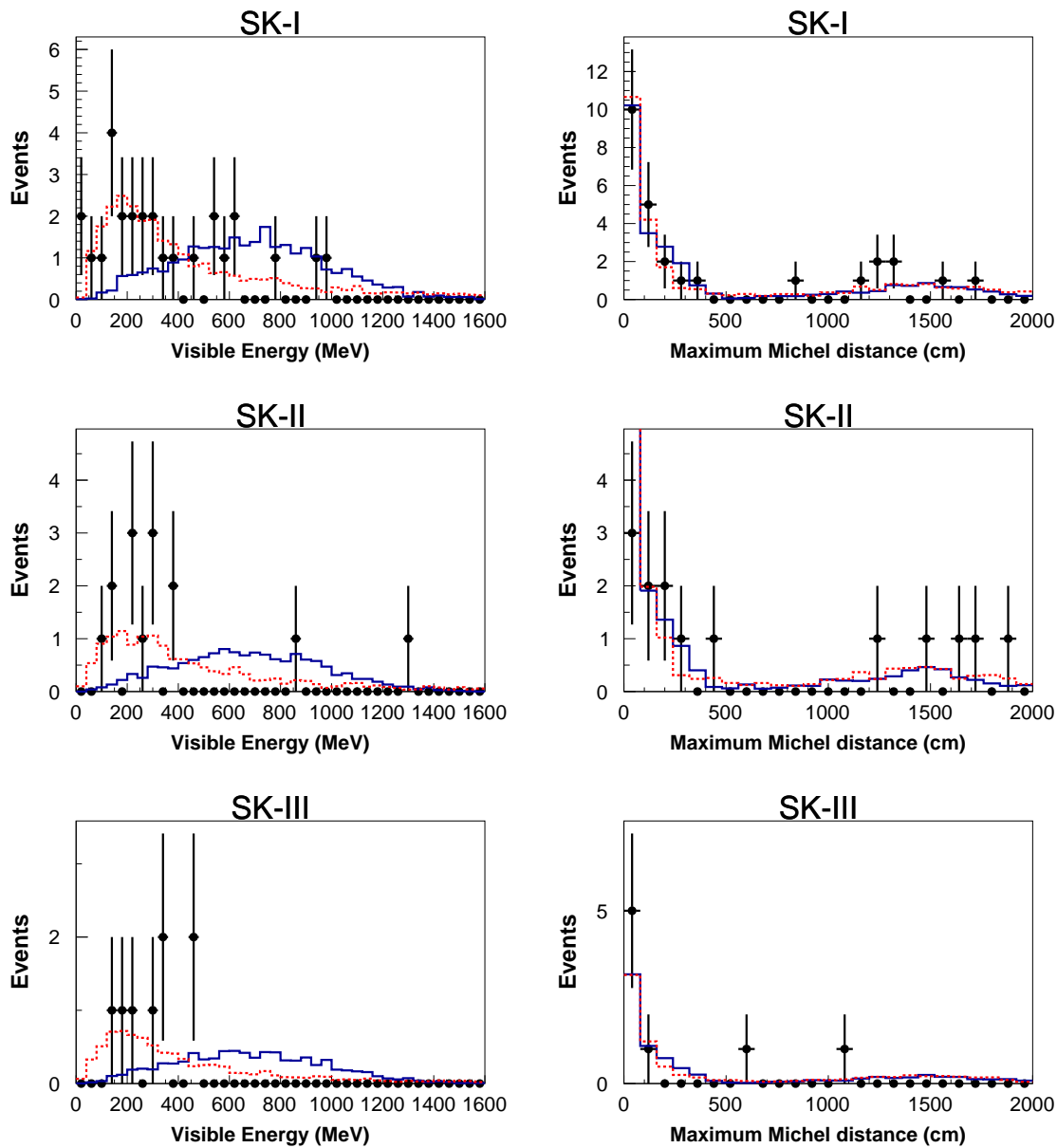


Figure B.2: The visible energy (left) and the maximum distance between the primary vertex and a decay electron vertex (right) for the $pp \rightarrow \pi^+ \pi^+$ search, for signal MC (solid histogram), atm.- ν MC (dashed histogram), and data (crosses). Distributions are normalized to the number of events in the data. Details of each variable are described in the text, in Section 7.2.2.

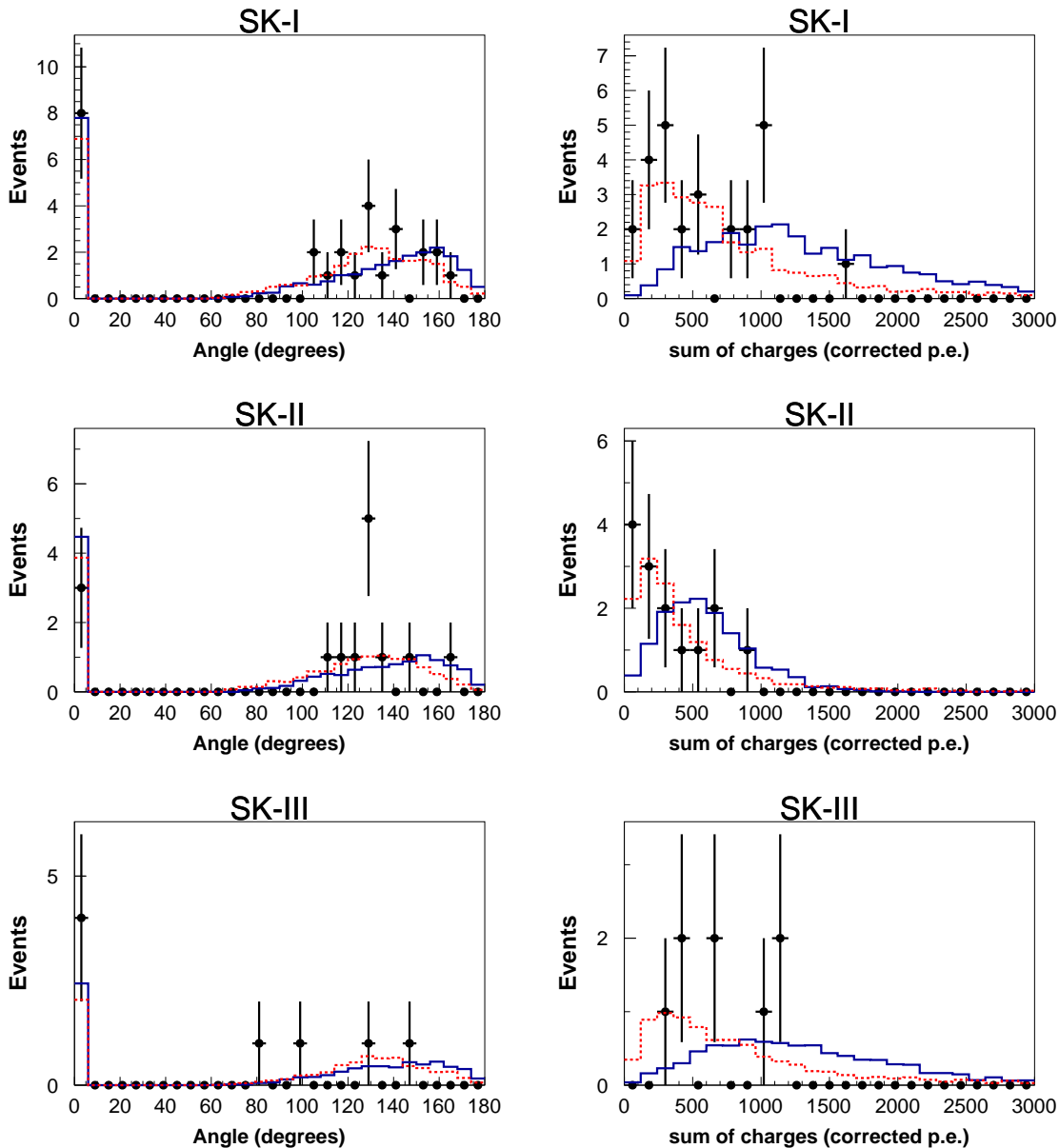


Figure B.3: The largest angle between a μ -like ring direction and a decay electron vertex (left) and the magnitude of the vector sum of RTOT (right) for the $pp \rightarrow \pi^+\pi^+$ search, for signal MC (solid histogram), atm.- ν MC (dashed histogram), and data (crosses). Distributions are normalized to the number of events in the data. Details of each variable are described in the text, in Section 7.2.2.

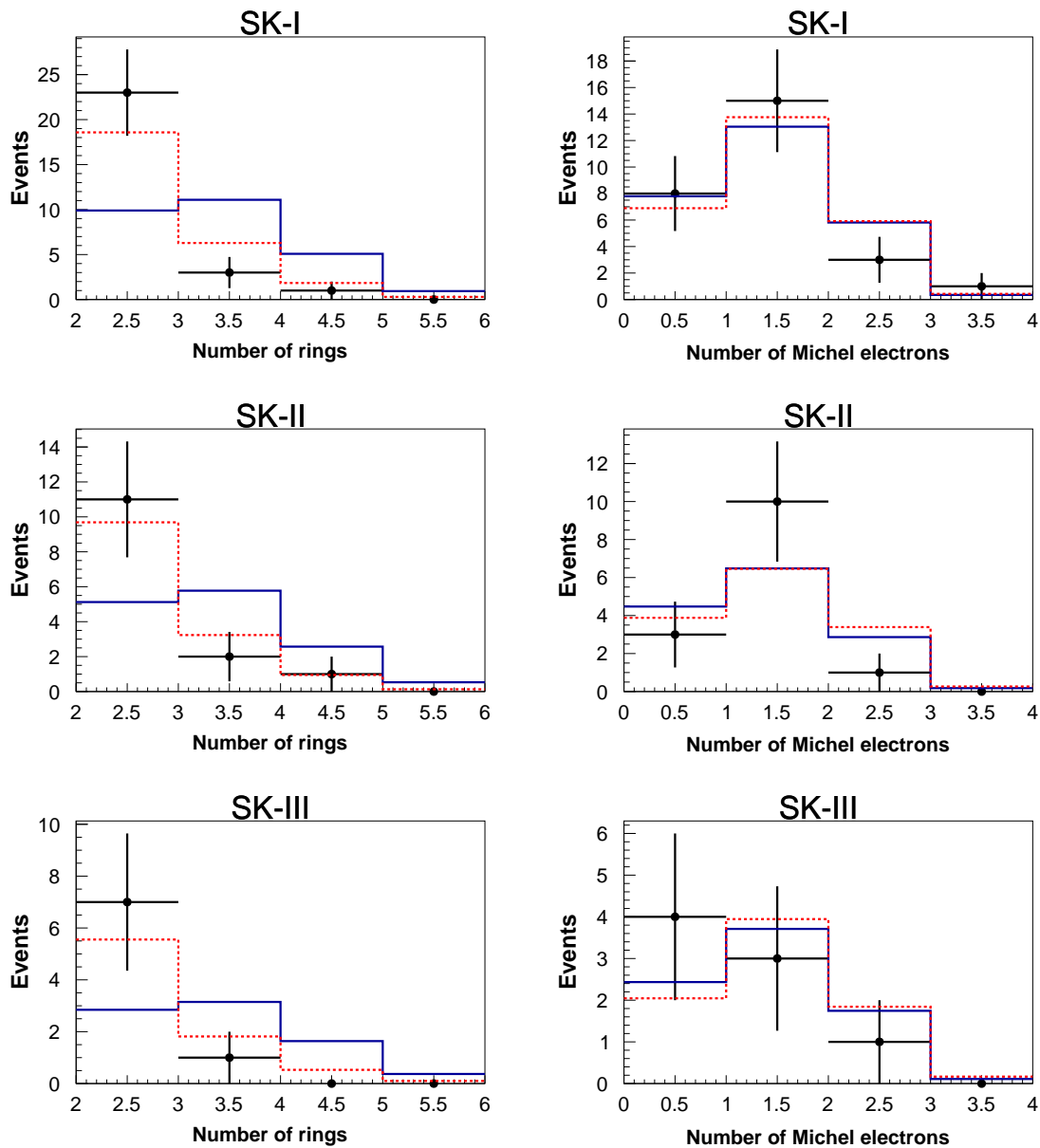


Figure B.4: The number of Cherenkov rings (left) and the number of decay electrons (right) for the $pp \rightarrow \pi^+\pi^+$ search, for signal MC (solid histogram), atm.- ν MC (dashed histogram), and data (crosses). Distributions are normalized to the number of events in the data. Details of each variable are described in the text, in Section 7.2.2.

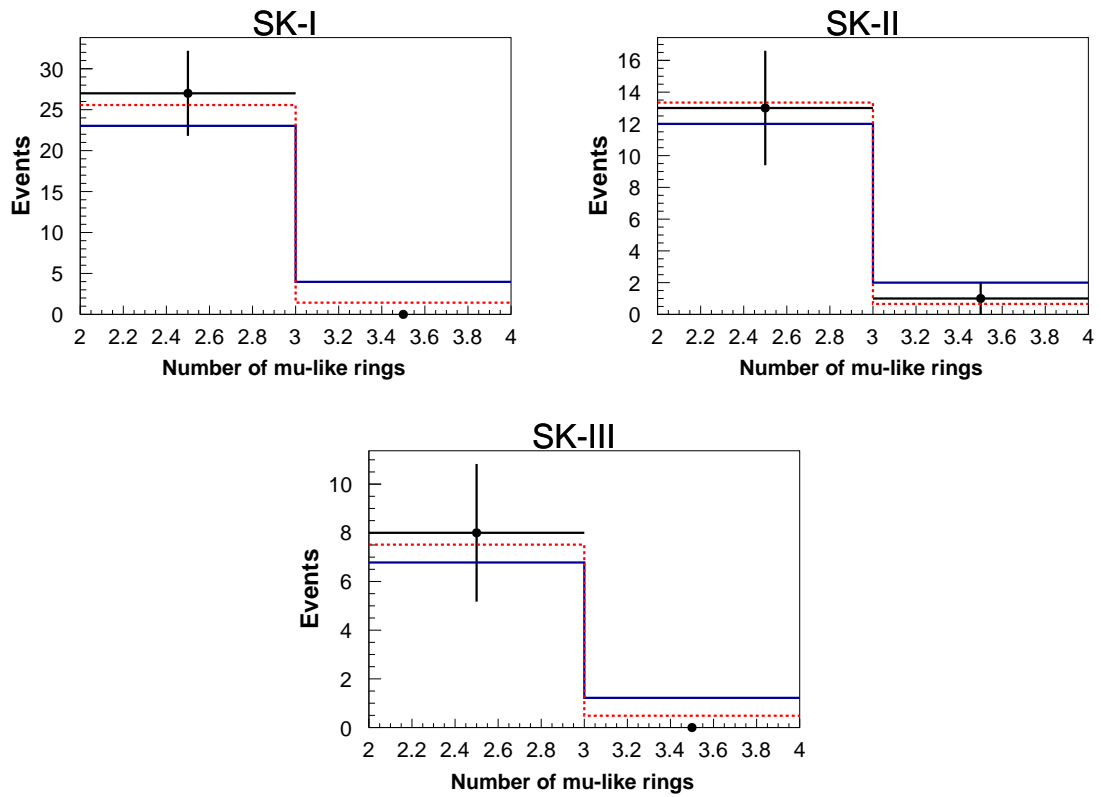


Figure B.5: The number of μ -like rings for the $pp \rightarrow \pi^+\pi^+$ search, for signal MC (solid histogram), atm.- ν MC (dashed histogram), and data (crosses). Distributions are normalized to the number of events in the data. Details are described in the text, in Section 7.2.2.

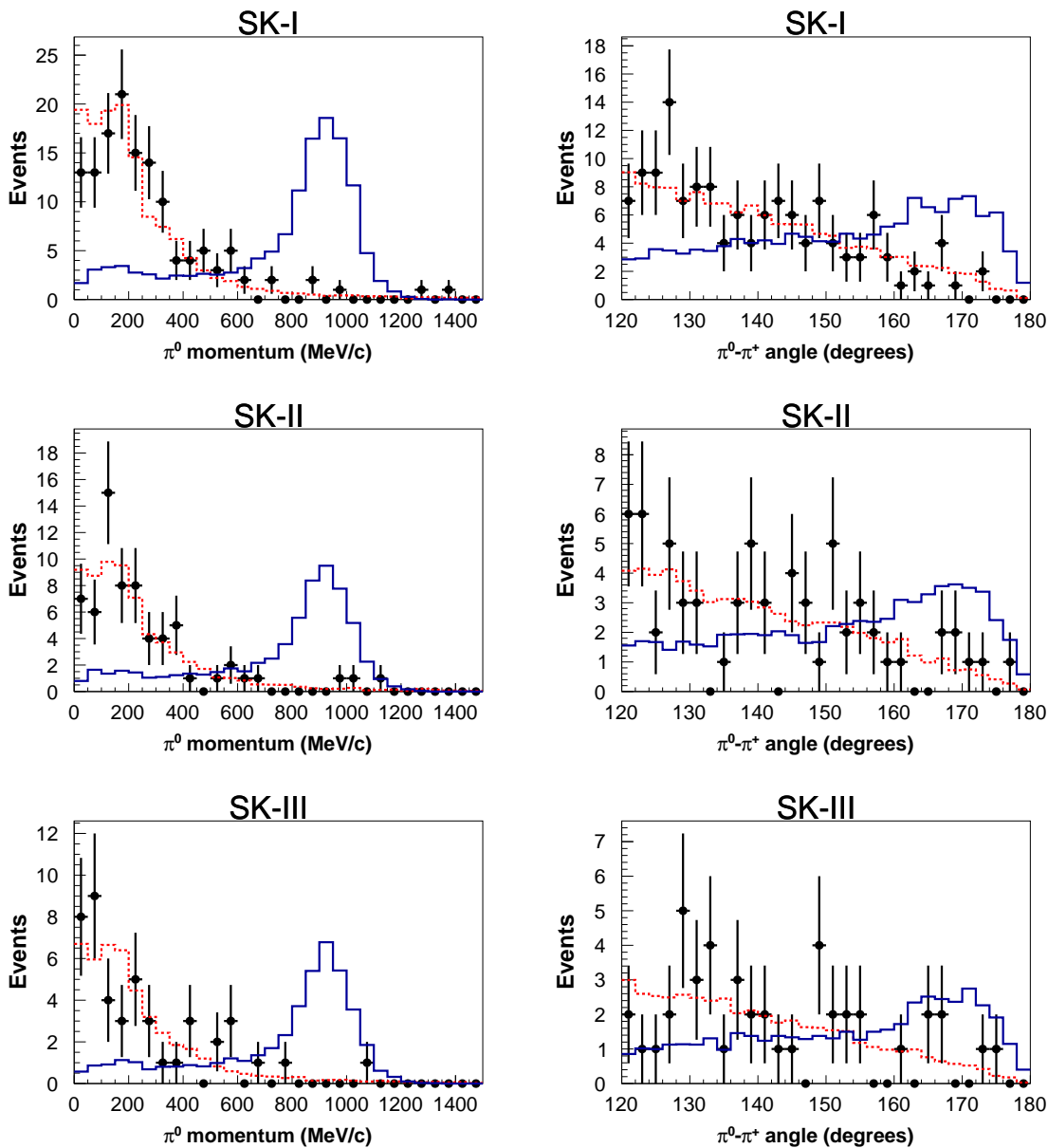


Figure B.6: The π^0 candidate momentum (left) and the angle between the π^0 and π^+ candidate rings (right) for the $pn \rightarrow \pi^+\pi^0$ search, for signal MC (solid histogram), atm.- ν MC (dashed histogram), and data (crosses). Distributions are normalized to the number of events in the data. Details of each variable are described in the text, in Section 7.3.2.

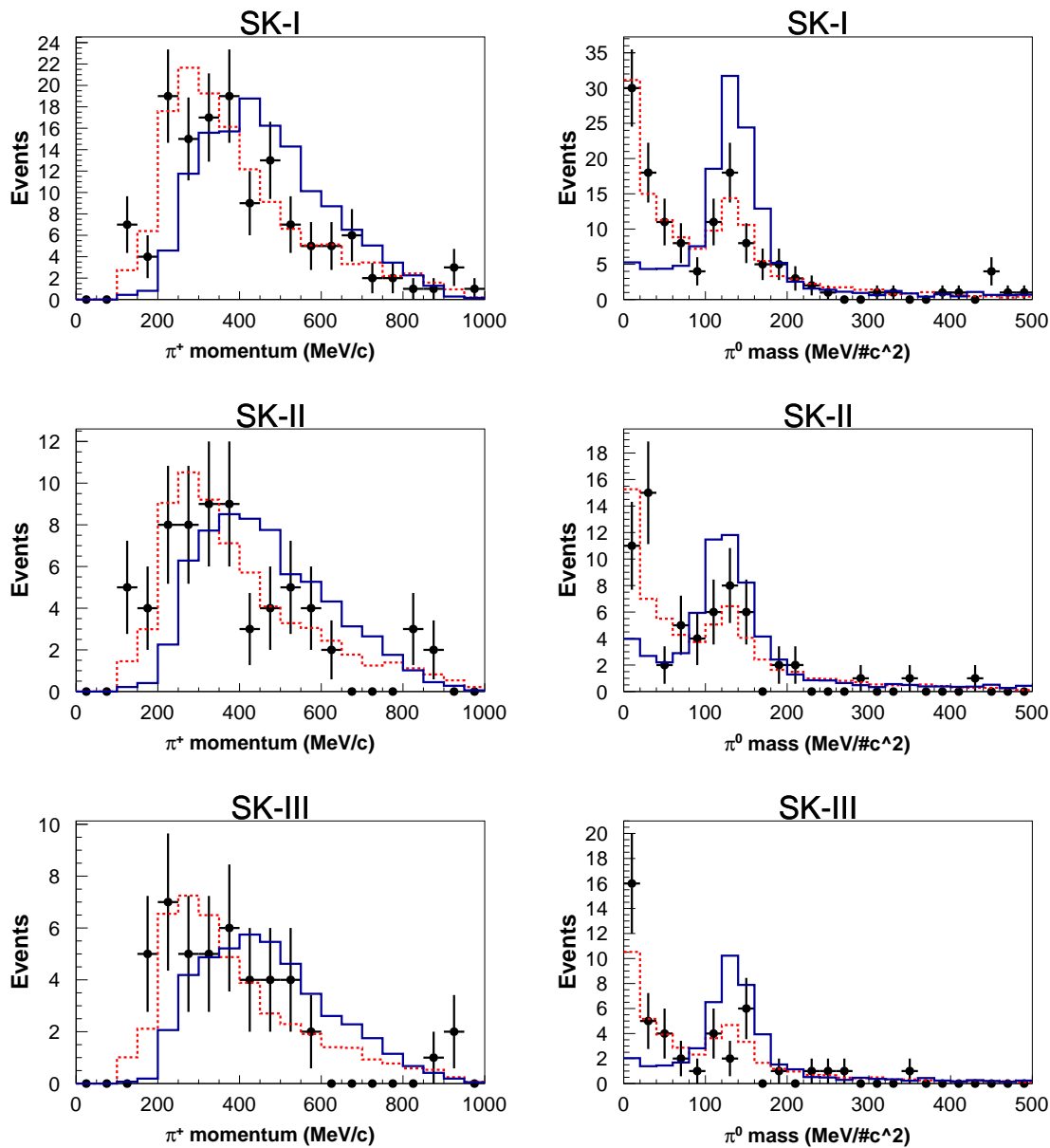


Figure B.7: The π^+ candidate momentum (left) and the invariant mass of the π^0 candidate (right) for the $pn \rightarrow \pi^+\pi^0$ search, for signal MC (solid histogram), atm.- ν MC (dashed histogram), and data (crosses). Distributions are normalized to the number of events in the data. Details of each variable are described in the text, in Section 7.3.2.

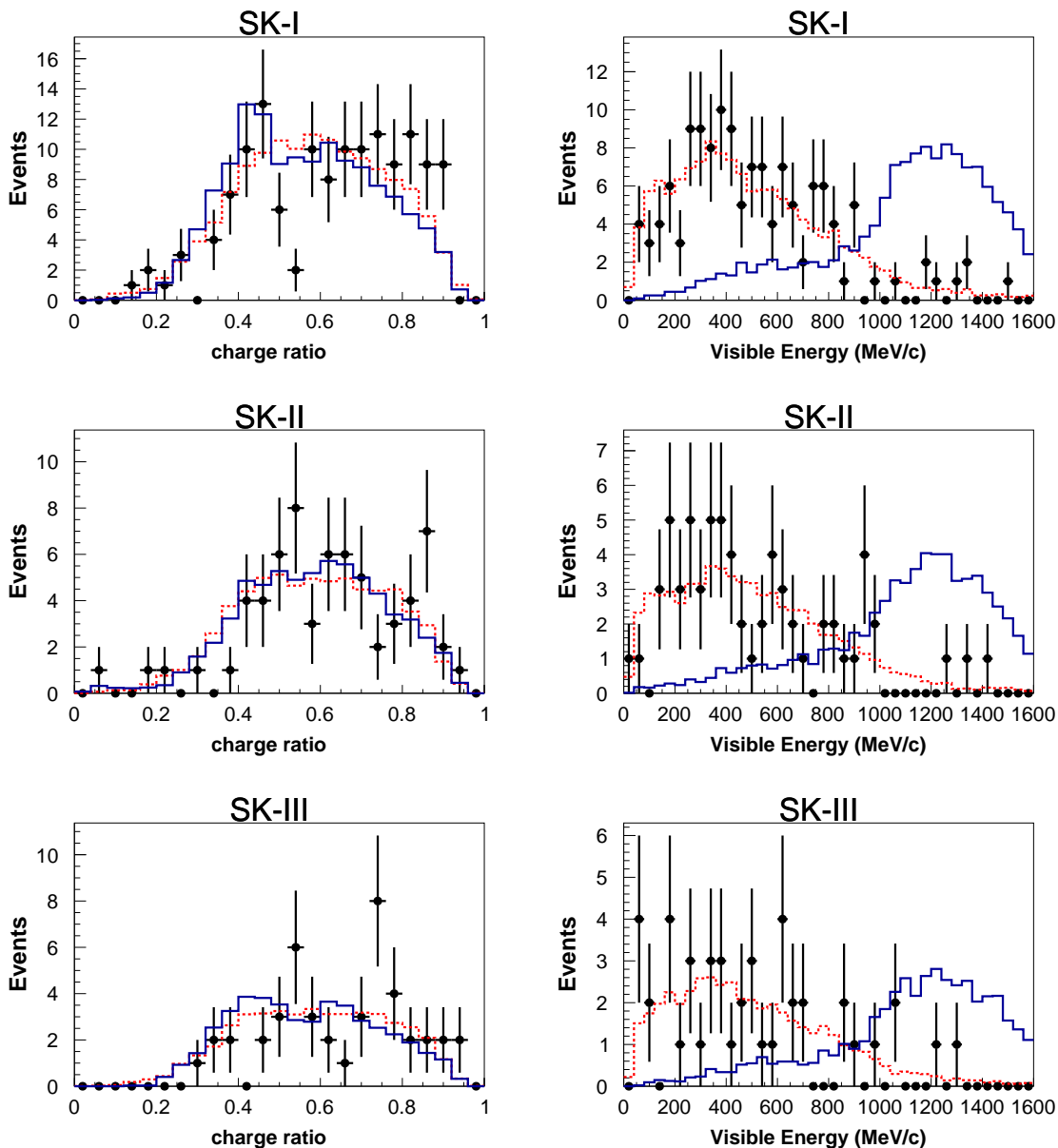


Figure B.8: The ratio of charge carried by the most energetic ring (left) and the visible energy (right) for the $pn \rightarrow \pi^+\pi^0$ search, for signal MC (solid histogram), atm.- ν MC (dashed histogram), and data (crosses). Distributions are normalized to the number of events in the data. Details of each variable are described in the text, in Section 7.3.2.

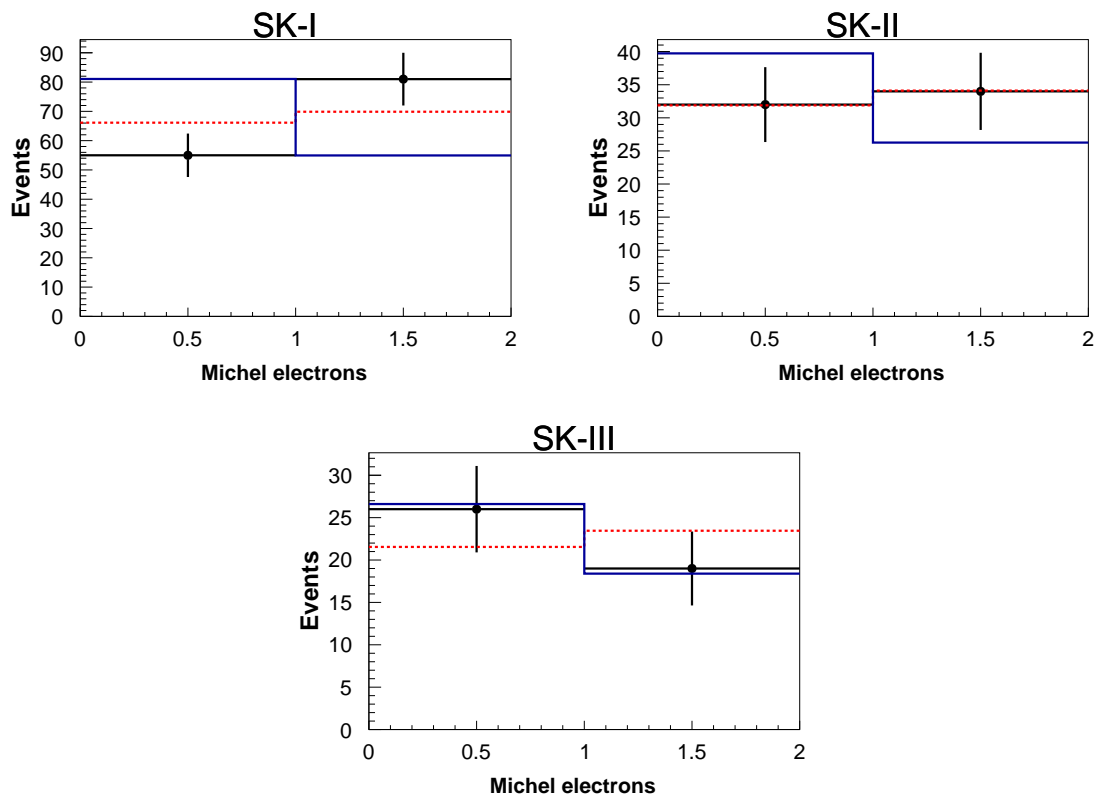


Figure B.9: The number of decay electrons for the $pn \rightarrow \pi^+\pi^0$ search, for signal MC (solid histogram), atm.- ν MC (dashed histogram), and data (crosses). Distributions are normalized to the number of events in the data. Details of each variable are described in the text, in Section 7.3.2.

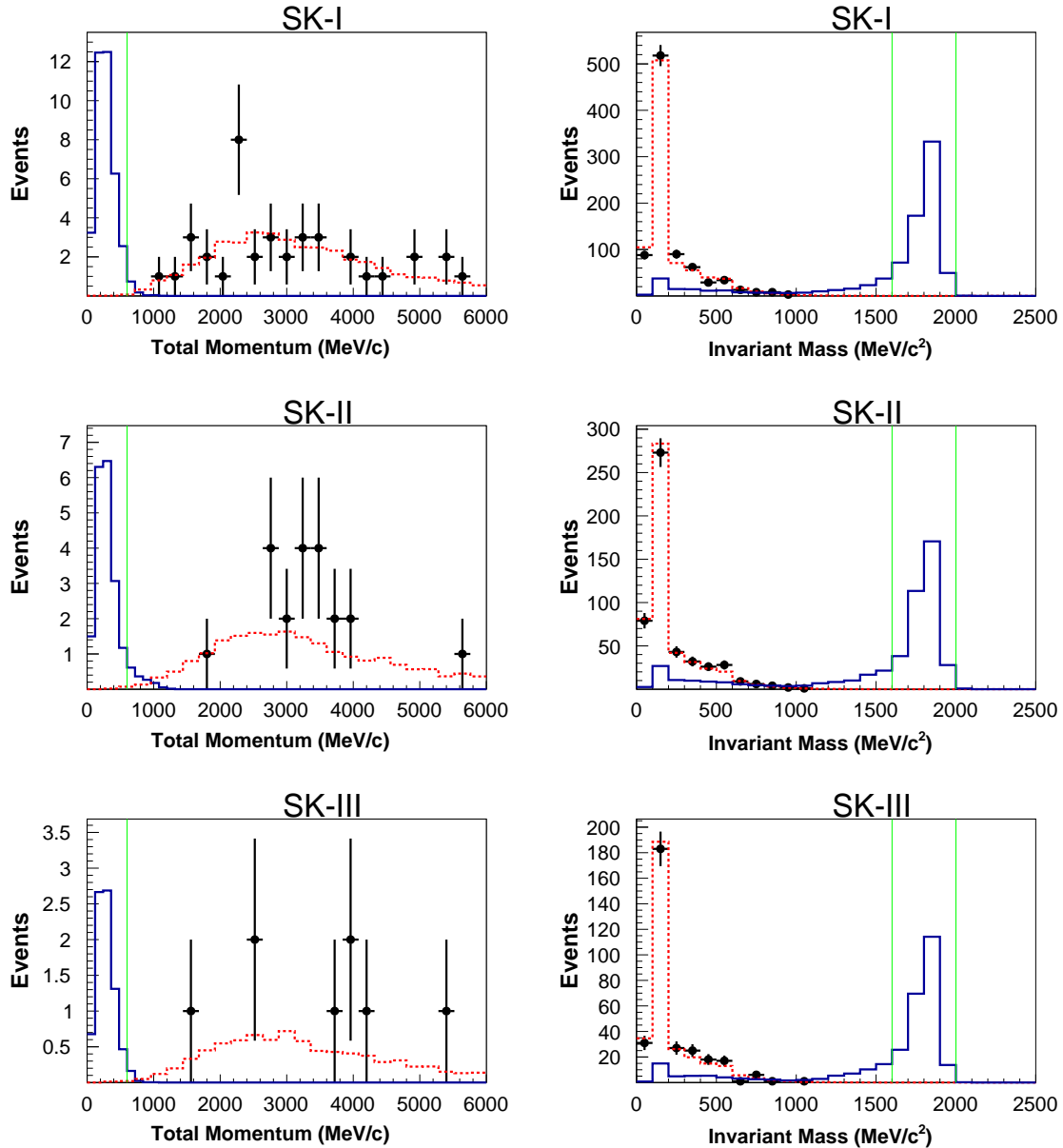


Figure B.10: Total momentum (left) and invariant mass (right) for data (crosses), $nn \rightarrow \pi^0\pi^0$ MC (solid histogram), and atmospheric neutrino MC (dashed histogram). Cuts (C1)-(C3) are applied to both plots. The invariant mass cut (C5) has been applied to the total momentum, and the total momentum cut (C4) to the invariant mass. The thin green vertical lines indicate the locations of the final cuts for each variable. Details of the selection criteria can be found in Section 7.4.1.

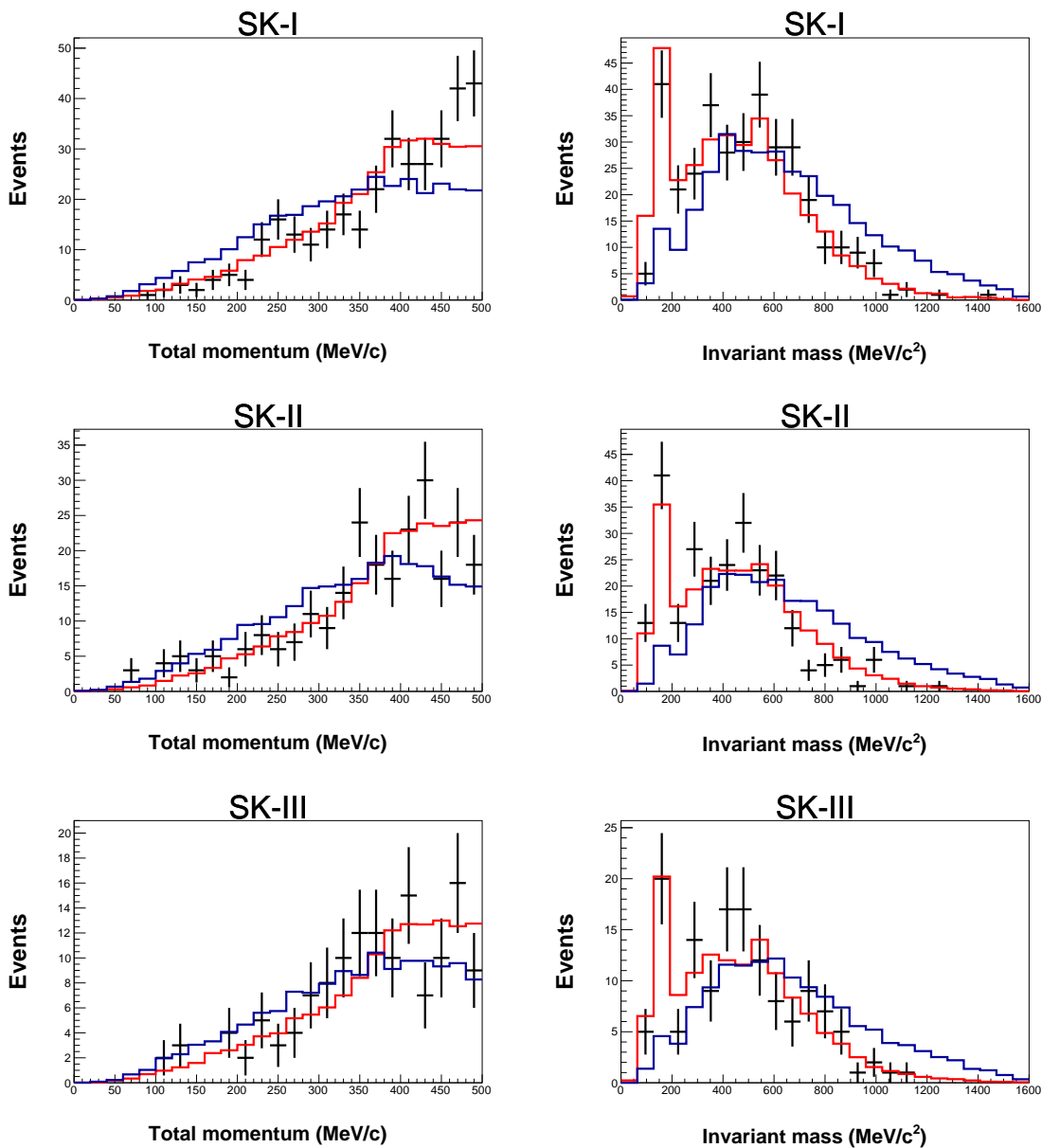


Figure B.11: The total momentum (left) and invariant mass (right) for the $n \rightarrow \bar{n}$ search, for signal MC (solid histogram), atm. ν MC (dashed histogram), and data (crosses). Distributions are normalized to the number of events in the data. Details of each variable are described in the text, in Section 8.2.

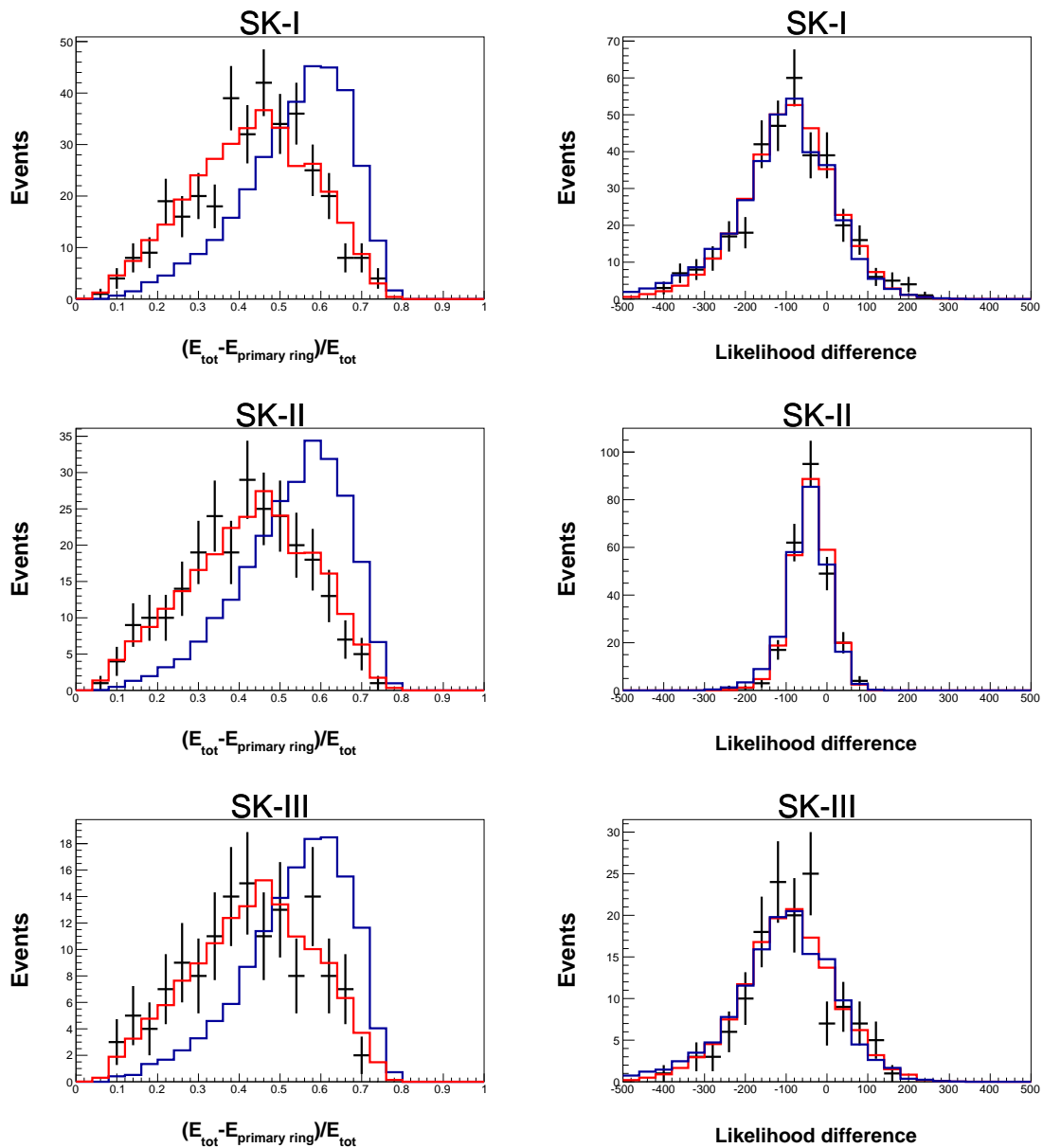


Figure B.12: $(E_{\text{total}} - E_{\text{primary}})/E_{\text{total}}$ (left) and the PID likelihood difference of the leading ring (right) for the $n \rightarrow \bar{n}$ search, for signal MC (solid histogram), atm. ν MC (dashed histogram), and data (crosses). Distributions are normalized to the number of events in the data. Details of each variable are described in the text, in Section 8.2.

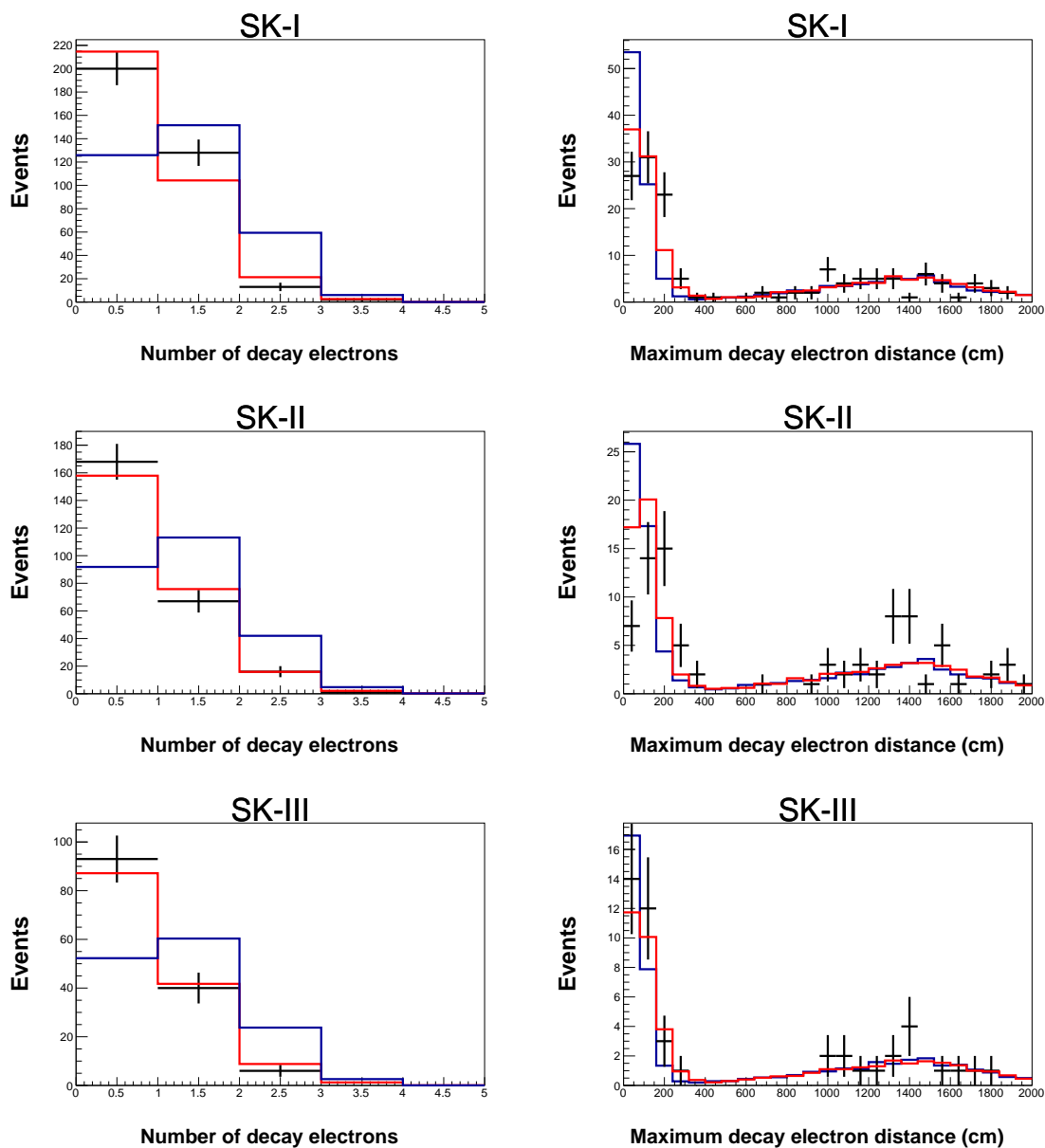


Figure B.13: The number of decay electrons (left) and the maximum distance from the primary vertex to a decay electron vertex (right) for the $n \rightarrow \bar{n}$ search, for signal MC (solid histogram), atm. ν MC (dashed histogram), and data (crosses). Distributions are normalized to the number of events in the data. Details of each variable are described in the text, in Section 8.2. The distance is only shown for events with one or more decay electron.

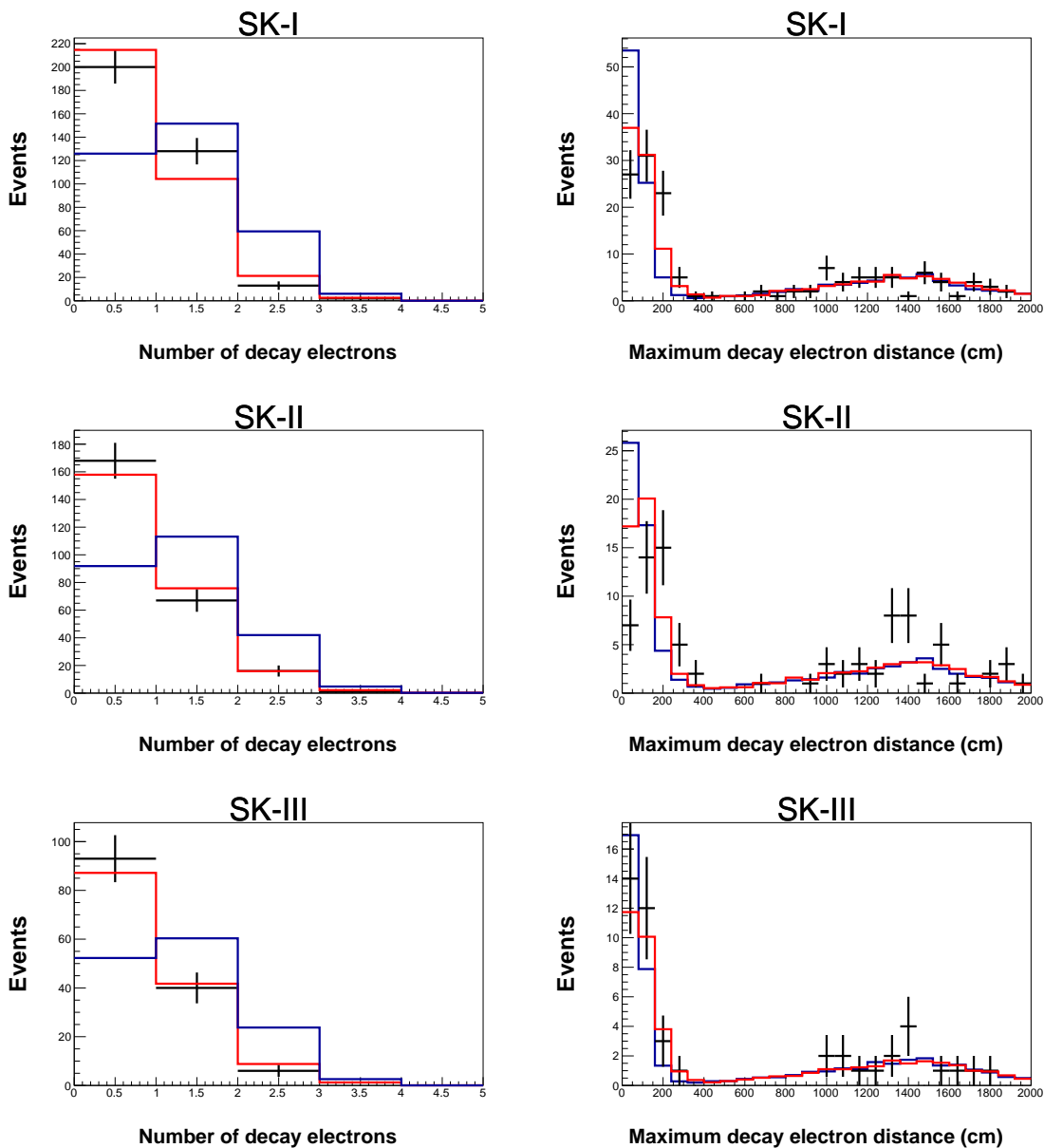


Figure B.14: The sphericity (left) and the number of potential rings (right) for the $n \rightarrow \bar{n}$ search, for signal MC (solid histogram), atm.- ν MC (dashed histogram), and data (crosses). Distributions are normalized to the number of events in the data. Details of each variable are described in the text, in Section 8.2.

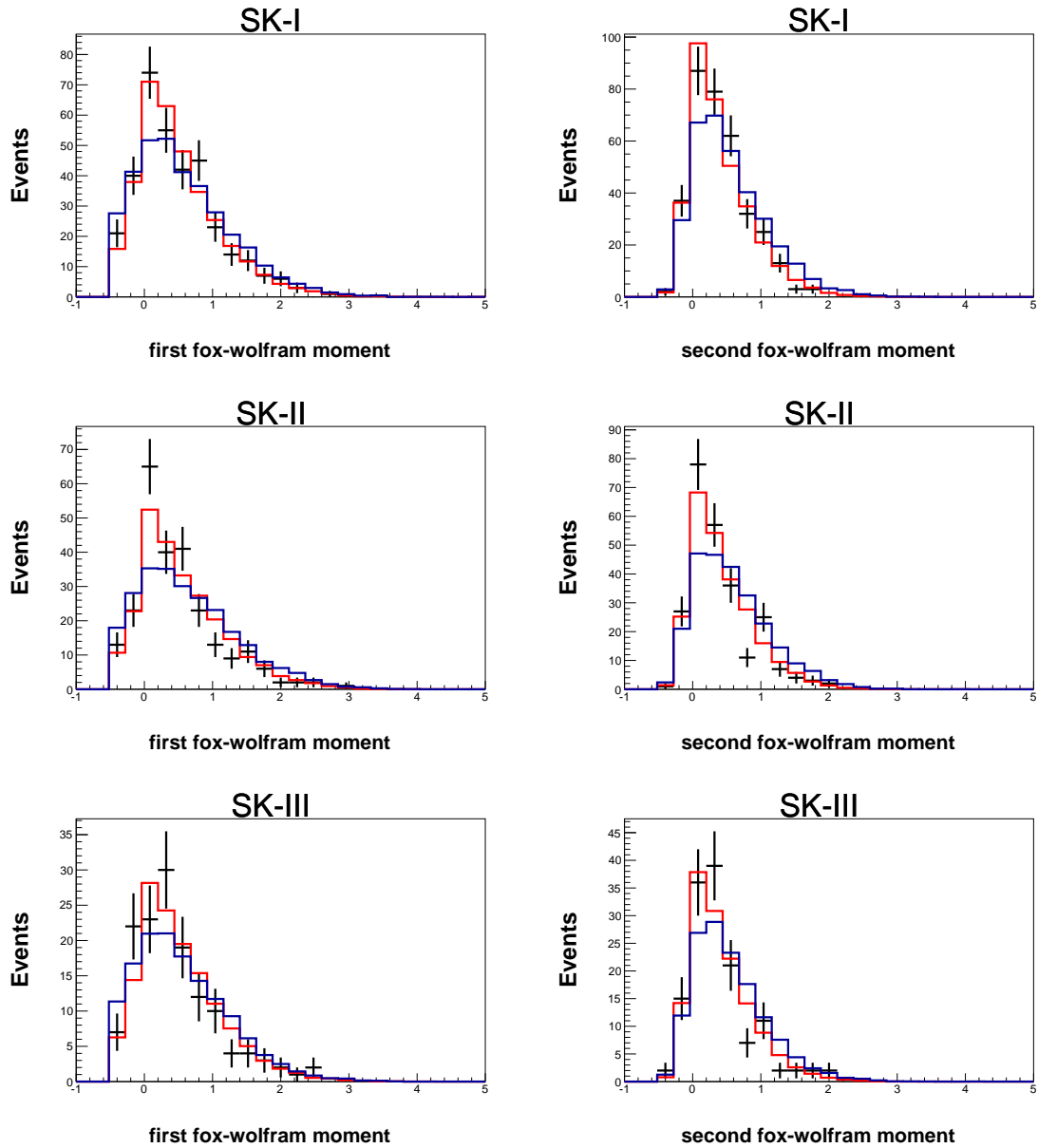


Figure B.15: The first and second Fox-Wolfram moments (left and right, respectively) for the $n \rightarrow \bar{n}$ search, for signal MC (solid histogram), atm.- ν MC (dashed histogram), and data (crosses). Distributions are normalized to the number of events in the data. Details of each variable are described in the text, in Section 8.2.

Appendix C

Limit Calculations

In each of the searches in this analysis, we seek to measure the lifetime (or inversely, the rate) of the process. The results of the searches of course depend on whether any signal events are observed. If signal events are observed in significant excess of the expected background, then the rate Γ is calculated simply as

$$\Gamma = \frac{n_{sig}}{NT\epsilon}, \quad (\text{C.1})$$

where n_{sig} is the number of observed signal events, N the number of targets (for these searches, either ^{16}O nuclei or individual neutrons within the nuclei), T the running time of the experiment, and ϵ the signal detection efficiency.

In the absence of evidence for any signal process, lower limits are set on the time scale of the process. There are two ways to do this, one using purely frequentist statistics and one using Bayesian inference. The Bayesian method is used for these analyses, but the frequentist approach is simple and instructive, and so I briefly discuss it first.

In setting the limit, a *confidence level* is also set. For a counting experiment,

this entails finding a parameter $\mu_{\text{C.L.}}$ associated with the signal process that is the mean of a Poisson distribution, such that any value taken from this distribution has a probability of C.L. to be larger than $\mu_{\text{C.L.}}$. The confidence level in these searches is set to 90%. For a signal process with some expected background b and a number of observed candidates n , μ_{90} can be found by solving

$$0.9 = 1 - \frac{\sum_{m=0}^n e^{-(\mu_{90}+b)} \frac{(\mu_{90}+b)^m}{m!}}{\sum_{m=0}^n e^{-b} \frac{b^m}{m!}}. \quad (\text{C.2})$$

The value of μ_{90} from the solution to Equation C.2 can then be substituted for n_{sig} in Equation C.1.

The main limitation of the frequentist approach is that it has no mechanism for incorporating systematic uncertainties. Intuitively, our notion of “confidence” should include uncertainties on the signal and background processes, which for the searches in this thesis are quite substantial. By assuming prior distributions for these parameters, the Bayesian approach naturally incorporates systematic uncertainties, although it makes the calculation much more complicated.

The limits are calculated using a Bayesian method [91] as follows. The probability of observing n events, given a true process rate of Γ , a true exposure λ (the product of N and T in Equation C.1), a true efficiency ϵ , and a true background rate b , is calculated with the Poisson formula:

$$P(n|\Gamma\lambda\epsilon b) = \frac{e^{-(\Gamma\lambda\epsilon+b)} (\Gamma\lambda\epsilon + b)^n}{n!}. \quad (\text{C.3})$$

As the parameter of interest is the true rate Γ , we apply Bayes’ theorem to get

$$P(\Gamma\lambda\epsilon b|n) = \frac{1}{A} P(n|\Gamma\lambda\epsilon b) P(\Gamma\lambda\epsilon b), \quad (\text{C.4})$$

where A is a normalization constant. The process rate, efficiency, exposure, and background are all independent parameters, so that $P(\Gamma\lambda\epsilon b)$ can be written as a product $P(\Gamma)P(\lambda)P(\epsilon)P(b)$. The probability density function for Γ is obtained by integrating over the exposure, efficiency, and background rate:

$$P(\Gamma|n) = \frac{1}{A} \int \int \int \frac{e^{-(\Gamma\lambda\epsilon+b)} (\Gamma\lambda\epsilon + b)^n}{n!} P(\Gamma) P(\lambda) P(\epsilon) P(b) d\lambda d\epsilon db. \quad (\text{C.5})$$

A confidence level can be obtained by integrating $P(\Gamma|n)$ up to an upper limit on the rate, Γ_{limit} :

$$\text{C.L.} = \int_0^{\Gamma_{\text{limit}}} P(\Gamma|n) d\Gamma, \quad (\text{C.6})$$

and the lower lifetime limit τ_{limit} is just the inverse of Γ_{limit} .

The benefit of this approach is that it allows incorporation of systematic uncertainties. The probabilities for λ , ϵ , and b are taken to be Gaussian, with symmetric σ values for ϵ and b taken from the systematic uncertainties described in Sections 7.5; the uncertainty in λ is assumed to be negligible in each search. The probability for Γ is assumed to be uniform for $\Gamma > 0$.

Since the searches were performed for four different detectors, Equation C.5 must be generalized for detector-specific n , λ , ϵ , and b :

$$P(\Gamma|n_1, n_2, n_3, n_4) = \frac{1}{A} \prod_{i=1}^4 \int \int \int \frac{e^{-(\Gamma\lambda_i\epsilon_i+b_i)} (\Gamma\lambda_i\epsilon_i + b_i)^{n_i}}{n_i!} P(\Gamma) P(\lambda_i) P(\epsilon_i) P(b_i) d\lambda_i d\epsilon_i db_i. \quad (\text{C.7})$$

In this calculation, systematic uncertainties are conservatively assumed to be fully correlated across SK detectors. This is a reasonable assumption, since the dominant

systematic uncertainties in these searches are related to MC simulation, and thus are roughly detector-independent.

Finally, for very low background searches, the statistical uncertainty is taken into account by convoluting the Gaussian prior with a Poisson distribution:

$$P(b) = \int \frac{e^{-b_{MC}} (b_{MC})^{n_b}}{n_b!} \exp\left(-\frac{(bC - b_{MC})^2}{2\sigma_b^2}\right) db_{MC}, \quad (\text{C.8})$$

where n_b is the number of background in the un-normalized MC, b_{MC} is the number of true un-normalized background, and C is the MC oversampling factor.

Bibliography

- [1] H. Weyl. Zeitschrift für Physik **56** 330 (1929). [Surveys in High Energy Physics 5, 261 (1986)]
- [2] E. C. G. Stueckelberg. Helvetica Physica Acta **11** 299 (1938)
- [3] E. P. Wigner. Proceedings of the American Philosophical Society **93** (1949)
- [4] C. Sutton. New Scientist **27** 1016 (1980)
- [5] G. N. Flerov, *et al.* Soviet Physics-Doklady. **3** 79 (1958)
- [6] D. H. Perkins. Annual Review of Nuclear and Particle Science **34** 1 (1984)
- [7] S. Glashow. Nuclear Physics **22** 579 (1961)
- [8] S. Weinberg. Physical Review Letters **19** 1264 (1967)
- [9] A. Salam. American Institute of Physics Conference Proceedings **C680519** 367 (1968)
- [10] G. Aad, *et al.* Physics Letters **B716** 1 (2012)
- [11] S. Chatrchyan, *et al.* Physics Letters **B716** 30 (2012)
- [12] A. Sakharov. JETP Letters **5** 32 (1967)

- [13] K. Abe, *et al.* Physical Review **D90**, 7 072005 (2014)
- [14] V. Takhistov, *et al.* Physical Review Letters **113**, 10 101801 (2014)
- [15] K. Abe, *et al.* Physical Review Letters **113**, 12 121802 (2014)
- [16] H. Nishino, *et al.* Physical Review **D85** 112001 (2012)
- [17] C. Regis, *et al.* Physical Review **D86** 012006 (2012)
- [18] J. L. Raaf. Nuclear Physics Proceedings Supplements **229-232** 559 (2012)
- [19] H. Georgi, S. Glashow. Physical Review Letters **32** 438 (1974)
- [20] M. Fukugita, T. Yanagida. Physics Letters **B174** 45 (1986)
- [21] S. Rao, R. Shrock. Physics Letters **B116** 238 (1982)
- [22] J. M. Arnold, B. Fornal, M. B. Wise. Physical Review **D87**, 7 075004 (2013)
- [23] K. Abe, *et al.* Physical Review **D91** 072006 (2015)
- [24] K. S. Babu, R. N. Mohapatra, S. Nasri. Physical Review Letters **97** 131301 (2006)
- [25] K. S. Babu, P. S. Bhupal Dev, R. N. Mohapatra. Physical Review **D79** 015017 (2009)
- [26] K. Babu, *et al.* Physical Review **D87**, 11 115019 (2013)
- [27] E. Friedman, A. Gal. Physical Review **D78** 016002 (2008)
- [28] S. Gardner, E. Jafari. Physical Review **D91**, 9 096010 (2015)
- [29] M. Baldo-Ceolin, *et al.* Zeitschrift für Physik **C63** 409 (1994)

- [30] K. Babu, *et al.* Arxiv preprint **hep-ex/1310.8593** (2013)
- [31] T. Jones, *et al.* Physical Review Letters **52** 720 (1984)
- [32] M. Takita, *et al.* Physical Review **D34** 902 (1986)
- [33] C. Berger, *et al.* Physics Letters **B240** 237 (1990)
- [34] J. Chung, *et al.* Physical Review **D66** 032004 (2002)
- [35] M. Bergevin. Ph.D Thesis, University of Guelph (2010)
- [36] C. Dover, A. Gal, J. Richard. Physical Review **D27** 1090 (1983)
- [37] J. Goity, M. Sher. Physics Letters **B346** 69 (1995)
- [38] C. Csaki, E. Kuffik, T. Volansky. Physical Review Letters **112** 131801 (2014)
- [39] C. Berger, *et al.* Physics Letters **B269** 227 (1991)
- [40] M. Litos, *et al.* Physical Review Letters **112**, 13 131803 (2014)
- [41] B. Henning. Undergraduate Thesis **Boston University** (2009)
- [42] Y. Fukuda, *et al.* Nuclear Instruments and Methods in Physics Research **A501** 418 (2003)
- [43] H. Nishino. Ph.D Thesis, University of Tokyo (2009)
- [44] H. Kume, *et al.* Nuclear Instruments and Methods in Physics Research **205** 443 (1983)
- [45] A. Suzuki, *et al.* Nuclear Instruments and Methods in Physics Research **A329** 299 (1993)

- [46] R. Becker-Szendy, *et al.* Nuclear Instruments and Methods in Physics Research **A324** 363 (1993)
- [47] S. Yamada, *et al.* IEEE Transactions on Nuclear Science **57** 428 (2010)
- [48] H. Nishino, *et al.* Nuclear Instruments and Methods in Physics Research **A610** 710 (2009)
- [49] K. Abe, *et al.* Nuclear Instruments and Methods in Physics Research **A737** 253 (2014)
- [50] T. Tanaka. Ph.D Thesis, University of Tokyo (2011)
- [51] M. Dziomba. Ph.D Thesis, University of Washington (2012)
- [52] M. Nakahata, *et al.* Nuclear Instruments and Methods in Physics Research **A421** 113 (1999)
- [53] M. Honda, *et al.* Physical Review **D83** 123001 (2011)
- [54] M. Honda, *et al.* Physical Review **D70** 043008 (2004)
- [55] M. Honda, *et al.* Physical Review **D75** 043006 (2007)
- [56] G. Battistoni, *et al.* Astroparticle Physics **19** 269 (2003). [Erratum: Astropart. Phys.19,291(2003)]
- [57] G. D. Barr, *et al.* Physical Review **D70** 023006 (2004)
- [58] Y. Hayato. Acta Physica Polonica **B40** 2477 (2009)
- [59] C. H. Llewellyn Smith. Physics Reports **3** 261 (1972)

- [60] R. A. Smith, E. J. Moniz. Nuclear Physics **B43** 605 (1972). [Erratum: Nucl. Phys.B101,547(1975)]
- [61] L. Ka Pik. Ph.D Thesis, University of Tokyo (2012)
- [62] D. Rein, L. M. Sehgal. Annals of Physics **133** 79 (1981)
- [63] M. Gluck, E. Reya, A. Vogt. European Physical Journal **C5** 461 (1998)
- [64] A. Bodek, U. K. Yang. In *2nd International Workshop on Neutrino-Nucleus Interactions in the Few GeV Region (NuInt 02) Irvine, California, December 12-15, 2002* (2003)
- [65] M. Derrick, *et al.* Physical Review **D17** 1 (1978)
- [66] S. Barlag, *et al.* Zeitschrift für Physik **C11** 283 (1982). [Erratum: Z. Phys.C14,281(1982)]
- [67] T. Sjostrand. CERN Program Library **CERN-TH-7112-93** (1994)
- [68] P. de Perio. American Institute of Physics Conference Proceedings **1405** 223 (2011)
- [69] L. L. Salcedo, *et al.* Nuclear Physics **A484** 557 (1988)
- [70] R. Brun, F. Carminati, S. Giani. CERN Program Library **CERN-W5013** (1994)
- [71] M. Nakahata, *et al.* Journal of the Physical Society of Japan **55** 3786 (1986)
- [72] C. Zeitnitz, T. A. Gabriel. Nuclear Instruments and Methods in Physics Research **A349** 106 (1994)
- [73] K. Nakamura, *et al.* Nuclear Physics **A268** 381 (1976)

- [74] T. Yamazaki, Y. Akaishi. *Physics Letters* **B453** 1 (2000)
- [75] R. Armenteros, B. French. *High Energy Physics*, volume 4. Academic, New York (1969)
- [76] P. Pavlopoulos, *et al.* *American Institute of Physics Conference Proceedings* **41** 340 (1978)
- [77] G. Backenstoss, *et al.* *Nuclear Physics* **B228** 424 (1983)
- [78] E. Klempt, C. Batty, J.-M. Richard. *Physics Reports* **413** 197 (2005)
- [79] C. Amsler, *et al.* *Nuclear Physics* **A720** 357 (2003)
- [80] T. Bressani, A. Filippi. *Physics Reports* **383** 213 (2003)
- [81] E. Richard. Ph.D Thesis, University of Tokyo (2015)
- [82] M. Litos. Ph.D Thesis, Boston University (2010)
- [83] Y. Takenaga. Ph.D Thesis, University of Tokyo (2008)
- [84] K. Abe, *et al.* *Physical Review Letters* **110**, 18 181802 (2013)
- [85] T. Barszczak. Ph.D Thesis, University of California Irvine (2005)
- [86] R. Wendell, *et al.* *Physical Review* **D81** 092004 (2010)
- [87] K. Abe, *et al.* *Physical Review* **D88**, 3 032002 (2013)
- [88] A. Hocker, *et al.* *Proceedings of Science* **ACAT** 040 (2007)
- [89] B. P. Roe, *et al.* *Nuclear Instruments and Methods in Physics Research* **A543**, 2-3 577 (2005)

- [90] V. M. Abazov, *et al.* Physical Review **D78** 012005 (2008)
- [91] R. M. Barnett, *et al.* Physical Review **D54** 1 (1996)
- [92] K. Abe, *et al.* Arxiv preprint **hep-ex/1109.3262** (2011)

Curriculum Vitae

Jeffrey D. Gustafson

590 Commonwealth Avenue
Department of Physics, Boston University
Boston, MA 02215, U.S.A.

Mobile: (651)357-6771
Office: (617)353-6040
E-mail: jdgustaf@bu.edu

EDUCATION

- Boston University, Boston, Massachusetts
 - **PhD** in Experimental Particle Physics, expected in May 2016
 - **MA** in Physics, January 2012
- Macalester College, St. Paul, Minnesota
 - **Bachelor of Arts** in Physics, May 2009
 - **Additional Major** in Mathematics, May 2009

RESEARCH EXPERIENCE

- Super-Kamiokande
 - Simulation software:
 - * Update of Monte Carlo generator for dinucleon decay
 - * Design of custom Monte Carlo generator for neutron-antineutron oscillation
 - Reconstruction and Analysis software:
 - * Update and maintenance of upward-going muon reduction and analysis software
 - * Custom analysis modules for dinucleon decay and neutron-antineutron oscillation analyses

TEACHING EXPERIENCE

- Boston University Academy
 - Discussion and lab teaching assistant for high-school physics, Spring 2015
- Boston University

- Discussion session teaching assistant for physics, Fall 2010 - Fall 2011
- Macalester College
 - Tutoring center, Fall 2007 - Spring 2009

PRESENTATIONS

- **Searches for $\Delta B = 2$ processes at Super-Kamiokande**
 Jeff Gustafson
International Conference on Baryon and Lepton Number Violation Conference, Parallel Talk
 Amherst, MA, April 2015

SELECTED PUBLICATIONS

- **Search for dinucleon decay into pions at Super-Kamiokande**
 J. Gustafson *et al.* [Super-Kamiokande Collaboration]
 Phys. Rev. D **91**:072009 (2015)

OTHER PUBLICATIONS

- **Limits on sterile neutrino mixing using atmospheric neutrinos in Super-Kamiokande**
 K. Abe *et al.* [Super-Kamiokande Collaboration]
 Phys. Rev. D **91**:052019 (2015)
- **Test of Lorentz invariance with atmospheric neutrinos**
 K. Abe *et al.* [Super-Kamiokande Collaboration]
 Phys. Rev. D **91**:052003 (2015)
- **Search for trilepton decay via $p \rightarrow e^+ \nu \nu$ and $p \rightarrow \mu^+ \nu \nu$ in the Super-Kamiokande experiment**
 V. Takhistov *et al.* [Super-Kamiokande Collaboration]
 Phys. Rev. Lett. **113**:101801 (2014)

REFERENCES

- Prof. Edward Kearns
 Boston University
 Department of Physics
 590 Commonwealth Avenue
 Boston, MA 02215
 Office Phone: (617)353-3425
 E-mail: kearns@bu.edu